

A SEARCH FOR THE HIGGS BOSON IN ITS ASSOCIATED PRODUCTION WITH A  $W$   
VECTOR BOSON IN  $p\bar{p}$  COLLISIONS AT  $\sqrt{s} = 1.96$  TeV

The members of the Committee approve the doctoral  
dissertation of Venkatesh S. Kaushik

Jaehoon Yu  
Supervising Professor

---

Andrew Brandt

---

Kaushik De

---

Alex Weiss

---

Andy White

---

Dean of the Graduate School

---

A SEARCH FOR THE HIGGS BOSON IN ITS ASSOCIATED PRODUCTION WITH A  $W$   
VECTOR BOSON IN  $p\bar{p}$  COLLISIONS AT  $\sqrt{s} = 1.96$  TeV

by  
VENKATESH S. KAUSHIK

Presented to the Faculty of the Graduate School of  
The University of Texas at Arlington in Partial Fulfillment  
of the Requirements  
for the Degree of

DOCTOR OF PHILOSOPHY

THE UNIVERSITY OF TEXAS AT ARLINGTON

December 2007

Copyright © by Venkatesh S. Kaushik 2007

All Rights Reserved

To My Parents — Mrs. Laxmi and Mr. Srinivasa Murthy

A verse from the *Bhagavad Gita*

पूर्णमदः पूर्णमिदं पूर्णात् पूर्णमुदच्यते ।  
पूर्णस्य पूर्णमादाय पूर्णमेवावशिष्यते ॥  
ॐ शान्तिः शान्तिः शान्तिः

ईशोपनिशद्

## ACKNOWLEDGEMENTS

I could not have been where I am today without the constant support, unconditional love and encouragement of my parents Laxmi and Srinivasa Murthy, and my brother Srikanth, who have made tremendous sacrifices for my well being and success. My parents have taught me the virtues of delayed gratification, hard work and patience. I am deeply indebted to them for supporting me in every step of the way.

I sincerely express my gratitude towards my supervising professor Dr. Jaehoon Yu for his mentoring and advice during the past five years. He has always stressed the importance of good communication and being trustworthy. He was always available to answer my questions pertaining to physics, or otherwise. He bestowed moral and financial support in time of need. I respect and admire him tremendously for his patience, and for setting a great example for me to follow. I would also like to thank him for giving me the opportunity to conduct good quality research at Fermilab and to present the results of my work at various levels. I had the unique experience of working among dedicated, smart and diverse group of people who have positively influenced my career as a physicist.

I wish to thank Dr. Kaushik De for introducing me to my advisor and for rescuing me from all the troubles I have gotten into in the past. He encouraged me to assume a significant role in the assembly of tile calorimeter modules for the ATLAS experiment. I learned the skills of assembling parts of a sub-detector component and perform its quality control with the help of Dr. Jia Li and Victor Reece.

Dr. Andy White helped me to learn and contribute in the study and calibration of a significant sub-detector (inter cryostat detector) system at the DØ experiment. Dr. Alex Weiss provided me the opportunity to teach in the capacity of a clinic tutor and as a teaching assis-

tant with the Physics department. Dr. Asok Ray, Dr. Truman Black have provided me with scholarships in the past I am grateful for their support.

I wish to thank Dr. Andrew Brandt, Dr. Kaushik De, Dr. Alex Weiss and Dr. Andy White for serving on my dissertation committee, their valuable suggestions and reviewing my dissertation. I wish to thank Dr. Mark Sosebee for taking the time to painstakingly proof-read this manuscript and correct grammatical and typographical errors.

I extend my appreciation to my colleagues at the DØ experiment at Fermilab, especially the Higgs group led by Dr. Gregorio Bernardi and Dr. Suyong Choi. I thank Gregorio for sharing his expertise in conducting quality data analysis, for arranging and participating in group meetings that monitored my progress. I sought Suyong's guidance in choosing the right tasks that helped me focus on the data analysis as well as service-related activities toward authorship. Striking a balance between the two was crucial for the timely completion of my analysis. I thank the spokespersons Dr. Dmitri Denisov and Dr. Terry Wyatt, who kept track of my progress, provided me with ample opportunities to contribute to the experiment and were willing to provide the letters of recommendation for me.

I thank Ambikacharan, Barry and Shahnoor immensely for providing financial support and friendly advice. Rishi and Mustafa have played a big role in my transition to physics. Kerri and Stephen Parmer have been good friends who care about us. I appreciate their support.

I have a long list of people to thank, which includes my grandparents, all my teachers, starting with my mother, who encouraged me to aim higher and work harder to achieve my goals. Lastly, but most importantly, I would like to thank my wife Kairi for her infinite patience, for putting up with me during the last four years, helping me get through the phase of graduate studies. It has all been a worthwhile experience because of the newest and most precious member of our family, our son Henri Aprameya.

November 5, 2007

## ABSTRACT

### A SEARCH FOR THE HIGGS BOSON IN ITS ASSOCIATED PRODUCTION WITH A $W$ VECTOR BOSON IN $p\bar{p}$ COLLISIONS AT $\sqrt{s} = 1.96$ TeV

Publication No. \_\_\_\_\_

Venkatesh S. Kaushik, Ph.D.

The University of Texas at Arlington, 2007

Supervising Professor: Jaehoon Yu

We present the results of a search for the Standard Model Higgs boson in its associated production with a  $W$  vector boson in  $p\bar{p}$  collisions at  $\sqrt{s} = 1.96$  TeV using the complete Run IIA dataset with an integrated luminosity of  $1.04 \text{ fb}^{-1}$  collected by the  $D\bar{O}$  experiment. The salient features of this analysis are the extended geometric acceptance by including the pseudorapidity covered by the end cap calorimeter, optimization in  $b$ -tagging and event selection criteria. We observe very good agreement in the data compared to the expectation from the modeling of Standard Model background for the  $WH$  signal. No excess events in data are observed over the predicted background. We establish that the evidence for observing the Higgs boson in this channel is inconclusive and proceed to set upper cross section limits on the associated  $WH$  production at 95% confidence level. We derive the cross section upper limits for the Higgs mass ( $m_H$ ) ranging from  $105 \text{ GeV}/c^2$  to  $145 \text{ GeV}/c^2$ . For  $m_H = 115 \text{ GeV}/c^2$ , the observed (expected) upper limit is  $0.8$  ( $0.9$ ) pb compared to the Standard Model expectation of  $0.13$  pb.

## TABLE OF CONTENTS

ACKNOWLEDGEMENTS . . . . .	v
ABSTRACT . . . . .	vii
LIST OF FIGURES . . . . .	xiii
LIST OF TABLES . . . . .	xvii
Chapter	
1. INTRODUCTION . . . . .	1
2. THEORY . . . . .	3
2.1 The Standard Model of Elementary Particle Physics . . . . .	3
2.1.1 Particles . . . . .	4
2.1.2 Interactions . . . . .	6
2.2 Example of Spontaneously Broken Symmetry . . . . .	15
2.3 Higgs Mechanism . . . . .	18
2.3.1 Phenomenology of the Higgs Boson . . . . .	22
2.3.2 $WH$ Associated Production at the Tevatron . . . . .	25
2.3.3 Higgs Sensitivity Studies . . . . .	26
3. EXPERIMENTAL APPARATUS . . . . .	28
3.1 The Fermilab Chain of Accelerators . . . . .	28
3.2 Cross section and Luminosity . . . . .	36
3.3 Upgraded DØ Run II Detector . . . . .	38
3.4 Coordinate System and Kinematic Quantities . . . . .	39
3.5 Inner Tracking System . . . . .	42
3.5.1 Silicon Microstrip Tracker (SMT) . . . . .	42



3.5.2	Central Fiber Tracker (CFT)	44
3.5.3	Preshower Detectors	45
3.6	Calorimeter System	47
3.6.1	Energy Measurement	47
3.6.2	Calorimeter Performance	48
3.6.3	DØ Calorimeters	49
3.6.4	Inter Cryostat Detector	51
3.7	Muon Detectors	52
3.8	Luminosity Monitor	55
3.9	Trigger and Data Acquisition (DAQ) System	56
4.	MONTE CARLO SIMULATION	60
4.1	Physical Process of Hadron Collisions	60
4.2	Monte Carlo Event Generators	62
4.2.1	PYTHIA Event Generator	62
4.2.2	ALPGEN Event Generator	64
4.3	DØ Detector Simulation	66
5.	OFFLINE EVENT RECONSTRUCTION	69
5.1	Offline Object Reconstruction Efficiencies	70
5.2	Luminosity	70
5.3	Track Reconstruction	71
5.4	Primary Vertex Reconstruction	73
5.5	Electron Reconstruction and Identification	76
5.5.1	Reconstruction	76
5.5.2	Identification	77
5.6	Jet Reconstruction	86
5.7	Missing $E_T$	88

5.8	<i>b</i> -tagging . . . . .	90
5.8.1	<i>b</i> -tagging Methods . . . . .	91
5.9	Neural Network (NN) Tagging: . . . . .	95
6.	DATA AND MC SAMPLES . . . . .	100
6.1	Data Processing Chain . . . . .	100
6.2	Run IIA Dataset . . . . .	101
6.3	EM+Jet Trigger Suite . . . . .	102
6.4	Integrated Luminosity of the Run IIA Dataset . . . . .	103
6.5	Simulated Dataset . . . . .	104
7.	OBJECT RECONSTRUCTION AND SELECTION EFFICIENCIES . . . . .	108
7.1	Electron Reconstruction Efficiency . . . . .	108
7.1.1	Tag and Probe Method . . . . .	109
7.1.2	Signal and Background Modeling . . . . .	109
7.1.3	Event Selection Criteria . . . . .	110
7.1.4	Preselection Efficiency . . . . .	112
7.1.5	Post-preselection Efficiency . . . . .	114
7.2	Trigger Efficiency . . . . .	118
7.2.1	Normalization . . . . .	120
7.3	Jet Reconstruction Efficiency . . . . .	122
7.3.1	Jet Energy Scale Correction . . . . .	122
7.3.2	Jet ID Efficiency in Data . . . . .	130
7.3.3	Jet Smearing, Shifting and Removal . . . . .	131
7.3.4	Jet ID Efficiency in MC . . . . .	133
7.4	Recalculation of $\cancel{E}_T$ . . . . .	134
7.5	<i>b</i> -tagging Efficiency . . . . .	136
7.5.1	TRF and TSF Methods . . . . .	136

7.5.2	Tag Rate Functions (TRF) . . . . .	136
7.5.3	Taggability Scale Factor (TSF) . . . . .	140
8.	DATA ANALYSIS . . . . .	142
8.1	Analysis Strategy . . . . .	142
8.2	Analysis Flow . . . . .	143
8.3	Data Quality . . . . .	145
8.4	Event Selection Criteria . . . . .	146
8.4.1	Preselection Cuts . . . . .	146
8.4.2	Post-preselection Cuts . . . . .	146
8.5	Background Modeling . . . . .	149
8.5.1	$t\bar{t}$ Production . . . . .	149
8.5.2	Single Top Quark Production . . . . .	150
8.5.3	Diboson Production . . . . .	151
8.5.4	$W$ +jets and $Z$ +jets Production . . . . .	152
8.5.5	$Wb\bar{b}$ Production . . . . .	152
8.5.6	QCD/Multijet . . . . .	153
8.6	Summary of Data and Expected Background . . . . .	158
8.6.1	Normalization . . . . .	160
8.6.2	Evidence for $W + 2$ jets Production . . . . .	160
8.7	$b$ -tagging . . . . .	172
8.7.1	Tagging MC Jets . . . . .	173
8.7.2	Event Yield . . . . .	181
8.7.3	$W + 3$ Jets Control Sample . . . . .	183
9.	SYSTEMATIC UNCERTAINTIES AND CROSS SECTION LIMITS . . . . .	186
9.1	Background Uncertainties . . . . .	186
9.1.1	Electron Reconstruction/Identification . . . . .	187

9.1.2	Electron Energy Resolution/Smearing . . . . .	187
9.1.3	Trigger Efficiency . . . . .	187
9.1.4	Jet Reconstruction/Identification . . . . .	187
9.1.5	Jet Energy Scale . . . . .	188
9.1.6	NN $b$ -tagging . . . . .	188
9.1.7	Estimation of QCD Background . . . . .	189
9.1.8	Luminosity . . . . .	189
9.2	Theoretical Uncertainties . . . . .	189
9.3	$WH$ Cross Section Limit . . . . .	191
9.3.1	Limit Calculation Method . . . . .	192
9.4	Cross Section Limits . . . . .	196
10.	CONCLUSIONS AND DISCUSSION . . . . .	202
10.1	Combined $WH \rightarrow \ell\nu b\bar{b}$ Result . . . . .	202
10.2	Full SM Combination of $D\bar{O}$ Searches . . . . .	203
10.3	Future Work . . . . .	204
10.4	Concluding Remarks . . . . .	205
	REFERENCES . . . . .	208
	BIOGRAPHICAL STATEMENT . . . . .	218

## LIST OF FIGURES

Figure	Page
2.1 Feynman diagram depicting the Coulomb scattering process . . . . .	9
2.2 Feynman diagram showing weak $\beta$ -decay . . . . .	11
2.3 Feynman diagram for dijet production . . . . .	14
2.4 Scalar potential $V(\phi) = \frac{1}{2}\mu^2\phi^2 + \frac{1}{4} \lambda \phi^4$ . . . . .	17
2.5 The shape of the 3-d wine bottle potential . . . . .	19
2.6 Theoretical bounds on the Higgs mass . . . . .	24
2.7 Experimental bounds using precision EW fits on the Higgs mass . . . . .	25
2.8 Higgs production and decay modes at the Tevatron . . . . .	26
2.9 Discovery potential for the Higgs at the Tevatron . . . . .	27
3.1 Tevatron accelerator complex . . . . .	29
3.2 Magnetron surface plasma source . . . . .	30
3.3 Cockroft-Walton generator . . . . .	31
3.4 Alvarez-type drift tube linac . . . . .	32
3.5 Lithium lens used to collect $\bar{p}$ . . . . .	34
3.6 Integrated luminosity for Run IIA . . . . .	38
3.7 Side view of the DØ Run II detector . . . . .	39
3.8 Diagram showing the coordinate system at DØ . . . . .	40
3.9 Run II tracking system at DØ . . . . .	43
3.10 Schematic diagram of the DØ Run II SMT detector . . . . .	44
3.11 Schematic diagram of a quadrant of the DØ Run II CFT detector. . . . .	45
3.12 Schematic diagram of DØ Run II calorimeter . . . . .	49

3.13	A unit cell of the DØ calorimeter (two units are shown) . . . . .	50
3.14	A quadrant of the cross sectional view of the DØ calorimeter . . . . .	52
3.15	Schematic view of the ICD modules . . . . .	53
3.16	The muon system of the upgraded Run II DØ detector . . . . .	54
3.17	Diagram of the Run II DØ Luminosity Monitor . . . . .	55
3.18	The three-level sequential triggering system at DØ . . . . .	57
4.1	Event structure in a $p\bar{p}$ collision . . . . .	61
4.2	The CTEQ6M parton distribution functions . . . . .	63
4.3	Peak instantaneous Run IIA luminosity . . . . .	68
5.1	Histogramming track finding method . . . . .	74
5.2	Illustration of primary vertex reconstruction . . . . .	76
5.3	EM fraction and isolation distributions . . . . .	79
5.4	Track match probability $P(\chi^2_{spatial})$ and $E_T/p_T$ distributions . . . . .	81
5.5	Seven-variable H-matrix $\chi^2$ distribution . . . . .	83
5.6	Likelihood discriminant for real and fake electrons . . . . .	85
5.7	A depiction of the characteristics of a $b$ -jet . . . . .	91
5.8	Performance of secondary vertex $b$ -tagging algorithm . . . . .	93
5.9	Illustration of signed impact parameter . . . . .	94
5.10	Jet lifetime probability distributions . . . . .	95
5.11	NN-tagger output for $b$ -quarks and light-quarks . . . . .	97
5.12	Comparison of the performance of NN and JLIP taggers . . . . .	99
6.1	A flowchart depicting the data processing chain . . . . .	100
7.1	$Z$ candidate events for tag-and-probe method . . . . .	110
7.2	Preselection efficiency for probe electrons . . . . .	113
7.3	Post-preselection efficiency of the probe electrons . . . . .	115
7.4	H-matrix, likelihood and track-matching efficiencies vs. $\eta_D$ . . . . .	116

7.5	H-matrix, likelihood and track-matching efficiencies vs. electron $p_T$ . . . . .	117
7.6	Trigger efficiencies of calorimeter-based triggers . . . . .	119
7.7	Offset jet-energy correction . . . . .	123
7.8	$\cancel{E}_T$ projection fraction method . . . . .	124
7.9	Relative jet-energy response correction . . . . .	126
7.10	Absolute jet-energy response correction . . . . .	127
7.11	Showering jet-energy correction . . . . .	128
7.12	Jet-energy scale corrections for 0.5 cone jets . . . . .	129
7.13	Jet identification efficiencies . . . . .	130
7.14	Smearing factor for jet- $p_T$ correction in MC . . . . .	133
7.15	Jet identification efficiency turn-on curves for MC . . . . .	134
7.16	Jet identification efficiencies in data . . . . .	134
7.17	Scale factors for correcting MC jets . . . . .	135
7.18	NN-tagger $b$ -jet efficiencies and scale factors . . . . .	139
7.19	Taggability scale factors for $b$ -tagging MC jets . . . . .	141
8.1	Feynman diagram for $WH$ associated production . . . . .	142
8.2	Analysis flowchart for data and simulation . . . . .	144
8.3	Triangle cut to reduce QCD background . . . . .	148
8.4	Feynman diagrams for $t\bar{t}$ background . . . . .	150
8.5	Feynman diagrams for single top background . . . . .	150
8.6	Feynman diagrams for diboson background . . . . .	151
8.7	Feynman diagrams for $W$ +jets background . . . . .	152
8.8	Feynman diagrams for $Wb\bar{b}$ background . . . . .	153
8.9	Feynman diagrams for QCD/multijet background . . . . .	154
8.10	QCD Fake rate in the CC region vs. electron $p_T$ . . . . .	157
8.11	EM likelihood efficiency vs. electron $p_T$ . . . . .	159

8.12	Legend for data and MC comparisons . . . . .	161
8.13	$W + 2$ jets CC analysis: $e$ kinematic distributions . . . . .	162
8.14	$W + 2$ jets CC analysis: $\nu_e$ and $W$ kinematic distributions . . . . .	163
8.15	$W + 2$ jets CC analysis: $p_T$ of jets . . . . .	164
8.16	$W + 2$ jets CC analysis: angular distributions of jets . . . . .	165
8.17	$W + 2$ jets CC analysis: properties of dijet system . . . . .	166
8.18	$W + 2$ jets EC analysis: $e$ kinematic distributions . . . . .	167
8.19	$W + 2$ jets EC analysis: $\nu_e$ and $W$ kinematic distributions . . . . .	168
8.20	$W + 2$ jets EC analysis: $p_T$ of jets . . . . .	169
8.21	$W + 2$ jets EC analysis: angular distributions of jets . . . . .	170
8.22	$W + 2$ jets EC analysis: properties of dijet system . . . . .	171
8.23	$W + 2$ jets CC analysis: invariant mass of $b$ -tagged jets . . . . .	175
8.24	$W + 2$ jets CC analysis: properties of $b$ -tagged jets . . . . .	176
8.25	$W + 2$ jets CC analysis: properties of $b$ -tagged dijet system . . . . .	177
8.26	$W + 2$ jets EC analysis: invariant mass of $b$ -tagged jets . . . . .	178
8.27	$W + 2$ jets EC analysis: properties of $b$ -tagged jets . . . . .	179
8.28	$W + 2$ jets EC analysis: properties of $b$ -tagged dijet system . . . . .	180
8.29	$W + 3$ jets CC and EC analyses: invariant mass of $b$ -tagged jets . . . . .	185
9.1	Illustration of the $CL_S$ method . . . . .	195
9.2	LLR distributions for $b$ -only and $s + b$ hypotheses . . . . .	198
9.3	$W + 2,3$ jets CC and EC analyses: 95% CL cross section limit-ratio . . .	200
9.4	95% CL cross section limits for $W(H) \rightarrow e\nu(b\bar{b})$ production . . . . .	201
10.1	95% CL cross section limits for $W(H) \rightarrow ell\nu(b\bar{b})$ NN-analyses . . . . .	206
10.2	Higgs cross section limits for full $D\bar{O}$ combination . . . . .	207



## LIST OF TABLES

Table	Page
2.1 The Standard Model of particle physics . . . . .	5
2.2 Summary of the forces described by the SM . . . . .	15
3.1 Operating parameters for the central calorimeter . . . . .	50
5.1 Input variables for NN-tagger . . . . .	96
5.2 Efficiency and fake rate of the NN-tagger . . . . .	98
6.1 The Run IIA EMinclusive skimmed dataset . . . . .	102
6.2 Trigger terms for EM+Jet trigger suite . . . . .	102
6.3 Recorded luminosity for EM+Jet triggers of the Run IIA data . . . . .	103
6.4 Summary table of diboson MC samples . . . . .	104
6.5 Summary table of $t\bar{t}$ MC samples . . . . .	105
6.6 Summary table of $WH$ and $ZH$ MC samples . . . . .	106
6.7 Summary table of $W$ +jets and $Z$ +jets MC samples . . . . .	107
7.1 Average preselection efficiency in data . . . . .	114
7.2 Average post-preselection efficiency in data . . . . .	116
7.3 Average $b$ -tagging efficiencies and scale factors . . . . .	140
8.1 Fit parameters for QCD fake rate . . . . .	158
8.2 Summary table of QCD fake rates . . . . .	158
8.3 NN-tagging efficiency for oldLoose and Tight operating points . . . . .	172
8.4 $W + 2$ jets CC analysis: event yield . . . . .	181
8.5 $W + 2$ jets EC analysis: event yield . . . . .	182
8.6 $W + 3$ jets CC analysis: event yield . . . . .	183

8.7	$W + 3$ jets EC analysis: event yield . . . . .	184
9.1	Systematic errors on $b$ -tagging scale factors . . . . .	189
9.2	Systematic Uncertainties: exclusive single $b$ -tag . . . . .	191
9.3	Systematic Uncertainties: double $b$ -tag . . . . .	192
9.4	Summary table of expected and observed cross section limits . . . . .	200
10.1	Higgs cross section limits for $W(H) \rightarrow \ell\nu(b\bar{b})$ combination . . . . .	203

## CHAPTER 1

### INTRODUCTION

The most sensitive production channel for a Standard Model (SM) Higgs boson at the Tevatron is its associated production with  $W/Z$  vector bosons. The production is dominated by gluon fusion process ( $gg \rightarrow H$ ) with a cross section in the range 0.8 - 0.2 pb for higgs masses ranging from 105 - 145  $\text{GeV}/c^2$  followed by WH production channel with cross section in the range 0.2 - 0.03 pb for the same range of higgs masses. The  $WH$  channel provides a clean event signature with well-modeled backgrounds, whereas the gluon fusion channel is dominated by multijet backgrounds that are difficult to model. The analysis results presented here correspond to a total of  $1.04 \text{ fb}^{-1}$  of Run IIA data. Several improvements (to be discussed in the following chapters) have been implemented in the current analysis to achieve  $\sim 30\%$  improvement in search sensitivity. This is in addition to that achieved by an increase in integrated luminosity compared to the previous analysis with  $400 \text{ pb}^{-1}$  data.

This thesis is organized into the following chapters:

- Chapter 2: Theoretical introduction and the motivation to search for the Higgs boson are presented.
- Chapter 3: Experimental apparatus of the Fermilab Tevatron collider and the DØ detector is described.
- Chapter 4: Simulation, *i.e.*, Monte Carlo (MC) tools used in this analysis are explained.
- Chapter 5: Offline event reconstruction is explained in detail with emphasis on objects used in this analysis, which include electrons, neutrinos and jets.
- Chapter 6: Data and MC samples used in the analysis are summarized.
- Chapter 7: Object reconstruction and identification efficiencies are presented.

- Chapter 8: High level analysis, which includes event selection, signal and background modeling, as well as identification of  $b$ -jets which are critical to this search, are presented.
- Chapter 9: Systematic uncertainties are explained. Cross section limits on production of the Higgs boson are presented.
- Chapter 10: A brief summary and the outlook for future Higgs searches are presented.

## CHAPTER 2

### THEORY

This chapter presents a concise theoretical overview of our understanding of nature's fundamental constituents and their interactions which are incorporated into a successful framework called the Standard Model (SM) [1–4] of elementary particle physics. Although very successful in its prediction of experimentally observed facts, it still remains an incomplete theory of nature. One of the unresolved problems of the SM is the origin of mass of the fundamental particles. The most popular theory to introduce the generation of masses of the fundamental particles is the Higgs mechanism, which is also discussed here. Interested readers are directed to the extensive literature available [5–7], which provide a rigorous exposition of the SM and the Higgs mechanism.

#### 2.1 The Standard Model of Elementary Particle Physics

At the turn of the 20<sup>th</sup> century two significant advancements in theory *viz.*, Special Relativity and Quantum Mechanics, led to our increased understanding of the fundamental<sup>1</sup> constituents of matter, which at that time was limited to the proton, neutron and the electron together with the carrier of the electromagnetic force, the photon. The SM is a quantum field theory since it incorporates quantum mechanics and the special theory of relativity.

The current knowledge of the fundamental building blocks of matter and their interactions is more complete and integrated into the beautiful structure of the SM. In the SM, all matter is grouped into three *families* or *generations*, each containing of two particles. All mat-

---

<sup>1</sup>A particle is said to be fundamental if it does not have a known substructure, *i.e.*, it cannot be a bound state of smaller constituents. For example the electron is a fundamental particle where as a proton is made up of quarks and hence not fundamental.

ter particles are called *fermions*; they have half-integer spin (spin 1/2) and obey Fermi-Dirac statistics and the Pauli exclusion principle. The fermions are divided into *quarks* which carry fractional electric charge ( $\pm 1/3 e$ , or  $\pm 2/3 e$ ), or *leptons* that carry an integral electric charge of  $\pm 1 e$  or zero. Quarks have two distinct features that qualitatively distinguish them from leptons: they have fractional electric charge and they interact via the strong nuclear force which binds quarks together inside nuclei.

Particle interactions are also described by the SM. The forces responsible for the interactions are electromagnetic, weak and strong nuclear forces. Gravity is not included in the SM because of its weak strength compared to other forces. The SM is a theory of interacting fields. Each particle in the SM can be thought of as a quantum excitation of its field. Each separate field then corresponds to a different particle type (or flavor).

Our understanding currently includes the existence of massive  $W/Z$  particles, the carriers of the weak nuclear force, eight flavors of gluons, the mediators of the strong nuclear force, and the photon which mediates the electromagnetic force. They are collectively referred to as *gauge bosons* because they have integer spin and obey Bose-Einstein statistics. The theory of electromagnetic interactions is called Quantum Electro-Dynamics (QED) and that of strong interactions is called Quantum Chromo-Dynamics (QCD). In the SM, weak and electromagnetic interactions are unified into a single *electroweak* (EW) force, as described later in this chapter.

### 2.1.1 Particles

The lepton group contains both charged and neutral particles. The charged particles include electrons ( $e$ ), muons ( $\mu$ ) and taus ( $\tau$ ). The neutral leptons (neutrinos)<sup>2</sup> include the electron neutrino ( $\nu_e$ ), the muon neutrino ( $\nu_\mu$ ) and the tau neutrino ( $\nu_\tau$ ). The quarks are spin 1/2 fermions that carry fractional electric charge as well as a *color charge* described by QCD. The six types of quarks are *up*, *down*, *charm*, *strange*, *top* and *bottom*. The properties of quarks and

---

<sup>2</sup>Meaning “the little neutral one”.

Table 2.1. The matter particles (fermions) of the SM are classified into three families which are shown color-coded here. The fermions can either be leptons or quarks. Each of the fermions has its own anti-particle (not shown here). Values for masses are adopted from [8].

Leptons				Quarks			
spin = 1/2				spin = 1/2			
Symbol	Name	Mass GeV/c <sup>2</sup>	Electric Charge	Symbol	Name	~ Mass GeV/c <sup>2</sup>	Electric Charge
$\nu_e$	electron neutrino	$< 1 \times 10^{-8}$	0	<b>u</b>	up quark	0.003	$+\frac{2}{3}$
<b>e</b>	electron	0.000511	-1	<b>d</b>	down quark	0.006	$-\frac{1}{3}$
$\nu_\mu$	muon neutrino	$< 0.0002$	0	<b>c</b>	charm quark	1.3	$+\frac{2}{3}$
$\mu$	muon	0.105	-1	<b>s</b>	strange quark	0.1	$-\frac{1}{3}$
$\nu_\tau$	tau neutrino	$< 0.02$	0	<b>t</b>	top quark	175	$+\frac{2}{3}$
$\tau$	tau	1.7771	-1	<b>b</b>	bottom quark	4.3	$-\frac{1}{3}$

leptons are summarized in Table. 2.1. An interesting feature of quarks and leptons is that there are two of each kind in a family. In the table, fermions corresponding to a particular species (or family) are shown with the same color. Most of the mass observed in our universe consists of elements whose nuclei contain protons and neutrons, which in turn are made of *up* and *down* quarks. Other types of quarks are created in high energy cosmic rays or particle accelerators. They are generally unstable and decay into particles belonging to the first generation. For each fermion there is an associated anti-matter particle with exactly the same properties, except it is oppositely charged. The anti-leptons are the anti-electron (or positron,  $e^+$ ), anti-muon, *etc.* The neutrinos are their own anti-particles since they have no electric charge. Similarly the anti-quarks are the anti-up quark ( $\bar{u}$ ) anti-down quark, *etc.*

Quarks cannot be observed in isolation, but only in association with other quarks (bound states). It requires a large amount of energy to separate the quarks from their bound state (for example, in high energy hadron collisions). Immediately following their separation, a series

of new bound states of quarks and anti-quarks are produced from the available energy used in separating them. Quarks also have two distinct bound state combinations, the *baryons* and the *mesons* which are collectively referred to as *hadrons*. Baryons are bound states of three quarks ( $qqq$ ). Examples of hadrons include protons ( $uud$ ) and neutrons ( $udd$ ). Mesons are bound states of a quark and an anti-quark ( $q\bar{q}$ ). Pions ( $\pi^\pm, \pi^0$ ) and kaons ( $K^0, \bar{K}^0$  and  $K^\pm$ ) are a few examples of mesons.

### 2.1.2 Interactions

The four fundamental interactions in nature are electromagnetic, strong, weak nuclear and gravitational. Due to the extremely weak strength of the gravitational force acting between subatomic particles, it is ignored in the SM. In quantum field theory the particle interactions are interpreted as the exchange of field particles. The photon is the field carrier of the electromagnetic interaction, which binds electrons to nuclei in atoms. The photon is also massless, which implies that the distance scale at which electromagnetism operates is infinitely large. The gluons are the carriers of the strong force which binds the protons and neutrons together in a nucleus. The  $W$  and  $Z$  bosons are the carriers of the weak force responsible for radioactive  $\beta$  decay. Unlike the massless photon, the  $W$  and  $Z$  are quite heavy. This implies that unlike electromagnetism, the weak force will operate at relatively short distance scales.

#### 2.1.2.1 Electromagnetic Interactions

In the next two subsections, the important concepts pertaining to electromagnetic interactions in the framework of QED are briefly discussed.



- Gauge Invariance

The force carriers are naturally introduced into the SM by requiring the Lagrangian<sup>3</sup> to be invariant under certain symmetry transformations. Group transformations that vary in space and time are called *local gauge transformations*. By forcing a Lagrangian that describes a free particle to be invariant under a local group transformation, it is necessary to introduce a *gauge field* to maintain the invariance of the Lagrangian. These gauge fields lead to spin 1 bosons, which are the carriers of the fundamental interactions.

To illustrate the principle of gauge invariance, consider the free Dirac field  $\Psi = \Psi(x)$  and  $\bar{\Psi} = \Psi^\dagger \gamma^0$ , which is a quantum field whose quanta are the fermions. Therefore it describes spin 1/2 particles such as quarks and leptons. The Lagrangian of this field is given by

$$\mathcal{L}_{Dirac} = \bar{\Psi}(i\gamma^\mu \partial_\mu - m)\Psi, \quad (2.1)$$

where  $\gamma^\mu$  are the  $4 \times 4$  gamma matrices. A U(1) local gauge transformation of the Dirac field is defined as an arbitrary change in the phase of the field at each point in space and time independently as given by Eq. 2.2

$$\begin{aligned} \Psi &\rightarrow \Psi' = e^{i\theta(x)}\Psi \\ \bar{\Psi} &\rightarrow \bar{\Psi}' = e^{-i\theta(x)}\bar{\Psi} \end{aligned} \quad (2.2)$$

where  $\theta(x)$  is a function of space-time coordinates. Substituting Eq. 2.2 into Eq. 2.1 yields the new Lagrangian of the form

$$\mathcal{L}_{Dirac} \rightarrow \mathcal{L}'_{Dirac} = \mathcal{L}_{Dirac} - \bar{\Psi}\gamma^\mu \partial_\mu \theta(x)\Psi \quad (2.3)$$

---

<sup>3</sup>The Lagrangian is an equation that describes the state of motion of a dynamical system. It is equal to kinetic energy (T) minus the potential energy (V):  $\mathcal{L} = T - V$ .

To maintain the invariance of the Lagrangian a real gauge field,  $A_\mu$ , is introduced whose transformation exactly cancels out the extra term in Eq. 2.3:

$$A_\mu \rightarrow A'_\mu = A_\mu - \frac{1}{e} \partial_\mu \theta(x) \quad (2.4)$$

Effectively, Eq. 2.4 implies that the Lagrangian stays the same when the charged particle wave function undergoes an arbitrary phase change accompanied by a suitable change in the photon field (which is the real gauge field introduced above). Invariance also leads to a conservation law; in this case the electric charge and currents are conserved.

For completeness, an invariant kinetic energy term for the gauge field is also added to the Lagrangian of the form:

$$\mathcal{L}^{K.E} = -\frac{1}{4} F_{\mu\nu} F^{\mu\nu} \quad F_{\mu\nu} = \partial_\mu A_\nu - \partial_\nu A_\mu \quad (2.5)$$

By introducing the covariant derivative,  $D_\mu \equiv \partial_\mu + ieA_\mu$ , the resulting Lagrangian can be written as:

$$\begin{aligned} \mathcal{L}_{QED} &= \bar{\Psi}(i\gamma^\mu D_\mu - m)\Psi - \frac{1}{4} F_{\mu\nu} F^{\mu\nu} \\ &= \bar{\Psi}(i\gamma^\mu \partial_\mu - m)\Psi - \underbrace{e\bar{\Psi}\gamma^\mu\Psi A_\mu}_{\text{Interaction Term}} - \frac{1}{4} F_{\mu\nu} F^{\mu\nu} \end{aligned} \quad (2.6)$$

The Lagrangian in Eq. 2.6 describes the interactions of electrons and photons, which is QED. By simply requiring the invariance of a free Dirac field under U(1) unitary local gauge transformation a free system changes into an interacting system.

- Renormalization

Another important feature of the QED is that it is said to be *renormalizable*. For example, we know that a free electron interacts with the EM field by constantly emitting and reabsorbing virtual photons. No restriction is placed on the momentum ( $k$ ) of these virtual particles and their contribution to the mass and charge of the electron are of the form  $\int dk/k$  which becomes logarithmically divergent. But we know that the electron has a finite mass from experiment. To remedy this, a procedure called renormalization is introduced by defining a new normalization of the electron mass and charge in these calculations. The new definitions are replaced with their experimentally determined values to yield finite predictions for cross sections when presented in terms of the physical quantities (like the mass of the electron).

- Example of a QED Process

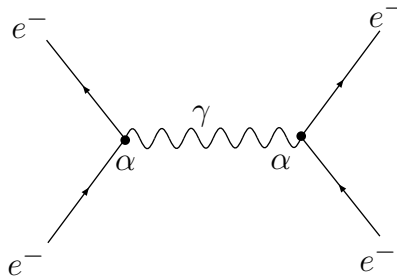


Figure 2.1. Feynman diagram depicting the Coulomb scattering process. Two electrons approach each other, one emits a photon and recoils while the other absorbs the emitted photon and changes its motion.

Consider the Coulomb repulsion between two electrons. This process can be described in QED as the one in which the two charged particles exchange a photon. Mathematically the SM equations couple the field of a gauge boson (a photon in this example) with fields of all the particles (two charged electrons in this case) which feel that particular force (the

electromagnetic force). Interactions between two particles thus involve two couplings of the particles to the gauge boson wherein the particles exchange a virtual gauge boson. It is depicted by the *Feynman diagram* shown in Fig. 2.1. The solid lines represent the fermions while the wavy line represents the virtual gauge boson. The arrows indicate time flow; the event on the left precedes the one on the right. The fermion and boson lines meet at a vertex where energy, momentum and charge are conserved. The strength of the interaction is represented by  $\alpha$ , which in the case of QED is the so-called *fine structure constant*; its value is given by Eq. 2.7. The coupling constant  $\alpha$  is not exactly a constant, but a *running constant* which means that it increases in value as the energy involved in the interaction increases.

$$\alpha = \frac{e^2}{\hbar c} \simeq \frac{1}{137} \quad (2.7)$$

#### 2.1.2.2 Weak Interactions

Weak interactions occur among quarks and leptons and are mediated by massive  $W$  and  $Z$  bosons. The  $W$  and  $Z$  bosons have experimentally determined masses of  $m_W = 80.398 \pm 0.025 \text{ GeV}/c^2$  and  $m_Z = 91.1875 \pm 0.0021 \text{ GeV}/c^2$ , respectively [10]. The quantum theory that describes the weak interactions was first described successfully by Glashow, Salam and Weinberg (GSW) in 1967-68. The GSW theory unified the electromagnetic and weak interactions into a single theory. The unified EM and weak forces are introduced by requiring invariance under  $SU(2)_L \times U(1)_Y$  local gauge transformations. Local gauge invariance under  $SU(2)$  group transformations requires the introduction of three massless spin 1 gauge bosons  $W^+$ ,  $W^-$  and  $W^0$ . The conserved quantity is called *weak isospin*. The  $SU(2)$  group is then combined with  $U(1)$  leading to the introduction of another spin 1 gauge boson  $B^0$ . This combination leads to the conservation of the *weak hypercharge* which is a combination of weak isospin and electric charge. In order to account for the two observed bosons *i.e.*, the photon ( $\gamma$ )

and  $Z^0$ , the weak eigenstates  $W^0$  and  $B^0$  are mixed. This leads to the orthogonal combinations of photon and  $Z^0$

$$\gamma = W^0 \sin \theta_W + B^0 \cos \theta_W \quad (2.8)$$

$$Z^0 = W^0 \cos \theta_W - B^0 \sin \theta_W \quad (2.9)$$

where  $\theta_W$  is the weak mixing angle, the value of which is not specified in the theory. The experimentally measured value of  $\sin^2 \theta_W \equiv 1 - m_W^2/m_Z^2$  is  $0.2324 \pm 0.0012$ . The gauge bosons are all massless in order to maintain the invariance of the Lagrangian. This is however at odds with the experimental evidence of massive  $W$  and  $Z$  bosons. The mechanism responsible for the generation of masses of the fermions and the gauge bosons while preserving the gauge invariance is the Higgs mechanism, which will be discussed later. An example of a weak interaction is the nuclear  $\beta$ -decay in which a neutron decays into a proton, an electron and an electron anti-neutrino *i.e.*,  $n \rightarrow p + e^- + \bar{\nu}_e$  which is illustrated in Fig. 2.2.

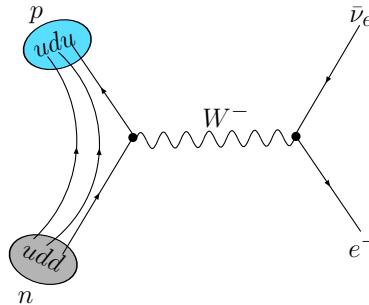


Figure 2.2. Feynman diagram showing the weak decay of the neutron into a proton.

### 2.1.2.3 Strong Interactions

Strong interactions occur among the quarks that make up the hadrons. The mediators of the strong force are called *gluons*. The quarks have an additional internal degree of freedom

called *color charge*. Each quark can carry one of the three primary color charges, *viz.*, red, green or blue ( $rgb$ )<sup>4</sup>. Its anti-quark carries the corresponding anti-color ( $\bar{r}\bar{g}\bar{b}$ ). The force carriers themselves can have a color charge. Gluons having color charge implies that they can interact among themselves, unlike the bosons of the weak and electromagnetic forces which do not self-interact. The color of the gluon is independent of the colors of the interacting quarks. Gluons carry a color and anti-color label such that the color is conserved at each interaction. For example, a red quark emits a red-anti-blue ( $r\bar{b}$ ) gluon and turns into a blue quark.

Since gluons have color and anti-color and there are three primary colors, a total of  $3^2 = 9$  color combinations are possible one of which, ( $r\bar{r} + g\bar{g} + b\bar{b}$ ), is a colorless singlet. The group that describes these interactions is the SU(3) group. The invariance under local gauge transformations of this group leads to the existence of eight gauge bosons. The conserved quantity is color charge.

- Asymptotic Freedom

The strength of the strong interaction is determined by the strong coupling constant,  $\alpha_s$ , which is a running constant similar to electromagnetic coupling constant. However, its strength decreases as the interaction energy increases. In high energy hadronic processes like the  $p\bar{p}$  collisions at the Fermilab Tevatron or  $pp$  collisions at CERN LHC, where the energy of interaction is large (or equivalently the distance scale being probed is smaller than the size of a nucleus), the constituent quarks inside the colliding hadrons behave as nearly free particles. This behavior is called the asymptotic freedom. The interaction can be described by QCD using perturbative techniques much like those in QED. As the energy of interaction decreases (or equivalently the distance between the quarks increases), the coupling strength becomes larger, and in the typical case of a nucleon the coupling becomes large enough so that perturbative theory is no longer applicable.

---

<sup>4</sup>Color charges are quantum numbers with these labels.

- Color Confinement

Asymptotic freedom ensures that quarks always appear in bound states at distances larger than the size of a nucleus. The coupling strength increases in magnitude at a distance scales of order the size of a nucleus and ensures that the quarks are confined inside of the hadron. The confinement of quarks is such that the net color charge of the hadron is zero. This phenomenon is called color confinement. From experimental observation, we know that all hadrons like proton, neutron, kaons, pions, *etc.*, are color neutral and have integral electric charge. We also know that these hadrons are combinations of quarks. Therefore, it can be regarded that these combinations of quark triplets or quark-anti-quark pairs form bound states, such that the color charge of the combination exactly cancels and the fractional electric charges add up to an integral total charge.

- Parton Distribution Functions

The partons which constitute a hadron carry a fraction of its total momentum as described by Parton Distribution Functions (PDF's). The PDF's give the probability of observing a specific flavor parton with a given momentum fraction. PDF's are measured for different hadrons and are parameterized as a function of fractional parton momentum, ( $x$ ), defined as  $x \equiv |\vec{p}_{parton}|/|\vec{p}_{hadron}|$ . Protons are made up of three quarks ( $uud$ ) which are known as *valence* quarks. Other partons can be produced inside the proton as virtual quark pairs. One can imagine a sea of quark and anti-quark pairs being created and annihilated continuously. These quarks are therefore called *sea* quarks. A collection of gluons holds all these quarks together inside the proton. The PDF's are measured for the valence quarks and gluons from different experiments. Refer to section 4.2.1 for more details.

- Hadronization

Hadronization<sup>5</sup> is the process by which quarks combine with other quarks to form hadrons. Hadronization is a direct consequence of color confinement. To illustrate this, consider the Feynman diagram in Fig. 2.3, which shows the collision of two hadrons ( $p$  and  $\bar{p}$ ) with suf-

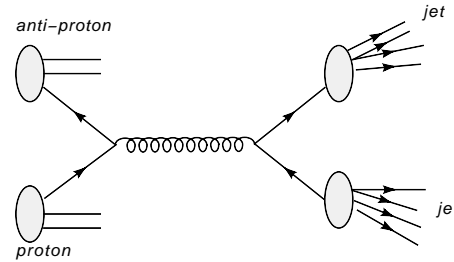


Figure 2.3. Feynman diagram depicting the  $p\bar{p}$  interaction resulting in dijet production.

ficient<sup>6</sup> momentum transfer. The valence and sea quarks of the colliding hadrons have their momentum fractions described by the PDF's. The two incoming partons fuse to create a virtual gluon which then splits into a quark anti-quark pair. The exact nature of hadronization is not fully understood. Several models exist, and one of these models, the Lund String Model, is explained in section 4.2.1. The process of hadronization results in a *jet* of colorless particles which can be detected with a total momentum nearly equal to that of the initial parton.

Table. 2.2 summarizes the three interactions described by the SM. If the strength of the strong force is normalized to one, the EM force is a hundred times weaker and the weak force is a million times weaker than the strong force.

---

<sup>5</sup>Also referred as “fragmentation” in the literature.

<sup>6</sup>Of the order of a few GeV.



Table 2.2. Summary of the forces described by the SM indicating the force carrier, its mass and electric charge. The form of potential term in the Lagrangian  $V(r)$ , the relative strength of the force and the group that describes the forces are also shown. The effective range of EM interactions are infinite whereas the range of strong force is limited to the size of a nucleon. The range of weak force is about the size of an atom.

Force	Boson	Group	Mass $GeV/c^2$	Electric Charge	$V(r)$	Effective Range (m)	Relative Strength
strong	gluon	SU(3)	0	0	$r$	$10^{-15}$	1
weak	$W^\pm$	SU(2)	80.4	$\pm 1$	$\frac{e^{-Mr}}{r}$	$10^{-12}$	$10^{-6}$
	$Z^0$		91.2	0			
EM	photon	U(1)	0	0	$1/r$	$\infty$	$10^{-2}$

## 2.2 Example of Spontaneously Broken Symmetry

The  $SU(2)_L \times U(1)_Y$  local gauge invariance leads to the presence of massless gauge bosons in the EW theory. Experimental values of the masses of the  $W$  and  $Z$  gauge bosons suggest otherwise. Their masses are significantly large;  $\sim 85$ - $90$  times the mass of a proton, which is not a small effect. The Higgs mechanism [11–13] is one approach to remedy this problem by introducing mass terms in the GSW and SU(3) Lagrangians without violating local gauge invariance. This mechanism renders the  $W$  and the  $Z$  bosons massive. It also generates the masses of the fermions which couple to the Higgs field. A simple mathematical formalism [5] is introduced in this section to illustrate this mechanism. Its implementation in the framework of the SM is considered in the subsequent section.

Consider the U(1) gauge invariant Lagrangian,  $\mathcal{L}$ , of a scalar field  $\phi$  given by Eq. 2.10. The first two terms in Eq. 2.10 are the kinetic energy terms while the third is the potential term. The effective vacuum potential is given by:

$$\mathcal{L} = \frac{1}{2}(\partial_\mu \phi)(\partial^\mu \phi) - V(\phi). \quad (2.10)$$

$V(\phi)$  is chosen such that it is an even function of the scalar field, *i.e.*,

$$V(\phi) = V(-\phi) \quad (2.11)$$

so that the Lagrangian is invariant under the parity transformation  $\phi \rightarrow -\phi$ . The potential is chosen so as to ensure bounded oscillations about the vacuum state and that the theory be renormalizable. The simplest potential satisfying these requirements is given by 2.12

$$V(\phi) = \frac{1}{2}\mu^2\phi^2 + \frac{1}{4}|\lambda|\phi^4 \quad (2.12)$$

The lowest energy state of the system occurs at the minima of the potential  $V(\phi)$ . The parameter  $\mu^2$  can assume positive or negative values depending on which minimum potential changes. If the parameter  $\mu^2$  is positive, then the minimum of the potential occurs for:

$$\langle\phi\rangle_0 = 0 \quad (2.13)$$

The shape of the potential  $V(\phi)$  for this case is illustrated in Fig. 2.4(a) with the minimum at  $\langle\phi\rangle_0 = 0$ . The original Lagrangian (Eq. 2.10) is unchanged for small perturbations around the minimum and the parity transformation is also maintained. The theory described by this Lagrangian is simply QED with a massless force carrier (photon) and a charged scalar field  $\phi$  with a mass  $\mu$ . Another interesting scenario is when  $\mu^2$  is negative. The minimum occurs at

$$\langle\phi\rangle_0 = \pm\sqrt{\frac{-\mu^2}{|\lambda|}} \equiv \pm v. \quad (2.14)$$

The minima do not occur at  $\phi = 0$ , rather at  $\langle\phi\rangle_0 = \pm v$ . They are called the vacuum expectation values (VEV) and correspond to two degenerate vacuum (ground) states. The shape of the potential, shown in Fig. 2.4(b), is commonly referred to as *mexican hat* or *wine bottle* potential.

A choice of either ground state leads to the breaking of the symmetry of the Lagrangian in Eq.

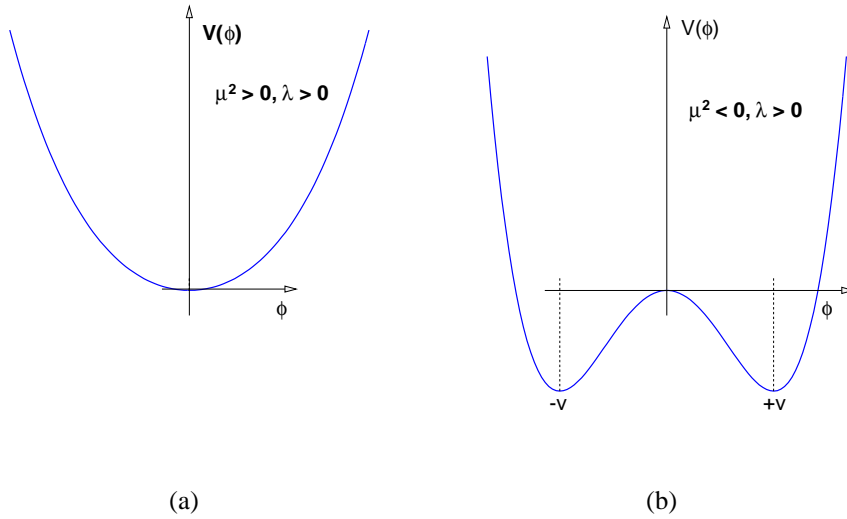


Figure 2.4. Scalar potential  $V(\phi) = \frac{1}{2}\mu^2\phi^2 + \frac{1}{4}|\lambda|\phi^4$  with (a)  $\mu^2 > 0, \lambda > 0$  and (b)  $\mu^2 < 0, \lambda > 0$ .

2.10. For example, consider the oscillations about  $\langle\phi\rangle_0 = +v$  and transform the coordinates such that

$$\phi' = \phi - v. \quad (2.15)$$

In the transformed coordinates, we may rewrite the Lagrangian as:

$$\mathcal{L} = \frac{1}{2}(\partial_\mu\phi')(\partial^\mu\phi') - |\mu^2| \left( \frac{\phi'^4}{4v^2} + \frac{\phi'^3}{v} + \phi'^2 - \frac{v^2}{4} \right). \quad (2.16)$$

The global U(1) symmetry of the Lagrangian is no longer preserved by this transformation. The vacuum state does not share the symmetry of the Lagrangian and it is said to be *spontaneously broken*. For small oscillations (s.o) about the vacuum we can rewrite Eq. 2.16 as:

$$\mathcal{L}_{s.o} = \frac{1}{2}(\partial_\mu \phi')(\partial^\mu \phi') - |\mu^2| \phi'^2, \quad (2.17)$$

which is the Dirac Lagrangian for small oscillations of a particle of mass  $m = \sqrt{2|\mu^2|}$ .

### 2.3 Higgs Mechanism

In order to achieve the goal of generating masses for the  $W$  and the  $Z$  bosons, while keeping the photon massless, we require at least three degrees of freedom for the scalar field. Simultaneously we require that QED remain an exact symmetry. The simplest choice would be to select a complex SU(2) doublet of scalar fields  $\phi$  which has two components;  $\phi^+$ , the charged component and  $\phi^0$ , the neutral component:

$$\Phi = \begin{pmatrix} \phi^+ \\ \phi^0 \end{pmatrix}, \quad Y_\phi = +1. \quad (2.18)$$

The simplest type of potential which is bounded, invariant and for which the theory is renormalizable can be expressed as:

$$V(\Phi) = \mu^2 \Phi^\dagger \Phi + \lambda (\Phi^\dagger \Phi)^2. \quad (2.19)$$

$\lambda > 0$  is required for the potential to be bounded, so that there exists a state of minimum energy. There are two cases of interest,  $\mu^2 > 0$  and  $\mu^2 < 0$ , which yield different shapes for the potential as described in the previous section. For  $\mu^2 < 0$ , the neutral component<sup>7</sup> develops

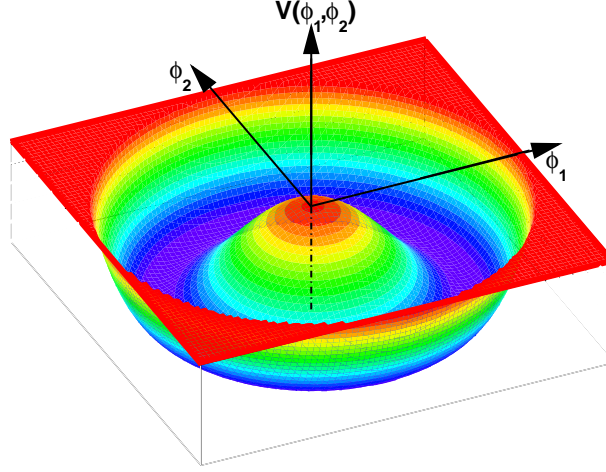


Figure 2.5. The shape of the wine bottle potential,  $V(\Phi) = \mu^2\Phi^\dagger\Phi + \lambda(\Phi^\dagger\Phi)^2$ , with degenerate minima.

a vacuum expectation value given by:

$$\langle\Phi\rangle_0 \equiv \langle 0|\Phi|0\rangle = \frac{1}{\sqrt{2}} \begin{pmatrix} 0 \\ v \end{pmatrix} \quad v = \sqrt{\frac{-\mu^2}{\lambda}}. \quad (2.20)$$

The Abelian Higgs model of the previous section can be applied to the GSW Lagrangian in a straightforward manner. The GSW model is a  $SU(2)_L \times U(1)_Y$  gauge theory containing three  $SU(2)_L$  gauge bosons (see section 2.1.2.2). which are labeled  $W_\mu^i$ ,  $i=1,2,3$ , and one  $U(1)_Y$  gauge boson  $B_\mu$ . The kinetic energy terms can be written as:

$$\begin{aligned} \mathcal{L}_{K.E} &= -\frac{1}{4}W_{\mu\nu}^i W^{\mu\nu i} - \frac{1}{4}B_{\mu\nu}B^{\mu\nu}, \\ W_{\mu\nu}^i &= \partial_\nu W_\mu^i - \partial_\mu W_\nu^i + g\epsilon^{ijk}W_\mu^j W_\nu^k, \\ B_{\mu\nu} &= \partial_\nu B_\mu - \partial_\mu B_\nu. \end{aligned} \quad (2.21)$$

---

<sup>7</sup>the charged component should remain unchanged to preserve the symmetry of  $U(1)_{QED}$ .

The Lagrangian for the  $SU(2)_L \times U(1)_Y$  is therefore:

$$\begin{aligned}\mathcal{L}_S &= \mathcal{L}_{K.E} - V(\Phi) \\ &= -\frac{1}{4}W_{\mu\nu}^i W^{\mu\nu i} - \frac{1}{4}B_{\mu\nu}B^{\mu\nu} - \mu^2\Phi^\dagger\Phi - \lambda(\Phi^\dagger\Phi)^2\end{aligned}\quad (2.22)$$

$$= (D^\mu\Phi)^\dagger(D_\mu\Phi) - \mu^2\Phi^\dagger\Phi - \lambda(\Phi^\dagger\Phi)^2$$

$$D_\mu \equiv \partial_\mu - i\frac{g_2}{2}\tau_\alpha \cdot W_\mu^\alpha - i\frac{g_1}{2}B_\mu Y. \quad (2.23)$$

We can re-write the complex scalar  $SU(2)$  doublet  $\Phi$  as four scalar fields  $\theta_{1,2,3}(x)$  and  $H(x)$ :

$$\Phi(x) \equiv \begin{pmatrix} \theta_2 + i\theta_1 \\ \frac{1}{\sqrt{2}}(v + H) - i\theta_3 \end{pmatrix} = e^{i\theta_\alpha(x)\tau^\alpha(x)/v} \begin{pmatrix} 0 \\ \frac{1}{\sqrt{2}}(v + H) \end{pmatrix} \quad (2.24)$$

The next step is to perform a suitable gauge transformation on  $\Phi$  by moving to the unitary gauge:

$$\Phi(x) \rightarrow e^{-i\theta_\alpha(x)\tau^\alpha(x)}\Phi(x) = \frac{1}{\sqrt{2}} \begin{pmatrix} 0 \\ v + H(x) \end{pmatrix} \quad (2.25)$$

Expanding the term  $(D^\mu\Phi)^\dagger(D_\mu\Phi) \equiv |D_\mu\Phi|^2$  in the Lagrangian  $\mathcal{L}_S$ :

$$\begin{aligned}|D_\mu\Phi|^2 &= \left| \left( \partial_\mu - i\frac{g_2}{2}\tau_\alpha \cdot W_\mu^\alpha - i\frac{g_1}{2}B_\mu Y \right) \Phi \right|^2 \\ &= \frac{1}{2} \left| \begin{pmatrix} \partial_\mu - \frac{i}{2}(g_2W_\mu^3 + g_1B_\mu) & -\frac{ig_2}{2}(W_\mu^1 - iW_\mu^2) \\ -\frac{ig_2}{2}(W_\mu^1 + iW_\mu^2) & \partial_\mu + \frac{i}{2}(g_2W_\mu^3 - g_1B_\mu) \end{pmatrix} \begin{pmatrix} 0 \\ v + H \end{pmatrix} \right|^2 \\ &= \frac{1}{2}(\partial_\mu H)^2 + \frac{1}{8}g_2^2(v + H)^2|W_\mu^1 + iW_\mu^2|^2 + \frac{1}{8}(v + H)^2|g_2W_\mu^3 - g_1B_\mu|^2.\end{aligned}\quad (2.26)$$

Defining the new fields by  $W_\mu^\pm$  and  $Z_\mu$  such that  $A_\mu$  is orthogonal to  $Z_\mu$  we get:

$$W^\pm = \frac{1}{\sqrt{2}}(W_\mu^1 \mp iW_\mu^2), \quad Z_\mu = \frac{g_2 W_\mu^3 - g_1 B_\mu}{\sqrt{g_2^2 + g_1^2}}, \quad A_\mu = \frac{g_2 W_\mu^3 + g_1 B_\mu}{\sqrt{g_2^2 + g_1^2}}. \quad (2.27)$$

Substituting the new fields defined above into Eq. 2.26 and identifying the bilinear terms in the fields  $W^\pm, Z, A$  yields:

$$M_W^2 W_\mu^+ W^{-\mu} + \frac{1}{2} M_Z^2 Z_\mu Z^\mu + \frac{1}{2} M_A^2 A_\mu A^\mu$$

$$M_W = \frac{1}{2} v g_2, \quad M_Z = \frac{1}{2} v \sqrt{g_2^2 + g_1^2}, \quad M_A = 0. \quad (2.28)$$

The  $W^\pm$  and  $Z$  bosons have acquired masses, while the photon remains massless. We say that the EW symmetry is spontaneously broken ( $SU(2)_L \times U(1)_Y \rightarrow U(1)_Q$ ) and the three Goldstone bosons have been absorbed by the  $W^\pm$  and  $Z$  bosons to form their longitudinal components. The  $U(1)_Q$  is still unbroken since the photon is massless. The remaining field  $H(x)$  is the Higgs field. The Lagrangian for the Higgs field can be written as:

$$\mathcal{L}_H = \frac{1}{2} (\partial_\mu H) (\partial^\mu H) - V(\Phi)$$

$$= \frac{1}{2} (\partial_\mu H)^2 - \lambda v^2 H^2 - \lambda v H^3 - \frac{\lambda}{4} H^4 \quad (2.29)$$

The first term in Eq. 2.29 is the kinetic energy term. The second term gives the mass of the Higgs boson as  $M_H^2 = 2\lambda v^2 = -2\mu^2$ . The third and fourth terms are the so-called *self interaction* terms which indicate the coupling of the Higgs boson to itself.

Generation of masses to fermions is achieved using the same complex scalar doublet  $\Phi$  with hypercharge  $Y_\theta = +1$  and the isodoublet  $\tilde{\Phi} = i\tau\Phi^*$  with hypercharge  $Y_\theta = -1$ . The Yukawa invariant Lagrangian is chosen for this exercise. A suitable gauge is chosen for the

scalar field and the Lagrangian is expanded in terms of the field. For example, the electron mass is obtained as follows:

$$\begin{aligned}
\mathcal{L}_F &= -\lambda_e \bar{L} \Phi e_R - \lambda_d \bar{Q} \Phi d_R - \lambda_u \bar{Q} \tilde{\Phi} u_R \\
&= -\frac{1}{\sqrt{2}} \lambda_e (\bar{\nu}_e, \bar{e}_L) \begin{pmatrix} 0 \\ v + H \end{pmatrix} e_R + \dots \\
&= -\frac{1}{\sqrt{2}} \lambda_e (v + H) \bar{e}_L e_R
\end{aligned} \tag{2.30}$$

The constant term in front of  $\bar{e}_L e_R$  is identified as the mass of the electron  $m_e = \frac{\lambda_e v}{\sqrt{2}}$ . Similarly the other fermion masses are obtained. The masses of the weak vector bosons and the fermions are obtained as a result of their interaction with the Higgs field. The mass terms manifest themselves by applying the spontaneous symmetry breaking mechanism and demanding that the Lagrangian be invariant under a suitable unitary gauge transformation of the scalar field. This process is known as the Higgs mechanism. Out of the four degrees of freedom for the scalar field, three are absorbed by the  $W^\pm$  and  $Z$  bosons which acquire mass, the fourth field corresponds to the Higgs field with a massive scalar particle, the Higgs boson, with  $M_H = \sqrt{-2\mu^2}$ . The vacuum expectation value ( $v$ ) of the Higgs field is determined from muon decay and is expressed in terms of the Fermi coupling constant  $G_F$  as:

$$v = \frac{1}{(\sqrt{2}G_F)^{1/2}} \sim 246 \text{ GeV}. \tag{2.31}$$

### 2.3.1 Phenomenology of the Higgs Boson

Through EW symmetry breaking and the Higgs mechanism the weak vector bosons and the fermions acquire masses. The theoretical framework presented in the previous section introduces a massive spin 0 scalar, the Higgs boson. Its existence is crucial to prove the validity of the theory. The Higgs boson (henceforth referred to as ‘Higgs’) has not yet been observed



experimentally. Despite the prediction of such a particle, the theory does not provide a direct estimate of its mass. There are a few theoretical constraints which will be discussed briefly in this section.

- Triviality

Assuming no new physics exists and the current EW theory is an effective field theory valid up to the *cutoff or Planck* energy scale ( $\sim 10^{19}$  GeV), we can set a bound on the Higgs mass. Because of quantum corrections, the masses and couplings in the SM Lagrangian depend on the energy scale. The Higgs boson couples to itself and one of the coupling terms is a quartic term ( $\lambda^4$ ) which increases monotonically with the energy scale  $|Q|$ . The quartic term varies logarithmically with the energy squared,  $Q^2$ . The requirement that the quartic self-coupling remain finite (non zero) at some cutoff energy leads to an upper bound on the Higgs mass known as the *triviality bound*. Otherwise, at this energy scale, the coupling becomes very small and vanishes rendering the theory trivial, *i.e.*, non-interacting. From this triviality argument the upper bound on the Higgs mass, assuming the cutoff scale to be ( $\Lambda_C \sim 10^{16}$  GeV), is  $M_H < 160$  GeV.

- Vacuum Stability

The coupling  $\lambda$  can be small at a certain cutoff scale, at which stage the contribution from the Higgs coupling to the top quark can be dominant and can drive it to a negative value ( $\lambda(Q^2) < 0$ ). This leads to a negative scalar potential,  $V(Q^2) < V(v)$ , which in turn implies an unstable vacuum or a potential energy not bounded from below. In order to have a stable vacuum the Higgs mass must be bounded from below. The lower bound on the Higgs mass with this argument, assuming a cutoff scale to be the EW unification scale ( $\Lambda_C \sim 10^3$  GeV), is  $M_H > 70$  GeV. The indirect limits from theory on the Higgs mass is shown in Fig. 2.6.

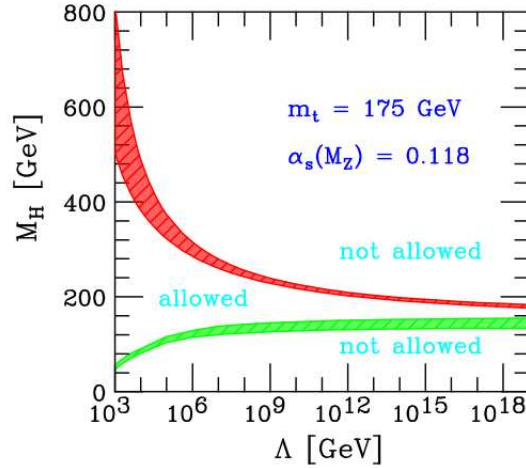


Figure 2.6. The triviality upper bound and vacuum stability lower bound on the Higgs mass as a function of the cut off energy scale,  $\Lambda$ . The colored/shaded bands indicate the impact of uncertainties. Plot adopted from [9].

- Electroweak Precision Measurements

The LEP EW working group [10] has combined the experimental data from several precision EW measurements of SM parameters. These measurements are sensitive to the Higgs mass. Through direct searches for the Higgs boson, the LEP experiment has set a 95% confidence level (CL) limit on the Higgs mass:  $m_H > 114.4 \text{ GeV} @ 95\% \text{ CL}$ . This exclusion region is shown as the yellow band in Fig. 2.7(a), which is a plot of the goodness of fit to EW data compared to theory,  $\Delta\chi^2 = \chi^2 - \chi_{min}^2$ , as a function of the unknown Higgs mass  $m_H$ . The blue band indicates the theoretical uncertainty and the solid black line indicates the best  $\Delta\chi^2$ . These constraints yield a Higgs mass of  $76_{-24}^{+33} \text{ GeV} @ 68\% \text{ CL}$  and  $< 144 \text{ GeV} @ 95\% \text{ CL}$ .

Higgs boson couples to the heaviest quark, *i.e.*, the top quark and the  $W$  boson. For example, the mass of  $W$  is sensitive to the mass of the top quark and that of the Higgs boson through higher order loop corrections. The  $W^\pm$  mass corrections have a logarithmic dependence on the Higgs mass and a quadratic dependence on the top-quark mass. This dependence can be used to set experimental constraints on the Higgs mass as shown in Fig. 2.7(b). The red(blue) contour is a 68% CL interval in which the  $W$  and top masses are expected to lie from

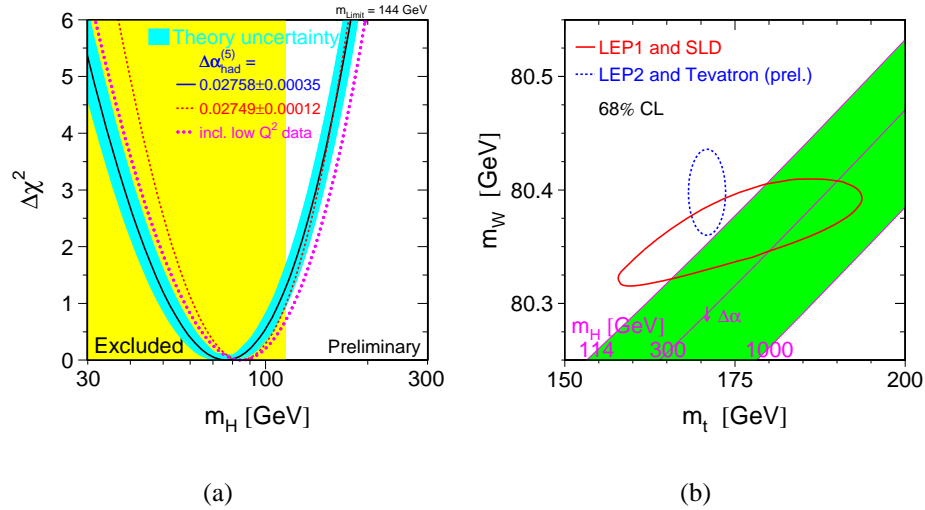


Figure 2.7. (a) The goodness of fit of EW precision variables compared to their experimental values,  $\Delta\chi^2$ , is plotted as a function of the Higgs mass. The yellow band indicates the LEP excluded region based on experimental search. (b) Higher order loop corrections to the masses of the top quark and the  $W$  boson are sensitive to the Higgs mass, which enables us to set indirect constraints on its mass. Plots adapted from [10].

the combined LEP1 and the SLD data (LEP2 and Tevatron data). The green band indicates the functional dependence of  $W$  and top masses for a fixed value of Higgs mass. A heavier  $W$  mass is measured using the latest Tevatron data which seems to favor (unfavorably to the LEP exclusion limit) a Higgs mass lighter than 114.4 GeV.

### 2.3.2 $WH$ Associated Production at the Tevatron

Figure 2.8(a) shows different ways to produce a SM Higgs boson at the Fermilab Tevatron collider. The gluon fusion channel ( $gg \rightarrow H$ ), is the dominant production mechanism followed by the *higgsstrahlung* process in which a quark and anti-quark pair from the colliding hadrons fuse to create a virtual EW boson ( $W^\pm$  or  $Z$ ) which in turn decays into a real EW boson and a Higgs boson. This production channel is commonly referred to as *associated* production.

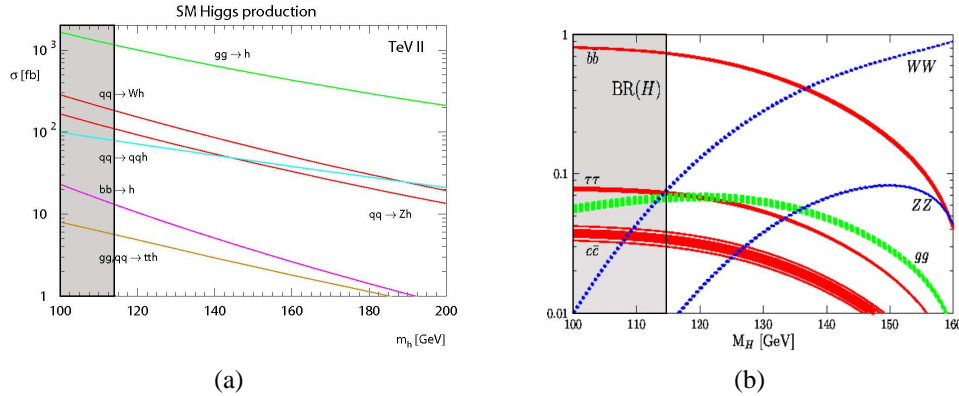


Figure 2.8. Dominant (a) production channels and (b) branching ratios for the Higgs boson at the Tevatron with  $p\bar{p}$  collisions at  $\sqrt{s} = 2$  TeV.

Although the gluon fusion channel has a high production rate, it is overwhelmed by QCD dijet/multijet processes which reduce the discrimination power for discovering a relatively small Higgs signal. However, associated production channels provide a better separation of Higgs from QCD multijet and other SM backgrounds, since the leptonic decay of the associated vector bosons can be exploited to better differentiate the signal. A light Higgs ( $m_H < 135$  GeV/ $c^2$ ) primarily decays into a  $b$ -quark and its anti-quark since it couples to quarks, and  $b$ -quarks are the heaviest particles kinematically allowed below 135 GeV/ $c^2$ . Other decay channels with a Higgs decaying into a virtual EW boson become dominant as the Higgs mass increases. Various branching ratios are shown in Fig. 2.8(b).

### 2.3.3 Higgs Sensitivity Studies

In August 2003, the Tevatron Higgs working group conducted an analysis with  $\sim 500$   $pb^{-1}$  of data to estimate the discovery potential for the SM Higgs boson [14]. The summary plot from this study is shown in Fig. 2.9. The plot shows the projected upper limits on the production cross section of the Higgs as a function of integrated luminosity acquired per experiment for the mass region  $115 < m_H < 200$  GeV/ $c^2$ . The shaded region below 114.4 GeV/ $c^2$  is excluded by the LEP experiments.

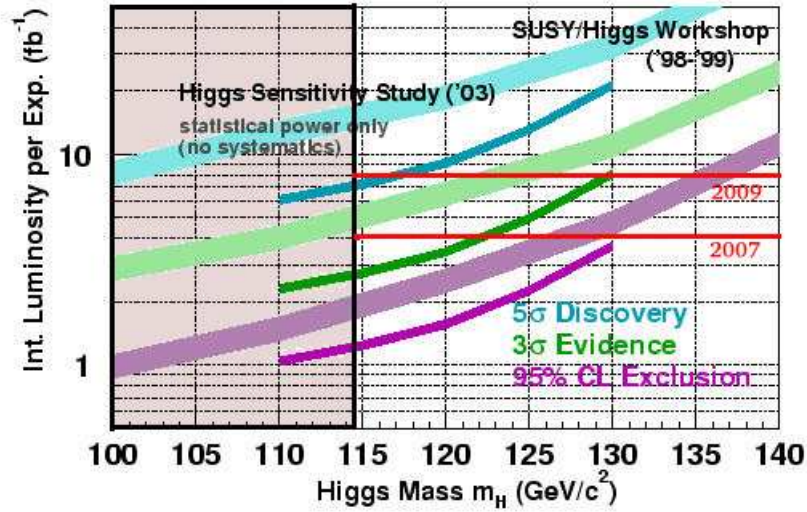


Figure 2.9. Integrated luminosity per experiment required at the Tevatron to discover the Higgs boson is shown as a function of the Higgs mass. The projected 95% CL,  $3\sigma$  and  $5\sigma$  limits are shown. The shaded region is excluded by LEP experiments. Plot adopted from [14].

The Tevatron is expected to acquire a total of  $\sim 8 \text{ fb}^{-1}$  of data per experiment by the year 2009. If no Higgs signal is observed the 95% CL lower limit on the SM Higgs mass is projected to be  $m_H > 138 \text{ GeV}/c^2$ . If there is evidence of a signal at the  $3\sigma$  level, then the Higgs mass is expected to be  $m_H < 129 \text{ GeV}/c^2$ , and for a  $5\sigma$  discovery it is necessary that  $m_H < 117 \text{ GeV}/c^2$ . This study provides a benchmark for the future Higgs sensitivity. As of August 2007, the integrated luminosity recorded by the DØ experiment is  $\sim 3 \text{ fb}^{-1}$ . The results presented in this analysis are combined with other SM higgs searches from DØ and combined with the results from CDF experiment [15] to obtain a combined exclusion limit, which will be presented in the final chapter.

## CHAPTER 3

### EXPERIMENTAL APPARATUS

An overview of the Fermilab Tevatron particle accelerator (or the collider) and the DØ detector is presented in this chapter. Both the Tevatron collider and the DØ detector have undergone several upgrades since they began operating; the description given here corresponds to their current state. The Tevatron collider started its operation in 1983, and the first collisions were observed and recorded in 1985 with a center-of-mass collision energy,  $\sqrt{s} = 1.8$  TeV [16]. This remarkable epoch (also called Run I) lasted for ten years and led to the discovery of the top quark in 1995 [17, 18].

The goal of Run II is to deliver about 100 times the number of collisions to the experiments by the year 2009 with at a slightly higher energy,  $\sqrt{s} = 1.96$  TeV. In addition, upgrades to the detectors to enhance their capabilities make Fermilab a unique place for high energy physics research. The data analyzed in this study was recorded with the DØ detector during the Run IIA phase of operation at the Tevatron, starting from March 2002 and ending in February 2006. The Tevatron is currently the highest energy accelerator in the world.

#### 3.1 The Fermilab Chain of Accelerators

The Fermilab chain of accelerators are used to accelerate beams of protons ( $p$ ) and anti-protons ( $\bar{p}$ ) close to the speed of light and collide them head on. The largest of these accelerators is the Tevatron synchrotron, which has a circumference of 6283 m (about four miles) and uses about 1000 superconducting magnets. Stochastic cooling technologies are employed to accelerate and store 980 GeV protons and anti-protons that circulate in opposite directions, and steer them to a head on collision at two interaction points. Thus the Tevatron serves the dual

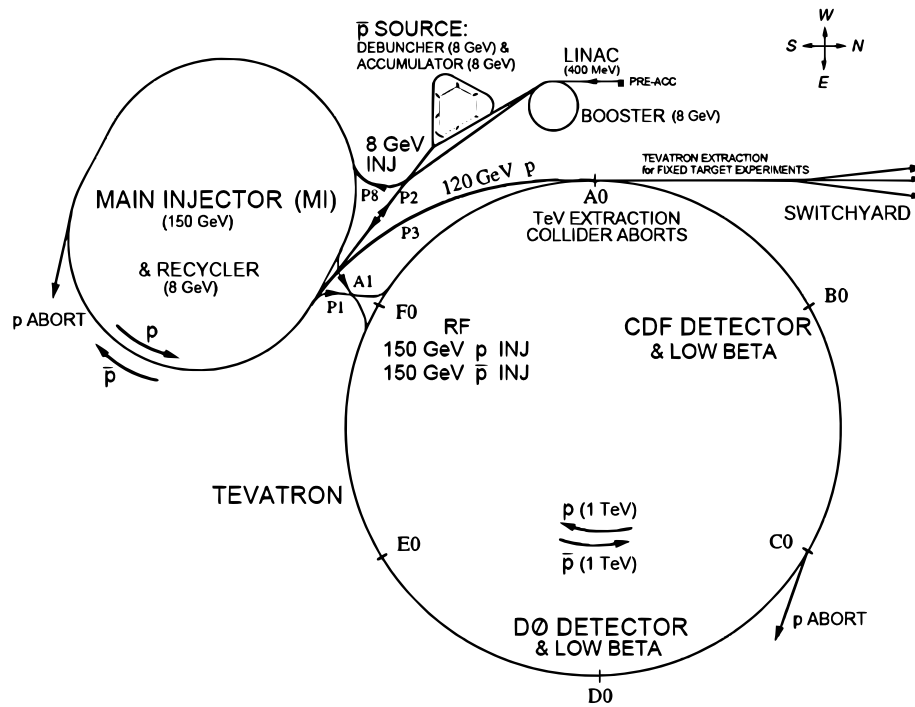


Figure 3.1. Schematic diagram of Tevatron Accelerator Complex during its Run IIA phase (not to scale). Plot adopted from [19].

purposes of a storage ring and a synchrotron. The  $D\bar{O}$  and the CDF detectors surround the two interaction points to record the collisions. A general layout of the Fermilab Accelerator Complex is shown in Fig. 3.1. The Tevatron itself is the last piece in a series of accelerating stages that are essential for the successful operation of the Fermilab Accelerator Complex. More information and technical details of this complex can be found in [20, 21]. A brief description of their operation is given below.

- Ion Source and Pre-Accelerator

Negatively ionized hydrogen gas ( $H^-$ ) is produced using a magnetron surface plasma source [22] and accelerated to a beam energy of 18 keV. A schematic of the apparatus is shown in Fig. 3.2.

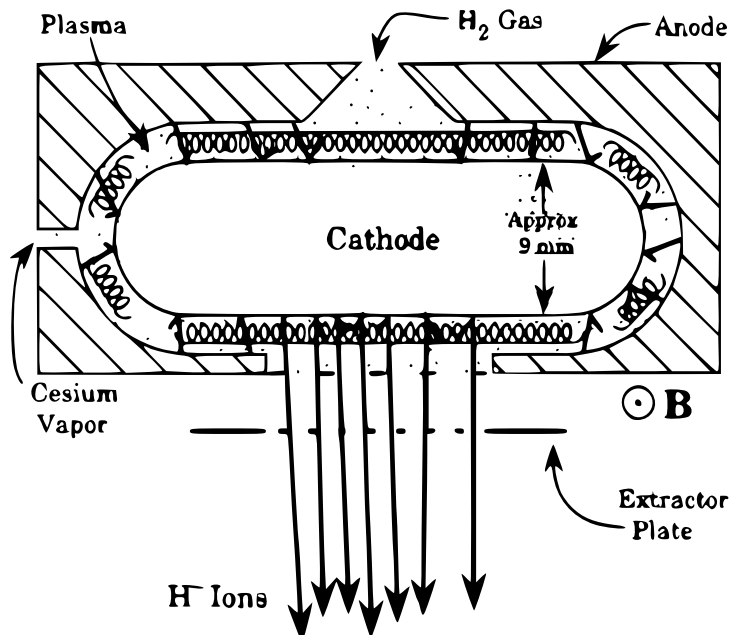


Figure 3.2. Schematic diagram of magnetron surface plasma source [23].

The magnetron source consists of an oval shaped cathode surrounded by an anode. They are separated by a small gap ( $\sim 1$  mm) where an electric field is applied as shown in the schematic. A uniform magnetic field is also applied through the apparatus. Hydrogen gas ( $H_2$ ) is introduced into the gap at low pressure. The electrons are stripped off hydrogen atoms by the presence of the electric and magnetic fields. The electrons spiral around in the gap, filling it with a dense plasma of ions and electrons. The positively charged hydrogen ions strike the cathode and occasionally collect two extra electrons to become negatively charged hydrogen ions ( $H^-$ ). This process attains 10% efficiency when the cathode surface is coated with a cesium vapor 0.6 mono-layers thick. The negative ions are extracted from the aperture and accelerated to 18 keV through the extractor plate.

The Cockroft-Walton accelerator is a solid state device that generates high voltage using a voltage multiplier circuit. Fermilab uses a “dual leg five stage” Cockroft-Walton device to yield a factor of ten increase in the output voltage. Using this device the  $H^-$  ions pick up 750



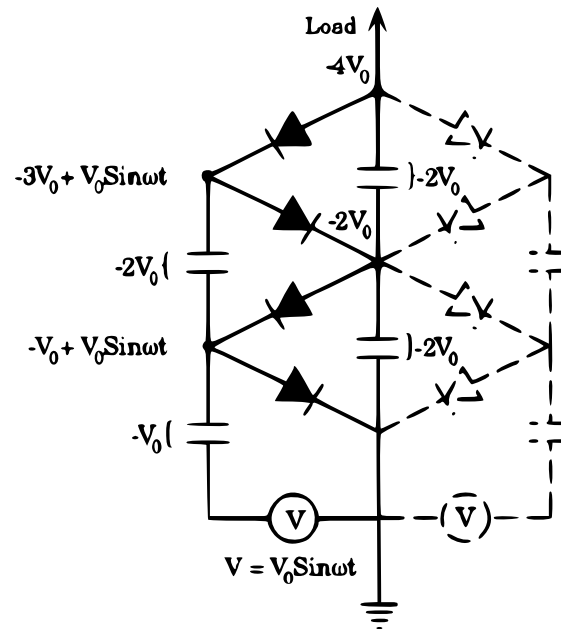


Figure 3.3. Schematic diagram of a typical Cockcroft-Walton Generator [24]. The filled lines indicate a voltage multiplier circuit consisting of two stages of diodes. Each stage doubles the output voltage. The dotted lines indicate the addition of a second leg to stabilize the circuit by reducing ripple. A total of five stages in the Fermilab Cockcroft-Walton generator yields a ten fold increase in the output voltage.

keV of energy. After being accelerated to 750 keV the beam is then transferred to the next stage of acceleration in the *linac*. The hydrogen ion source, the Cockcroft-Walton generator, an electrostatic accelerating column and a transport line that injects the beam into the linac are collectively referred to as the *pre-accelerator*.

- The Linac

The Fermilab LINear ACcelerator (linac) accelerates the  $H^-$  ions from 750 keV to 400 MeV in two stages. The Alvarez-type drift tube linac is about 79 m long and accelerates the ions in five electrically resonant cylindrical tanks. Each radio frequency (RF) tank consists of many drift tubes that are suspended in the center along the axis of the tank. Each drift tube has a bore hole through which the ion beam passes. The RF tanks (also called RF resonant

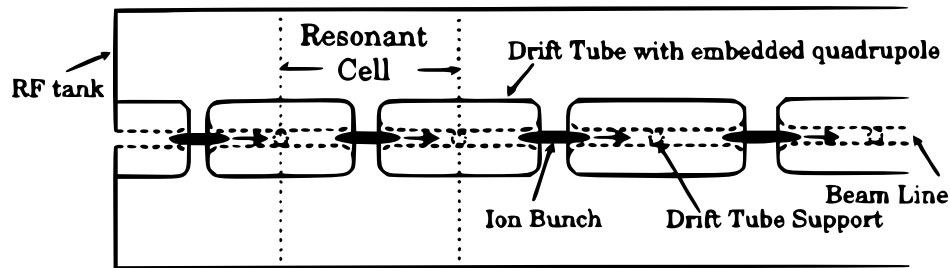


Figure 3.4. Top view of a simple Alvarez-type drift tube Linac showing the RF Tank, the drift tubes and particle bunches filling each RF bucket [24].

cavities) resonate at high frequency (201.25 MHz), causing the ions to attain 116 an energy of MeV.

The side-coupled cavity linac is similar to the Alvarez-type drift tube linac except that its tubes are designed differently, thereby enabling it to operate with higher efficiency. This portion of the linac is 67 m long with seven cavities operating at a resonant frequency of 805 MHz. The hydrogen ions attain an energy of 400 MeV at this stage. The linac also makes bunches of hydrogen ions (as opposed to a continuous beam) with pulses of 201.25 MHz frequency before it is transferred to the Booster.

- The Booster

Before entering the Booster accelerator, bunches of  $H^-$  are passed through a Debuncher which reduces the momentum spread of the bunches in the beam. The bunch length at this stage is approximately 8 mm. The bunches are then stripped of their electrons by forcing the beam through a carbon foil, leaving only the protons.

The Booster is a 75.47 m radius synchrotron ring and is the first synchrotron in the chain of accelerators. It accelerates the bunches of protons from 400 MeV to 8 GeV through RF cavities and alternating gradient magnets [23, 25]. The proton bunches are kept in orbit by

these magnets while the RF is varied from 37.77 MHz at injection to 52.81 MHz when they acquire a kinetic energy of 8 GeV.

- The Main Injector

The Main Injector is a larger synchrotron with a circumference of approximately two miles [26]. Proton bunches are accelerated from 8 GeV up to 150 GeV using the same principle as the booster with RF cavities and gradient magnets. The proton beam at 150 GeV is transferred to the Tevatron accelerator. Proton bunches are also transferred to the anti-proton source when they reach 120 GeV. The Main Injector replaced the Main Ring from the Run I era in order to deliver higher luminosity beams to various Run II physics programs. The use of the Main Injector in place of the Main Ring offers several benefits:

- Increase in proton intensity from  $4.5 \times 10^{15}$ /hour to  $12 \times 10^{15}$ /hour.
- Increase in total number of protons injected to the Tevatron up to  $6 \times 10^{13}$ .
- Acceleration of anti-protons in stacks of  $2 \times 10^{12}$  for injection into the Tevatron.

- The Anti-Proton Source

The proton bunches from the Main Injector are used to make anti-protons. This process is very cumbersome compared to the production of protons. The difficulty arises due to the fact that a million protons are required to produce about 15 anti-protons. The production of anti-protons is a limiting factor in achieving higher luminosities<sup>1</sup> at the Tevatron. The anti-proton source is a facility that includes the Debuncher and the Accumulator rings, along with a Target Station consisting of a nickel target onto which the protons bunches are focused [27].

The proton bunch from the Main Injector is a stack of  $5 \times 10^{12}$  protons with 120 GeV of energy. This beam of protons is diverted to the Target Station where it is brought to focus into the small area of the nickel target using a series of quadrupole magnets. These protons undergo

---

<sup>1</sup>Luminosity is defined in section 3.2.

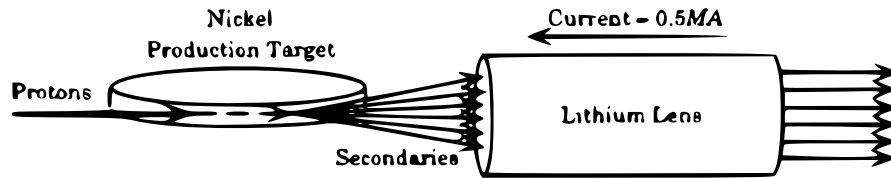


Figure 3.5. Diagram depicting the operation of the lithium lens used to collect the anti-protons [27].

collisions with the nickel nuclei, disintegrate and produce a shower of secondary particles. This shower of particles is further focused using a lithium lens (also called the “collection lens”). Negatively charged particles from the secondary beam are extracted using dipole magnets and the remainder of the particles are absorbed at a beam dump. A diagram depicting this operation is shown in Fig. 3.5.

- The Debuncher and Accumulator

The anti-protons have 8 GeV of energy with significant spread in the range of particles’ momenta when they enter the Debuncher. One of the tasks of the Debuncher is to remove the bunch structure remnant from the proton bunches introduced by the Main Injector. It accepts the anti-protons generated from the target and reduces their momentum spread through a process called *adiabatic debunching*. The randomness of the momenta of the anti-protons is best described by its temperature; hence the *stochastic cooling* process reduces the temperature of the beam to maintain its homogeneity on a particle-by-particle basis. Stochastic cooling also reduces the phase space occupied by the beam and aids in fitting the beam through the small aperture of the Accumulator.

The Accumulator synchrotron is used to collect large a quantity of anti-protons before injection into the Main Injector. The Accumulator also creates a bunch structure of anti-protons that coincides with the bunch structure of protons in the Main Injector. The anti-protons are

then injected into the Main Injector and ramped up to 150 GeV. Accumulation of anti-protons takes a significant amount of time ( $\sim 10^{12}$  in a few hours).

- The Tevatron

The Tevatron is the last of the accelerating synchrotrons. It accepts protons and anti-protons from the Main Injector at 150 GeV and accelerates them in opposite directions to 980 GeV each. All its magnets, *i.e.*, 774 dipoles, 216 quadrupoles and correction magnets that form the lattice of its structure, are superconducting and are cooled by liquid helium to a temperature of 4.6 K. It has a radius of 1 km and is situated  $\sim 65$  cm below the Main Ring within the same tunnel enclosure. Its RF system operates  $\sim 53$  MHz. The Tevatron keeps beams of protons and anti-protons orbiting in opposite directions inside a 4 T magnetic field provided by the dipoles. The beams are focused further near the interaction regions (where the collisions occur and the detectors are located) using quadrupole focusing magnets. This focusing results in increased luminosity. The shape of the interaction region has a 3-d Gaussian profile with a width,  $\sigma_z$ , of about 30 cm along the beam axis, the  $z$  direction, and  $30 \mu m$  in the transverse,  $x$  and  $y$ , directions. The available energy in the center-of-mass frame,  $\sqrt{s} = 2 \times 980 \text{ GeV} = 1.96 \text{ TeV}$ . The beams consist of 36 bunches (each) of protons and anti-protons traveling in opposite directions with a bunch spacing of 396 ns (2.5 MHz crossing rate). Some bunch crossing intervals are intentionally left empty to bring stability to the beam and for calibration purposes. When the beams cross, the beam halos<sup>2</sup> are removed by a process called *scraping*, using devices called collimators. A *store* is the amount of time during which the collisions are recorded by the detectors, and typically lasts for about a day (24 hours). The luminosity of the beams fall exponentially with time and are eventually dumped. On rare occasions a malfunction<sup>3</sup> may result in loss of beam; when this occurs the Tevatron is said to have *quenched* [28].

---

<sup>2</sup>Protons and anti-protons in irregular orbits far from the beam center.

<sup>3</sup>The cryogenic magnet goes from a superconductive temperature to normal.

### 3.2 Cross section and Luminosity

Cross section,  $\sigma$ , is a frequently used term in particle physics. In modern particle experiments, the particles that are typically collided have small effective interacting areas. It is intuitive to relate cross section to a geometrical area as is the case for classical elastic collisions between two objects. These experiments often look for rare processes (*e.g.*, the production of a Higgs boson). The rate of production is expressed as a cross section. The unit of cross section is a ‘barn’ (1 barn  $\equiv 10^{-24}$  cm<sup>2</sup>), which is a large unit for expressing the cross section of rare physical processes. Hence the units used to express the cross sections are pico barn (pb or  $10^{-12}$  barn) or femto barn (fb or  $10^{-15}$  barn). Although it is analogous to a geometrical area, the cross section is merely a measure of the (quantum mechanical) interaction probability per unit flux, unlike elastic collisions in classical mechanics.

In collider experiments like the CDF and DØ the flux is the size and amount of particles in the colliding beams and is referred to as *luminosity* ( $\mathcal{L}$ ). Luminosity depends on the beam characteristics *viz.*, number of particles in each colliding beam, the number of bunches and the transverse size of these bunches. Equation 3.1 is the expression for the Tevatron luminosity, expressed in units of cm<sup>-2</sup>s<sup>-1</sup> [29].

$$\mathcal{L} = \frac{fBN_pN_{\bar{p}}}{2\pi(\sigma_p^2 + \sigma_{\bar{p}}^2)} F\left(\frac{\sigma_\ell}{\beta^*}\right) \quad (3.1)$$

where;

$f \equiv$  revolution frequency

$B \equiv$  number of bunches

$N_q \equiv$  number of protons or anti-protons

$\sigma \equiv$  gaussian width of the proton or anti-proton beam

$F\left(\frac{\sigma\ell}{\beta^*}\right) \equiv$  form factor

The rate of occurrence ( $\mathcal{R}$ ) of a particular physical process is proportional to the cross section for that process and the luminosity. It can be written as in Eq. 3.2:

$$\mathcal{R} = \sigma \cdot \mathcal{L}. \quad (3.2)$$

For a given process, the cross section is a constant but the luminosity changes over time. It is useful to define the number of occurrences ( $N$ ) of a process over a fixed period of time. As shown in Eq. 3.3, this can be achieved by defining *Integrated Luminosity*, which is the integral of the luminosity over a given time interval ( $\Delta t$ ).

$$N = \sigma \int_{t_0}^{t_0+\Delta t} \mathcal{L} dt \quad (3.3)$$

For example, if the process has a cross section of 0.01 pb it is expected to occur 10 times during the delivery of 1000 pb<sup>-1</sup> integrated luminosity. The Tevatron delivered 1.6 fb<sup>-1</sup> of data during the period, April 2002 to April 2006. The data recorded by the DØ experiment during this period was 1.3 fb<sup>-1</sup>. The results presented in this thesis correspond to the Run IIA dataset which is about 1.1 fb<sup>-1</sup> of recorded DØ data (see Fig. 3.6).

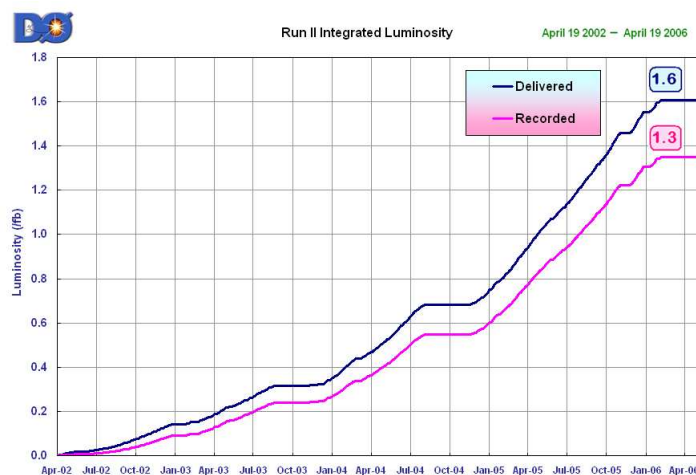


Figure 3.6. Integrated luminosity delivered to (and recorded by) the DØ experiment between April 2002 and April 2006.

### 3.3 Upgraded DØ Run II Detector

The DØ detector is a complex apparatus composed of several sub-detector components housed in a 2000 m<sup>3</sup> collision vault centered at the DØ interaction point of the Tevatron ring. The DØ detector is a massive structure with nearly 5000 tons of detector material and about a million readout channels to record the interactions. It surrounds the interaction point and is designed to accurately identify, measure and record the properties of the particles emanating from the proton anti-proton ( $p\bar{p}$ ) collisions. The innermost layers surrounding the beam pipe at the interaction point are the tracking chambers, which precisely record the paths taken by the charged particles. Surrounding the tracking system is the calorimeter, which measures the energy of electromagnetic (EM) and the hadronic particles. The muon chambers measure the momenta of muons that make it through the calorimeter leaving a small amount of energy, and pass through the thick iron toroid magnets. A diagram of the DØ detector is shown in Fig. 3.7.



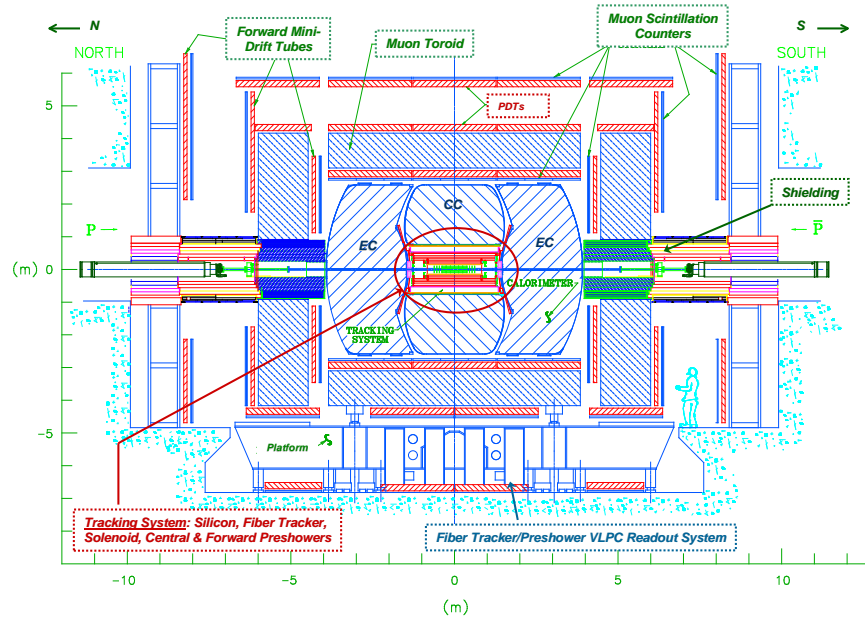


Figure 3.7. Side view of the upgraded DØ Run II Detector showing the sub-systems [30].

### 3.4 Coordinate System and Kinematic Quantities

The DØ detector employs a right-handed coordinate system with its origin at the center of the detector. It has cylindrical symmetry about the beam axis, whereas the particle collisions exhibit spherical symmetry (in their rest frame) about the nominal interaction point. This motivates the choice of a combination of cylindrical and spherical coordinates  $(z, \theta, \phi)$ . Figure 3.8 shows the coordinate system used at DØ. The polar angle  $\theta$  is defined such that  $\theta = 0$  lies along the beam pipe in the  $+z$  direction, while  $\theta = \pi/2$  is perpendicular to the beam pipe. The azimuthal angle  $\phi$  is defined such that  $\phi = 0$  points away from the center of the Tevatron ring (this direction is also the positive  $x$ -axis). The upward direction,  $\phi = \pi/2$ , defines the positive  $y$ -axis.

It is necessary to define a kinematic variable called *rapidity* ( $y$ ) to be used in place of the polar angle. The number ( $N$ , or multiplicity) of particles produced in a given range of rapidity *i.e.*,  $dN/dy$  is invariant under relativistic Lorentz transformation (*boost*) along the  $z$ -axis, provided the particles' energies are sufficiently large compared to their masses. The colliding

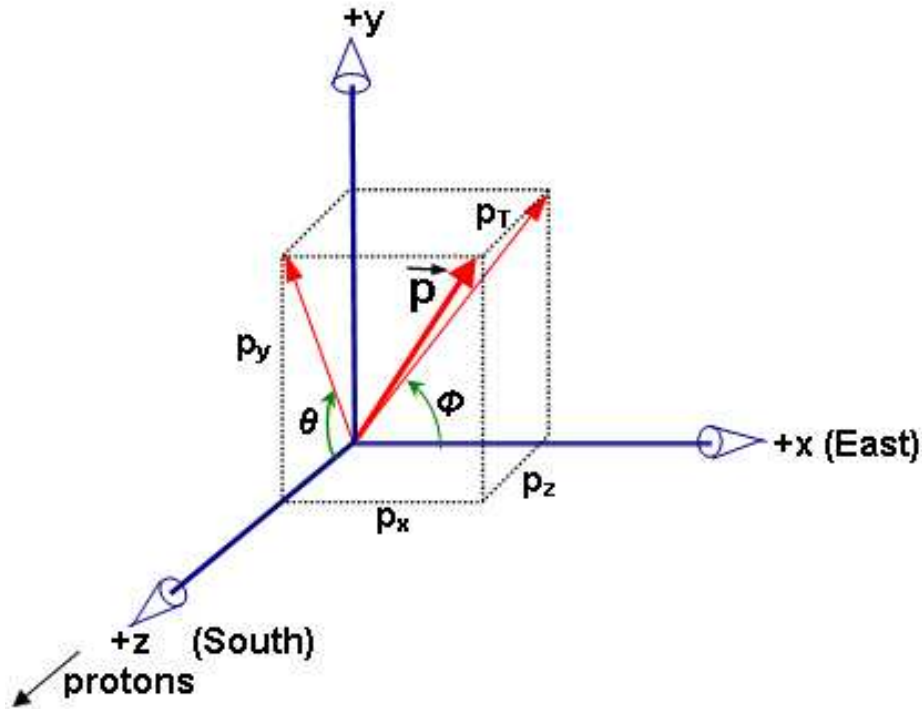


Figure 3.8. Diagram showing the coordinate system at DØ .

beams have almost negligible net boost in the transverse direction ( $xy$ -plane). Therefore it is suitable to describe the kinematic properties of particles resulting from the collision in the laboratory frame reference. However, this is not the case for the  $z$ -axis, where the particles in the beam may experience a net boost. The interactions and physical phenomena occur in a dynamical frame which is adjusted for each collision (*event*). The nominal interaction point or the origin (also called the *primary vertex*) does not coincide with the geometrical center of the detector. Rapidity is defined as

$$y = \frac{1}{2} \ln \left( \frac{E + p_z}{E - p_z} \right) \quad (3.4)$$

where  $p_z$  is the particle's momentum along the  $z$ -axis and  $E$  is its energy. Although  $y$  is useful, the quantity that is most often utilized is *pseudorapidity* ( $\eta$ , also called the physics pseudorapidity) which is defined as:

$$\begin{aligned}\eta &\equiv \lim_{m/E \rightarrow 0} y & (3.5) \\ \eta &= -\ln \tan\left(\frac{\theta}{2}\right) \\ &= \tanh^{-1}(\cos \theta)\end{aligned}$$

Pseudorapidity approximates the true rapidity when the mass of the particle is much smaller than its energy. In a  $p\bar{p}$  experiment like DØ, the beam dimensions in the transverse direction are negligible compared to the  $z$ -axis, where the beam is much wider due to the longitudinal bunch length of the protons and anti-protons (refer to section 3.1). As a result of this beam structure, another variable called the *detector pseudorapidity* ( $\eta_D$ ) is computed with respect to an interaction point centered exactly at  $z = 0$  (as opposed to the real interaction point which has a 3-d Gaussian distribution around  $z = 0$ ). Detector pseudorapidity may be different from pseudorapidity ( $\eta \neq \eta_D$ ). The physics pseudorapidity of a particle is determined by  $\theta$ , which is measured from the interaction point or the primary vertex using Eq. 3.5. Solid angles are often measured in terms of the quantity  $\Delta R$ , which is defined as:

$$\Delta R = \sqrt{\Delta\eta^2 + \Delta\phi^2}. \quad (3.6)$$

$\Delta R$  is approximately invariant under boosts in the  $z$  direction.

Since the parton-parton collisions do not occur at fixed  $\sqrt{s}$  and a significant fraction of the energy escapes the detector as the nucleon remnants carry it away down the uninstrumented beam pipe, the longitudinal boost of hard scatter particles is difficult to measure. There is also the possibility of more than one interaction occurring for every bunch crossing. However,

these particles can be still be studied by applying conservation of energy and momentum in the transverse plane. Before the collision occurs the transverse energy of the system is zero. After the hard scatter the transverse energy of the nucleon (proton and anti-proton) remnants is negligible, facilitating the study of the hard scatter particles in this plane. Several variables are defined to study the hard scatter particles in the transverse plane. Some of the particles (*e.g.*, neutrinos) escape detection and the energy carried away by them manifests itself as a net imbalance in the energy when conservation of energy is applied in the transverse plane. This is called missing transverse energy  $\cancel{E}_T$ .

### 3.5 Inner Tracking System

The entire tracking system (see Fig. 3.9) in Run II is new and is the closest system to surround the beam pipe. It is composed of two sub-detector components, *viz.*, the Silicon Microstrip Tracker (SMT) and the Central Fiber Tracker (CFT). One standard method for measuring the momentum of a charged particle is to determine the curvature of its trajectory in a magnetic field. The superconducting solenoid that surrounds the tracking system is 2.7 m long and provides a uniform magnetic field of strength 2 T inside the tracking volume [31, 32]. It has two layers of superconducting coils which store 5 MJ of energy. Charged particle paths are bent such that the curvature of their trajectories are inversely proportional to their momenta. Precise measurement of a charged particle's momentum as well as the sign of its electrical charge is possible by using the information from the tracking system.

#### 3.5.1 Silicon Microstrip Tracker (SMT)

The demand for precise measurement of tracks prompted the design of a silicon detector for the Run II DØ detector. Its purpose is to provide a very good momentum resolution for tracks and good vertex reconstruction. Being the highest resolution sub-detector compo-

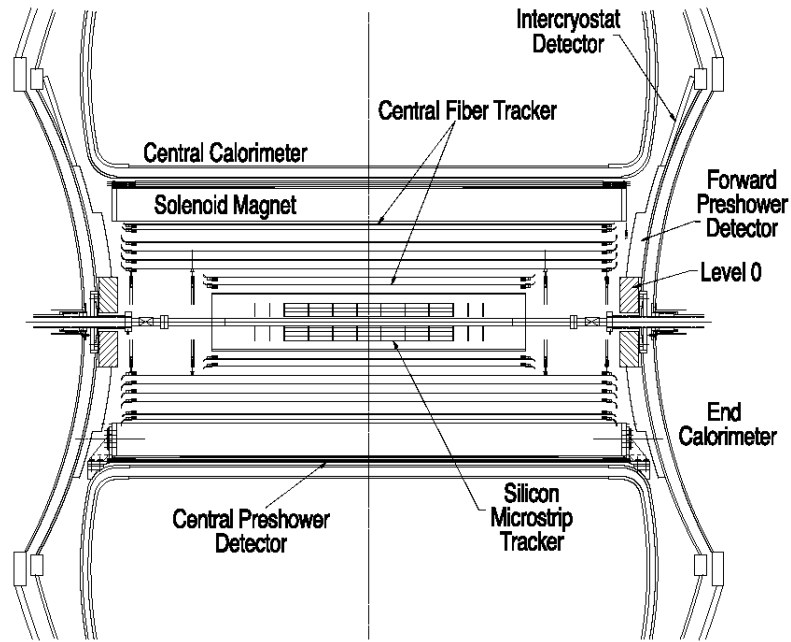


Figure 3.9. Run II tracking system at DØ [30].

ment and closest to the interaction region, the SMT provides excellent vertexing and impact parameter capability. Some of the requirements of the SMT are:

- Three dimensional track reconstruction capability with transverse impact parameter resolution better than  $30 \mu\text{m}$  and a good vertex resolution in the longitudinal direction.
- Radiation hard detector which can withstand the increased luminosity environment of Run II.
- Fast readout system that can be operated at 2.5 MHz bunch crossing rate.

The SMT meets all the above requirements. It is composed of a hybrid system: barrel (strips running parallel to the beam direction) and disk (strips perpendicular to the beam direction) geometry detectors [33] which form the innermost layers of the DØ detector ( $r_{SMT} < 10 \text{ cm}$ ) as shown in Fig. 3.10. The large  $z$  distribution of the  $p\bar{p}$  interaction region ( $\sigma_z \sim 30 \text{ cm}$ ) provides a motivation for the above detector geometry. The SMT provides good tracking coverage for large pseudorapidity regions (up to  $|\eta_D| = 3$ ). It has approximately 793,000 readout channels

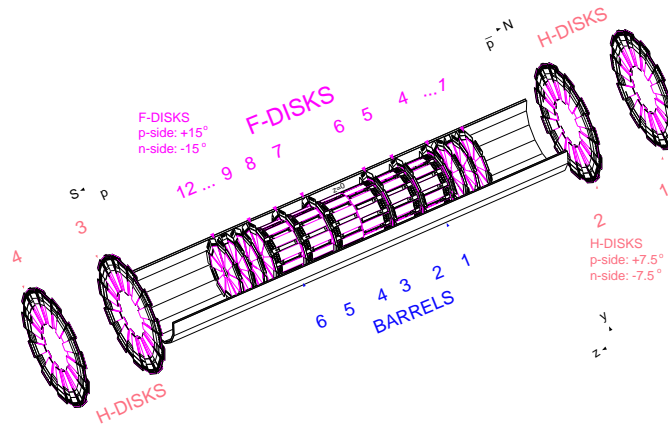


Figure 3.10. Schematic diagram of the DØ Run II Silicon Microstrip Tracker detector.

and provides a spatial resolution of  $10 \mu\text{m}$  in the  $r\phi$  plane and  $100 \mu\text{m}$  in the  $rz$  plane. There are a total of 16 disks (12 F-disks and 4 H-disks) of silicon wafers that provide a good track pattern recognition capability. The tracks for large  $\eta$  particles are reconstructed in three dimensions primarily by the disks, while particles at small  $\eta$  are detected primarily by the barrels.

### 3.5.2 Central Fiber Tracker (CFT)

The scintillating Central Fiber Tracker (CFT) [34] surrounds the SMT detector and extends the effective tracking volume to  $|\eta_D| < 2$ . The combined hit information from CFT and SMT improves the overall momentum resolution. The desired impact parameter resolution is not achievable by either detector alone. Another useful feature of the CFT is that it provides triggering<sup>4</sup> capability for tracks. It consists of eight layers of concentric carbon fiber barrels. Enclosed in each layer are double-layers of scintillating fibers. Each barrel supports the axial fibers which are oriented parallel to the beam line. The odd numbered barrels (moving radially outward) hold an additional doublet offset (also called the  $u$  and  $v$  stereo layers) at alternating angles of  $\pm 3^\circ$ . The axial fibers provide  $\phi$  measurements at a given radius, and when

<sup>4</sup>Explained in section 3.9.

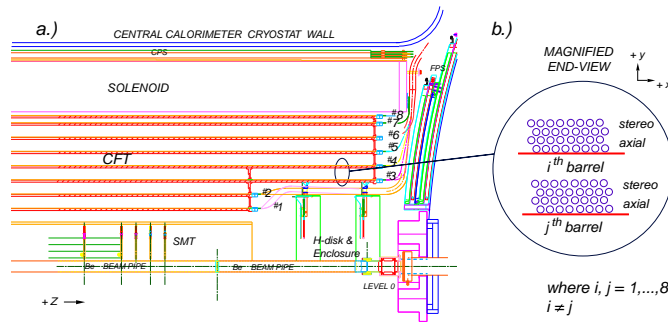


Figure 3.11. Schematic diagram of a quadrant of the DØ Run II Central Fiber Tracker showing the eight scintillating layers enclosed inside the solenoid. The SMT along with the central and forward Preshower Detectors are also shown.

combined with the stereo layers provide a measurement along  $z$ -axis. In all, the CFT contains 76,800 readout channels and extends in radial coverage from 20 cm to 50 cm. The transverse momentum of tracks (track  $p_T$ ) is measured well in the CFT. Each ionizing particle produces approximately ten photons in each fiber, which are collected as signal (or a hit) using a Visible Light Photon Counter (VLPC) that converts photons into an electrical pulse. The position resolution provided by the CFT is of order  $100 \mu\text{m}$  along the  $z$ -axis corresponding to a  $\phi$  resolution of  $2 \times 10^{-4}$  rad.

### 3.5.3 Preshower Detectors

The Preshower detectors play an important role in improving the energy measurement of electromagnetic particles such as electrons and photons in the calorimeter, and are also sensitive enough to aid in tracking measurements. There are two preshower detectors: the Central Preshower (CPS) covering  $|\eta_D| < 1.2$ , and the Forward Preshower (FPS) covering the region  $1.4 < |\eta_D| < 2.5$ , as shown in Fig. 3.9 and 3.11. The Run I DØ calorimeter had an excellent energy resolution. For Run II the design was altered by placing the solenoid magnet inside the calorimeter. The solenoid material can interact with particles resulting from the collision, causing them to shower ahead of the calorimeter, thereby degrading the energy resolution. The CPS

is a scintillating detector placed just outside the tracking volume, sandwiched in a 5 cm radial space between the solenoidal magnet and the central calorimeter cryostat [35, 36]. The CPS is designed to recover the energy resolution by sampling the energy of the particles that have passed through the solenoid, which is a dense un-instrumented region two radiation lengths thick at normal incidence.

#### 3.5.3.1 Central Preshower

The CPS is cylindrical and consists of lead radiator two radiation lengths thick followed by three layers of scintillating strips with triangular cross section. The innermost layer is arranged axially (parallel to the beam), while the two outer layers are arranged at stereo angles of  $\pm 23^\circ$ . The scintillator strip has a hole in the center where wavelength shifting fibers transmit the signal to clear wave guides. The wave guides carry the signal to VLPC cassettes, similar to those in the CFT. The lead radiator serves to initiate a narrow electromagnetic shower for electrons and photons, thereby providing early energy sampling. The hits in the stereo layers provide precision position measurements to improve the spatial resolution. Thus the CPS serves its dual purpose of a tracker and a sampling calorimeter.

#### 3.5.3.2 Forward Preshower

There are two FPS detectors located in the forward regions (one each on the south and north sides) as indicated in Fig. 3.9. They are very similar to the CPS in their design and purpose. The FPS detectors contain an absorber material (lead) two radiation lengths thick. The lead is sandwiched between two layers of scintillating material. Each scintillating layer is made of two fibers arranged in a  $u-v$  geometry at  $\pm 23^\circ$  stereo angle. Unlike the CPS, there are no axial layers. The layers closest to the interaction point (upstream) detect minimum ionizing



particles and are called MIP-layers, while the two layers that are behind the lead absorber material are called shower-layers.

### 3.6 Calorimeter System

#### 3.6.1 Energy Measurement

The role of calorimeter system at DØ is to detect and measure the energy and shape of electromagnetic (EM) and hadronic (HD) showers initiated by particles such as electrons, photons and jets. The particles are made to pass through large amounts of dense material, thereby inducing them to create secondary showers. The energy in the showers is then sampled at many points. By measuring the total visible energy deposition in the event and using momentum conservation in the transverse plane, the calorimeter provides a means of measuring the missing energy due to the undetected particles like neutrinos. The calorimeter is constructed from alternating layers of heavy absorber plates and active ionization layers. The EM and HD showers are reconstructed from their characteristic signals in the layers of the calorimeter. EM objects interact with materials primarily via the following processes:

- Pair production ( $\gamma \rightarrow e^+e^-$ )
- Bremsstrahlung ( $e \rightarrow e\gamma$ )

For each successive interaction the number of secondary particles increases while the average energy per particle decreases. Information about the energy of the original EM object is obtained by sampling and measuring the secondary particles. The energy of the original EM particle is expected to drop exponentially according to eq. 3.7:

$$E(x) = E_0 e^{-x/X_0} \tag{3.7}$$

where  $E_0$  is the initial energy of the particle (before its interaction with the detector),  $x$  is the distance traveled in the detector and  $X_0$  is the radiation length of the material through which the particle passes.

HD objects interact primarily via the strong nuclear force with the nuclei of the materials through which they pass. As in EM showers, hadrons also produce secondary particles; most of them are neutral and charged pions ( $\pi^0$ ,  $\pi^\pm$ ). Neutral pions interact electromagnetically via the process  $\pi^0 \rightarrow \gamma\gamma$ , and charged pions undergo strong nuclear interaction to produce more secondary particles in the showering process. Hadronic showers develop over longer distances and also are larger in their transverse profile. The radiation length of uranium is about 3.2 mm. Analogous to it, the nuclear interaction length ( $\lambda_0$ ) is defined for such interactions, and is about 10.5 cm. As an example, if a calorimeter has a thickness of seven nuclear absorption lengths ( $7\lambda_0$ ), then a photon has a probability of  $1/e^7$  of not interacting when it traverses the calorimeter.

### 3.6.2 Calorimeter Performance

The development of showers in the calorimeter is sampled via the active ionization medium. Hence the term “sampling” calorimeter. The energy of the original particle ( $E$ ) that initiated the shower is directly proportional to the total sampled energy (as in Eq. 3.8), indicating that the response is linear.

$$E \propto \sum_{i=1}^N E_i \quad (3.8)$$

where  $i=1 \dots N$  are the different sampling layers and  $E_i$  is the energy measured in each layer. By “compensating” it is meant that the ratio of the electromagnetic to the hadronic response ( $e/h$ ) of the calorimeter is close to one.

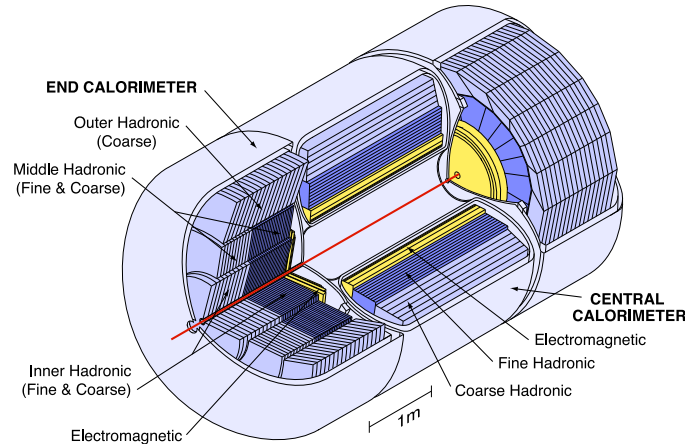


Figure 3.12. Schematic diagram of DØ Run II Calorimeter showing the central and two end sections. All three sections are further divided into a finely segmented electromagnetic section and the fine and coarse hadronic sections.

### 3.6.3 DØ Calorimeters

Figure 3.12 shows an overview of the Run II DØ calorimeter system. It is a *compensating, sampling* calorimeter with fine segmentation [37]. The primary ionization medium (the active medium) is liquid argon (LAr), and the passive medium or absorber is depleted Uranium, ( $^{238}\text{U}$ ) and stainless steel/copper plates. It is divided into three cryostats inside which the central calorimeter (CC) and two end calorimeters (EC) are housed. The calorimeter is segmented in the longitudinal and transverse shower directions, thereby enabling measurements of the shape of the shower development and the direction of the incident particles. A quadrant of the cross-sectional view of the calorimeter is shown in Fig. 3.14. The CC spans a region in rapidity of  $|\eta_{\text{D}}| < 1.1$  while the EC's extend the forward pseudorapidity region to  $1.5 < |\eta_{\text{D}}| < 4.2$ . The longitudinal depth of the CC is about seven absorption lengths and the EC's, nine absorption lengths. Each calorimeter is subdivided into three sections consisting of different absorber materials and their thickness. The innermost concentric layers are called EM sections, followed by fine hadronic (FH) and coarse hadronic (CH) sections. A summary of the different parameters for each section of the central calorimeter is given in Table. 3.1 [38].

Table 3.1. Useful set of operating parameters for the Central Calorimeter [38].

CC Modules	EM	FH	CH
Rapidity Range	$ \eta_D  \leq 1.2$	$ \eta_D  \leq 1.0$	$ \eta_D  \leq 0.6$
Primary Absorber	Uranium	Uranium	Copper
Absorber Thickness	2.3 mm	6.0 mm	46.5 mm
Total Radiation Length ( $X_0$ )	20.5	96	32.9
Total Nuclear Absorption Length	0.76	3.2	3.2
Number of Readout Sections	4	3	1
Number of Channels	10368	3000	1224

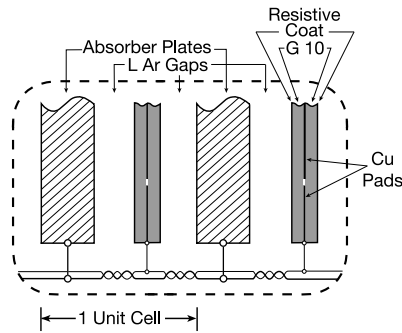


Figure 3.13. A unit cell of the DØ calorimeter (two units are shown).

Each layer of the calorimeter represents a discrete set of readout *cells* or units. A unit cell consists of alternating layers of grounded absorber plates and signal boards, filled with LAr and maintained at a high voltage. A schematic view of the calorimeter unit cell is shown in Fig. 3.13. The signal boards are made of copper readout pads sandwiched between 0.5 mm thick G10 insulator<sup>5</sup>. The outer surface of the boards are coated with a highly resistive epoxy. A high voltage (2.0-2.5 kV) is applied between the resistive surfaces of the signal boards and the absorber to create an electric field. When a particle enters the calorimeter it showers inside the absorber plate, creating secondary particles which ionize the argon atoms. The ionization electrons drift toward the signal boards, inducing a signal on the copper pads. The gap between

<sup>5</sup>Material formed by inserting a glass woven fabric impregnated with an epoxy resin under high pressure.

the absorber plates is 2.3 mm and the electron drift time across the liquid argon gap is about 450 ns<sup>6</sup>.

The readout electronics sample the charge accumulated on the pad and convert it into an analog signal proportional to the ionization charge recorded. The size and pattern of the readout cells were chosen to optimize the measurement of transverse and longitudinal shower development. The transverse sizes of cells are  $\Delta R \sim 0.2$  for EM showers and  $\Delta R \sim 0.5$  for HD showers. The cells from each layer are arranged radially to form a  $\Delta\eta \times \Delta\phi = 0.2 \times 0.2$  readout geometry, referred to as a *tower*. Readout towers have a *pseudo-projective* geometry meaning that the cell centers of increasing shower depth lie along rays projecting from the center of the detector, but the cell boundaries are aligned perpendicular to the absorber plates. The LAr active layer provides a uniform gain over the entire calorimeter and has several advantages:

- a. Provides flexibility in segmenting the calorimeter volume into readout cells.
- b. Easy to calibrate and radiation hard.
- c. Provides stable channel-to-channel response over time.

The depleted uranium absorber has high density and allows for a compact detector that can contain most of the shower energy while keeping the cost reasonable, as well as improving the  $e/h$  compensation ratio.

### 3.6.4 Inter Cryostat Detector

The region between the central and end cryostats is called the inter-cryostat region (ICR) and covers a pseudorapidity range of  $1.1 < |\eta_D| < 1.4$ . The ICR suffers from lack of detector instrumentation because of the support structures and the cryostat walls. In order to improve the energy sampling of particles passing through the ICR, a pair of Inter Cryostat Detectors (ICD) are mounted on the inner faces of the end cryostats [39]. The ICD consists of

---

<sup>6</sup>The gap thickness was chosen to observe MIP signals and to avoid fabrication difficulties.

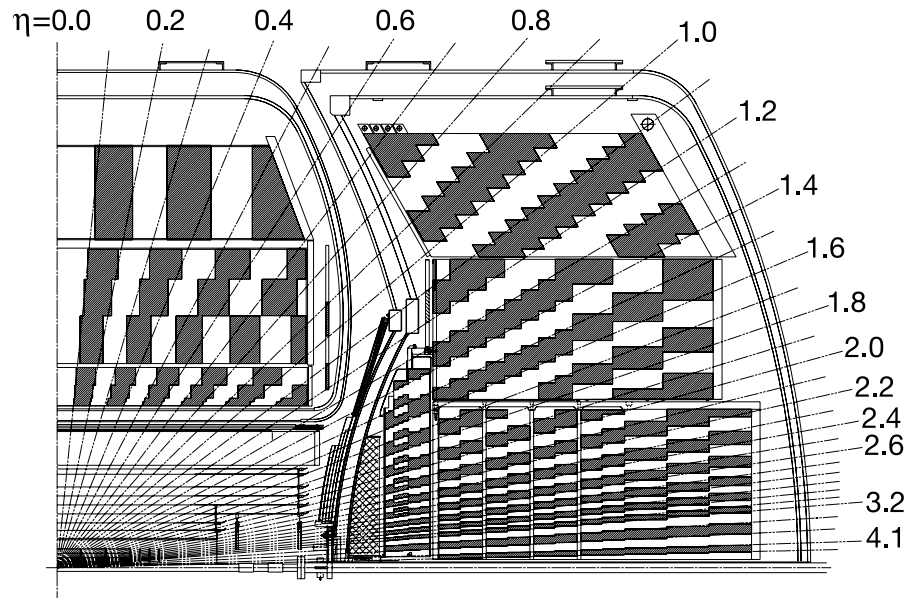


Figure 3.14. SA quadrant of the cross sectional ( $r$ - $z$  plane) view of the  $D\bar{O}$  calorimeter is shown, indicating the segmentation. The segments that correspond to the same range of pseudorapidity form a tower. The size of the segments increases with increasing distance from the interaction point along each tower. The cells are arranged in a pseudo-projective geometry.

scintillating tiles arranged in  $22.5^\circ$  wedge structures spanning the entire  $2\pi$  solid angle of the uninstrumented ICR. Wavelength shifting and clear fibers transmit the light via optical connectors to photo multiplier tubes (PMT). The PMT's are housed in crates mounted on the outer surface of the end cryostat walls. Figure 3.15 shows the ICD modules and the wedge structure of the individual modules.

### 3.7 Muon Detectors

The muon system surrounds the calorimeter system and forms the outermost layer of the detector. It is designed to detect the passage of muons and measure their momenta. Muons are heavy compared to electrons ( $\sim 200 m_{\text{electron}}$ ) and therefore lose very little energy via bremsstrahlung. Thus they do not initiate EM showers, unlike other EM objects. The pri-

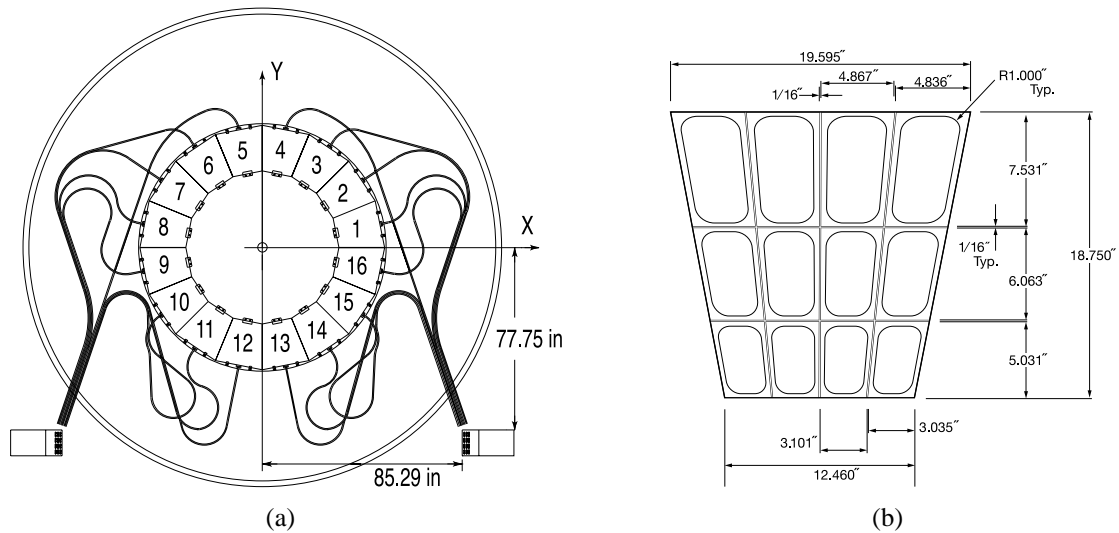


Figure 3.15. Schematic view of the ICD modules mounted on the inner surface of the end cryostats. a) The wedge structure with a total of 16 wedges that form the ICD detector and the optical cabling is shown. b) Individual wedge segmented into an array of 12 scintillating tiles is shown.

mary energy loss mechanism for muons with energy above a threshold of approximately 3.5 GeV is ionization and excitation of the detector media. The muons behave as MIP's and undergo minimal energy loss in the detector system. Because of this, the muon system is the outermost system and typically the largest of the detectors (see Fig. 3.16).

The muon system consists of the following components:

- Wide Angle MUon Spectrometer (WAMUS) covering  $|\eta_D| < 1$ .
- Forward Angle MUon Spectrometer (FAMUS) covering  $1 < |\eta_D| < 2$ .
- A 2000 ton solid iron toroid magnet that generates a field of 1.8 tesla.

The WAMUS consists of two types of detector components *viz.*, the proportional drift tubes (PDT) and scintillator tiles [41]. These components are arranged in three layers labeled A, B and C. The drift tubes collect the ionization created by muons in the organic, gaseous argon mixture onto gold wires held at high voltage. A three-dimensional position measurement is possible by measuring the arrival times of the ionization pulses relative to the beam crossing

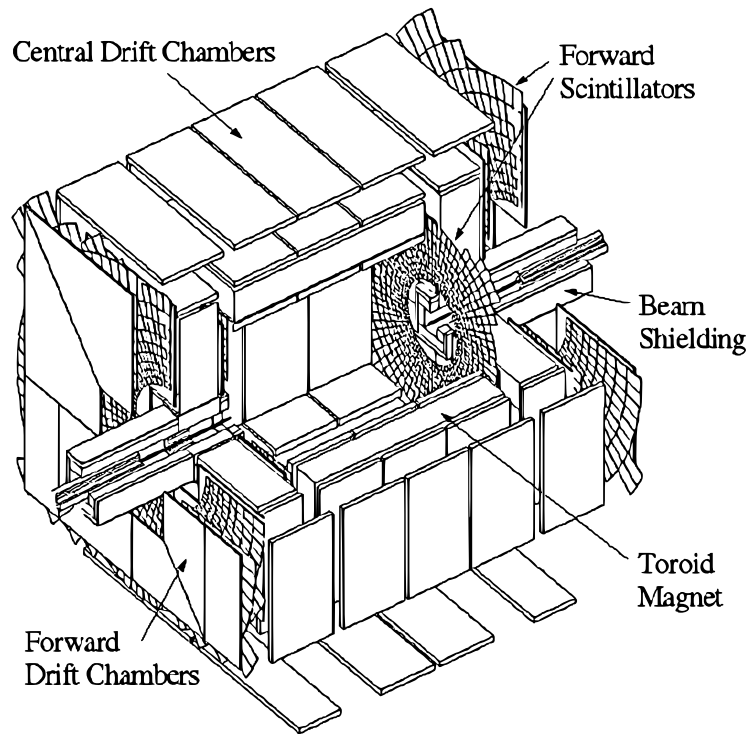


Figure 3.16. The muon system of the upgraded Run II DØ detector [40].

time and at each end of the wire. The scintillator tiles provide more spatial measurements of trajectories of muons and give an excellent resolution ( $\leq 10$  ns) for the arrival times of the particles. The detector is constantly being bombarded by cosmic ray muons. The timing information from the detector is crucial to reject the cosmic ray background. The toroidal magnetic field exists between layers A and B.

The FAMUS is made of mini drift tubes (MDT) and scintillator pixels [42] and has a similar A, B and C structure. The path of a muon is measured in the A, B and C layers. Using the information from the three hits (one before the toroid and two after) the momentum can be ascertained with reasonable accuracy. The transverse momentum of a muon is measured precisely by matching its trajectory with a high  $p_T$  track reconstructed in the tracking chambers. In addition, its energy is also measured in the calorimeter as a MIP signal ( $\sim 3$  GeV).



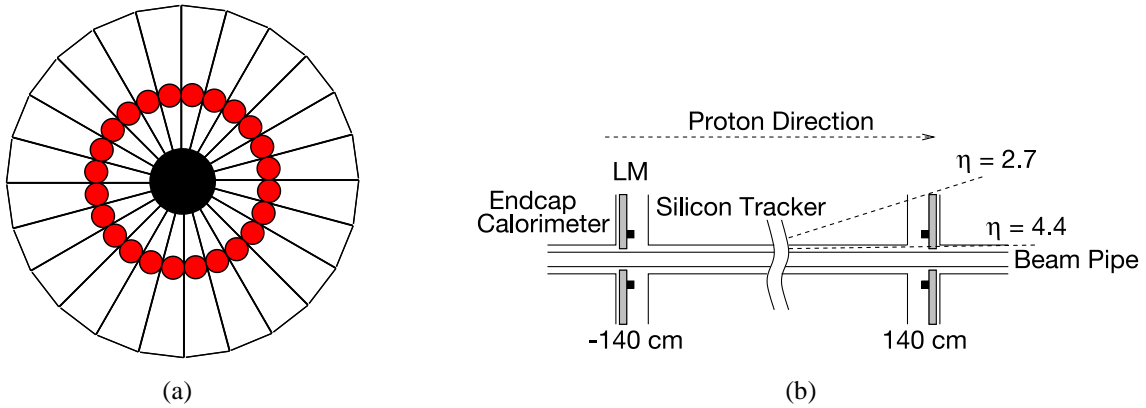


Figure 3.17. Diagram of the Run II DØ Luminosity Monitor. a) An  $r$ - $\phi$  view of the monitors is shown with the red circles indicating the PMT's on each tile. b) an  $r$ - $z$  view of the monitors showing their position along the  $z$ -axis relative to the center of the detector.

### 3.8 Luminosity Monitor

The luminosity monitor is used to calculate the effective inelastic cross section of  $p\bar{p}$  collisions at DØ [43]. There are two luminosity detectors, one upstream (+140 cm along the  $z$ -axis) and the other downstream (-140 cm along the  $z$ -axis) of the collision point surrounding the beam pipe. They cover an  $\eta_D$  range of  $2.7 < |\eta_D| < 4.4$  as shown in Fig. 3.17(b). Either detector consists of 24 wedge-shaped scintillating tiles 15 cm long and 1.6 cm thick. They are read out by high gain PMT's attached perpendicularly to each tile. The time-of-flight equation is given by:

$$z_v = \frac{c}{2}(t_- - t_+) \quad (3.9)$$

where  $t_-$  and  $t_+$  are the times when the decay products from the interaction hit the downstream and upstream luminosity monitors respectively. Events that satisfy  $z_v < 100$  cm are used in counting the number of inelastic  $p\bar{p}$  collisions.

### 3.9 Trigger and Data Acquisition (DAQ) System

$p\bar{p}$  collisions occur at a rate of 1.7 million per second in the DØ detector. Not every collision (event) is of interest for physics studies. Interesting physics processes occur in only a small fraction of all the collisions and therefore not every event needs to be recorded. Furthermore, once the event is fully reconstructed, the information stored contains about 300 kB of data per event. This would require about 7.5 GB of disk space for every second of recording, and  $10^8$  GB of disk space per year assuming only 50% of recording uptime. This amount of data is impractical from the perspective of resource availability the physicists required to analyze the data. *Triggering* is a technique which is used to identify interesting events that should be recorded for further investigation. This is achieved by matching event properties (or signatures) with a set of predefined patterns characteristic of a particular physics process. The triggering system selects interesting events and the data acquisition (DAQ) system logs the selected events into permanent storage. The interaction rate for high  $p_T$  phenomena, production of weak vector bosons and heavy quarks, and possibly exotic non SM phenomena occur only rarely in comparison with the much more common inclusive  $p\bar{p}$  collisions.

At DØ the triggering is implemented in a three level hierarchical system. The levels are labeled *Level 1 (L1)*, *Level 2 (L2)* and *Level 3 (L3)*. As data is processed from L1 to L3, the triggering algorithms increase in complexity. A flow diagram of the triggering system is shown in Fig. 3.18. An initial level *Level 0 (L0)* also exists to trigger the presence of inelastic  $p\bar{p}$  collisions and is used to determine the instantaneous luminosity.

- L1 Trigger

The L1 trigger [44] provides the largest reduction in the event rate (factor of 1/500) since it has to make a decision every bunch crossing. L1 is necessarily hardware based due to the very short decision time ( $4.6 \mu\text{s}$ ). Its decision is based on the raw detector information, and

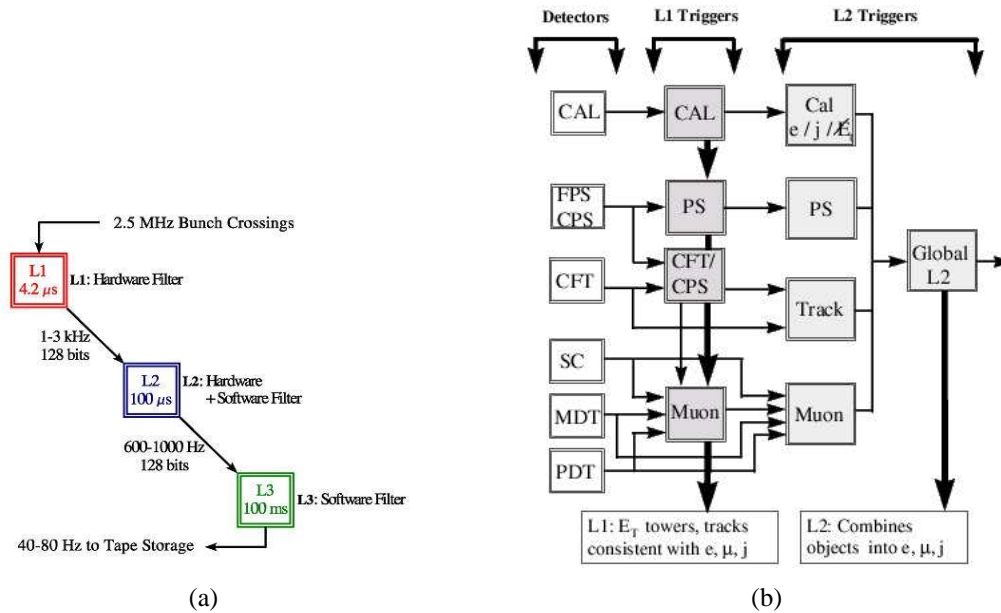


Figure 3.18. a) Diagram of the three level sequential triggering system employed at DØ indicating the input/output rates of data for each level. b) A block diagram showing the basic data flow path for Level 1 and Level 2 trigger systems.

simple algorithms are implemented using field programmable gate arrays (FPGA) on specialized microprocessors. Condensed information from the calorimeter, preshower, CFT and the muon detectors is processed in parallel to reduce the event rate while retaining the acceptance for leptons and jets in the event. Successive events are stored in a buffer (or data pipeline) until the decision for the current event is made. The predefined conditions that L1 is programmed to identify are summarized below:

- A count of calorimeter towers over a certain EM or HD transverse energy threshold.
- A count of central tracks composed of axial layers of the CFT, sorted into several  $p_T$  bins.
- Counts of preshower detector energy clusters in the central and forward regions.
- Central and forward muons in various  $p_T$  bins and  $\eta_D$  regions, as well as their quality indicators based on the number of hits.

- L2 Trigger

The L2 trigger [45] receives information from the L1 output and processes the information in order to reconstruct basic physics objects such as electrons, muons, tracks and jets. The event rate reduction is much smaller compared to L1 and therefore the decision time for L2 is about  $100 \mu\text{s}$ . L2 is partly hardware-based, but also relies on reconstruction algorithms (software) to select events of interest before it passes them on to the L3 system. As in L1, the L2 has buffers to store successive events until a decision is made for the event being processed. Some of the L2 algorithms that are applied in the decision making process are summarized below:

- Calorimeter jet reconstruction in groups of  $5 \times 5$  calorimeter trigger towers based on a jet *cone algorithm* to make available the information on kinematic variables like jet  $E_T$ ,  $\eta$  and  $\phi$ .
- Calorimeter-level electron and photon identification algorithms. To distinguish the electrons from photons, the total tower energy is compared to the energy of the EM layers alone by the pre-processors as well as tracking information and a trigger decision is made [46].
- Missing Transverse Energy ( $\cancel{E}_T$ ) calculations are performed by summing the  $E_T$  of the individual trigger towers vectorially and checking for an imbalance in the total  $E_T$ .
- Tracks are ordered by  $p_T$  based on information from the CFT.
- Tracks not emerging from the primary vertex are found, in order to trigger on long lived particles such as  $b$ -quarks.
- Precise timing information scintillators are used to identify and trigger on muons and the tracks corresponding to their trajectories.

- L3 Trigger

The L3 system [47] is completely software based, unlike L1 and L2, and operates using a farm of parallel commercial PC's ( $\sim 200$  node Linux cluster). At this stage of decision making, complete detector information is available for each event through the readout crates (ROC). Fully digitized output routed to a PC from the ROC is processed in complete detail with sophisticated algorithms. Each PC has an identical copy of the software, *i.e.*, the filtering software, reconstruction packages used to arrive at the final decision. At this stage, the acceptance rate for events is about 50-80 Hz. These events are stored on a robotic tape system accessible for offline event reconstruction.

The rate of 50-80 Hz sets the overall upper limit on the number of events that can be recorded. Since only a fraction of the total bandwidth is available for a given trigger, acceptable events have to be discarded occasionally, regardless of their content. This circumstance might occur at high luminosities at the beginning of a store, or when the rate of acceptance of data from a trigger is greater than the bandwidth allocated for it. The DAQ coordinator is forced to conform to the limited bandwidth availability and to discard some of the accepted (triggered) events. In such cases, the trigger is said to be *prescaled*. By assigning a prescale number, the DAQ coordinator is allowed to reject the event based on the prescale. For example, if a trigger is assigned a prescale of 50 at a certain instantaneous luminosity during a store, the DAQ will accept only one 1 out of 50 triggered (and accepted) events for offline storage. Prescaling is an undesirable situation, and hence a significant effort is devoted to minimizing its effect by cleverly designing the triggers for a wide range of physics requirements, and also by limiting the number of triggers used.

## CHAPTER 4

### MONTE CARLO SIMULATION

Monte Carlo (MC) generators are used to simulate both signal and background high energy physics events. They provide a representation of nature that is as accurate as possible. All stages of interactions that occur in high energy collisions are simulated by these generators: initial-state radiation; hard scattering of partons; final-state radiation; hadronization of partons and the interaction of the final state particles with the detector elements. The simulated MC events allow the optimization of cuts, understanding of the detector and event reconstruction performance, estimation of acceptances and direct comparison of theoretical predictions to data. Some of the MC generators used in this analysis are PYTHIA [48], ALPGEN [49, 50] and CompHEP [51]. This chapter provides details about the application of the MC simulation tools.

#### 4.1 Physical Process of Hadron Collisions

The basic steps in MC event generation can be explained most easily by first understanding the physics of hadron-hadron collisions. A typical event of interest is the process wherein two partons moving toward each other undergo an interaction resulting in two outgoing partons. The initial and final states of these partons can be described by  $2 \rightarrow 2$  hard scattering matrix elements (*i.e.*, the lowest or the leading order QCD process). The event structure in a hadron-hadron collision is illustrated in Fig. 4.1

In  $p\bar{p}$  collisions, proton (antiproton) is a composite object made up of partons (quarks and gluons) which carry a fraction of its momentum. The fractional momenta of the partons inside the hadron are described by parton distribution functions (PDF) [52]. The accelerating partons in a magnetic field undergo the reaction ( $q \rightarrow qg$ ) resulting in initial state radiation. It is

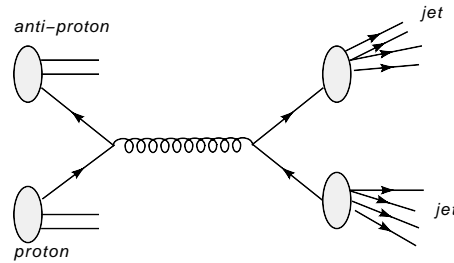


Figure 4.1. Feynman diagram depicting the  $p\bar{p}$  interaction. A quark from the proton and an antiquark from the antiproton undergo strong interaction to produce two outgoing partons. In this example, the outgoing quarks hadronize to form two jets in the final state.

one of the partons from each of the incoming hadrons that undergoes a hard scatter and which may result in a short-lived resonance like the  $W$  or  $Z$  gauge boson.

The outgoing partons may undergo reactions similar to those of the incoming partons and radiate gluons (final state radiation). Due to the large momentum transfer that occurs from the hard scatter, the final state partons may undergo several branchings to fill up the phase space available to them. This is the process of parton shower evolution. The parton shower development can be explained using perturbative QCD and is terminated at a low scale of the order of  $\Lambda_{\text{QCD}}$ . The color structure of the incoming partons is retained by the outgoing partons. QCD confinement ensures that the outgoing quarks and gluons are not directly observable, but undergo fragmentation into color neutral hadrons, some of which are unstable and decay into stable hadrons with well-known branching ratios. These hadrons can be observed in a real experiment as collimated objects called “jets” which deposit energy in the calorimeter and may have associated tracks in the tracking system. Although not very well understood, the fragmentation process can be described by several hadronization models in which a partonic final state is converted into an exclusive hadronic final state [53].

The initial state partons that do not participate in the hard scatter constitute the remnants. The remnant particles may undergo further semi-hard interactions. Since their momenta are

small compared to the hard scattered partons, their collision can be described as a soft underlying event.

## 4.2 Monte Carlo Event Generators

MC event generators produce events which contain a collection of final state particles resulting from a hard/soft scatter that are interesting to an experiment. In a real experiment, the colliding beams typically undergo one hard scatter in a million bunch crossings. Unlike the real world, the production of simulated physics events of interest proceeds in an opposite manner - event generators assume that a hard scatter occurs and generate the final state particles resulting from it. The process of event generation proceeds much like the real world, with our understanding of the physics built into it. Despite an impressive amount of work and detailed calculations, our understanding of the event structure is incomplete. To fill in this void several models have to be incorporated, with inputs to these models coming from real data. This enables the generated MC event to mimic the real event as accurately as possible. Several aspects of event generation from the currently available tools can be summarized as:

- Hard scattering process
- Parton showering process
- Hadronization process
- Modeling the underlying event

### 4.2.1 PYTHIA Event Generator

PYTHIA is a general purpose event generator that can model some 240 different hard processes which are classified based on the number of particles in the final state and the physics signature. PYTHIA is optimized for  $2 \rightarrow 1$  and  $2 \rightarrow 2$  processes and does not provide a generic treatment of three or more particles in the final state. It can simulate hard processes (*e.g.*,  $qg \rightarrow qg$ ), soft QCD processes like diffractive and elastic scattering, minimum bias events,  $W/Z$



and SM Higgs boson production to name a few. The distribution of momenta of the partons that constitute the proton or anti-proton is given by the parton distribution functions (PDF). The PDF's give the probability that a parton carries a fraction  $x$  of the total momentum of the proton or anti-proton of which it is a constituent. The PDFs are a function of longitudinal momentum fraction ( $x$ ) and momentum transfer ( $Q^2$ ), and are parameterized from global fits to experimental data. The CTEQ6M parton distribution functions for different quarks are shown for two different momentum scales  $Q = 2$  and  $100$  GeV in Figs.4.2 (a) and (b), respectively.

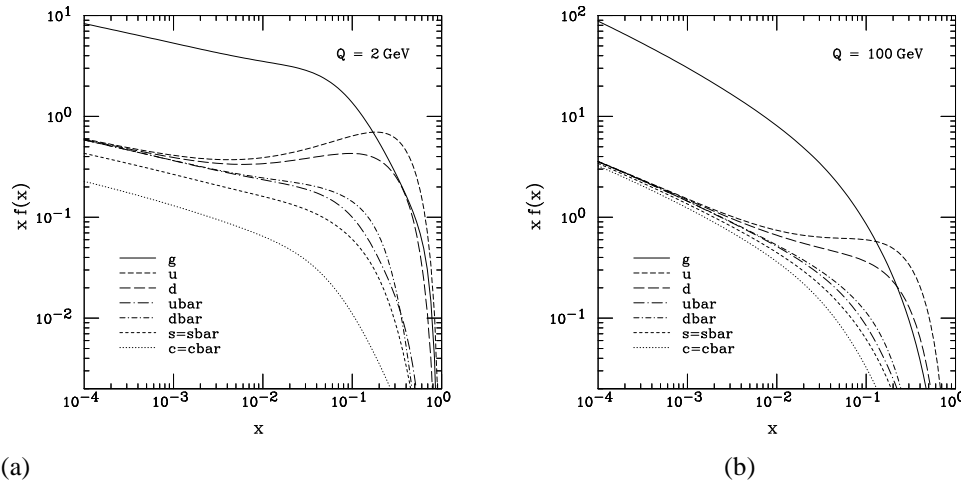


Figure 4.2. The CTEQ6M parton distribution functions showing the momentum density,  $Xf(x)$ , as a function of the momentum fraction,  $x$ , for gluons and all the quark flavors for two different values of momentum scale ( $Q = 2$  and  $100$  GeV) .

The evolution equations that describe the initial and final state partons were studied and published by **Dokshitzer, Gribov, Lipatov, Altarelli and Parisi** and are called the DGLAP equations [54–56].

Parton showering evolves from the initial high momentum scale  $Q$  down to a cut off value  $Q_0$  to obtain the final state partons. PYTHIA uses the ‘Lund string fragmentation model’ for hadronization, which starts with a gluon forming a  $q\bar{q}$  pair with a string attached to the pair. As the quark pair travel in opposite directions from the common production vertex, the potential

energy of the string increases (to model the quark confinement with a linearly rising potential) until enough energy is gathered to break the string by the production of a new  $q\bar{q}'$  pair thereby splitting the original system into two color singlet systems. String breaking proceeds until only the on-mass-shell hadrons remain. Each hadron corresponds to a small piece of string with a quark and anti-quark pair attached at its ends. An accurate description of multiple hard and large angle emissions (events with multijets) through the evolution of  $2\rightarrow 2$  processes is not accurate with PYTHIA which uses a collinear parton shower algorithm. The jets produced by PYTHIA simulation are soft and collinear and are not suitable for modeling multiple jets in an event, which is typical in hadron-hadron collisions. Hence the need for a specialized MC generator like ALPGEN which is described in the next section.

#### 4.2.2 ALPGEN Event Generator

ALPGEN is a MC generator that can calculate exactly the leading order matrix elements of a large set of parton-level processes in QCD and EW interactions. The advantage of using ALPGEN is that it models accurately events with multiple jets which are well-separated and hard. The drawback of using this model is the lack of a good description of the parton shower development. To provide a good description of both the full matrix elements of the hard process as well as their subsequent development into jets of hadrons, the ALPGEN simulation is combined with PYTHIA. The exact matrix elements are calculated using ALPGEN to describe the final state partons. The output of ALPGEN is then interfaced with PYTHIA, which provides the parton showering and hadronization. This combination leads to a difficulty in unambiguously separating the components of the event [57] that belong to the hard process (calculated exactly using matrix elements) from those developing during its evolution (which is described by the parton shower). This can be illustrated with an example. Consider an event with  $W + 3$  jets. The three jets in the final state can be obtained in two ways. There could be two partons in the final state, and a large angle emission from one of the partons during its evolution can lead to

an extra jet. The other possibility is that there are three partons in the final state which evolve into a three jet final state.

- MLM Matching Scheme

A matching (or factorization) scheme is necessary to avoid double counting events (by preventing events from appearing twice, one for each path). A matching scheme called the MLM jet-parton matching scheme [58] is employed within ALPGEN to avoid the problem of double counting. The matching is done using the following steps:

1. Events are generated with exclusive parton multiplicity. For example, the  $W + 2$  light parton ( $Wgg$ ) sample is generated separately from  $W + 3$  light-parton ( $Wggg$ ). The light parton ( $lp$ ) refers to the number of partons at tree level. For the highest jet bin, the samples are generated inclusively. Inclusive samples are allowed to have additional parton-level jets produced from the PYTHIA parton shower.
2. These events are input into PYTHIA to simulate parton showering. The resulting event will have additional quarks and gluons originating from the shower.
3. Before the final state partons are hadronized, a UA1 type jet cone algorithm [59] is invoked to cluster the quarks and gluons into jets.
4. Match the generated partons from step 1 with the jets from step 3, using a one-to-one correspondence such that each parton matched to one and only one jet, with the criteria:  $p_T > 15 \text{ GeV}$  and  $\Delta R(jet, parton) < 0.7$ . The event is retained only if a match is found. Otherwise, steps 1-4 are repeated.
5. Combine all the samples together with weights relative to their cross sections and the number of events generated.

- Combining the Matched ALPGEN Samples

Once the exclusive and the inclusive samples of a particular process (*e.g.*,  $W + 3lp$ ) are generated, they have to be properly combined to obtain a complete sample for that process. The combination process can be explained using the  $W + 3lp$  sample as an example.  $W + jets$  sample can be obtained by combining exclusive samples of  $(W + 0lp)$ ,  $(W + 1lp)$ ,  $(W + 2lp)$  and an inclusive sample of  $(W + 3lp)$ . These samples are assumed to be combined at constant luminosity. The combination weights ( $f_i$ ) for each sample and the formula are given in eq. 4.1

$$\begin{aligned}
 W + jets &= f_0 \cdot (W + 0lp) + f_1 \cdot (W + 1lp) + f_2 \cdot (W + 2lp) + f_3 \cdot (W + 3lp) \quad (4.1) \\
 &= \sum_{i=0}^K f_i \cdot (W + ilp) \quad i = 0, 1, 2, \dots, K \\
 f_i &= \frac{\sigma_{matched}^i}{N_f^i} \text{ where}
 \end{aligned}$$

$\sigma_{matched}^i \equiv$  matched cross section of  $W + ilp$  sample

$N_f^i \equiv$  Number of events of the  $W + ilp$  sample after matching

### 4.3 DØ Detector Simulation

Although the final set of particles from the simulation are interesting to study, the real data gathered from an experiment is not in the same form. Energy depositions in the calorimeters and tracks of charged particles in the tracking system etc., are in the form of electronic signals collected, digitized and stored on tape. The hard scatter and the underlying event have to be reconstructed from this information. To mimic real data, the events from the MC generator are processed through a full simulation of the DØ detector. The full simulation package consists of two main programs:

- DØgstar, DØ GEANT Simulation of the **Total Apparatus Response** [60].

- DØSim, DØ **Simulation** [61].

DØgstar simulates the passage of particles resulting from the hard interaction through various components of the detector as they deposit energy and possibly leave tracks. The information about the geometry of the detector subsystems and their material density is modeled with the CERN package GEANT (GEometry ANd Tracking) [62]. A simulation of electromagnetic and hadronic showers in the calorimeter, the trajectories of charged particles in the tracking detectors and through the solenoidal and toroidal magnetic fields are modeled using this package.

The DØSim package performs a simulation of the sampling electronics, calorimeter pile-up from previous events, electronic noise and detector losses from the subdetector components. In addition, it models the soft underlying event (soft interaction of the remnants) and/or additional inelastic  $p\bar{p}$  collisions. An event is labeled as minimum bias event if it is triggered by the luminosity monitor, signaling the presence of at least one  $p\bar{p}$  interaction for each bunch crossing. To properly model the additional inelastic  $p\bar{p}$  collisions, all generated MC events are overlaid with minimum bias events from real data. This is done by the program DØRaw2Sim. Since the number of minimum bias interactions per crossing increases with growing instantaneous luminosity, the overlaid events have a similar luminosity profile as the real data. The luminosity profile in fig. 4.3 shows the peak values of luminosity as a function of time.

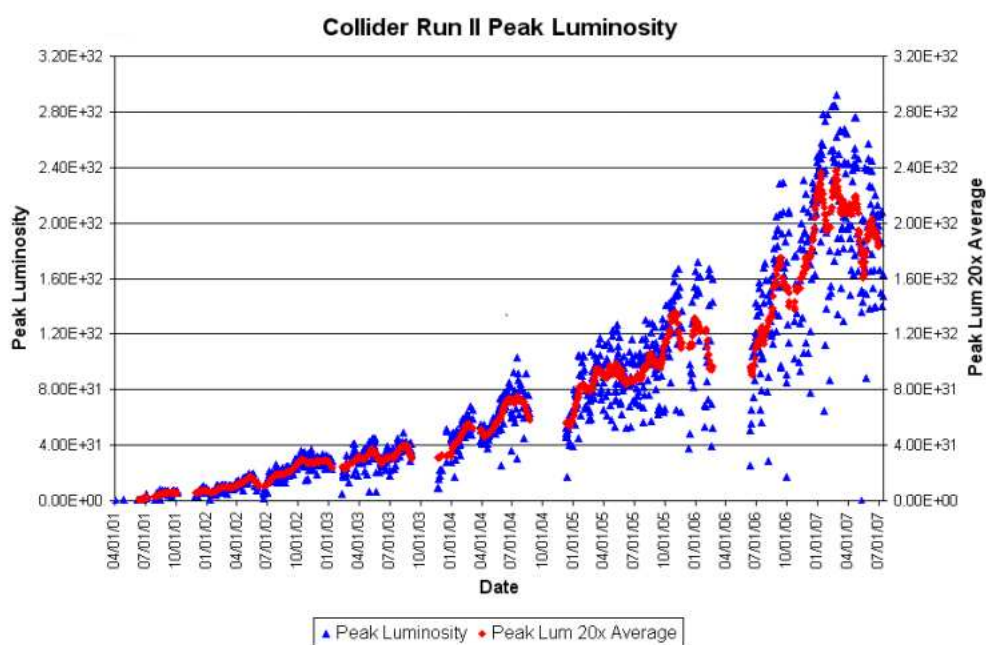


Figure 4.3. Peak instantaneous luminosity (shown as blue triangles) for the Tevatron Run II as a function of time [63].

## CHAPTER 5

### OFFLINE EVENT RECONSTRUCTION

The data acquisition system records digitized data collected from the various sub-detector systems. The data undergoes a transformation as it is calibrated and reconstructed with the help of sophisticated algorithms. Raw information is converted into physics objects (like electrons and muons) by these algorithms. These algorithms are a part of the DØ offline event reconstruction package called the DØreco [64]. This chapter describes the process of offline event reconstruction. Measurements from the luminosity system are recorded to obtain the  $p\bar{p}$  luminosity delivered to the experiment. Measurements of the trajectories of charged particles as they pass through the wires and strips of the tracking system are in the form of digitized signals. These signals are clustered into *hits* in order to determine the possible locations through which they pass. Pattern recognition algorithms reconstruct charged particle *tracks* from these hits. The tracks are used to measure particles' momenta and locate the  $p\bar{p}$  interaction points or *primary vertices*. The energy detected in calorimeter cells and preshower hits is clustered into *jets* which represent the energy of the original quarks and gluons from the hard scatter. The energy of jets is calibrated using the *jet energy scale*. Particle identification algorithms convert useful information from the tracks, calorimeter energy depositions and the muon system hits into high level objects like electrons, photons, muons and jets. The tracks associated with the jets are used by *b-tagging* algorithm to search for the evidence of bottom quarks in the jets, as they could possibly indicate a decay of the Higgs boson.

## 5.1 Offline Object Reconstruction Efficiencies

Although the offline event reconstruction is discussed in detail here, the object identification efficiencies — jet ID, jet energy scale corrections, electron reconstruction and ID efficiencies, single electron trigger efficiencies and  $b$ -tagging efficiencies are discussed in chapter seven.

## 5.2 Luminosity

During each beam crossing, the luminosity scintillators (refer to section 3.8) detect *coincident* particles that originate from the interaction point, if an inelastic  $p\bar{p}$  scattering has occurred. The timing resolution of the scintillators is very good (0.2 ns) which enables them to determine the collision point along the beam axis with an uncertainty of about  $\pm 6$  cm. The reconstructed interaction point is required to be within the expected interaction region (typical value of  $\pm 60$  cm from the interaction point along the beam axis) to reject beam halo particles.

The number of inelastic collisions per bunch crossing is Poisson distributed with a small probability of interaction per proton, despite the large number of protons in each bunch. The probability of “ $n$ ” interactions per crossing is given by  $P(n, \mu) = \mu^n e^{-\mu} / n!$ , where  $\mu$  is the average number of inelastic collisions per crossing. The probability of no interaction in a crossing is simply  $P(0, \mu) = e^{-\mu}$ . Therefore the probability of at least one interaction per crossing is given by Eq. 5.1.  $\mu$  can be expressed in terms of the effective inelastic  $p\bar{p}$  cross section,  $\sigma_{eff}$  (corrected for acceptance and efficiency), the rate “ $\Gamma$ ” at which the bunch crossing



occurs and the instantaneous luminosity  $\mathcal{L}$ , as in Eq. 5.2. Instantaneous luminosity can be obtained by solving for  $\mathcal{L}$  using Eqs. 5.1 and 5.2. The result is given in Eq. 5.3.

$$P(n > 0) = 1 - P(0, \mu) = 1 - e^{-\mu} \quad (5.1)$$

$$\mu = \mathcal{L}\sigma_{eff}/r \quad (5.2)$$

$$\mathcal{L} = -(r/\sigma_{eff}) \ln(1 - P(n > 0)) \quad (5.3)$$

The crossing rate ( $r$ ) is very well measured and equals 7.58 MHz. The effective  $p\bar{p}$  inelastic cross section was revised by the DØ luminosity group after reanalysis of the world's data performed by Klimenko *et al.*, [66] to  $60.7 \pm 2.4$  mb at  $\sqrt{s} = 1.96$  TeV. An improvement in the estimate of the overall detector acceptance and efficiency yields a value of  $75.8 \pm 3.8\%$  for their product.  $P(n > 0)$  is measured by the luminosity system. At intervals of approximately one minute, a *luminosity block* is written to a database; these blocks contain the average luminosity for each bunch during this time period. It also records the information whether the data acquisition system and the detector components were performing properly.

### 5.3 Track Reconstruction

The two tracking sub-detectors, the silicon microstrip tracker (SMT) and the central fiber tracker (CFT) provide strip hits along the trajectory of charged particles that pass through them. These hits are converted into tracks using pattern recognition algorithms. The trajectories of these particles are helical due to the presence of the 2 T solenoidal magnetic field.

#### Hit Reconstruction

Adjacent silicon and fiber strips with signals above some threshold are grouped into clusters. The center of a cluster is defined to be the charge weighted average of the strip positions in the cluster [40]. Due to the presence of the solenoidal magnetic field the electrons

and holes drift with a certain velocity at an angle, the *Lorentz angle* which depends on the electron or hole *Hall mobility* and the magnetic field strength. The holes are larger and have smaller Hall mobility compared to the electrons and therefore smaller Lorentz angles ( $4^\circ$  for holes and  $18^\circ$  for electrons). Particles going through the silicon strips create clusters on both the p-side and n-side of the silicon detectors. The strips are oriented at stereo angles, enabling the clusters to be combined in order to determine the location along the strips where the particles pass through. The position of a hit can be reconstructed with an accuracy of  $\leq 10 \mu\text{m}$  in the axial direction (x-y) and  $\leq 35 \mu\text{m}$  in the z-direction.

The CFT fibers above a certain signal threshold can either be grouped into single-fiber clusters (singlet) or doublet clusters containing one fiber from each sub-layer of the doublet layer. CFT hits are obtained by grouping overlapping CFT clusters from each of the eight CFT super-layers consisting of two doublet layers at a  $3^\circ$  relative angle. Hits represent spatial (x,y,z) measurements of the particles' trajectories. The geometry of the doublet layers allows for a hit resolution of  $\leq 100 \mu\text{m}$  in the axial direction and 2 cm in z-direction.

### Pattern Recognition

Pattern recognition performed on reconstructed hits yields a set of particle paths originating near the interaction region. The magnetic field is very well mapped in the tracking detectors, taking into account the fringe effects near the ends of the solenoid that create a small radial component of the field. The location and density of detector material is mapped as well. The particles' trajectories are not perfectly helical and are slightly altered (in a predictable way) due to these effects. DØ currently uses two algorithms for track reconstruction - these are called the Histogramming Track Finder (HTF) [67] and the Alternative Algorithm (AA) [68].

The HTF algorithm is based on forming track templates using the Hough transform technique [69] and local road finding. The hits produced by a particle in the transverse plane will have a unique curvature and azimuthal angle. The Hough transform converts these hits in x-y

coordinates to a space defined by curvature ( $\rho$ ) and azimuthal angle ( $\varphi$ ). Hits from the same particle produces a peak in the  $\rho$ - $\varphi$  space, whereas random hits will uniformly populate the space. A histogram of hits in possible trajectories is created. No two trajectories share the same set of contributing hits. Sets of hits contributing to peaks in these histograms are taken as initial track candidates. The number of trajectories is proportional to the number of hits. The track candidates are fitted in three dimensions and filtered using a Kalman filtering algorithm [70]. Fig. 5.1 depicts the HTF method applied to a 1.5 GeV/c muon track. The Kalman filter attempts to remove noisy tracks (fits having large  $\chi^2$  values) and incorporates the material density map and the magnetic fringe effects in determining the track curvature and azimuth.

The AA tracking finding method uses a seed hit in the first layer of the SMT and builds a track by incrementally including more layers of the SMT and CFT detectors. From the innermost layers of SMT, the track is extrapolated outward if the radius of curvature is greater than 30 cm (indicating that the  $p_T$  of the track is greater than 180 MeV/c). All possible combinations of tracks which meet this criterion are stored. The algorithm allows for missing hits in the SMT or CFT if a hit in one of the outer layers is consistent with a previously found track. If there are hits in the CFT but fewer than four hits in the SMT, the tracks are allowed and are termed ‘‘CFT-only’’ tracks. Allowing tracks to be built in this manner dramatically increases the track finding efficiency of the algorithm.

#### 5.4 Primary Vertex Reconstruction

The primary interaction vertex is a 3-d region where the hard scatter occurs. Primary vertex (PV) reconstruction involves identifying the exact location of the hard scatter in this region and separating it from other inelastic  $p\bar{p}$  vertices<sup>1</sup>, which enables the discrimination of physics objects from noise in the detector as well as cosmic ray particles (primarily muons).

---

<sup>1</sup>At  $\mathcal{L} = 10^{32} \text{cm}^{-2} \text{s}^{-1}$  an average of 2.5 additional minimum bias interactions accompany the hard scatter.

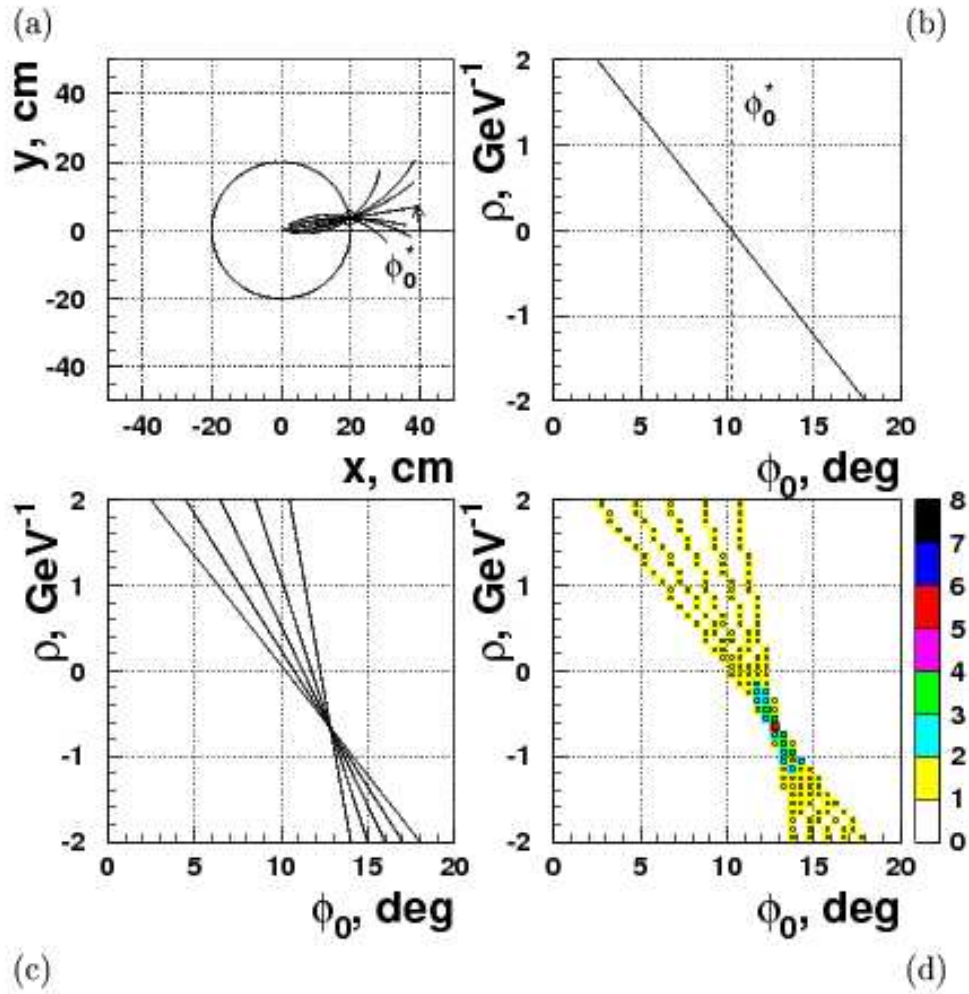


Figure 5.1. Histogramming track finding (HTF) method is shown for a 1.5 GeV/c muon track with five hits. (a) For a given hit at radius  $r = 20$  cm, a family of circles can be drawn passing through it, centered at  $(0,0)$  in the  $x$ - $y$  plane. (b) When transformed to  $\rho$ - $\phi$  parameter space, they correspond to the solid line. (c) When the family of circles corresponding to each of the five hits are transformed, they intersect at one point. (d) The parameter space is transformed back to a 2-d histogram which peaks at the point of intersection of the lines and is used as an input to the Kalman filtering algorithm [67].

The adaptive primary vertexing algorithm [71] attempts to assign all tracks with  $p_T > 0.5$  GeV and having at least two SMT hits to a vertex where the extrapolated track trajectories might intersect. This intersection point is chosen as the first-pass primary vertex. The track  $\chi^2$  contribution to this primary vertex is estimated. Distant tracks tend to have large  $\chi^2$  contribu-

tion to the fitted primary vertex and are therefore removed. The track errors are re-weighted according to their  $\chi^2$  contribution to the vertex by a sigmoidal function:

$$w_i(\chi^2) = \frac{1}{1 + e^{(\chi_i^2 - \chi_{cutoff}^2)/2T}} \quad (5.4)$$

where  $\chi_i^2$  is the  $\chi^2$  contribution of track  $i$  to the vertex,  $\chi_{cutoff}^2$  is the distance where the weight function drops to 0.5 and  $T$  is a parameter<sup>2</sup> that controls the sharpness of the function. The standard Kalman vertex fitting algorithm [72] is shown in the black curve in Fig. 5.2(a) (with  $T = 0$ ) in which the weight can either be zero (track is rejected) or one (track is accepted). Adaptive vertexing is different ( $T > 0$ ), in the sense that a track from a secondary vertex may contribute to both the primary and the secondary vertices, with a weight smaller than 1. The algorithm works iteratively by first fitting the primary vertex track candidates using the Kalman Filter algorithm. Each track is weighted according to its  $w_i(\chi^2)$  given by Eq. 5.4. Initially all tracks have their weights set to 1.0. At the  $k^{th}$  iteration, the weight of the track depends on the distance to the vertex at the  $(k - 1)^{th}$  iteration. In the next step, for each track used in the fit, its weight is recomputed according to the  $\chi^2$  distance to the new fitted vertex. If the weight  $w_i(\chi^2) < 10^{-6}$ , track  $i$  is eliminated from the fit and its weight is set to 0.0. The above two steps are repeated until the weights converge.

The adaptive vertexing algorithm produces a list of possible primary vertices which might contain a hard scatter vertex. To determine which one is the hard scatter vertex, all tracks are assigned a probability not to originate from the hard scatter vertex. Tracks from an inelastic  $p\bar{p}$  collision (a *minimum bias* interaction) have smaller values of  $p_T$  compared to tracks from the hard scatter interaction, as is evident from Fig. 5.2(b). The  $\log_{10}(p_T)$  of tracks is chosen as the variable and the probability for each track to be from minimum bias interaction is calculated. The data chosen for this study is real minimum bias data from the detector.

---

<sup>2</sup>Analogous to the temperature  $T$  in the Fermi function of statistical thermodynamics.

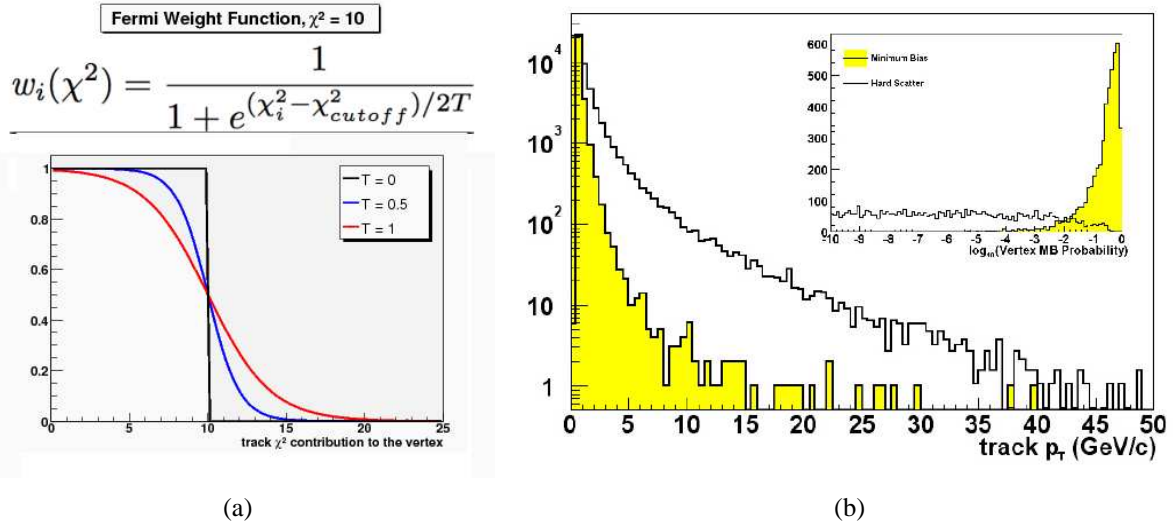


Figure 5.2. (a) Weight of a track with respect to a vertex as a function of the  $\chi^2$  distance to the vertex for different values of temperature ( $T$ ). In Adaptive vertexing, all tracks contribute to the fit when  $T > 0$  [71]. (b) Comparison of the  $p_T$  of reconstructed tracks in (GeV/c) from simulated minimum bias (yellow shaded region) and hard scatter events (open histogram). The inset shows the  $\log_{10}$  of the probability of the track to be associated with a minimum bias vertex. [40].

The minimum bias probabilities for each track are combined into a probability for each of the primary vertices to be from a minimum bias interaction. The primary vertex with the least probability to form a minimum bias interaction is selected as the hard scatter primary vertex. This vertex is used to determine the energy of each calorimeter tower ( $E_T$ ) and for  $b$ -tagging (see section 5.8).

## 5.5 Electron Reconstruction and Identification

### 5.5.1 Reconstruction

Electrons are characterized by narrow showers in the electromagnetic calorimeter, with the showers initiated in the preshower detectors, along with an associated track in the central tracking detectors [73]. The showers from photons are similar to those for electrons, but there is no associated track. Electrons and photons are reconstructed with the same algorithm, with

the distinction made by the presence or absence of a central track or a preshower signature. Electrons and photons are collectively referred to as ‘EM’ objects. There are two main approaches to reconstructing EM clusters: the simple cone algorithm and the nearest neighbor algorithm.

### Simple Cone Algorithm

The simple cone algorithm constructs clusters of calorimeter towers within a cone of  $R \equiv \sqrt{\Delta\eta^2 + \Delta\varphi^2} = 0.4$ . An EM tower consists of the four EM layers plus the first hadronic layer (FH1) of the calorimeter. The highest  $E_T$  EM towers are chosen as seeds for building clusters. Adjacent EM towers above a threshold energy of 0.5 GeV are added to the cluster if they are in the neighborhood of  $\eta \times \varphi = 0.3 \times 0.3$ . In the following step, all towers within a cone of radius 0.4 with respect to the energy weighted axis of the original cluster are added. The axis is recalculated and the steps are reiterated until a stable cluster is formed.

### Cell Nearest Neighbor (CellNN) Algorithm

As the name suggests, the reconstruction is performed from calorimeter cells rather than towers. In each calorimeter layer, the cell with highest energy deposition is chosen as the seed to build the cluster. Neighboring cells are added to this seed in a given calorimeter layer (termed as *floor clustering*). Choosing the floor cluster from the third EM layer (EM3) as the global cluster, the floor clusters matching an angular requirement are added to the global cluster to form the final EM cluster [74].

#### 5.5.2 Identification

Clustering algorithms described in section 5.5.1 do not distinguish between electrons and photons. The distinction is primarily done by looking for a track associated with the cluster in the central tracking system. Photons are neutral objects and do not leave tracks. In order to

reconstruct a candidate track associated with the EM cluster, a road of  $0.05 \times 0.05$  in  $\Delta\eta \times \Delta\varphi$  is defined between the center of the EM cluster and the hard scatter primary vertex. Tracks with  $p_T > 1.5 \text{ GeV}/c$  are searched for within the road [75]. If one or more tracks are found, the candidate is considered an electron, otherwise it is a photon. An ID of +11 is assigned for positrons, -11 for electrons and 10 for photons. An EM cluster with  $|\text{ID}| = 10$  or 11 is termed a ‘‘loose’’ electron. Once an EM cluster is identified as an electron with this method, a detailed  $\chi^2$  track and cluster matching is performed for the electron candidates, along with several sophisticated identification variables and methods listed below. They are described in detail in the following subsections.

1. Electromagnetic fraction,  $f_{\text{EM}}$
2. Isolation fraction,  $f_{\text{iso}}$
3. Track match  $\chi^2$
4. Seven-variable H-matrix  $\chi^2$
5. Likelihood

The electron identification studies were performed using two samples. The signal sample consists of  $243 \text{ pb}^{-1}$  of dielectron (*i.e.*,  $Z \rightarrow ee$ ) events. The background sample is obtained from  $226 \text{ pb}^{-1}$  of EM+jet events where the EM object and the jet are back-to-back in azimuth. These are mainly QCD dijet and  $\gamma$ +jet events where the jet or a photon fakes the reconstructed electron.

- Electromagnetic Fraction,  $f_{\text{EM}}$

The fraction of the total energy of the cluster deposited in the EM layers of the calorimeter is called the electromagnetic fraction (EMF or  $f_{\text{EM}}$ ).  $E_{\text{total}}(0.4)$  is calculated within a cone of radius 0.4 using both the electromagnetic and the hadronic calorimeters, whereas  $E_{\text{EM}}(0.2)$



is calculated within a cone of radius 0.2 for the electromagnetic calorimeter alone. An EM candidate object is required to have an EMF larger than 90%.

$$f_{EM} = \frac{E_{EM}(0.2)}{E_{total}(0.4)} \quad (5.5)$$

Electrons deposit almost all of their energy in the EM section of the calorimeter with a narrow

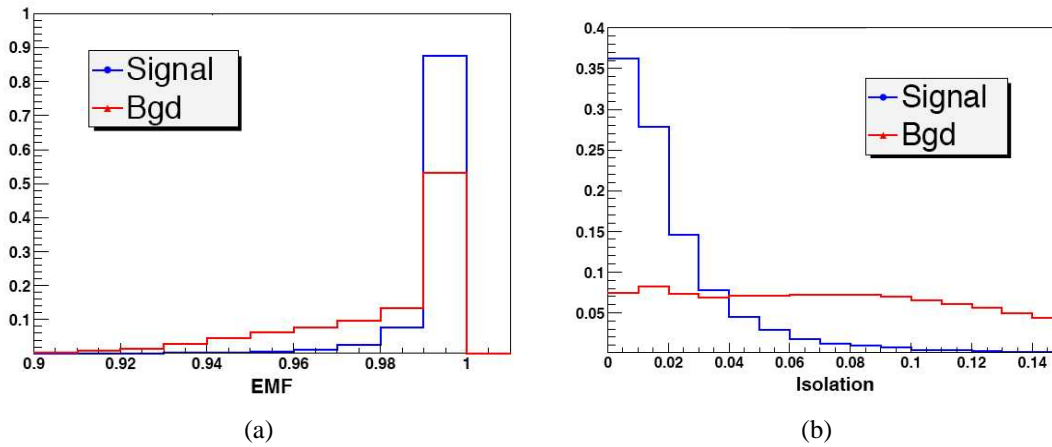


Figure 5.3. Electromagnetic fraction ( $f_{EM}$ ) and Isolation ( $f_{iso}$ ) distributions for real electrons (in blue) and fake electrons (in red) [76].

transverse profile (collimated), whereas hadron showers are more penetrating and have a larger transverse profile. As such, two discriminating variables (*i.e.*, the electromagnetic fraction and the isolation fraction) can be used to distinguish them. EM showers have a large EM fraction ( $f_{EM} > 0.9$ ), which is shown in Fig. 5.3(a). This is a powerful discriminant against pions and electrons that escape the EM calorimeter through the  $\phi$ -module boundaries since they deposit more than 10% of their energy in the hadronic calorimeter.

- Isolation Fraction,  $f_{\text{iso}}$

The isolation fraction (or isolation) is designed to reduce the possibility of highly collimated jets faking an electron. Even though these jets are not EM objects, they can still deposit most of their energy in the EM section of the calorimeter. The fake rate can be reduced by an optimized cut on isolation fraction defined below:

$$f_{\text{iso}} = \frac{E_{\text{total}}(0.4) - E_{\text{EM}}(0.2)}{E_{\text{EM}}(0.2)} \quad (5.6)$$

EM showers from high  $p_T$  electrons tend to be isolated in the calorimeter. The degree of isolation is given by the isolation fraction.  $f_{\text{iso}} < 0.15$  for the EM candidates correspond to energy deposition in a narrow region in  $\eta$ - $\phi$  space. This is not the case for fake electrons which tend to have broader shower profiles and are relatively non-isolated. The isolation fraction for signal and background candidates are shown in Fig. 5.3(b) indicating the small values of isolation fraction for good electrons.

- Track match  $\chi^2$

A candidate electron having one or more tracks is chosen. Two distinct definitions are chosen for a track match  $\chi^2$

$$\chi_{\text{spatial}}^2 = \left( \frac{\delta\phi}{\sigma_\phi} \right)^2 + \left( \frac{\delta z}{\sigma_z} \right)^2 \quad (5.7)$$

$$\chi_{E/p}^2 = \chi_{\text{spatial}}^2 + \left( \frac{E_T/p_T - 1}{\sigma_{E_T/p_T}} \right)^2 \quad (5.8)$$

where  $\delta\phi = \phi_{\text{track}} - \phi_{\text{clus}}$ , with the azimuthal angles measured in the EM3 floor.  $\sigma_\phi$  is the expected width of  $\delta\phi$  for an electron.  $\delta z = z_{\text{track}} - z_{\text{clus}}$ , with the z positions measured in the EM3 floor.  $\sigma_z$  is the expected width of  $\delta z$  for an electron.  $E_T(p_T)$  is the transverse energy (momentum) of the cluster (track).  $\sigma_{E_T/p_T}$  is the expected width of the  $E_T/p_T$  distribution for

an electron. For electrons,  $E_T/p_T \approx 1$  as shown in Fig. 5.4(b), unless the track is randomly associated with the calorimeter cluster. The probability of a track to have a certain  $\chi^2$ , *i.e.*,  $P(\chi^2)$ , defines the quality criteria for the track matching.

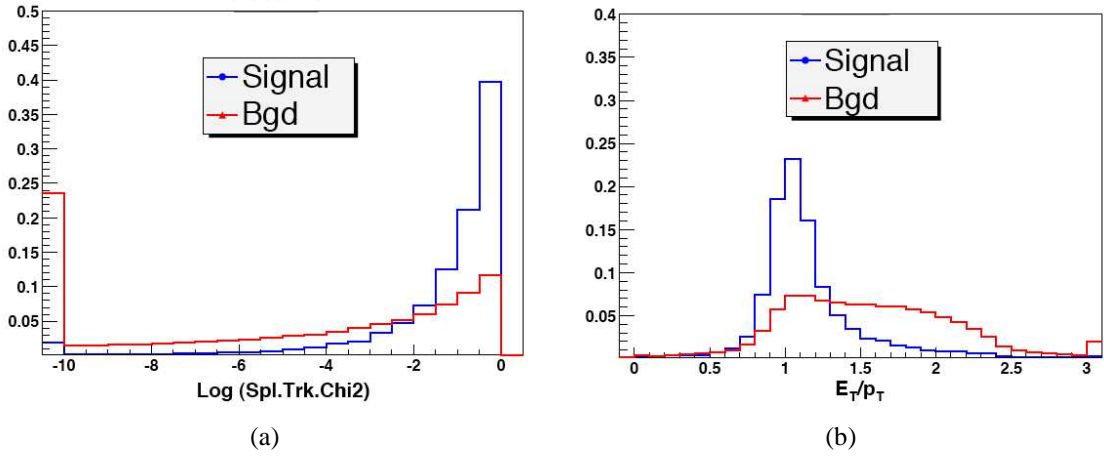


Figure 5.4. Track match probability  $P(\chi^2_{\text{spatial}})$  and  $E_T/p_T$  distributions for real electrons (in blue) and fake electrons (in red) [76] .

In order to suppress the QCD background, the EM cluster is required to be associated to a track in the central tracking system in a road satisfying the following conditions:

$$|\Delta\eta_{EM,trk}| < 0.05 \quad \text{and} \quad |\Delta\phi_{EM,trk}| < 0.05 \quad (5.9)$$

The quality of the cluster-track matching is determined by calculating the spatial  $\chi^2$  probability for each track, by extrapolating the track into the EM3 layer of the calorimeter. The track with the highest  $\chi^2$  probability is considered as a match to the EM cluster. The logarithm of the  $\chi^2$  probability is shown in Fig. 5.4(a), which peaks at zero (*i.e.*, the probability is close to one) for good EM candidates, while it peaks at negative values (*i.e.*, the probability is close to zero) for fake electrons.

- H-matrix  $\chi^2$

The shower development of EM objects is distinct from that of hadronic jets. The H-matrix is the inverse of a covariance matrix that characterizes the shower shape of EM objects. In order to obtain the best discrimination against jets, both longitudinal and transverse shower shapes as well as correlations between the cell energies are used to construct the matrix [77]. The seven variables used are listed below. The first four variables describe the longitudinal shower development, the fifth describes the transverse shower development, and the last two provide a parameterization of the total energy and the impact parameter dependence.

1. Fraction of shower energy in the 1<sup>st</sup> EM layer (EM1) of the calorimeter.
2. Fraction of shower energy in the 2<sup>nd</sup> EM layer (EM2) of the calorimeter.
3. Fraction of shower energy in the 3<sup>rd</sup> EM layer (EM3) of the calorimeter.
4. Fraction of shower energy in the 4<sup>th</sup> EM layer (EM4) of the calorimeter.
5. Width of the shower in the  $r$ - $\phi$  plane in the EM3 floor.
6. Logarithm of the total shower energy,  $\log_{10}(E_{\text{total}})$
7. Expected width of the  $z$  position of the primary vertex,  $Z_{\text{vtx}}/\sigma_{z\text{vtx}}$

The elements of the covariance matrix ( $\mathbf{M}$ ) are given by Eq. 5.10

$$M_{ij} = \frac{1}{N} \sum_{n=1}^N (x_i^n - \langle x_i \rangle) \cdot (x_j^n - \langle x_j \rangle) \quad (5.10)$$

$$\mathbf{H} \equiv \mathbf{M}^{-1} \quad (5.11)$$

$$\chi^2 = \sum_{i,j=1}^7 (x_i^k - \langle x_i \rangle) H_{ij} (x_j^k - \langle x_j \rangle) \quad (5.12)$$

where  $n$  is the event index and  $i$  represents the index of the shape variable. The covariance matrix is derived from  $N$  MC-generated electrons using seven shower shape variables. The H-matrix is defined as the inverse of this covariance matrix (Eq. 5.11). Test objects ( $\tilde{x}_k$ ) are chosen from the data events, and a likelihood for them to have a similar shower shape

compared to the electrons in the covariance matrix is determined. The shape agreement can be tested using a  $\chi^2$  as given in Eq. 5.12.

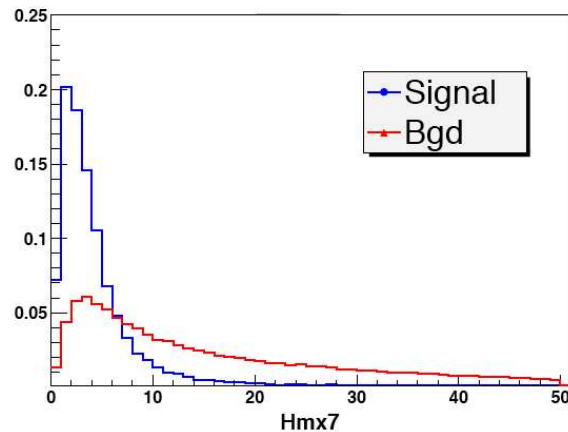


Figure 5.5.  $\chi^2$  distribution of a covariance matrix (H-matrix) with seven variables is shown for real electrons (blue) and fake electrons (red). By placing a cut ( $\chi^2 < 50$ ) one can separate real electrons from fake electrons [76].

The shower shape of an electron or a photon can be distinguished from that of a jet by the use of covariance matrix. The longitudinal and transverse shower shapes, and the correlations between the energy depositions in the calorimeter and preshower cells are used to distinguish electrons and jets. A separate matrix is built for each ring of calorimeter cells with the same  $|\eta|$  coordinate. Each cluster is attributed a  $\chi_{HMx7}^2$  which measures how closely the shower shape of an electron candidate matches the expectation from simulation. The shape of H-matrix  $\chi^2$  for signal and background are different, which is evident from Fig. 5.5. By placing a cut ( *i.e.*,  $\chi_{HMx7}^2 < 20$ , for example) one can distinguish an EM showers from hadronic showers.

- Likelihood

The use of a likelihood in electron identification enhances the separation of good electrons (the signal) from “fake electrons” by considering the shapes of kinematic variables for

each of them built into the likelihood. The term ‘fake electron’ is used to describe any object that is not a high  $p_T$  electron (*i.e.*, backgrounds). These backgrounds include photons and jets dominated by a leading neutral pion which decays into two photons ( $\pi^0 \rightarrow \gamma\gamma$ ). In either case there may be an associated track in the road to the EM cluster due to a photon conversion ( $\gamma \rightarrow e^+e^-$ ), or a low energy charged hadron close to a photon or a  $\pi^0$ . The seven parameters in the likelihood [76] (defined in Eq. 5.13) are listed below.

$$\mathcal{L}_n(x) = \frac{P_{\text{sig}}(x)}{P_{\text{sig}}(x) + P_{\text{bkg}}(x)} \quad (5.13)$$

$$P_{\text{sig}}(x) = \prod_{i=1}^7 P_{\text{sig},i}(x_i) \quad (5.14)$$

$$\text{and } P_{\text{bkg}}(x) = \prod_{i=1}^7 P_{\text{bkg},i}(x_i) \quad (5.15)$$

1. Spatial track match probability,  $P(\chi_{\text{spatial}}^2)$
2. Calorimeter cluster  $E_T$  / Track  $p_T$
3. The distance of closest approach (DCA) of the associated track to the primary vertex.
4. Seven-variable H-matrix  $\chi_{\text{hmx}7}^2$
5. EM fraction,  $f_{EM}$
6. The number of tracks in a cone of size  $R = 0.05$  in  $(\eta, \phi)$  around the track.
7. Sum of the  $p_T$  of all tracks, except the associated track, in a cone of size  $R = 0.4$ .

The chosen variables show good discriminating power between real and fake electrons. The first two variables were discussed in section 5.5.2. Isolated high  $p_T$  electrons originate from the primary vertex, therefore their distance of closest approach (DCA) tends to be small. Lower values of  $\chi_{\text{hmx}7}^2$  and  $f_{EM} \simeq 1.0$  are characteristics of signal-like candidates. The last two variables are track isolation variables. Tracks from good electrons are single, clean tracks whereas photon conversion has two tracks close to each other, and jets faking electrons tend to have more tracks associated with the EM cluster.

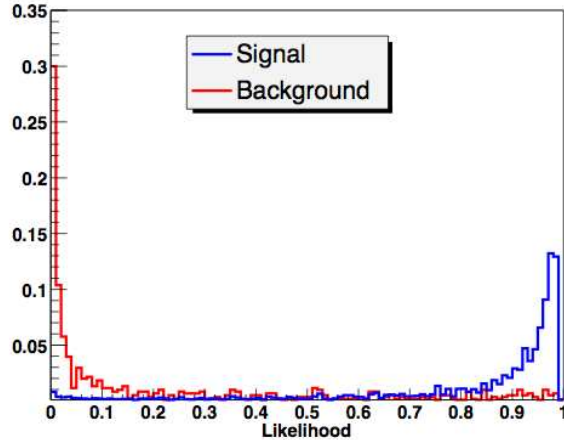


Figure 5.6. The likelihood discriminant for real electrons (blue) and fake electrons (red) showing a clear separation. The signal peaks at values close to one while the background peaks at values close to zero [76].

The distribution of each variable is normalized to unit area to produce its probability distribution. Each distribution can be used to assign a probability for a given EM object to be signal,  $P_{\text{sig}}(\mathbf{x})$ , or background,  $P_{\text{bkg}}(\mathbf{x})$ , where  $\mathbf{x}$  is a vector of likelihood variables. Assuming that the variables are uncorrelated, the overall probability is simply the product of each individual probabilities (Eq. 5.15). By construction the likelihood  $\mathcal{L}_n(x)$  approaches one for signal-like candidates and zero for background-like candidates. Thus the likelihood allows variables to be weighted by their effectiveness in discriminating signal from background. The likelihood discriminant for real and fake electrons are shown in Fig. 5.6. The separation power of the likelihood discriminant is evident from this plot. A cut on the likelihood (*i.e.*, EM-likelihood  $> 0.85$ , for example) can be used to distinguish signal (shown in blue) from background (shown in red). Likelihood-based confirmation of electron candidates has been proven to be efficient compared to cuts on EM fraction, isolation, track-matching and H-matrix  $\chi^2$  by themselves. This is due to the fact that likelihood allows variables to be weighted by their effectiveness in discriminating signal and background unlike the conventional cuts. It also considers the entire shape of signal and background distributions to distinguish them [78].

## 5.6 Jet Reconstruction

Jets are reconstructed using the Run II improved legacy cone algorithm [79] which builds clusters of calorimeter energy deposition created by the particles within jets. The reconstruction algorithm consists of the following steps [80]:

1. The basic building blocks of the jet clustering algorithm are the calorimeter towers which span  $0.1 \times 0.1$  ( $\eta \times \phi$ ). The The transverse energy  $E_T$  of the calorimeter cells in each tower is summed. A threshold of 0.5 GeV is applied. Towers with transverse energy below this threshold are ignored in jet reconstruction.
2. The tower with highest transverse energy is used as a seed in *preclustering* within a cone of  $R = \sqrt{\Delta\eta^2 + \Delta\phi^2} = 0.3$  around the seed tower. Preclusters with total transverse energy less than 1 GeV are discarded. Towers accepted as belonging to a precluster form a jet. The precluster axis is defined to be the  $E_T$  weighted centroid of the precluster towers [81]. The remaining towers undergo the same preclustering procedure until the list is exhausted, thereby identifying other preclusters in the event.

$$E_T \equiv \sum_i E_T^i = \sum_i E_i \times \sin \theta_i$$

$$\eta_{precluster} = \frac{\sum_i E_i \eta^i}{\sum_i E_i} \quad (5.16)$$

$$\phi_{precluster} = \frac{\sum_i E_i \phi^i}{\sum_i E_i} \quad (5.17)$$

3. The next step is jet clustering using all preclusters with  $E_T > 1$  GeV, and summing the calorimeter cells within a cone of  $\Delta R < 0.5$  or  $0.7$ . If the total transverse energy within the cone is above 8 GeV the jet axis corresponding to this cluster is determined using Eq. 5.16 and 5.17. All jets used in this analysis correspond to a  $\Delta R < 0.5$  cone.



4. If two stable reconstructed jets share calorimeter towers, the jets are merged if the shared energy between the two jets is larger than 50% of the lower  $E_T$  jet. Otherwise each shared tower is assigned to the closest jet.

Jets reconstructed in this manner are required to pass further selection cuts before they are used in this analysis. Some of these selection criteria are described below:

- **Electromagnetic Fraction (EMF):** Electromagnetic objects like electrons tend to deposit most of their energy in the EM layers of the calorimeter. Jets on the other hand tend to deposit their energy more uniformly across the EM and hadronic layers. Jets that are composed mostly of neutral objects with sufficient energy undergo showering in the hadronic section and therefore have a smaller EMF. Jets are required to have an EMF between 5% and 95%.
- **Coarse Hadronic Fraction (CHF):** The fraction of transverse energy of the jet that is deposited in the coarse hadronic layers of the calorimeter is called the coarse hadronic fraction (CHF). Jets are required to have CHF values less than 40%.
- **Hot Fraction:** The hot fraction is the ratio of transverse energy in the most energetic cell to that of the next leading cell in a cluster. It provides a means of controlling fake jets created when some cells systematically register high energy depositions due to problems in the corresponding readout electronics and spurious discharges. Reconstructed jets are required to have a hot fraction less than 10.
- **n90:** If the energy contained in a cell is  $\geq 90\%$  of the transverse energy of the jet, it is most likely that the jet is reconstructed due to a single hot calorimeter cell. *n90* provides a technique for reducing this effect, much like the hot fraction. The number of cells that constitute 90% of the jet's transverse energy (hence the name n90) is required to be larger than one.
- **L1 confirmation:** Due to the undesirable noise levels in the precision readout of the calorimeter cells, the calorimeter trigger readout is used to provide a confirmation of the

cell-level readout. The trigger readout occurs at the calorimeter tower level and hence it is inherently different from the cell-level readout. Not all the calorimeter layers are read out when the trigger decision is made at level 1 (L1, hardware level trigger). Hence the two readouts are different, and adjustments are made to account for these differences to provide a consistent L1 confirmation. The L1 confirmation is defined in Eq. 5.18. Jets are required to have  $L1_{conf} > 0.4$  in the central and the endcap calorimeter (CC and EC) regions and  $> 0.2$  in the intercryostat (ICR) region.

$$L1_{conf} = \frac{\sum_{Trigger} E_T^i}{E_T^{jet} \times (1 - CHF)} \quad (5.18)$$

Jets are also required to be within the pseudorapidity range  $|\eta| < 2.5$  and have a transverse energy  $E_T > 15$  GeV in order to be able to apply jet energy scale corrections (described in section 7.3). This is also the fiducial range for  $b$ -tagging.

### 5.7 Missing $E_T$

The initial state momenta of the colliding protons and antiprotons are in nearly opposite directions along the  $\pm z$ -direction (beam axis). The component of the total momentum in a plane perpendicular to the beam axis ( $x$ - $y$  or transverse plane) is zero, and that along the beam direction is negligibly small. When a hard scatter event occurs, momentum conservation requires that the vector sum of momenta of all the final state particles in the event be zero. However, one cannot apply total momentum conservation since some particles go undetected down the beam pipe. The fact that these particles escape implies they have negligible momentum in the transverse plane, and thus one can apply transverse momentum conservation. If the sum of the transverse momenta of the detected particles is significantly different from zero, this discrepancy is attributed to one or more neutrinos which escaped detection, with a vector

sum of transverse momenta exactly opposite to the total detected transverse momentum. This leads to the definition of Missing  $E_T$ , also denoted as  $\cancel{E}_T$ .

Each cell in the calorimeter is assigned a 4-vector, with an energy equal to the measured energy in the cell, a direction pointing from the interaction vertex to the center of the cell, and a mass of zero. The transverse components of these vectors are summed over all calorimeter and ICD cells. The negation of this vector is called the calorimeter missing  $E_T$ . It can be expressed as follows:

$$\vec{\cancel{E}}_T^{cal} = - \sum_i \vec{E}_T^i \quad (5.19)$$

The summation index  $i$  runs over all the calorimeter and ICD cells. Three other useful variables related to  $\cancel{E}_T$  are defined below:

- Scalar  $E_T$ : This is the scalar sum of the transverse energy of all the calorimeter cells.

$$S_{E_T} = \sum_i |\vec{E}_T^i| \quad (5.20)$$

- $\cancel{E}_{Tx}$  and  $\cancel{E}_{Ty}$  Projection of  $\cancel{E}_T$  along  $x$ -and- $y$ -axes:

$$\cancel{E}_{Tx} = \sum_i \left( E_{EM}^i + E_{HAD}^i \right) \sin \theta_i \cos \phi_i \quad (5.21)$$

$$\cancel{E}_{Ty} = \sum_i \left( E_{EM}^i + E_{HAD}^i \right) \sin \theta_i \sin \phi_i \quad (5.22)$$

$$E_T = \sqrt{\cancel{E}_{Tx}^2 + \cancel{E}_{Ty}^2} \quad (5.23)$$

Missing  $E_T$  is the sum of all the cell energies in the calorimeter. It follows that any calorimeter object that is mismeasured will cause the missing  $E_T$  to change by the exact amount of mismeasurement. Corrections are made to calorimeter objects like electrons and jets, and to high

energy muons which deposit very small amounts of energy. After each correction, the missing  $E_T$  is recomputed. The amount of correction applied to the  $\cancel{E}_T$  is given by

$$\vec{\cancel{E}}_{T_{corr}}^{cal} = \vec{\cancel{E}}_{T_{uncorr}}^{cal} + \vec{E}_T^{uncorr} - \vec{E}_T^{corr} \quad (5.24)$$

Details of the corrections to missing  $E_T$  are discussed in section 7.4.

## 5.8 $b$ -tagging

### • Introduction

The experimental signatures for quarks and gluons are jets. The identification of the original parton (quark or a gluon) as well as its flavor (light or heavy quark) is of primary importance. The process of classifying a jet as originating from a  $b$  quark is called  $b$ -tagging.  $b$  quarks resulting from, for example, the decay -  $H \rightarrow b\bar{b}$  undergo hadronization to form  $b$ -hadrons which have a longer lifetime (a few pico seconds) compared to other unstable hadrons. They travel a few millimeters inside the detector before they decay into secondary particles comprised of both charged and neutral hadrons. In addition to the primary interaction vertex, events with  $b$ -hadrons have a displaced secondary vertex where the  $b$ -hadron decayed. The primary and secondary vertices as well as the decay length (the distance traveled by the  $b$ -hadron before its decay) are shown in Fig. 5.7. Charged particles from the decay tend to have high momentum as well as large impact parameters (IP) with the IP defined to be the closest distance  $d_0$ <sup>3</sup> that the particle would come to the primary interaction point along its trajectory.

---

<sup>3</sup> $d_0$  is also referred to as radial distance of closest approach,  $DCA_r$ .

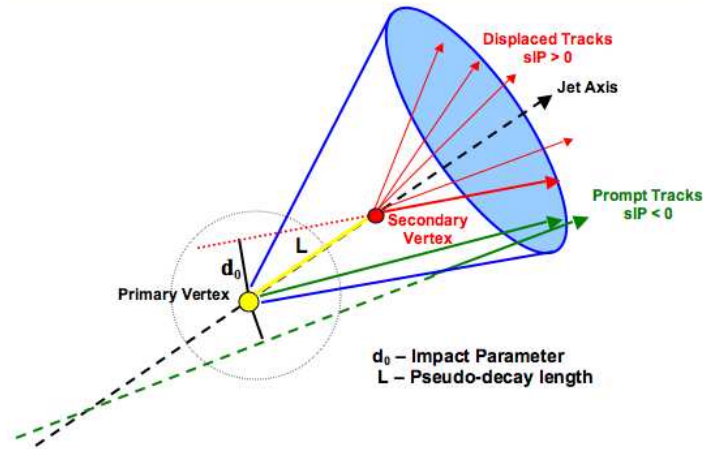


Figure 5.7. A depiction of the characteristics of a  $b$ -jet: (1) with the displaced secondary vertex reconstructed at the decay point of a  $b$ -hadron; (2) displaced tracks with large impact parameters and high  $p_T$  leptons .

- Taggability

In order to identify a  $b$ -jet it must meet certain minimal requirements. A jet that satisfies these requirements is called a *taggable* jet. Taggability of a jet is denoted by  $\epsilon_{taggability}$ , and its value is one for a jet that satisfies the taggability criteria [82] listed below and zero otherwise.

- A *track jet* is formed from the tracks found within  $\Delta R < 0.5$  of a seed track [83]. All tracks used in a track jet must have at least 2 hits in the SMT. The seed track must have  $p_T > 1.0$  GeV and the track jet is required to have at least two tracks.
- A calorimeter jet is matched to a track jet within a cone of  $\Delta R < 0.5$ .

### 5.8.1 $b$ -tagging Methods

$b$ -tagging algorithms are constructed to exploit the longevity of  $b$ -hadrons, their large IP and the presence of secondary vertex, and use them as observables to distinguish  $b$ -hadrons from other hadrons. Several  $b$ -tagging methods that have been used at DØ are discussed briefly in the following sections.

- Secondary Vertex Tagging:

The secondary vertex (SV)  $b$ -tagging algorithm identifies  $b$ -jets by reconstructing the displaced vertex where the  $b$ -hadron decays. The algorithm has three main steps:

- $V_0$  removal: Long lived particles other than  $b$ -hadrons, like  $K_s^0$ ,  $\Lambda$  or pairs of electrons from a photon conversion ( $\gamma \rightarrow e^+e^-$ ) contain *two track vertices* that can lead to a jet being  $b$ -tagged. The  $V_0$  removal procedure explicitly removes such jets by comparing the masses of two track vertices to the known masses of these long-lived particles.
- Track-jet finding: Track based jet finding attempts to combine pre-clustered tracks satisfying certain requirements into a cluster using a 3-d cone algorithm with  $\Delta R = 0.5$  as discussed briefly in the definition of taggability (section 5.8). At least two tracks from the track jet having an IP significance<sup>4</sup> larger than three and at least seven CFT hits are filtered and used to fit a secondary vertex from which these tracks are thought to originate. Additional tracks from the track jet are added and the fit is performed until the  $\chi^2$  of the fit exceeds 15. The resulting secondary vertices are further required to have a decay length significance  $|\vec{L}_{xy}|/\sigma_{|\vec{L}_{xy}|} > 5$ .
- For  $b$ -tagging the jets, reconstructed secondary vertices are matched to taggable calorimeter jets using  $\Delta R < 0.5$  between the calorimeter jet axis and the momentum vector of the vertex. If the angle between the secondary vertex decay length vector and its momentum is smaller than  $\pi/2$  radians, the matched jet is considered a positive  $b$ -tagged jet [84].

- Counting Signed Impact Parameter (CSIP) Tagging:

The impact parameter is considered to be a signed quantity with respect to a given jet axis. A track is assigned a positive impact parameter (sIP  $> 0$ ) with respect to the jet if the track crosses the jet axis in front of the primary vertex (towards the jet) and a negative impact parameter (sIP  $< 0$ ) if it crosses behind the primary vertex (away from the jet), as shown in

---

<sup>4</sup>significance is defined as the measurement of a quantity divided by its error; here sIP =  $d/\sigma(d_0)$

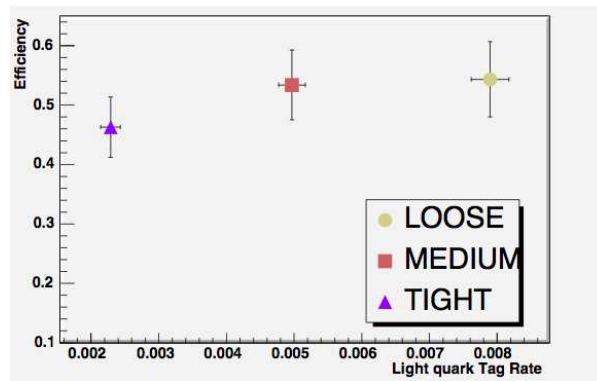


Figure 5.8. Performance of secondary vertex  $b$ -tagging in data for three different types of vertices defined so as to provide a flexible signal efficiency versus background rate control. Efficiency is measured as a function of *fake* (or *mistag*) rate, which is the  $b$ -tagging rate for light quark jets [84].

Fig. 5.9. Positive and large IP tracks are thought to be originating from the decay of heavy hadrons. The jet axis is determined accurately using the primary vertex and the calorimeter information. Tracks are within a cone of  $\Delta R < 0.5$  relative to the jet axis are considered and their IP significance with respect to the primary vertex is determined. If the event has at least 3 tracks with large IP significance ( $> 2$ ) or at least 2 tracks with IP significance greater than 3, then the jet is considered to be tagged. If the tagged jet is within a cone of  $R = 0.3$  around one of the quarks, the flavor of the quark is assigned to the jet [85].

- Jet Lifetime Probability (JLIP) Tagging:

Negative impact parameters of all the reconstructed tracks associated with a calorimeter jet is combined into a single variable called the jet lifetime probability ( $\mathcal{P}_{jet}$  [86]).  $\mathcal{P}_{jet}$  denotes the probability that the tracks in a jet originate from the primary vertex. The negative side of the IP significance distribution, *i.e.*, red histogram to the left of the vertical green line in Fig. 5.10(a), is parameterized using a sum of four Gaussian distributions and is called the IP

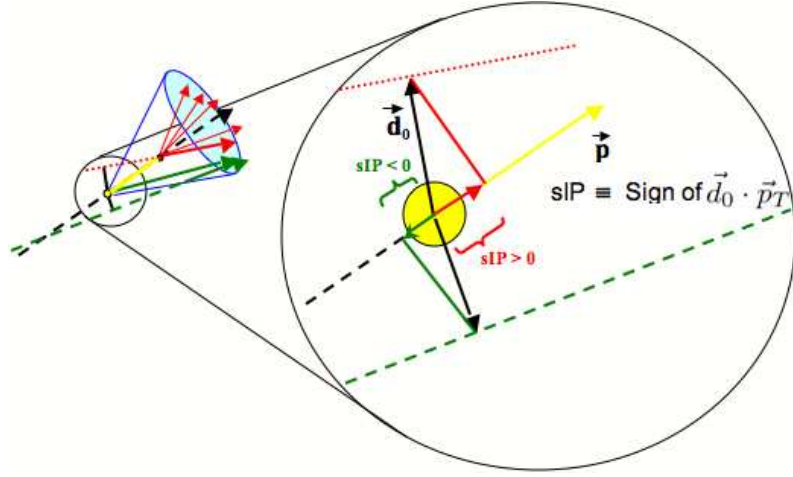


Figure 5.9. Sign of the projection of impact parameter  $d_0$  on the jet axis (i.e.,  $\vec{d}_0 \cdot \vec{p}_T$ ) is positive for displaced tracks originating from the secondary vertex and negative for prompt tracks originating from the primary vertex.

resolution function  $\mathcal{R}(S_{IP})$ . The probability that a track originates from the primary interaction point is defined in Eq. 5.25.

$$\mathcal{P}_{trk}(S_{IP}) = \frac{\int_{-50}^{-|S_{IP}|} \mathcal{R}(S_{IP}) ds}{\int_{-50}^0 \mathcal{R}(S_{IP}) ds} \quad (5.25)$$

$$\mathcal{P}_{jet}(S_{IP}) = \prod \cdot \sum_{i=1}^{N_{trk}-1} \frac{(-\log \prod)^i}{i!} \quad \text{where} \quad \prod = \prod_{j=1}^{N_{trk}} \mathcal{P}_{trk}^j(S_{IP}) \quad (5.26)$$

The IP probability of jets  $\mathcal{P}_{jet}(S_{IP})$  is shown in Fig. 5.10(b) for MC light jets and in Fig. 5.10(c) for  $b$ -jets. By construction, the light jets homogeneously occupy all probability values between 0 and 1 while  $b$ -jets are distinguished by small probability values. For all tracks in a jet (denoted by  $N_{trk}$ ) the jet lifetime probability is determined using Eq. 5.26. Jets are identified as  $b$ -jets by requiring this probability to be less than a preset value.



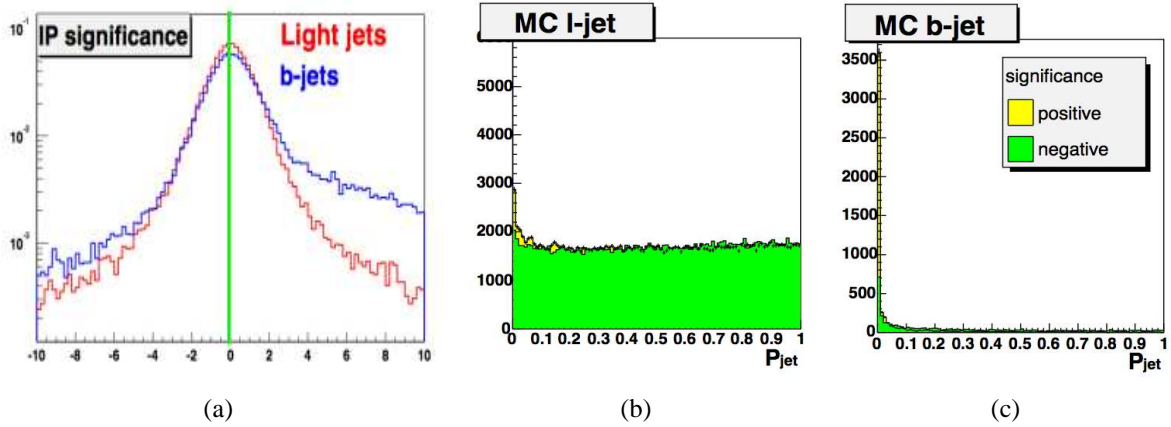


Figure 5.10. (a) Signed IP significance distribution for light flavor jets (in red) and  $b$ -jets (in blue) showing an excess of tracks on the positive side which is a signature of displaced tracks from the decay of heavy hadrons [85]. (b) The probability distribution for MC light jets reconstructed using positive (yellow fill) and negative (green fill) IP tracks and (c) the same for MC  $b$ -jets showing an excess of positive IP tracks at low probability values [86].

- Soft Lepton Tagging (SLT):

Soft lepton tagging identifies  $b$ -jets by the existence of a muon inside the jets.  $b$ -hadrons decay almost always into charm hadrons which further decay semi-leptonically with a branching fraction  $\text{Br}(c \rightarrow \mu X) = 9.58\%$  [87]. In addition,  $b$ -hadrons decay semi-leptonically with a branching fraction  $\text{Br}(b \rightarrow \mu X) = 10.95\%$  [88]. Thus about 20% of  $b$ -jets are associated with a muon. In contrast, the light hadrons produced in light jets either do not decay semi-leptonically or have a long enough lifetime to survive passing through the detector before decaying. Therefore a jet originating from  $b$  quark can be identified by the presence of a muon within the jet. In the soft lepton tagger, a jet is considered as tagged if a muon is matched to a jet within a cone of  $\Delta R < 0.5$  [89].

## 5.9 Neural Network (NN) Tagging:

The Neural Network  $b$ -tagging tool combines the powerful variables used in tagging algorithms discussed in the previous section to distinguish heavy flavor jets from light flavor

jets. The NN tagger achieves a significant enhancement in  $b$ -tagging efficiency and a reduction in the mistag rate, both in data and simulations. Its benefit is equivalent to a doubling of the luminosity [90]. The neural network is trained using seven  $b$ -hadron lifetime observables which show discrimination between  $b$ -quark and light-quark jets. These variables are listed in Table 5.1 in their order of relative importance, as determined from training the neural network. The SLT tagging variables are not used for the NN input since they are used to estimate the

Table 5.1. Neural network input variables chosen to distinguish  $b$ -jets from light-quark jets, listed in order of relative importance.

Rank	Variable Description	Tagger
1	Decay length significance $ \vec{L}_{xy} /\sigma_{ \vec{L}_{xy} }$ of the displaced vertex	SVT
2	Weighted combination of the input tracks' impact parameter significance $d_0/\sigma_{d_0}$	CSIP
3	Probability that the jet originates from the primary interaction vertex	JLIP
4	$\chi^2/N_{dof}$ of the fit to the displaced vertex	SVT
5	Number of tracks used to reconstruct the displaced vertex	SVT
6	Mass of the tracks used to reconstruct the displaced vertex	SVT
7	Number of displaced vertices found in the input jets	SVT

NN  $b$ -tagging efficiency. The calculation of  $b$ -tagging efficiency requires tagging algorithms uncorrelated from the ones used to construct the NN. It has been shown that SLT is uncorrelated with the JLIP, SVT and CSIP taggers [91]. The network is trained using  $Z \rightarrow b\bar{b}$  and QCD  $b\bar{b}$  processes for heavy flavor signal-like events and  $Z \rightarrow q\bar{q}$  and QCD  $q\bar{q}$  production for light flavor background-like events. The neural network produces a continuous output of a single variable which peaks at one for heavy flavor jets and zero for light flavor jets as shown in Fig. 5.11. The NN output shows a significant separation between  $b$ -jets (green histogram) and fake jets (red histogram). A fake jet is a jet that passes the input selection cuts for the NN-tagger and has a loosely defined  $b$ -tag.

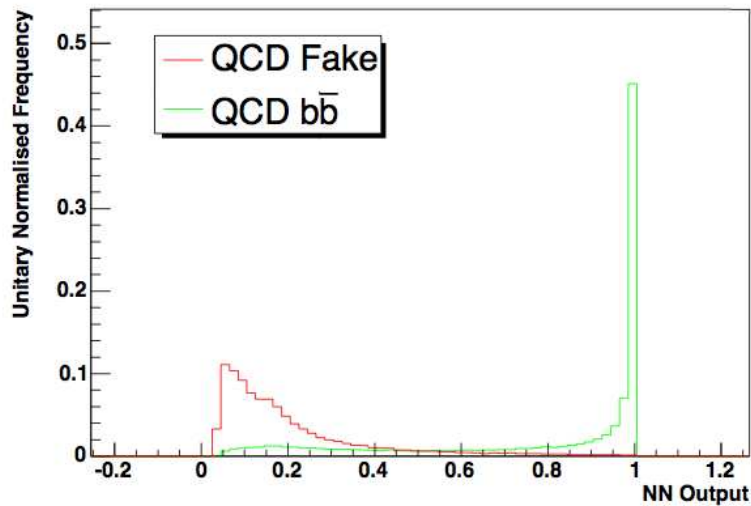


Figure 5.11. Output of the NN showing a separation between signal ( $b$ -quark jets) and background (light-quark jets). Signal peaks close to one and the background peaks close to zero.

A particular value of the cut on the NN output (also called an *operating point*) can be chosen to distinguish the  $b$ -quark jets from light-quark jets. A jet is said to either ‘pass’ (considered as a  $b$ -jet) or ‘fail’ (considered as a light-jet) at a chosen operating point. Several operating points are defined for different cut values and each is characterized by a particular  $b$ -tagging efficiency and a corresponding mistag rate. The twelve operating points available are summarized in Table 5.2.

The NN tagger achieves a large performance gain over the JLIP tagger, with increases in efficiency up to 50% for a fixed fake rate. It also reduces the fake rates by roughly a quarter to a third of their corresponding JLIP values for a fixed signal efficiency. This fact is illustrated in Fig. 5.12 which shows the comparison of the JLIP and the NN taggers, whose efficiencies are plotted as a function of the fake rate. Thus the NN tagger demonstrates a higher performance over the individual taggers and can be used to better discriminate  $b$ -jets from light-quark jets. The NN tagger has significantly better efficiency compared to JLIP tagger for all  $\eta$  (blue curve in Fig. 5.9).

Table 5.2. Efficiency and fake rate of the NN  $b$ -tagger for different operating points.

<b>NN Cut &gt; (%)</b>	<b>10.0</b>	<b>15.0</b>	<b>20.0</b>	<b>25.0</b>	<b>32.5</b>	<b>45.0</b>	<b>50.0</b>	<b>65.0</b>	<b>77.5</b>	<b>85.0</b>	<b>90.0</b>	<b>92.5</b>
Efficiency (%)	77	74.9	72.2	69.6	65.9	60.8	59.3	53.7	47.6	43.3	39.5	37.1
Total Syst. (%)	1.67	1.58	1.47	1.31	1.29	1.37	1.45	1.34	1.52	1.51	1.33	1.43
CC Mistag (%)	11.1	8.16	6.06	4.66	3.28	2.02	1.68	0.96	0.55	0.34	0.23	0.17
ICR Mistag (%)	10.8	7.93	5.86	4.48	3.12	1.84	1.50	0.80	0.41	0.24	0.17	0.13
EC Mistag (%)	10.9	8.08	5.92	4.35	2.98	1.69	1.35	0.65	0.23	0.17	0.09	0.06

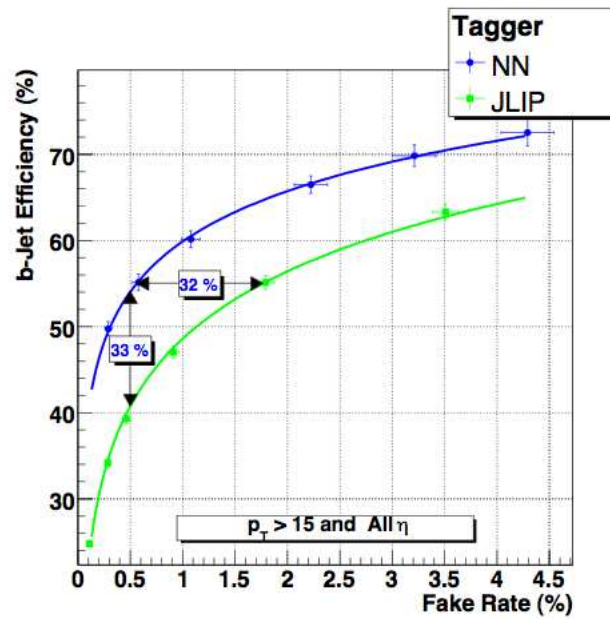


Figure 5.12. Comparison of the performance of NN and JLIP taggers using  $Z \rightarrow b\bar{b}$  and  $Z \rightarrow q\bar{q}$  samples. The errors represent the full statistical and systematic uncertainties in the samples. The NN tagger has smaller uncertainty on the  $b$ -tagging efficiency, but larger uncertainty on the fake rate for lower operating points.

## CHAPTER 6

### DATA AND MC SAMPLES

#### 6.1 Data Processing Chain

Data collected by the  $D\phi$  experiment between April 2002 and February 2006 are used in this analysis; they are referred to as the Run IIA dataset. The recorded data is digitized and stored on tape. Reconstruction is the first step in the data processing chain. A dedicated *re-*

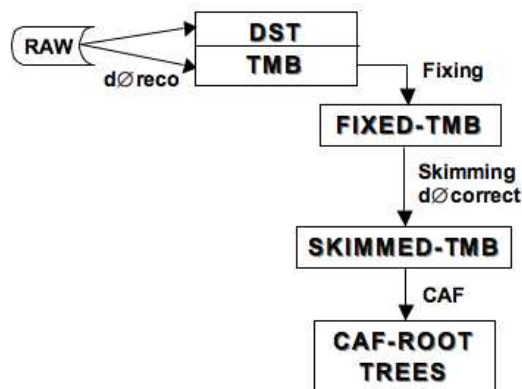


Figure 6.1. A flowchart depicting the data processing chain.

*construction farm* is used to perform the reconstruction of raw data using the program  $d\phi$ reco. The result of this data processing is a data tier called the DST, consisting of many Event Data Model (EDM) chunks. These EDM chunks contain the results of the reconstruction algorithms and require a large storage space per event. Reconstruction is also the most time consuming step in terms of the computer CPU utilization. In order to have data of manageable size which can be stored on computer hard-drives, a compact data format called the thumbnail (TMB) was

designed to have a single EDM chunk with a subset of the DST data packed into it. The reconstruction program was modified to produce the thumbnail data in addition to DST's. Over the years of detector operation, various problems with some of the sub-detectors were uncovered and remedied, and thus, a method of applying corrections to the earlier recorded data was required. The resulting phase is called *fixing*, which is a way of reconstructing the event from the thumbnail data as an alternative to running the complete reconstruction program. Two passes of fixing were carried out. In the first pass the vertex reconstruction was corrected, and in the second pass corrections were applied to remedy calorimeter hardware problems. The T42 [92] algorithm was used to suppress noisy cells as well as electronics noise in the calorimeter.

The Common Samples Group (CSG) assumes the task of providing reduced datasets suitable for various physics analyses. This process is called *skimming*. Skims are identified by a dataset definition and a name with which they can be uniquely accessed. Skimmed thumbnails are processed further using `d0correct` package, which performs post-processing by applying object corrections for muons, electrons and jets. It also recomputes the missing transverse energy after applying the object corrections. The resulting data is called the Common Analysis Format (CAF) data, and is suitable for user analysis in the ROOT [93] framework.

## 6.2 Run IIA Dataset

Data were obtained from the *EMinclusive* skim defined by the CSG [94]. This skim consists of the following definitions:

- At least one EM object with  $ID=10$  or  $\pm 11$ .
- Transverse momentum of EM object(s),  $p_T > 8 \text{ GeV}/c$ .

The complete Run IIA dataset collected from April 2002 to February 2006 is shown in Table 6.1. It is available as CAF *ROOT trees* for analysis.

Table 6.1. The Run IIA EMinclusive skimmed dataset used in this analysis is divided into three subsets. The total size of the dataset on tape is  $\sim 13$  terabytes, corresponding to  $\sim 335$  million events.

Dataset Definition	Events (M)	Size (TB)	Comment
CSG_CAF_EMinclusive_PASS3_p17.09.03	273.9	10.45	Refixed
CSG_CAF_EMinclusive_PASS3_p17.09.06	22.7	0.96	Cable-swap
CSG_CAF_EMinclusive_PASS3_p17.09.06b	38.6	1.46	Non-cable-swap

### 6.3 EM+Jet Trigger Suite

The triggers used are from the EM+Jet trigger suite and are designed to select events that have a good EM object and at least two good jets. The triggers chosen for the analysis are unrescaled for each run epoch (or trigger list) and are listed in Table. 6.2. The requirements at the three trigger levels are explained in detail below and were obtained by querying the trigger database. The entire Run IIA data can be classified into eight trigger lists corresponding to different run ranges, labeled v8, v9, v10, v11, v12, v13a, v13b and v14.

Table 6.2. A set of four triggers was used, corresponding to different data-taking epochs. The trigger terms for Level 1, 2 and 3 are listed for each trigger.

Trigger	L1	L1T(or 2)	L3 Tool,Cut (GeV)
EM15_2JT15	CEM(1,10) CJT(2,5)	EM(.85,10.) 2JET(10.)	Ele(ELE_LOOSE_SH_T,1,15.) Jet(SCJET_9,2,15.)
E1_SHT15_2J20	CEM(1,11)	-	Ele(ELE_NLV_SHT,1,15.) Jet(SC5JET_9_PV3,2,20.)
E1_SHT15_2J_J25	CEM(1,12)	L2CALEM(15,x)	Ele(ELE_NLV_SHT,1,15.) Jet(SC5JET_9_PV3,2,20.) Jet(SC5JET_9_PV3,1,25.)
E1_SHT15_2J_J30	CEM(1,11)	L2CALEM(15,x)	Ele(ELE_NLV_SHT,1,15.) Jet(SC5JET_9_PV3,2,20.) Jet(SC5JET_9_PV3,1,30.)



- CEM(1,10)CJT(2,5): one calorimeter EM trigger tower with transverse energy  $E_T > 10$  GeV and two calorimeter jet trigger towers with  $E_T > 5$  GeV and veto on calorimeter unsuppressed readout condition.
- CEM(1,X): one calorimeter EM trigger tower with  $E_T > X$  GeV and veto on calorimeter unsuppressed readout condition.
- EM(.85,10.)2JET(10.): requires two jet candidates with  $E_T > 10$  GeV and one EM candidate with  $E_T > 10$  GeV with no preshower or tracking requirement.
- Ele(ELE\_LOOSE\_SH\_T,1,15.) Jet(SCJET\_9,2,15.): the trigger bit is set to true if one loose electron is found satisfying transverse shower shape requirements and  $E_T > 15$  GeV and two jets are found each with  $E_T > 15$  GeV.
- Ele(ELE\_NLV\_SHT,1,15.) Jet(SC5JET\_9\_PV3,N,Y.): the trigger bit is set to true if an electron is found with  $E_T > 15$  GeV satisfying tight shower shape requirements. ‘N’ jets with  $E_T > Y$  GeV are required.

#### 6.4 Integrated Luminosity of the Run IIA Dataset

Table 6.3. Recorded luminosity for unrescaled EM+Jet triggers of the Run IIA dataset.

List	Trigger	Luminosity $\text{pb}^{-1}$
v8	EM15_2JT15	23.35
v9	EM15_2JT15	24.73
v10	EM15_2JT15	9.81
v11	EM15_2JT15	63.40
v12	E1_SHT15_2J20	227.35
v13a	E1_SHT15_2J_J25	55.22
v13b	E1_SHT15_2J_J30	298.21
v14	E1_SHT15_2J_J25	333.57
		Total 1035.64

The luminosity corresponding to the data is calculated using a tool provided by provided by the Luminosity-ID group [95]. The integrated luminosity of Run IIA dataset is  $1.04 \text{ fb}^{-1}$ . The recorded luminosity corresponding to each trigger list and the unrescaled trigger used for event selection are shown in Table 6.3. These triggers are *normalizable* in the analysis, *i.e.*, the luminosity blocks that are marked as unusable by any of the sub-detector systems have been removed. For more details refer section 8.3.

## 6.5 Simulated Dataset

All SM backgrounds to the Higgs signal are modeled using MC, except the multijets background which is estimated from data. This section lists the MC samples used and their expected SM cross section. Background modeling and normalization is explained in detail in chapter 8.

- Diboson MC Samples

Table 6.4. Diboson MC samples are generated using PYTHIA MC event generator. The number of events, cross section and the K-factors for each process are shown.

<b>Process</b>	<b>Events (K)</b>	$\sigma \times \text{BR}$ [pb]	<b>K-Factor</b>
$WW \rightarrow e\nu jj$	87	0.79	1.31
$WZ \rightarrow e\nu jj$	96	0.24	1.35
$WZ \rightarrow jj ee$	92	0.08	1.35
$ZZ$ Inclusive	95	1.02	1.38

Diboson MC samples have been generated using the PYTHIA [48] event generator (see section 4) using the CTEQ6L1 PDF's. The number of generated events and their corresponding cross sections are given in Table 6.4. To obtain an accuracy up to next to leading order (NLO), the diboson cross sections are multiplied by their respective K-factors. The cross section for

$W(W) \rightarrow \ell\nu(jj)$  is scaled by 31% (K-factor = 1.31) and those for  $WZ \rightarrow \ell\nu jj$  and  $W(Z) \rightarrow jj(\ell\ell)$  are scaled by 35% (K-factor = 1.35).  $ZZ$  inclusive samples are scaled by 38% [96].

- $t\bar{t}$  MC Samples

The  $t\bar{t}$  (lepton + jets) and (dilepton) samples were generated using CTEQ6L1 PDF's with scale  $Q^2 = m_t^2 + \sum_{jets} p_T^2$ , using the ALPGEN [49, 50] matrix element generator in different parton multiplicity bins. They were combined into a single sample as explained in Eq. 4.1. The relative cross sections used in the combination are shown in Table. 6.5. The  $t\bar{t}$  cross section (lepton + jets) is scaled by 41% (K-factor = 1.41) to obtain NLO accuracy. The  $t\bar{t}$  dilepton channel has a K-factor of 1.39 applied.

Table 6.5.  $t\bar{t}$  dilepton and lepton+jets ALPGEN MC samples in exclusive bins of zero and one light parton and an inclusive bin of two light partons.

Process	Type	Events (K)	$\sigma \times \text{BR}$ [pb]	K-Factor
$t\bar{t} \rightarrow b\bar{b} + 2\ell + 2\nu$	+0lp Exclusive	224	0.324	1.39
	+1lp Exclusive	96	0.151	1.39
	+2lp Inclusive	50	0.104	1.39
$t\bar{t} \rightarrow b\bar{b} + 2j + \ell\nu$	+0lp Exclusive	283	1.284	1.41
	+1lp Exclusive	98	0.625	1.41
	+2lp Inclusive	92	0.398	1.41

- $WH$  Signal Samples

The signal samples consist of  $WH$  process which are generated using PYTHIA for Higgs mass points of 105, 115, 125, 135 and 145 GeV/ $c^2$ . In order to estimate the  $ZH$  contamination of the signal for the final results and the combination of all signals,  $ZH$  process is also generated for the same mass points. They are summarized showing the cross sections for the different mass points (Table. 6.6).

Table 6.6. Simulated  $WH$  and  $ZH$  signal processes showing the number of events and cross sections.  $\ell$  is either  $e$  or  $\mu$ .

Process	$m_H$ (GeV)	Events (K)	$\sigma \times \text{BR}$ [fb]
$HW \rightarrow b\bar{b} + \ell\nu$	105	48.3	22.2
	115	32.1	15.0
	125	53.1	9.3
	135	51.8	4.5
	145	49.3	2.2
$HW \rightarrow b\bar{b} + \tau\nu, \tau \rightarrow \ell$	105	30.7	3.9
	115	46.7	2.6
	125	46.5	1.6
	135	48.1	0.8
	145	45.8	0.4
$HZ \rightarrow b\bar{b} + \ell\ell$	105	49.0	4.0
	115	32.1	2.8
	125	47.7	1.8
	135	48.3	1.1
	145	50.5	0.5
$HZ \rightarrow b\bar{b} + \tau\tau, \tau \rightarrow \ell$	105	47.8	0.7
	115	50.0	0.5
	125	47.5	0.3
	135	46.6	0.2
	145	46.7	0.09

- $W$ +jets and  $Z$ +jets MC Samples

$W$  + jets MC samples are generated using ALPGEN for different parton multiplicities *i.e.*,  $W + nlp$  where  $n = 1, 2, 3, 4, 5$  and similarly for  $Z + nlp$  and to which MLM matching scheme [58] (see section 4.2.2 for details) has been applied. The final state particles from these processes undergo fragmentation according to the Lund model using PYTHIA MC generator. All samples thus generated have been subjected a process of heavy flavor (HF) skimming, *i.e.*, additional heavy flavored partons generated by PYTHIA have been removed to obtain unbiased samples.  $Z$  + jets samples used in this analysis have not been HF-skimmed. The samples are listed with their cross sections in Table 6.7.

Table 6.7. List of simulated  $W$ +jets (light/heavy flavor) and  $Z$ +jets (heavy/light flavor) with number of events and cross sections (the light partons samples have jet  $p_T > 8$  GeV and  $|\eta| < 5$ ). The LO cross sections given in the table are scaled by the following K-factors: 1.35 for  $Wjj, Zjj$ , and 1.75 for  $Wc\bar{c}, b\bar{b}, Zc\bar{c}, b\bar{b}$ .  $\ell$  is a lepton *i.e.*, either  $e, \mu$  or  $\tau$ .

Process	Type	Events (K)	$\sigma \times \text{BR}$ [pb]
$Wjj \rightarrow \ell\nu$	+ 0 $l$ Exclusive	2300	4574.4
	+ 1 $l$ Exclusive	2800	1273.9
	+ 2 $l$ Exclusive	1600	298.6
	+ 3 $l$ Exclusive	790	70.6
	+ 4 $l$ Exclusive	780	15.8
	+ 5 $l$ Inclusive	58	11.3
$Wb\bar{b} \rightarrow \ell\nu b\bar{b}$	+ 0 $l$ Exclusive	740	19.2
	+ 1 $l$ Exclusive	261	7.9
	+ 2 $l$ Exclusive	171	2.6
	+ 3 $l$ Inclusive	164	1.7
$Wc\bar{c} \rightarrow \ell\nu c\bar{c}$	+ 0 $l$ Exclusive	482	71.1
	+ 1 $l$ Exclusive	336	29.9
	+ 2 $l$ Exclusive	333	10.3
	+ 3 $l$ Inclusive	372	18.4
$Zjj \rightarrow ee$	+ 0 $l$ Exclusive	1000	139.2
	+ 1 $l$ Exclusive	187	41.8
	+ 2 $l$ Exclusive	93	10.3
	+ 3 $l$ Inclusive	93	5.3
$Zjj \rightarrow \mu\mu$	+ 0 $l$ Exclusive	839	139.5
	+ 1 $l$ Exclusive	209	41.6
	+ 2 $l$ Exclusive	104	10.3
	+ 3 $l$ Inclusive	104	5.3
$Zjj \rightarrow \tau\tau$	+ 0 $l$ Exclusive	795	139.4
	+ 1 $l$ Exclusive	209	41.7
	+ 2 $l$ Exclusive	97	10.3
	+ 3 $l$ Inclusive	104	5.3
$Zb\bar{b} \rightarrow \ell^+\ell^- + b\bar{b}$	+ 0 $l$ Exclusive	604	0.97
	+ 1 $l$ Exclusive	271	0.36
	+ 2 $l$ Inclusive	144	0.21
$Zc\bar{c} \rightarrow \ell^+\ell^- + c\bar{c}$	+ 0 $l$ Exclusive	152	3.0
	+ 1 $l$ Exclusive	143	1.06
	+ 2 $l$ Inclusive	172	0.6

## CHAPTER 7

### OBJECT RECONSTRUCTION AND SELECTION EFFICIENCIES

This chapter describes the methods used to determine the reconstruction and identification (ID) efficiencies of objects used in this analysis. The efficiencies are measured separately for Data ( $\text{eff}_{\text{data}}$ ) and MC ( $\text{eff}_{\text{mc}}$ ). The MC is tuned for a given efficiency using a multiplicative factor (also called the scale factor) given by  $s_f = \text{eff}_{\text{data}}/\text{eff}_{\text{mc}}$  and is applied to each object. The ‘tag and probe’ method used to evaluate electron identification (EMID) efficiency is explained in detail in section 7.1. The jet ID efficiencies and the jet energy scale corrections are outlined in section 7.3. The propagation of these efficiencies to evaluate the missing transverse energy (Missing  $E_T$  or  $\cancel{E}_T$ ) is given in section 7.4. Finally, the  $b$ -tagging efficiencies are considered in section 7.5.

#### 7.1 Electron Reconstruction Efficiency

The event selection for the current analysis involves a final state electron. Single electron efficiencies are measured using samples rich in  $Z$  bosons. They provide clean signal events of  $Z$  candidates whose properties (the invariant mass and the width) are very well understood. The decay of the  $Z$  in the electron channel (*i.e.*,  $Z/\gamma^* \rightarrow e^+e^-$ ) provides a useful means of evaluating the EMID efficiencies using the so-called tag and probe method. The background contamination in these samples is negligible, rendering them a good choice for this study. To avoid biases in the selection of electrons, the efficiencies are measured for each electron rather than for each event. Either of the two highest  $p_T$  electrons in the candidate events can be chosen as the tag, with the other the probe.

### 7.1.1 Tag and Probe Method

$Z/\gamma^* \rightarrow e^+e^-$  events are chosen for study and the dielectron invariant mass is required to be consistent with that of a  $Z$  boson. One of the electrons is considered the ‘‘tag’’ and the other is the ‘‘probe.’’ The tag electron is required to satisfy stringent reconstruction criteria (cuts), in order to improve the purity of the sample. The other electron is used as an unbiased probe. The efficiency is defined as the fraction of events for which the probe electron passes the cut relevant to the efficiency being determined. To minimize bias in the measurement due to background contamination, the purity of the sample is estimated by fitting the dielectron invariant mass peak using signal and background hypotheses. The background subtracted sample is used in the efficiency determination. Efficiencies are binned as a function of kinematic ( $p_T$ ) and detector ( $\eta_D, \phi_{\text{det}}, z_0$ ) variables.

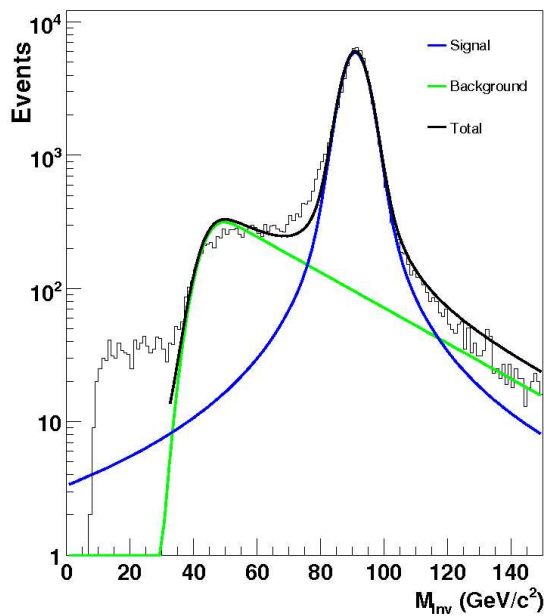
### 7.1.2 Signal and Background Modeling

To find the number of real  $Z$  candidates prior to and after the requiring the reconstructed probe track. The invariant mass spectrum is modeled using a Voigtian ( $f_{sig}$ )<sup>1</sup> signal shape and a continuous background shape of falling exponential with a sharp turn on ( $f_{bkg}$ ), as given in Eq. 7.1. The background shape models the Drell-Yan spectrum and the combinatoric background. The fit parameters  $a_i, i = 0, 1, \dots, 6$  are shown in Table. 7.1(b). The fit is performed iteratively until the fit parameters stabilize. A detailed description of the fitting procedure can be found in [97].

$$\begin{aligned}
 f_{tot} &= f_{sig} + f_{bkg} & (7.1) \\
 f_{sig}(x) &= a_2 \cdot \text{Voigt}\left(x - a_0, a_1, \frac{a_0 \Gamma_z}{m_z}\right) \\
 f_{bkg}(x) &= a_6 \cdot \text{Erfc}(a_4 \cdot (a_3 - x)) e^{-a_5(x-m_z)}
 \end{aligned}$$

---

<sup>1</sup>Convolution of a Breit-Wigner profile with a Gaussian.



(a)

$a_i$	Value	Description
$a_0$	90.89	mass peak
$a_1$	3.89	sigma of Voigtian
$a_2$	$69.15 \times 10^3$	signal scale
$a_3$	42.92	background turn-on
$a_4$	0.16	steepness of turn-on
$a_5$	0.03	exponential scale
$a_6$	46.92	background scale

(b)

Figure 7.1. The dielectron invariant mass spectrum is shown in (a). The histogram represents data, the signal shape is a Voigtian (blue curve) and the background is modeled as an exponentially falling distribution (green curve). The sum of the two fit functions is shown in black. (b) The values of fit parameters and their description.

A semi-log plot of the dielectron invariant mass of the candidate events chosen for study is shown in Fig. 7.1(a). A log-likelihood method is used to fit the range from  $[32, 105]$   $\text{GeV}/c^2$ . Typical values of the fit parameters are also shown in the figure. From the fits, the total number of real  $Z$  candidates is found within an invariant mass window  $[80, 100]$   $\text{GeV}/c^2$  by subtracting the fit value of the background function at the center of each bin from the total number of events in that bin.

### 7.1.3 Event Selection Criteria

1. Candidate EM objects must pass the following preselection criteria:

- $E_T > 25$  GeV.



- EMID = 10,  $\pm 11$ .
  - EM fraction  $> 0.9$ .
2. Candidate tracks must pass the following track criteria:
- $p_T > 12$  GeV
  - $1.5 < |\eta_D| < 3.6$  (EC Region);  $|\eta_D| < 1.1$  (CC Region).
  - Distance of closest approach in the transverse plane;  $|DCA| < 1.0$  cm.
  - Track does not overlap with a muon candidate;  $\Delta R(\text{track}, \mu) > 0.2$ .
  - $0.1 < \phi_{\text{mod}}$  of track at calorimeter  $< 0.9$  (CC Region Only).
  - Track must be isolated — sum of track  $p_T$  in a cone of 0.4 around the candidate track must be  $< 3$  GeV.
  - At least one SMT hit.
3. Additional criteria are imposed to ensure events are selected from  $Z$  boson decay.
- Both legs must originate from the same primary vertex;  $\Delta z(\text{EM Object}, \text{Track}) < 2$  cm.
  - Tracks must be sufficiently back to back in azimuth;  $\Delta\phi(\text{EM Object}, \text{Track}) > 2$  rad.
  - The invariant mass of track and EM Object pair  $> 65$  GeV/ $c^2$ .
4. Trigger Selection
- The EM candidate must pass the trigger requirements for at least one unpre-scaled trigger in the trigger combination.

A tag is a track-matched EM object which satisfies the above requirements and the following additional selection:

- Calorimeter isolation  $< 0.15$ .
- $\chi^2$  of H-Matrix(7)  $< 12$  in CC region;  $\chi^2$  of H-Matrix(8)  $< 20$  in EC region.
- EM object has a  $E/p$  track match.
- Track  $p_T/\sigma_{p_T} > 1$ .

All track-matched EM objects in an event are tested as potential tags. The probe is a track that is back to back in  $\phi$  with the tag electron. Probe tracks from all the (EM object,Track) pairs which satisfy items (2) and (3) above are tested against the preselection conditions, *i.e.*, item (1). The probe track is said to have an EM object match if  $\Delta R(\text{EM Object, probe Track}) < 0.1$ .

#### 7.1.4 Preselection Efficiency

The preselection efficiency is defined as the efficiency for an electron satisfying the kinematic and geometric requirements to form an EM cluster. All the EM objects are required to have EM ID = 10 or  $\pm 11$  in EC or EM ID =  $\pm 11$  in CC region, must be sufficiently isolated ( $f_{iso} < 0.15$ ) and must have most of their energy deposited in the EM portion of the calorimeter ( $f_{em} > 0.9$ ). The number of real electrons that satisfy the imposed conditions out of the total number of signal events obtained using the fit described in section 7.1.2 yields the preselection efficiency. It can be expressed mathematically as in Eq. 7.2 where  $P_s$  ( $F_s$ ) are the number of signal events that passed (failed) the preselection cuts. All other efficiencies are measured relative to the preselection efficiency.

$$\epsilon_{pre sel} = \frac{P_s}{P_s + F_s} \quad (7.2)$$

In Fig. 7.2(a) the preselection efficiency is shown as a function of  $\eta_D$  of the probe track. For  $|\eta_D| > 2.0$  statistical errors are large. For  $|\eta_D| < 1.1$  the efficiency is close to 100%. It decreases as  $|\eta_D|$  approaches 2.0. Some of the bins have unphysical values ( $\epsilon_{pre sel} > 1.0$  or  $\epsilon_{pre sel} < 0.0$ ) either due to lack of statistics or the method of background subtraction. These bins are truncated to the nearest boundary values before obtaining the scale factors. The preselection efficiency is shown as a function of  $p_T$  of the probe track in Fig. 7.2(b). The electrons in the CC and EC regions do not have any fiducial restrictions. The decrease

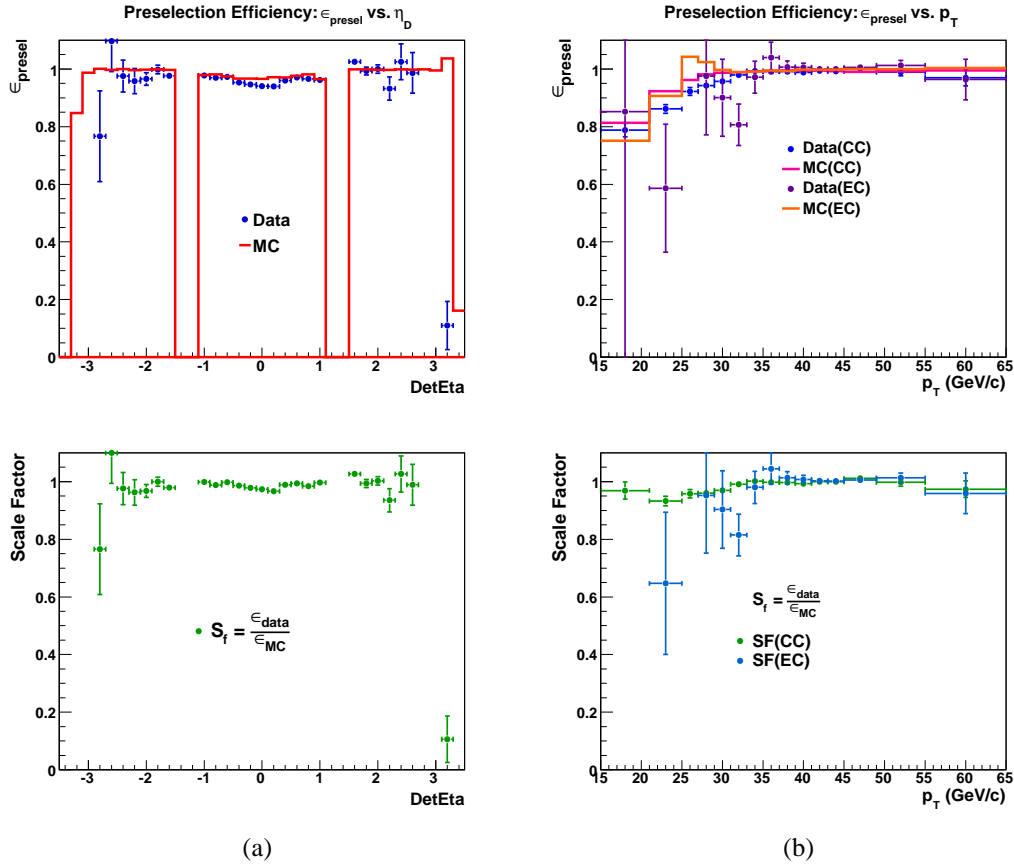


Figure 7.2. Preselection efficiency of the probe track is shown as a function of  $\eta_D$  in 7.2(a) and  $p_T$  in 7.2(b). The upper plots show the efficiencies obtained in data (markers) and MC (solid lines). The lower plots show the ratio of the efficiency of data to MC (which is the scale factor or the correction factor). In the right plot the preselection efficiencies and scale factors are shown as a function of  $p_T$  separately for for CC and EC probe tracks.

in preselection efficiency at low  $p_T$  is because of the electrons close to the  $\phi_{\text{mod}}$  boundaries, which are in the non-fiducial volume and therefore have their measured energy lower. The EC region suffers from low statistics. The scale factors are close to unity for both the CC ( $|\eta_D| < 1.1$ ) and EC region ( $1.5 < \eta_D < 2.5$ ), and as a function of  $p_T$  of the probe track (as shown in the bottom row of Fig. 7.2(a) and Fig. 7.2(b) respectively), indicating similar preselection efficiencies in data as well as MC events. A summary of the preselection efficiency is given in Table. 7.1.

Table 7.1. Average preselection efficiency in data and MC for CC and EC probe tracks.

$\epsilon_{pre\,sel}$ (%)	CC	EC
Data	$99.2 \pm 0.2$	$99.0 \pm 0.3$
MC	$99.8 \pm 0.1$	$99.4 \pm 0.1$

### 7.1.5 Post-preselection Efficiency

Post-preselection efficiency is defined relative to the preselection efficiency. Given an electron (probe track) satisfying all the preselection cuts defined in section 7.1.3, additional tighter selection cuts are applied according to the `top_tight` (v3) electron definition given below. The ratio of the number of probe tracks passing the tighter selection to those that pass the preselection cuts defines the post-preselection efficiency. The post-preselection efficiency takes into account the track-matching efficiency, the seven parameter H-matrix efficiency and the EM-likelihood efficiency of the electron measured with respect to the preselection efficiency.

- Calorimeter isolation fraction ( $f_{iso}$ )  $\leq 0.15$
- Electromagnetic fraction ( $f_{em}$ )  $\geq 0.9$
- $p_T \geq 15$  GeV (for measuring efficiency)
- $\chi^2$  of HMatrix(7)  $\leq 50$
- $\chi^2$  of  $E/p$  track match  $> 0.0$
- $p_T$  of the track  $\geq 5$  GeV
- EM Likelihood  $\geq 0.85$

The post-preselection efficiency is binned as a function of  $\eta_D$  (Fig. 7.3(a)) and  $p_T$  (Fig. 7.3(b)) of the probe track for CC and EC probe tracks. The scale factors as a function of electron  $p_T$  and  $\eta_D$  are indicated in the lower row. The efficiency in MC is higher than data in all cases. The EC efficiency is lower compared to the CC region. For  $\eta_D > 2.0$  the efficiency

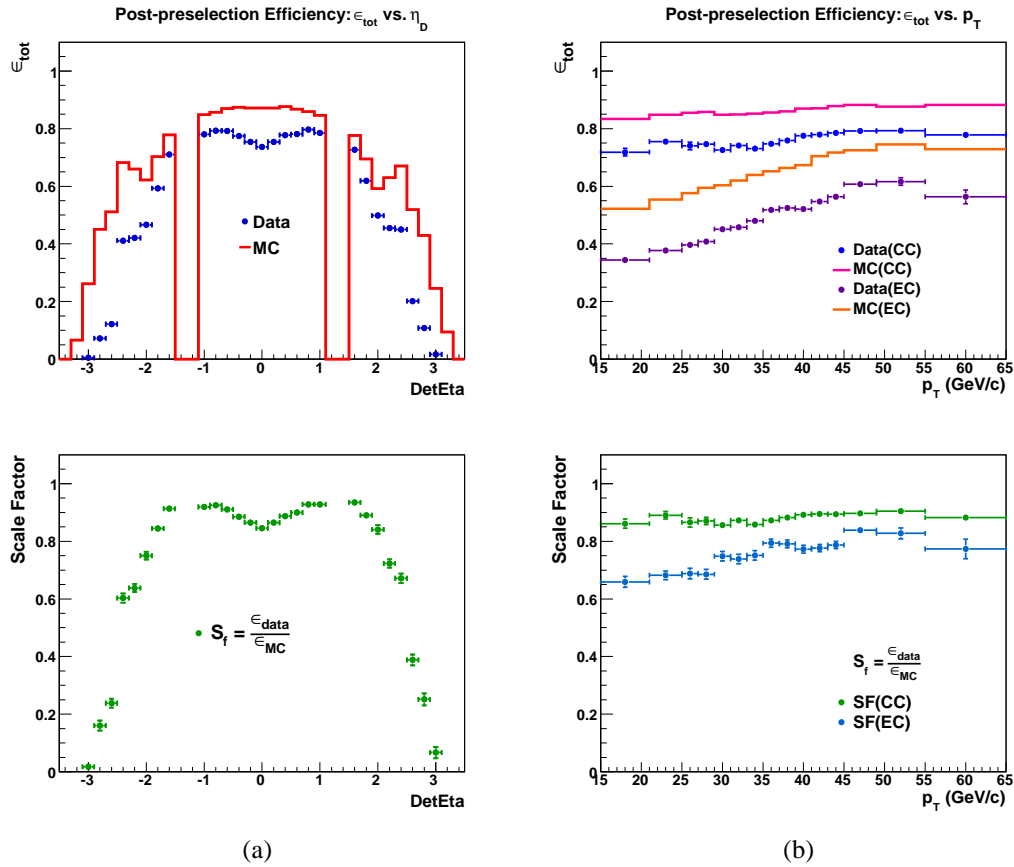


Figure 7.3. Post-preselection efficiency of the probe track is shown as a function of  $\eta_D$  in 7.3(a) and  $p_T$  in 7.3(b). The upper plots show the efficiencies obtained in data (markers) and MC (solid lines). The lower plots show the scale factors. In the right plot they shown separately for for CC and EC probe tracks.

drops rapidly. Low  $p_T$  probe tracks and those that are non-fiducial tend to lower the efficiency in the  $p_T$  region below 30 GeV/c. The lower efficiency at low  $p_T$  is largely due to the tracking efficiency of the central tracking system. The tracking efficiency is a dominant factor in the reduction of the post-preselection efficiency. The other components of the post-preselection efficiency are the seven parameter H-matrix efficiency and the seven parameter EM-likelihood efficiency, each measured with respect to the preselection cuts on the EM candidates. The average values of post-preselection efficiencies are summarized in Table 7.2.

Table 7.2. Average post-preselection efficiency in data and MC for CC and EC probe tracks.

$\epsilon_{preselect} (\%)$	CC	EC
Data	$77.6 \pm 0.3$	$63.3 \pm 0.4$
MC	$86.6 \pm 0.1$	$70.6 \pm 0.2$

Figure 7.4(a) shows the seven variable H-matrix efficiency in data and MC (top) and the corresponding scale factor (bottom) for a cut value of  $\chi^2_{Hmatrix7} < 50$ . The average H-matrix efficiency is close to 100% in both data and MC and the scale factors are close to one. The

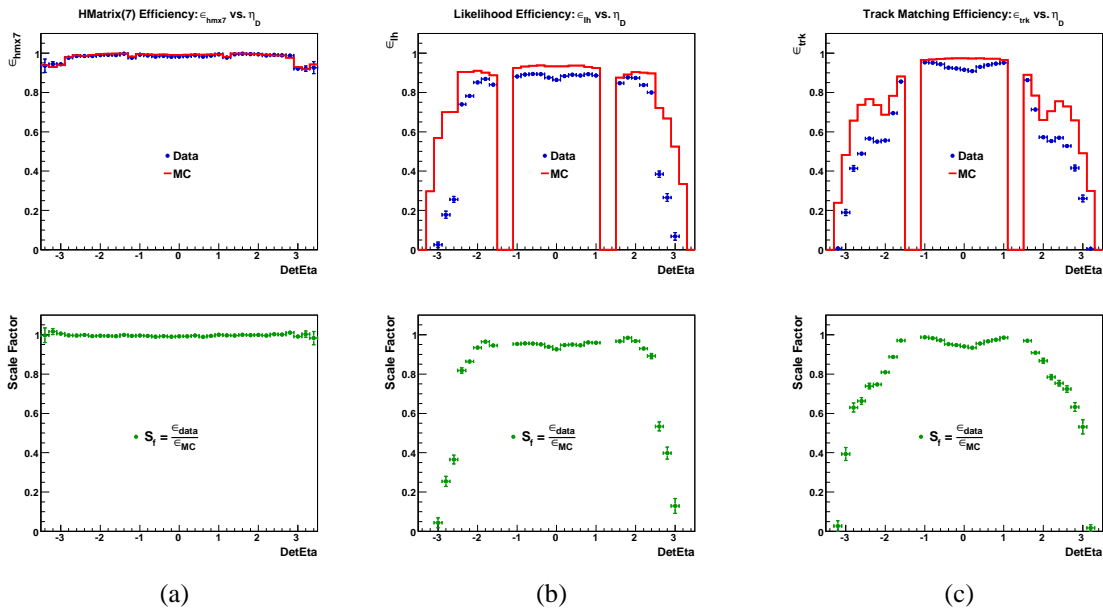


Figure 7.4. (a) Efficiency of H-matrix with seven variables, (b) EM likelihood efficiency and (c) track-matching efficiency as a function of  $\eta_D$  for probe electrons. The upper plots show the efficiencies obtained in data (markers) and MC (solid lines). The lower plots show the scale factors.

EM-likelihood efficiencies in data and MC are shown in Fig. 7.4(b) (top) and the corresponding scale factors (bottom). The EM likelihood efficiency in the CC region is close to 90% in MC and slightly lower in data. One of the variables in the EM likelihood is the requirement of a

matching track with a small  $\chi^2$  to an EM cluster, which is the limiting factor in the lowering of the likelihood efficiency. The track-matching efficiency for CC and EC probe tracks are shown in Fig. 7.4(c) (top) and the corresponding scale factors (bottom). The track-matching efficiency (and hence the EM likelihood efficiency) in the EC region falls off more rapidly in data compared to MC. The scale factors reflect this behavior.

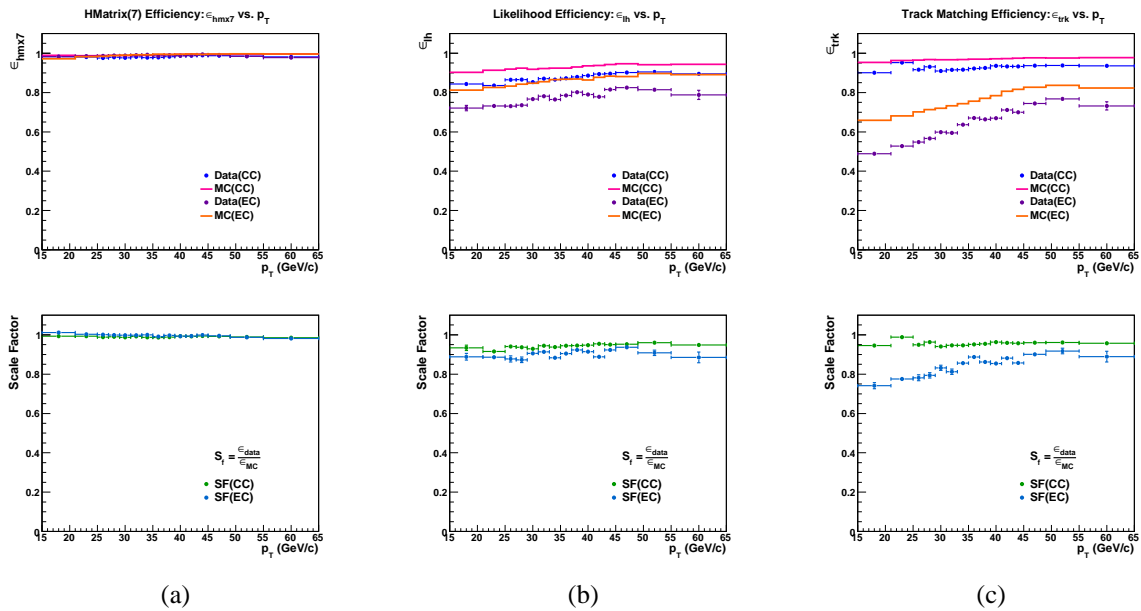


Figure 7.5. (a) Efficiency of H-matrix with seven variables, (b) EM likelihood efficiency and (c) track-matching efficiency as a function of  $p_T$  for probe electrons. The upper plots show the efficiencies obtained in data (markers) and MC (solid lines). The lower plots show the scale factors. CC and EC efficiencies are shown separately.

The seven parameter H-matrix efficiency as a function of  $p_T$  of probe track is shown in the top row of Fig. 7.5(a) and the corresponding scale factors in the bottom row. There is no  $p_T$  dependence since the efficiencies in both data as well as MC are close to 100% and hence the scale factors are close to one. The track matching efficiency of probe track as a function of  $p_T$  is shown in Fig. 7.5(c) (top) and the scale factor for the same in the bottom row. There is a definite  $p_T$  dependence in the lower  $p_T$  region, especially for EC probe tracks, since the

tracking efficiency is lower in the forward region. This, in turn, affects the EM likelihood efficiency which also shows a slight  $p_T$  dependence as shown in Fig. 7.5(b).

## 7.2 Trigger Efficiency

Event selection for the single electron final state used in this analysis is based on trigger requirements. The final state also contains two or more jets. The trigger-based selection mandates that we estimate the efficiency of the triggering system to select the candidate events. Three different trigger suites are studied in this analysis and the trigger efficiency is estimated for each configuration using the tag and probe method applied to  $Z/\gamma^* \rightarrow e^+e^-$  data events. The estimate of the trigger efficiency in MC requires a simulation of the three level triggering system at DØ using the `trigsim` [98] software, which is not carried out here. Instead, the trigger efficiencies estimated from data are applied directly to the MC events. The three trigger configurations studied here can be classified as

- a) single electron trigger suite with calorimeter-based information (EMCAL).
- b) single electron trigger suite with calorimeter-based and track-based information (EMCALTRK).
- c) single electron and jet triggers (EM+Jet).

The efficiency is determined using the tag and probe method as described in section 7.1.1. The background is subtracted as described in section 7.1.2. The event needs to have a reconstructed primary vertex with  $|\text{vtx}_z| < 60$  cm. The efficiency is measured for the `top_tight` (v3) definition of electron (section 7.1.5). The tag is required to pass the criteria described in section 7.1.3. For the trigger under study to pass, the reconstructed electron must have (a) L1 trigger tower passing the required  $E_T$  cut within  $\Delta R < 0.4$ ; (b) L2 object passing the required criteria (if any) with  $\Delta R < 0.4$ ; (c) L3 object passing the required criteria within  $\Delta R < 0.4$  and (d) that particular trigger must have fired for that event. The trigger efficiency is given by



the fraction of events where the probe electron passes the L1, L2 and L3 conditions. These are derived for various trigger lists and are parameterized as a function of  $p_T$  and  $\eta_D$  of the probe electrons. The trigger efficiencies are shown in Fig. 7.6 for four different trigger suites, corresponding to four data taking epochs, for the calorimeter-based triggers [99]. The average trigger efficiency is about  $91\% \pm 2\%$ . The EM+Jet trigger suite has lower EM thresholds and a higher efficiency than the calorimeter-based triggers, and hence, they are chosen for this analysis.

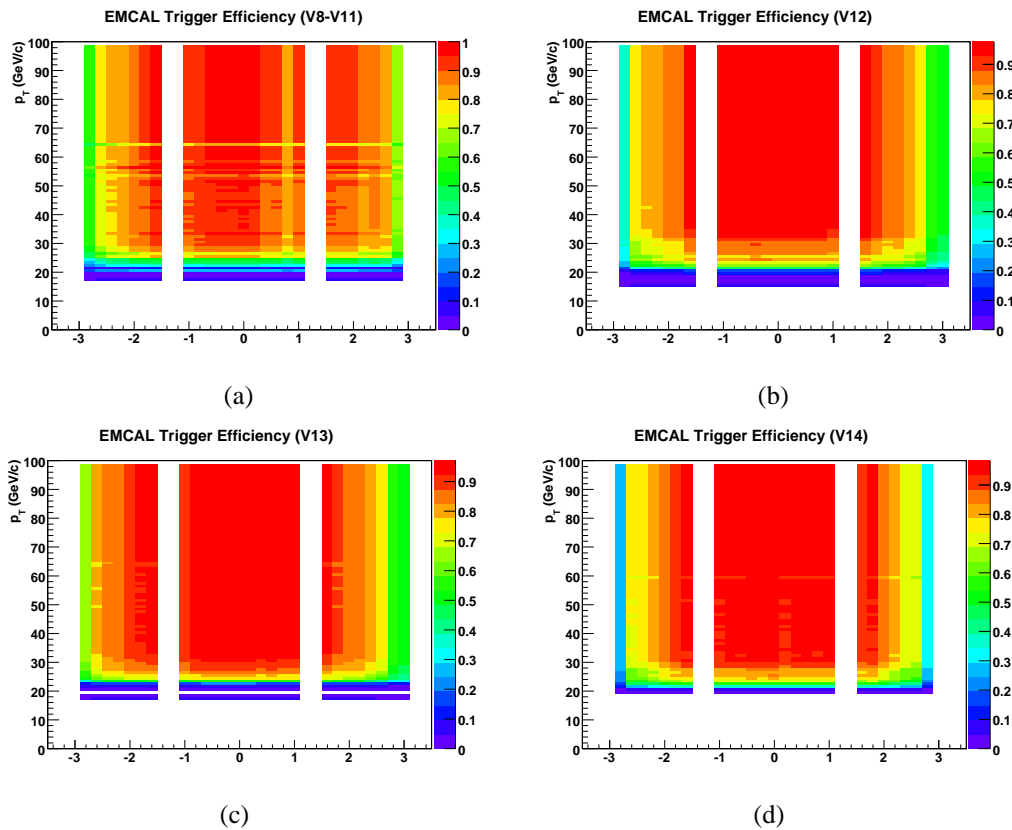


Figure 7.6. Trigger efficiencies of calorimeter-based triggers as a function of  $p_T$  of the probe electron and  $\eta_D$ . The efficiencies are shown for (a) v8-11 (b) v12 (c) v13 and (d) v14 trigger lists.

### 7.2.1 Normalization

From the standpoint of an analyser, using the trigger efficiencies for an ‘OR’ed set requires the knowledge of prescales for a given set of triggers and two interesting scenarios can be identified for normalising an analysis.

- Using a single trigger
- Using ‘OR’ed set of triggers

- Using Single Trigger

In this case the luminosity system keeps track of the prescales. When the analyser provides a list of good luminosity block numbers (LBN’s) and a trigger, the luminosity system gives the correct luminosity taking into account the prescale for that trigger. In this case one must always measure the efficiency removing any bias for prescales. Otherwise one is liable to double-count the prescales.

- Using ‘OR’ed set of triggers

When measuring a single trigger efficiency it is required that the tag electron be matched to that particular single EM trigger. For example, if the tag trigger requirement is purely the trigger E1\_SH30, for example, and if one wants to measure the E1\_SH30 trigger efficiency, one would not see any prescale bias because the sample will only contain events where that particular trigger E1\_SH30 has fired for the tag electron. One would measure, in this case, the probability that the the probe electron has fired given that it has fired for the tag electron as well. But what one wants to measure instead is the efficiency that a single electron has fired the trigger taking prescales into account.

However, one can use an OR of several triggers to have an as high statistics as possible and determine the trigger efficiency of the ‘OR’ed set. Forcing the tag to match a particular

trigger in the ‘OR’ed set might actually bias our measurement when it comes to prescales. As an example imagine a situation where one would only use E1\_SH30 on the tag but are trying to measure the efficiency for E2\_SHT22. In this case one can get events where the E2\_SHT22 trigger may not have fired because it was prescaled. But one will end up selecting all the events where E1\_SH30 fired for the tag. The measured trigger efficiency will be lower than the actual trigger efficiency, ignoring the effect of prescales. This situation is not remedied even if one allowed multiple triggers to fire the tag condition. To solve the problem of a trigger being prescaled biasing our measurement, one has to make an OR of triggers where one of them is required to be un-prescaled all the time. The luminosity of the sample is then defined by this un-prescaled trigger. We then take the prescales of the other triggers into account in our efficiency measurement rather than using the luminosity system. By measuring the ‘OR’ed efficiency on the exact running period our signal sample is derived from, automatically weight each trigger appropriately by its relative exposure. This includes the effects of correlations and the prescales. The condition on the tag will match the condition the probe has to pass. This guarantees that the biases from our selection are negligible.

If one intends to use these efficiencies, the user has to be aware of the following requirements:

- One must only analyse LBN’s where the “un-prescaled trigger” is un-prescaled. Otherwise there will be some bias in their normalisation.
- One must match objects at each trigger level to the offline object since this is done during the efficiency measurement. This will actually lead to a slightly lower efficiency since the cuts are then slightly tighter but guarantees that there is no bias.
- One cannot take the individual single trigger efficiencies and merge them without knowing the relative exposures of the triggers and their correlations.

### 7.3 Jet Reconstruction Efficiency

#### 7.3.1 Jet Energy Scale Correction

The precise measurement of the four-momenta of the final state particles arising from the hard scatter before they interact with the detector is a challenging task. This is especially true for jets at  $D\emptyset$ , due to the presence of four radiation lengths of detector material that separates the interaction region from the calorimeter system. The modification of the calorimeter electronics to accommodate the short bunch spacing of the Tevatron beam (396 ns) affects the degree of compensation of the calorimeter. This leads to systematic effects that contribute to the discrepancy between the measured jet energy and the energy of particle level jets. The goal of the jet energy scale correction is to determine the energy of stable-particle-level jets before they interact with the  $D\emptyset$  detector, by applying corrections to the measured jet energy [101]. The corrected jet energy of the final state partons before interaction with the detector is given by the Eq. 7.3 in terms of five quantities, described below:

$$E_{jet}^{corr} = \frac{E_{jet}^{uncorr} - O}{F_{\eta} \times R \times S} \quad (7.3)$$

- Uncorrected jet energy,  $E_{jet}^{uncorr}$

This is the energy of the jet determined by the jet reconstruction algorithm. Jets are reconstructed using the Run II cone algorithm [103] using a cone of radius  $\Delta R = 0.5$  or  $0.7$ . The jets are required to have a minimum transverse energy of 6 GeV applied to both the particle level jets and the reconstructed calorimeter level towers (calorimeter jets).

- Offset energy correction,  $O$

Offset energy is defined as the energy in the calorimeter from sources not related to the physics processes that lead to the formation of jets. Some of the sources include:

- The underlying event (beam remnants and multiple parton interactions).
- Radioactive noise from the decay of uranium in the calorimeter absorber plates.
- Electronics noise and the pile-up energy left over from previous beam crossings.
- Multiple interactions (soft or semi-hard) in the same bunch crossing.

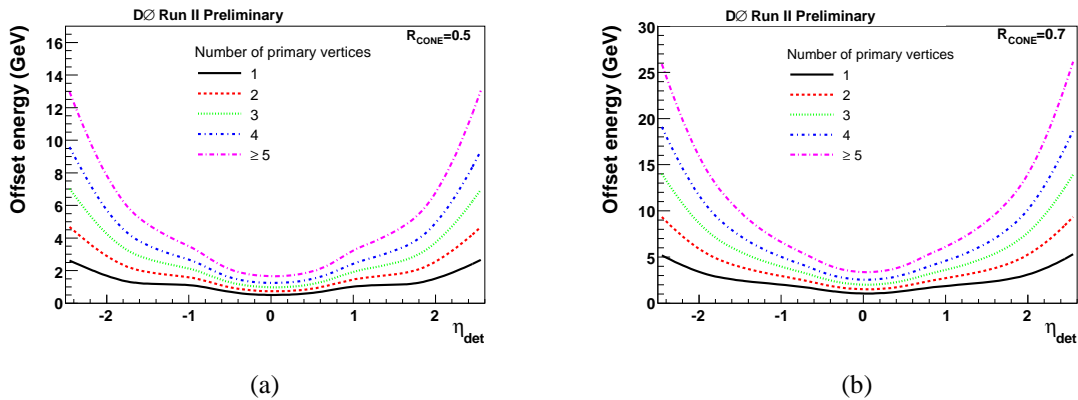


Figure 7.7. Offset energy correction is shown as a function of jet pseudorapidity for  $\Delta R = 0.5$  (a) and  $0.7$  (b) cone jets. It is measured by adding the estimated energy density of all the calorimeter towers within the cone. Correlation of offset energy with different primary vertex multiplicities is also shown.

The energy density in each tower is measured using minimum bias events with the assumption that all offset energy contributions listed above are present in this measurement. At higher instantaneous luminosity there is a possibility of many primary vertices, and the dependence of offset energy on the instantaneous luminosity is taken into account by performing the measurement with different primary vertex multiplicities. The offset energy as a function of jet pseudorapidity from the center of the detector is shown for cone size  $\Delta R = 0.5$  in Fig. 7.7(a) and  $\Delta R = 0.7$  in Fig. 7.7(b) for different primary vertex multiplicities ranging from one to five or more vertices.

- Relative response correction,  $F_\eta$

The gap between central and end cryostats is not very well instrumented, causing a non-uniformity in response as a function of pseudorapidity. The relative response correction (also called the  $\eta$ -intercalibration) is designed to correct the non-uniformities in the DØ calorimeter between the central (CC) and the endcap (EC) regions. The non-uniformity in response is expected to be the largest in the gap region that separates the CC and EC cryostats ( $0.5 < |\eta| < 1.8$ ). The relative response correction is measured using the *missing transverse energy projection fraction* (MPF) method with samples of photon+jet ( $\gamma$ +jet) and dijet events as illustrated in Fig. 7.8. This method [100] is based on two-body process where the incoming partons

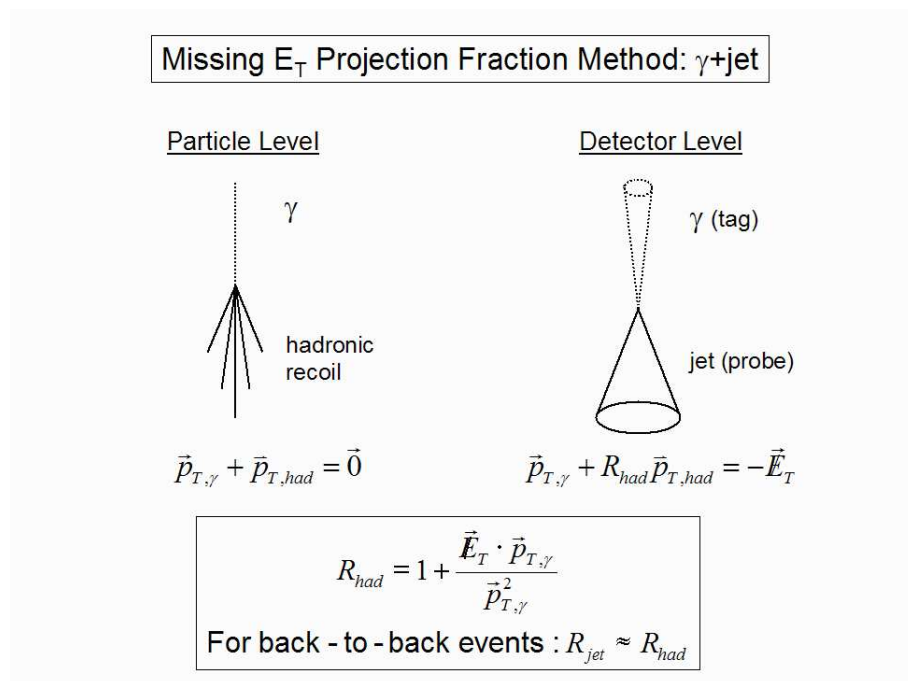


Figure 7.8. Diagram illustrating the  $\cancel{E}_T$  projection fraction method.

produce a direct photon and a jet. Since the initial state partons are traveling along the beam

axis with negligible transverse momenta, the momentum conservation can be applied to the outgoing photon and hadron (jet) ignoring the effects of hadronization, to yield:

$$\vec{p}_{T\gamma} + \vec{p}_{T\text{had}} = 0 \quad (7.4)$$

The calorimeter energy response to the photon,  $R_{em}$ , which is primarily an electromagnetic object, and hadronic response to the recoiled jet,  $R_{had}$  are different and hence they lead to an imbalance in transverse momentum, *i.e.*,  $\cancel{E}_T$ :

$$R_{em} \vec{p}_{T\gamma} + R_{had} \vec{p}_{T\text{had}} = -\cancel{E}_T \quad (7.5)$$

The EM response correction to  $\vec{p}_{T\gamma}$  changes the energy content of the measured energy of the photon, and hence necessitates a correction to the  $\cancel{E}_T$ . By adding  $(1 - R_{em})\vec{p}_{T\gamma}$  to both sides of Eq. 7.5 and using this quantity together with Eq. 7.4 we obtain:

$$\vec{p}_{T\gamma} + R_{had} \vec{p}_{T\text{had}} = -\cancel{E}_T^{EMcorr} \quad \text{where} \quad \cancel{E}_T^{EMcorr} = \cancel{E}_T - (1 - R_{em})\vec{p}_{T\gamma} \quad (7.6)$$

by projecting the  $\cancel{E}_T$  vector along the direction of the photon, we can obtain the expression for hadronic response:

$$-\vec{n}_{T\gamma} \cdot \cancel{E}_T^{EMcorr} = -\vec{n}_{T\gamma} \cdot (\vec{p}_{T\gamma} + R_{had} \vec{p}_{T\text{had}}) = p_{T\gamma} + R_{had} p_{T\text{had}} \quad (7.7)$$

$$\Rightarrow R_{had} = 1 + \frac{\cancel{E}_T^{EMcorr} \cdot \vec{n}_{T\gamma}}{p_{T\gamma}} = 1 + MPF \quad (7.8)$$

where MPF is the definition of  $\cancel{E}_T$  projection fraction, and this method of determining the hadronic response bears the same name. Figure 7.8 illustrates the method outlined above.

The tag object (a photon in the case of  $\gamma$ +jet) is required to be in  $|\eta_D| < 0.5$ , and back-to-back in azimuth ( $\varphi$ ) with a jet which can be anywhere in the pseudorapidity. Assuming perfect measurement of the photon energy, any  $E_T$  imbalance in the event is due to the effect of response. The  $E_T$  imbalance is projected in the direction of the tag object, as illustrated in Fig. 7.8. Corrections are obtained as a function of the tag object's transverse momentum. A similar approach is used in dijet events with two jets back-to-back in azimuth and one of them serving as the tag. The results from the two samples are combined to obtain more precise values of the response correction in the complete kinematic range. The relative response correction is shown in Fig. 7.9 as a function of  $\eta_D$  for 25, 100, 250 and 500 GeV jet  $E_T$ . The response corrections are large for the ICD region ( $0.8 < |\eta_D| < 1.4$ ) because of the uninstrumented region between the central and end calorimeter cryostats. Some of the energy of high  $p_T$  jets cannot be contained completely in the hadronic calorimeter, and hence the relative response corrections are large for high  $p_T$  ( $> 250$  GeV) jets.

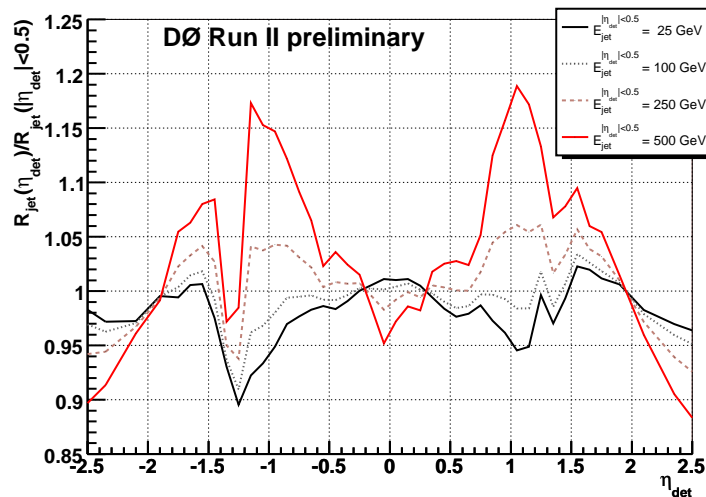


Figure 7.9. Combined relative response correction of the corrected probe jet energy as a function of pseudorapidity for jets with  $p_T = 25, 100, 250$  and  $500$  GeV [101].



- Absolute response correction,  $R$

The absolute energy response is defined as the ratio of the measured energy of the jet to the true energy deposited in the calorimeter. The absolute energy response is generally less than 100%, due to uninstrumented regions and dead material in the calorimeter. The absolute response correction ( $R$ ) accounts for energy lost in the uninstrumented regions of the detector as well as the lower energy response of the calorimeter to hadrons compared to electrons and photons. This correction is determined on photon+jet samples using the MPF method after applying offset and relative response corrections. Fig. 7.10 shows the absolute energy response for different pseudorapidity regions. The response in the CC and EC regions are consistent after applying the relative response term.

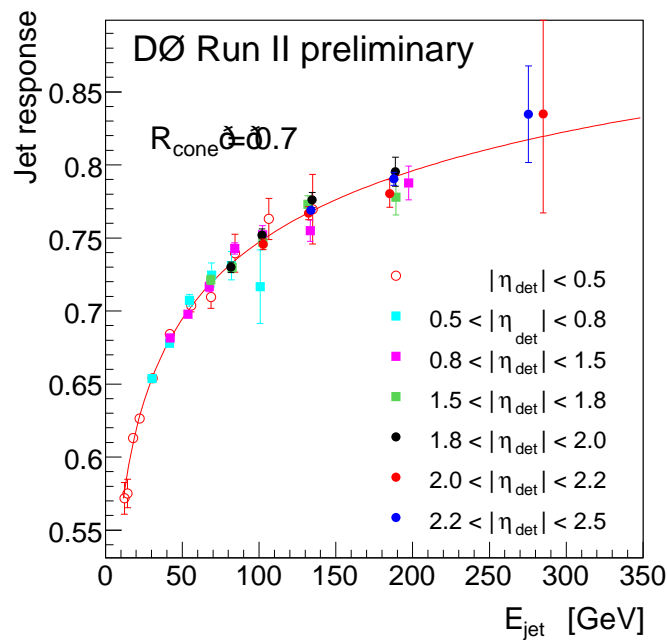


Figure 7.10. Absolute energy response of  $\Delta R = 0.7$  jets as a function of jet energy, obtained after offset and relative response corrections. The different markers show different  $\eta$  regions, and a global fit to all points (red curve) gives the parameterization for the absolute response [101].

- Showering correction, S

The showering correction (S) is less related to the instrumental effects unlike the other corrections, instead it is a consequence of jet formation and hadronization. This term corrects for energy deposition outside the cone radius of the reconstructed jet or additional energy deposits within the cone radius as a result of spurious particles in the calorimeter. The amount of correction is estimated by looking at the total energy deposited in concentric cones about the jet axis, with the cone radii varying from 0.1 to 2.0. This is called the *shower profile* and is used to find the amount of energy outside the cone, correlated to that measured inside the cone. The correction is parameterized as a function of jet energy and is shown in Fig. 7.11

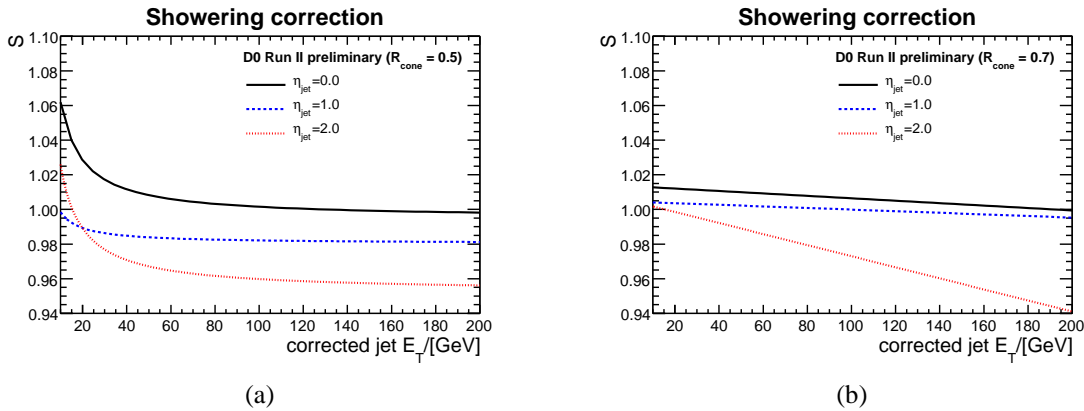
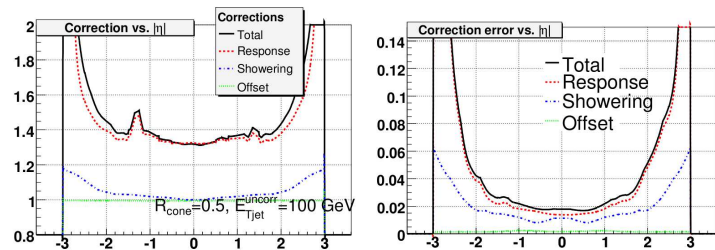


Figure 7.11. Showering correction as a function of jet transverse energy for  $\Delta R = 0.5$  (a) and  $\Delta R = 0.7$  (b) [101].

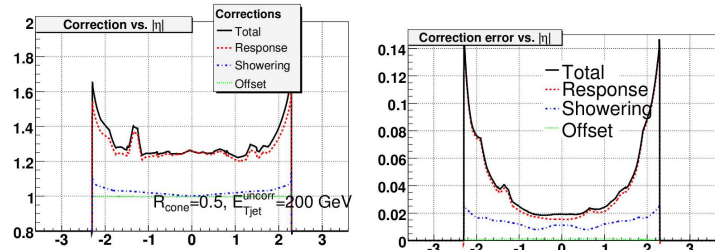
- Total Jet Energy Scale Corrections and Uncertainties

The total jet energy scale correction factors  $f_{JES}$  are obtained using Eq. 7.9

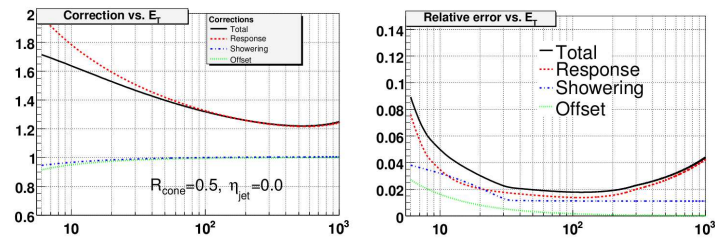
$$f_{JES} = \frac{E_{jet}^{corr}}{E_{jet}^{uncorr}} = \frac{1}{E_{jet}^{uncorr}} \times \frac{E_{jet}^{uncorr} - O}{F_{\eta} \times R \times S} \quad (7.9)$$



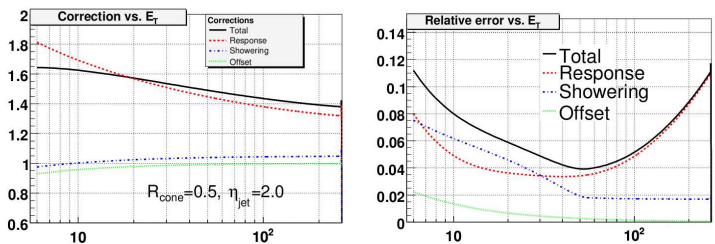
(a)



(b)



(c)



(d)

Figure 7.12. Jet energy scale corrections (left column) and relative jet energy scale uncertainties (right column) for  $\Delta R = 0.5$  jets in data as a function of pseudorapidity (a) for  $E_T = 100$  GeV and (b) for  $E_T = 200$  GeV and as a function of transverse energy (c) for  $\eta = 0.0$  and (d) for  $\eta = 2.0$ . The corrections decrease with increasing jet transverse energy, and the uncertainty is larger for low energy ( $E_T < 15$  GeV) as well as high energy ( $E_T > 100$  GeV) jets. The corrections are relatively flat (30-40%) for  $\eta < 2.0$  and increase rapidly thereafter. The corrections and uncertainties in the intercryostat region shows a bumpy structure with larger values [102].

The total jet energy scale corrections and their uncertainties as a function of two different jet pseudorapidities and jet transverse energies are shown in Fig. 7.12. Relative jet energy scale corrections are typically around +30% to +45% for data. The total uncertainty in jet energy scale corrections is about +2% to +5% which is dominated by systematic uncertainties. The main sources of uncertainty are luminosity dependent effects, variations from tighter primary vertex requirements, errors from the fits used to parameterize the corrections and differences observed when dijet data is used instead of  $\gamma$ +jet data when estimating corrections.

### 7.3.2 Jet ID Efficiency in Data

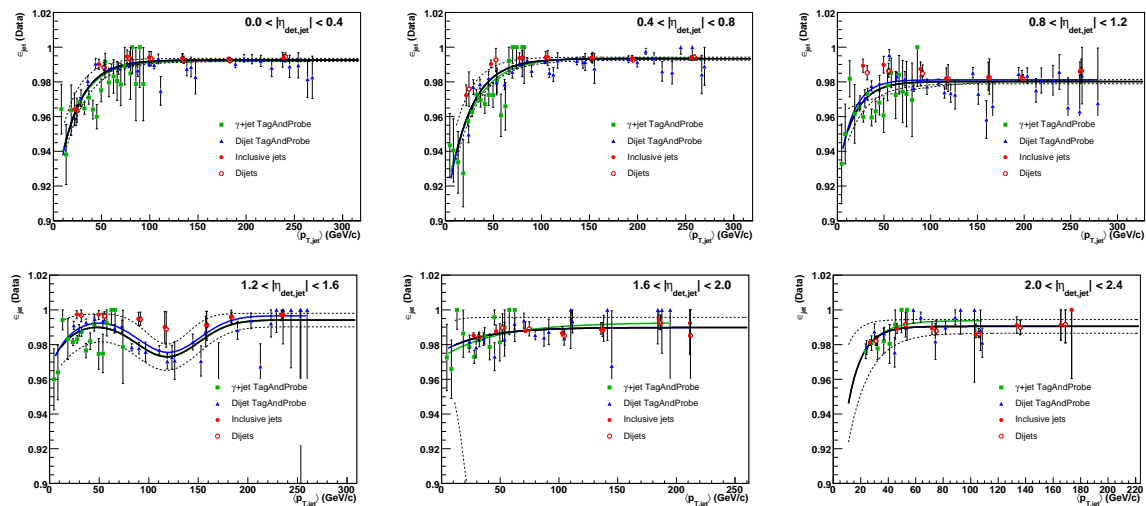


Figure 7.13. Jet ID efficiencies in data combined from tag and probe methods in dijet and  $\gamma$ +jets samples are shown as a function of  $p_T$  of the jet for different pseudorapidity regions. The green line shows the fit to tag and probe results, the blue line the fit to all results and the black line the preferred fit of the two [105].

The Jet ID efficiency is estimated for the basic selection criteria applied to jets, *i.e.* the electromagnetic fraction (EMF), coarse hadronic fraction (CHF) and L1 confirmation for jets reconstructed with the Run II cone algorithm ( $\Delta R = 0.5$ ).  $\gamma$ +jet events are chosen for study

with stringent selection criteria for the photon, which serves as the tag. The probe is a jet being studied to determine the efficiency. The jet is back-to-back in  $\varphi$  with the photon. To estimate the efficiency two methods are used. The first method is a ‘counting’ method which gives the efficiency of each cut based on the number of events that survive that cut. For example, the efficiency for the EMF cut,  $\epsilon_{EMF}$  is the ratio of the number of events that pass the EMF cut the total number of candidate events. The second method is a ‘fit’ method that extrapolates the fit to the distribution of each variable into the cut region, and the area under that region below the fit gives the fraction of events that are removed by that cut. The overall jet ID efficiency is estimated as a product of the efficiency of each cut [105] as given in Eq. 7.10, and the systematic uncertainties are assigned using the difference between the fit method and the counting method. The Jet ID efficiency is also derived from inclusive jet and dijet samples in a similar way and the results are combined.

$$\epsilon_{jetID} = \epsilon_{emf} \cdot \epsilon_{chf} \cdot \epsilon_{L1} \quad (7.10)$$

The Jet ID efficiency in data is shown as a function of jet  $p_T$  for the CC, EC and ICR regions in Fig. 7.13. The results show good agreement in the CC and EC regions between the two methods and the different data samples used for study. The ICR region shows a slight discrepancy due to the fact that the L1 confirmation in this region is not measured well [105]. Hence the fit is replaced with 50% signal and 50% background with  $\epsilon = 1 - (1 - \epsilon_{L1})/2$ . The fit is parameterized using  $\epsilon(p_T) = p_0 + p_1 \exp(-p_2 \cdot p_T)(1 - \text{gaus}(p_3, p_4, p_5))$ .

### 7.3.3 Jet Smearing, Shifting and Removal

Jets produced in MC simulations (following event generation, full detector simulation and reconstruction) exhibit an overestimation of jet energy resolution, jet energy scale and reconstruction efficiency. The primary reason for this is the limitation in the modeling of the  $D\emptyset$

detector. The simulation output is modified to match the performance observed in data using the Smearing, Shifting and Removal (SSR) method [104]. This method applied to simulated jets accounts for the relative differences in jet resolution, energy scale and efficiencies between data and MC.  $\gamma$ +jet events are chosen with stringent selection cuts on the photon. The jet is required to be back to back in  $\varphi$  with the photon. A variable known as  $p_T$  imbalance ( $\Delta S$ ) is used in studying the relative differences between data and MC; its definition is given in Eq. 7.11. The difference in mean values of  $\Delta S$  between data and MC provides a measure of the relative difference in jet energy scale.

$$\Delta S = \frac{p_T^{jet} - p_T^\gamma}{p_T^\gamma} \quad (7.11)$$

$$\mathcal{D} = \langle \Delta S \rangle_{data} - \langle \Delta S \rangle_{MC}$$

The  $p_T$  imbalance is determined in several regions of the photon  $p_T$  spectrum, and the differences between data and MC are de-convoluted by fitting Gaussian to the  $\Delta S$  distributions, multiplied by turn-on curves (described by error functions), as given in Eq. 7.12.

$$f_{\Delta S} = A_0 \times \left\{ 1 + \operatorname{erf} \left( \frac{\Delta S - A_1}{\sqrt{2}A_2} \right) \right\} \times \exp \left\{ - \frac{(\Delta S - \Delta S_0)^2}{2\sigma_{\Delta S}^2} \right\} \quad (7.12)$$

$$\sigma_{\Delta S} = \sigma_{p_T}/p_T^\gamma \quad \dots \text{(transverse energy resolution)} \quad (7.13)$$

These fits provide information about the jet energy scale, jet energy resolution and the reconstruction and ID efficiencies. The central value of the Gaussian,  $\Delta S_0$  describes the relative jet energy scale. The width of the Gaussian ( $\sigma_{\Delta S}$ ) describes the relative jet energy resolution and the turn-on curve (with constants  $A_1$  and  $A_2$ ) describes the jet reconstruction and ID efficiencies. To correct for the difference in jet energy resolution, the jet  $p_T$  is first smeared by

a Gaussian with width  $\sigma_{smear} = \sqrt{\sigma_{\Delta S,data}^2 - \sigma_{\Delta S,MC}^2}$ . The smearing factor is shown as a function of photon  $p_T$  for the CC, EC and ICR in Fig. 7.14

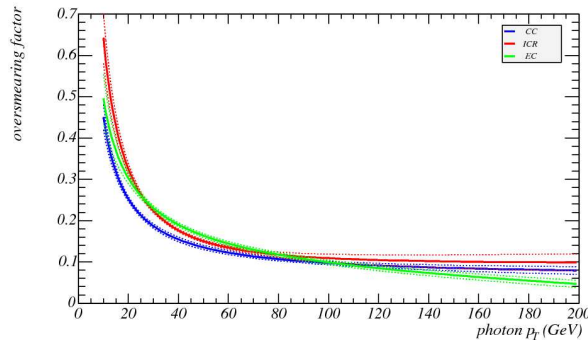


Figure 7.14. The smearing factor applied to correct the  $p_T$  of MC jets is shown for the CC, EC and ICR regions [104].

To account for the relative jet energy scale difference, the jets are smeared with a parameterization obtained for the variable  $\mathcal{D}$ , which describes the amount of shift in  $p_T$  imbalance between data and MC.  $\mathcal{D}$  was found to be negligible, indicating that shifting is not necessary [104]. The average turn-ons are shown for data and MC in Fig. 7.15 as a function of jet  $p_T$  for different detector regions. A suitable  $p_T$  cut to apply to jets below which they are discarded (removed) is determined as 15 GeV which is region where the jet ID efficiencies reach a plateau. If the generated jet  $p_T$  is below this value, it is removed from the event.

#### 7.3.4 Jet ID Efficiency in MC

The jet ID efficiency for MC is obtained using the same procedure as described in section 7.3.2. The SSR method is first applied to simulated  $\gamma$ +jet and dijet samples. The efficiency is shown in Fig. 7.16 as a function of the jet  $p_T$  for different pseudorapidity regions. The ratio of the data and MC efficiency is applied as a scale factor to correct the simulated jets in this analysis. The scale factors are shown for all pseudorapidity regions in Fig. 7.17.

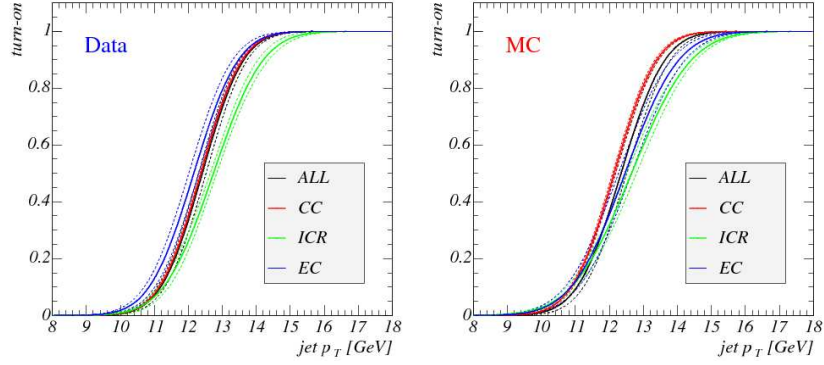


Figure 7.15. Turn-on curves describing the jet ID efficiency in data (left) and MC (right) for various pseudorapidity regions as a function of jet  $p_T$ . Solid lines indicate the different regions (red for CC, green for ICR, blue for EC and black for all regions) and dotted lines indicate the statistical errors. They reach a plateau around 15 GeV [104].

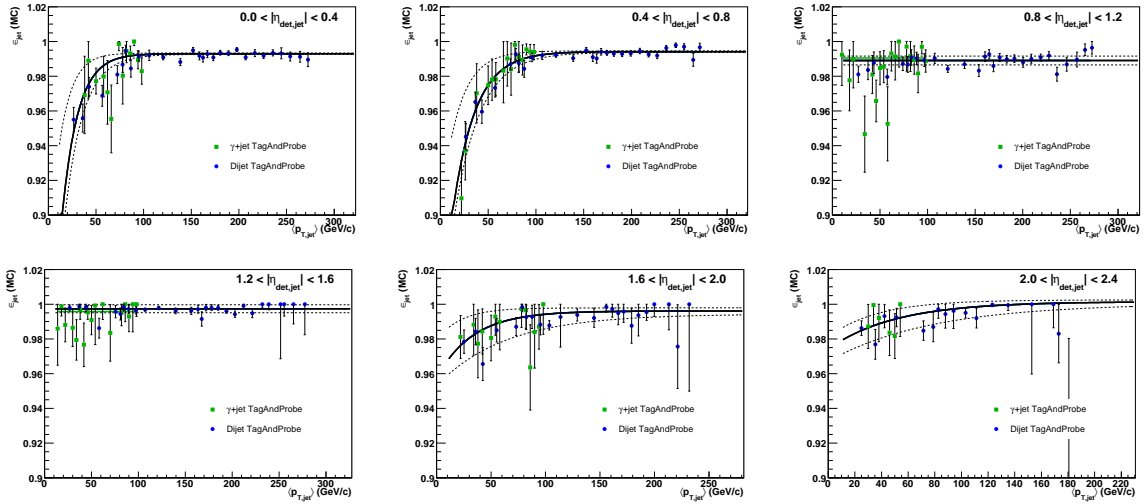


Figure 7.16. Combined JetID efficiencies from tag-and-probe methods in dijet and  $\gamma$ +jets samples. The green line shows the fit to tag-and-probe results, the blue line the fit to all results and the black line the preferred fit of the two. The  $\chi^2/ndf$  and parameters are shown for the black curve [105].

#### 7.4 Recalculation of $\cancel{E}_T$

$\cancel{E}_T$  is computed in the transverse plane by vectorial addition of the positive cell energies in the calorimeter such that there is no net transverse momentum in the event. The  $E_T$  of cells is summed in several stages using each calorimeter subdetector, *i.e.*, the electromagnetic



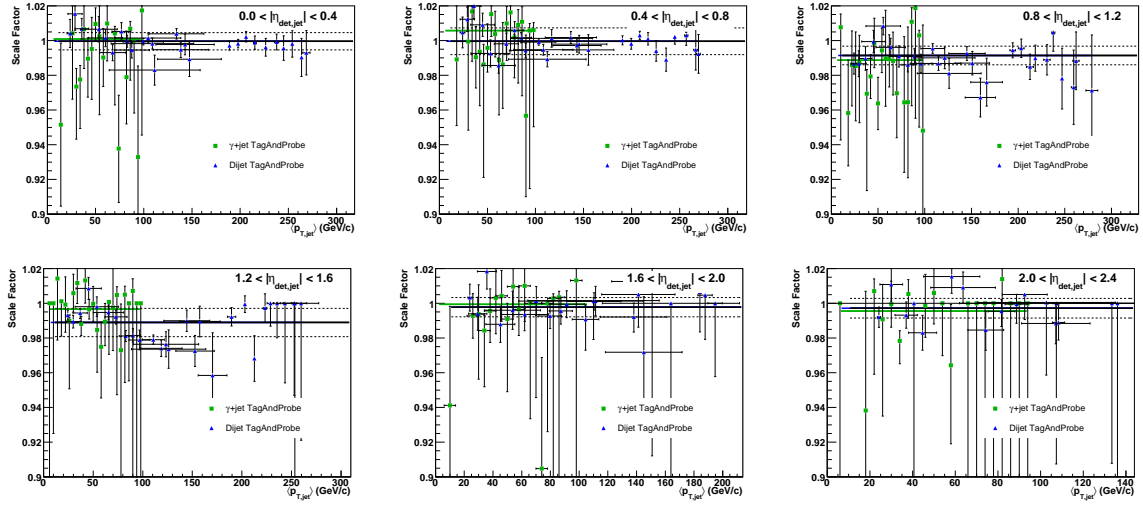


Figure 7.17. Scale factors for correcting MC events for various pseudorapidity regions. The green line shows the fit to tag-and-probe results, the blue line the fit to all results and the black line the preferred fit of the two. The  $\chi^2/ndf$  and parameters shown for the black curve [105].

(EM), fine hadronic (FH), coarse hadronic (CH), intercryostat detector (ICD) and massless gap (MG) detectors [106]. It can be expressed as in Eq. 7.14. Cells in the coarse hadronic section are noisy resulting in a poorer  $\cancel{E}_T$  resolution. to deteriorate. Therefore, the term  $\overrightarrow{ME}_T^{CH}$  is omitted from the sum [107]. However, since the coarse hadronic fraction  $f_{CH}$  is an important component in measuring the energy of jets,  $\cancel{E}_T$  is corrected to to account for this omission.

$$\overrightarrow{E}_T^C = \overrightarrow{E}_T^{EM} + \overrightarrow{E}_T^{FH} + \overrightarrow{E}_T^{CH} + \overrightarrow{E}_T^{ICD} + \overrightarrow{E}_T^{MG} \quad (7.14)$$

Muons are minimum ionizing particles that deposit small amount of energy in the detector, and can sometimes lead to fake  $\cancel{E}_T$ . The measured energy of the muons is subtracted from the  $\cancel{E}_T$  to account for this difference. The EM energy scale corrections (for electrons and photons) and jet energy scale for good jets alter the net  $\cancel{E}_T$  in the event. Therefore corrections are propagated to  $\cancel{E}_T$  after the EM and jet energy scale corrections.

## 7.5 $b$ -tagging Efficiency

The MC simulation of the tracking detector at DØ and the performance of tracking algorithms do not fully describe the real data. The tracking is overly optimistic in both the quality and number of tracks found in an event, which leads to an over estimation of  $b$ -jet tagging efficiency in MC compared to data by about 15-20% [109]. Hence  $b$ -tagging is applied to data and MC differently.

### 7.5.1 TRF and TSF Methods

Two equivalent approaches to tagging MC jets are discussed here. The first method is to calculate the overall probability of tagging a subset of jets in a MC event based on the so called Tag Rate Functions (TRF). This method is referred to as the TRF method in the following sections. The second (equivalent) approach is to directly tag the jets in the MC events as though they were real data, but apply a scale factor called the Tagging Scale Factor (TSF) to correct for the tagging difference between data and MC. This method is referred to as the TSF method in the sections to follow. The main distinction between the TRF and TSF methods is that the former does not tag MC jets directly, but provides an overall event probability of the jets being tagged, whereas the latter tags the MC jets and applies a correction factor (event weight) which accounts for the difference in MC and data.

### 7.5.2 Tag Rate Functions (TRF)

The probabilities for the NN algorithm to identify (or tag) a  $b$ -jet, charm-jet or light flavor jet are measured using data and are called the the Tag Rate Functions (TRF). The TRFs corresponding to  $b$ ,  $c$  and light jets are, respectively,  $TRF_b$ ,  $TRF_c$  and  $TRF_l$ . The probability

that a jet is tagged in an event is given by the product of its taggability (described in section 5.8) and the tag rate function, where  $\epsilon_{taggability} \in \{0, 1\}$

$$P_{jet}(\vec{x}) = \epsilon_{taggability} \times TRF(\vec{x}) \quad (7.15)$$

This can be extended to calculate an overall probability that a subset of a total of N-jets in an event are tagged. For example, the equations below give the probability of one/two out of N-jets being tagged. Denoting the probability of tagging one jet as  $P_{1tag}(\vec{x})$  and that of tagging two jets as  $P_{2tags}(\vec{x})$ , we obtain:

$$P_{1tag}(\vec{x}) = \sum_{i=1}^N P_{tag}(x_i) \prod_{i \neq j} (1 - P_{tag}(\vec{x}_j)) \quad (7.16)$$

$$P_{2tags}(\vec{x}) = \sum_{i=1}^N P_{tag}(x_i) \sum_{j \neq i}^N P_{tag}(x_j) \prod_{k \neq i \neq j} (1 - P_{tag}(\vec{x}_k)) \quad (7.17)$$

- Determination of TRF

A system of eight equations with eight unknowns (which include the NN  $b$ -tagging efficiency  $\epsilon_{b \rightarrow \mu}^{DATA}$ , as one of the unknowns) is constructed [110] by equating the number of tags found by two uncorrelated tagging algorithms (NN and SLT) on two different data samples having different  $b$ -jet contents. The first sample has relatively less  $b$ -content by requiring at least one muon with  $p_T > 4$  GeV inside a jet of  $\Delta R = 0.7$ . The second sample is a subset of the first, heavily  $b$ -enriched with one of the jets having a low impact parameter (JLIP) probability ( $< 0.01$ ), which indicates that the jet originated from a displaced secondary vertex, possibly from a semi-leptonic decay of the B-meson ( $B \rightarrow D\ell\nu$ ). The eight equations include the correlation between the two tagging algorithms, the tagging efficiencies for  $b$ ,  $c$  and light quark jets as well as the number of tags found by the two algorithms.

To estimate the tagging differences between the data and MC, the  $b$ -jet tagging efficiency ( $\epsilon_{b \rightarrow \mu}^{\text{MC}}$ ) is also measured. The ratio of these two efficiencies is a scale factor (SF) which provides a measure of the variation in tagging rate caused by these differences. The efficiencies and scale factors are parameterized as a function of detector pseudorapidity and jet  $p_T$ .

$$SF_{b \rightarrow \mu}(p_T, \eta) = \frac{\epsilon_{b \rightarrow \mu}^{\text{DATA}}}{\epsilon_{b \rightarrow \mu}^{\text{MC}}} \quad (7.18)$$

The above scale factor is derived only for semi-leptonic decays, but it is assumed that the same scale factor can be applied to *any* MC efficiency (for example an inclusive decay  $B \rightarrow X$ ) to account for the differences in data and MC. Any effects of this assumption on the  $b$ -tagging of MC are assumed to be small [91]. This allows one to define an inclusive  $b$ -jet TRF as

$$TRF_b(p_T, \eta) = \epsilon_{b \rightarrow \text{INC}}^{\text{MC}} \times SF_{b \rightarrow \mu}(p_T, \eta) \quad (7.19)$$

Similarly, one may define an inclusive  $c$ -jet TRF by including an additional scale factor for the relative inclusive  $c$ -jet to  $b$ -jet efficiency in MC:

$$TRF_c(p_T, \eta) = TRF_b(p_T, \eta) \times \frac{\epsilon_{c \rightarrow \text{INC}}^{\text{MC}}}{\epsilon_{b \rightarrow \text{INC}}^{\text{MC}}} \quad (7.20)$$

The NN  $b$ -tagging efficiency corresponding to the *oldLoose* operating point is shown as a function of jet  $p_T$  and detector pseudorapidity in Fig. 7.18(a). The average efficiencies for data is  $\sim 64\%$  and for MC  $\sim 68\%$  and show a minor dependence on jet  $p_T$  in the lower  $p_T$  region ( $p_T < 30$  GeV/c). The systematic errors are indicated by the black dotted lines. The scale factor is the ratio of the data to MC efficiencies and is shown in solid blue. A similar  $p_T$  dependence can be observed for *Tight* operating point in Fig. 7.18(b), but the corresponding efficiencies are slightly lower, *i.e.*,  $\sim 52\%$  in data and  $\sim 58\%$  in MC.

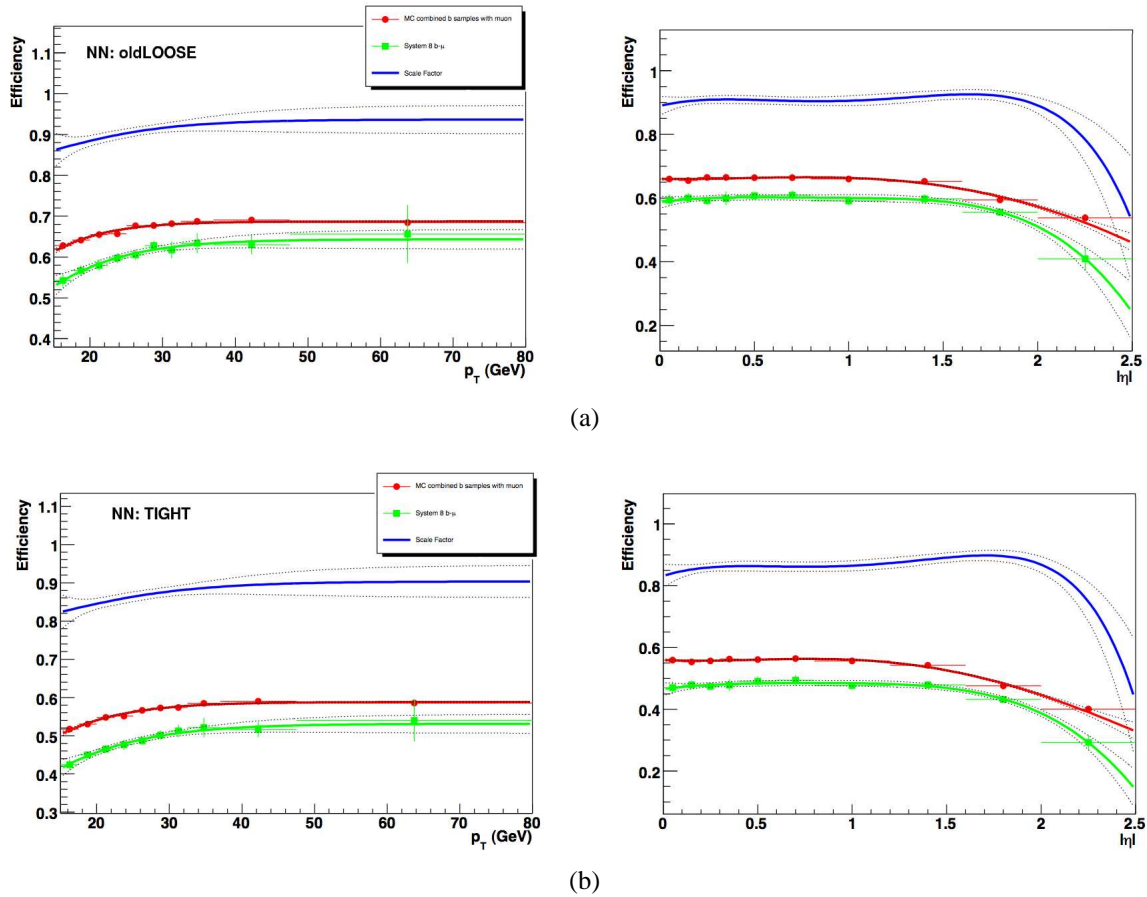


Figure 7.18. NN tagger  $b$ -jet efficiency as a function of  $p_T$  (left) and  $\eta_D$  (right) for oldLoose (top) and tight (bottom) operating points. The red (green) markers correspond to MC (data) and the corresponding curves are the best fit. The blue curve is the scale factor and the black dotted curves indicate the systematic uncertainties of  $b$ -tagging.

The  $\eta_D$  dependence of  $b$ -tagging efficiency for both operating points show a flat behavior for central region and the efficiencies drop significantly at forward pseudorapidity ( $|\eta_D| > 2.0$ ) because of poor tagging efficiency and jet identification, which affect the taggability. The average efficiencies for data and MC are  $\sim 60\%$  and  $\sim 65\%$  respectively for *oldLoose* operating point. The corresponding efficiencies for *Tight* operating point are  $\sim 48\%$  and  $\sim 55\%$  respectively. The tagging efficiencies and scale factors are summarized in Table. 7.3.

Table 7.3. Average  $b$ -tagging efficiencies for oldLoose and Tight operating points as a function of jet  $p_T$  and  $\eta_D$  are shown for data and MC. The ratio of the data to MC is used to obtain the scale factors, which are used to correct the MC efficiencies to match the data.

Avg. Efficiency	oldLoose (%)		Tight (%)	
	$p_T$	$\eta_D$	$p_T$	$\eta_D$
data	64	60	52	48
mc	68	65	58	55
scale factor	94	92	90	87

### 7.5.3 Taggability Scale Factor (TSF)

The taggability of jets in data and MC are shown as a function of detector pseudorapidity in Fig. 7.19(a), and of transverse momentum in Fig. 7.19(b), along with the scale factors (ratio of taggability in data to MC). The taggability in data and MC and the corresponding scale factors show a similar behavior to the  $b$ -tagging efficiency. As a function of jet  $p_T$  they show a slight dependence in the lower  $p_T$  region and reach a plateau. As a function of  $\eta_D$  they are flat in the region, *i.e.*,  $|\eta_D| < 1.5$  beyond which they drop rapidly due to poor jet identification and tracking in the forward pseudorapidity region.

The taggability criteria discussed in section 5.8 is different for data and MC jets. In order to use taggability in the TSF method, it is necessary to determine the taggability rate for data and MC. The taggability of jets in data and MC is determined as a function of jet  $p_T$  and  $\eta$  by the ratio of the number of taggable jets to the total number of jets in the sample:

$$\epsilon_{\text{taggability}}^{\text{DATA}}(p_T, \eta) = \frac{N_{\text{taggable}}^{\text{DATA}}(p_T, \eta)}{N_{\text{total}}^{\text{DATA}}(p_T, \eta)} \quad (7.21)$$

$$\epsilon_{\text{taggability}}^{\text{MC}}(p_T, \eta) = \frac{N_{\text{taggable}}^{\text{MC}}(p_T, \eta)}{N_{\text{total}}^{\text{MC}}(p_T, \eta)} \quad (7.22)$$

$$SF_{\text{taggability}} = \frac{\epsilon_{\text{taggability}}^{\text{DATA}}}{\epsilon_{\text{taggability}}^{\text{MC}}} \quad (7.23)$$

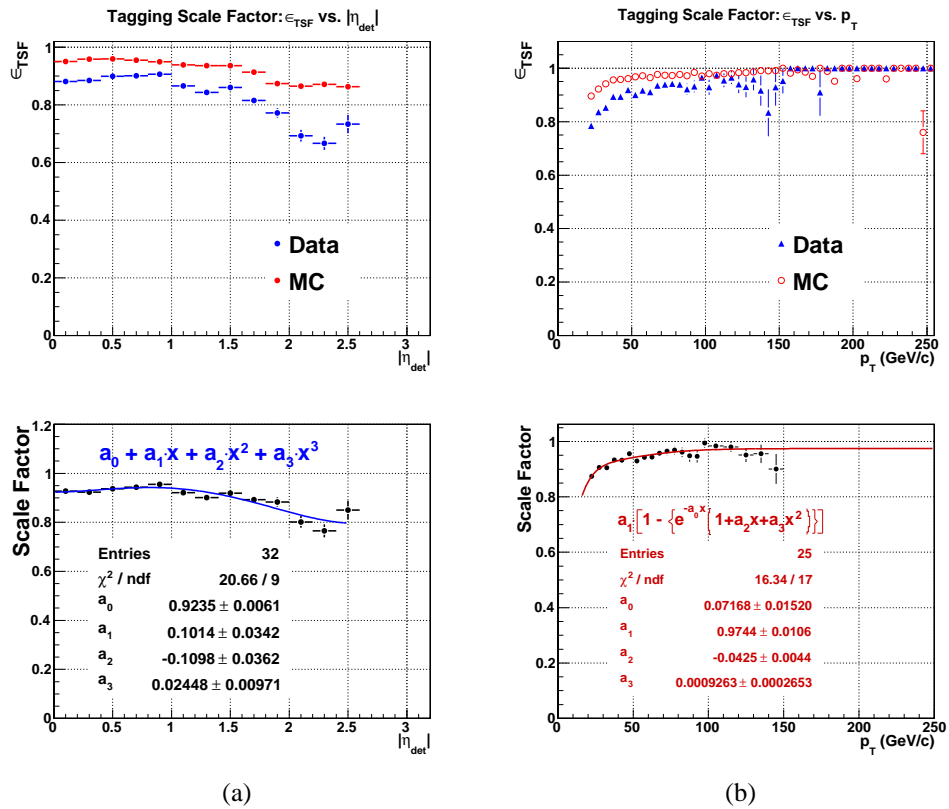


Figure 7.19. Taggability scale factors as a function of  $\eta_D$  (left) and  $p_T$  (right) for data and MC (top) and the corresponding scale factors (bottom). The fit parameters and functional form are indicated for a fit to the scale factors.

The taggability and the tagging efficiency are applied to data and MC, which is described in section 8.7.1.

## CHAPTER 8

### DATA ANALYSIS

The DØ collaboration has previously published a search for  $WH$  associated production in the  $e\nu b\bar{b}$  decay channel using  $174 \text{ pb}^{-1}$  of integrated luminosity [111]. An update of that result, using the  $e\nu b\bar{b}$  and  $\mu\nu b\bar{b}$  decay channels and a larger dataset of  $0.4 \text{ fb}^{-1}$  is under review for publication [112]. The CDF collaboration has published a similar search based on  $320 \text{ pb}^{-1}$  of data [113] and recently presented an update of the search with  $0.9 \text{ fb}^{-1}$  of data [114]. The analysis results presented here correspond to a total of  $1.04 \text{ fb}^{-1}$  of Run IIA data recorded by DØ experiment. Event selection criteria, search optimization and comparisons of data and background expectations are presented in the following sections.

#### 8.1 Analysis Strategy

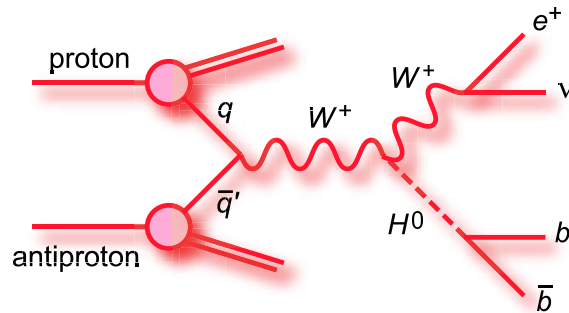


Figure 8.1. A leading order Feynman diagram showing the  $WH$  associated production. The Higgs decays into  $b\bar{b}$  pair while the  $W$  decays into a lepton and a neutrino .

The search strategy involves selecting candidate events corresponding to the process  $p\bar{p} \rightarrow WH \rightarrow \ell\nu b\bar{b}$ , as shown in Fig. 8.1. This event sample is labeled as  $W + 2 \text{ jets}$ . The



final state of interest (the signal) has a lepton *i.e.*, an electron or a tau ( $\ell = e$  or  $\tau$ , where the  $\tau$  decays in a leptonic mode), a neutrino ( $\nu$ ) which is inferred from missing transverse energy ( $\cancel{E}_T$ ) and two  $b$ -jets that originate from the  $b\bar{b}$  pair. The Higgs decays into two  $b$ -quarks which hadronize to form  $b$ -jets. The invariant mass of the dijet system is an important discriminant in the overall search strategy. Therefore  $b$ -tagging of jets is crucial to this analysis. Events with two or three jets with at least one of them  $b$ -tagged are considered in this analysis.

All Standard Model (SM) backgrounds and the signal processes are modeled using simulated data except for the multijet (QCD) background, which is estimated from real data. To achieve maximum search sensitivity, the  $W + 2$  jets analysis is separated into four disjoint subsets. Two of the subsets are based on  $b$ -tagging: events containing exclusively single  $b$ -tagged jet (exclusive single tag, EST analysis) and the other with two jets  $b$ -tagged (double tag, DT analysis). Based on the detector acceptance, the analysis is further divided into two disjoint sets: CC analysis and EC analysis. The CC (EC) analysis is based on event selection with an electron in the central (endcap) calorimeter. The dijet mass spectra from the four analyses (CC-EST, EC-EST, CC-DT and EC-DT analyses) are combined into a single search result. A control sample with an additional gluon jet in the final state, possibly radiated from a Higgs, is also considered for analysis. Accordingly, the control sample is labeled as  $W + 3$  jets.

## 8.2 Analysis Flow

Figure 8.2 indicates the different steps involved in the analysis chain. Collider data (labeled as RAW Data), which is stored on tape (indicated as SAM which stands for sequential access metadata) is first skimmed with a loose preselection (see section 8.4) in order to reduce the size of the dataset to a manageable proportion. The skimmed data is stored in thumbnail format (see section 6.1) and contains all the reconstructed objects for each event. The skimmed thumbnails are converted into a ROOT [93] format for user analysis.

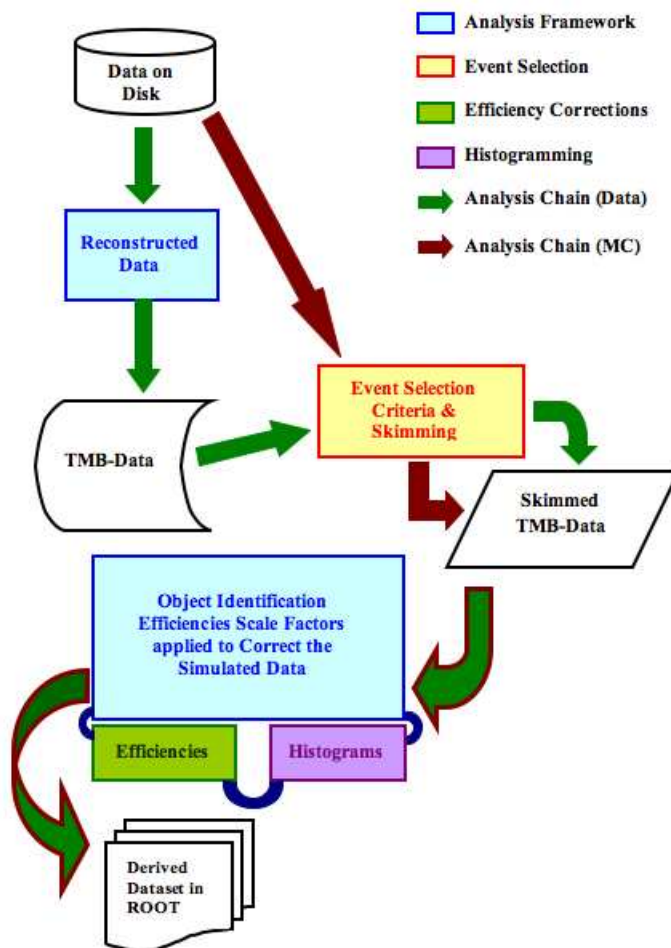


Figure 8.2. Analysis flowchart indicating the flow of data and simulated events from initial storage to analysis framework and subsequently into histograms for physics analysis.

Events are required to pass the data quality criteria (see section 8.3), following which the jet energy scale corrections (including the semi-leptonic corrections possibly due to the presence of muons in the jets) are applied to all the jets in the event. Electrons undergo energy scale and smearing corrections due to detector resolution effects. Jets that have an overlap with electron candidates with a  $\Delta R < 0.5$  are removed from the event. EM+Jet trigger based selection is performed as a next step following which  $\cancel{E}_T$  is recalculated. The tight event

selection criteria (refer section 8.4) is applied to select candidate events with one electron,  $\cancel{E}_T$  and exclusively two jets for  $W + 2$  jet analysis (exclusively three jets for  $W + 3$  jet analysis). NN  $b$ -tagging algorithm is applied to select the exclusive single tagged and double tagged events. These steps are performed as a part of the  $WH$  analysis framework shown in Fig. 8.2.

Simulated signal and background events (which have undergone full detector simulation and complete reconstruction) also have a similar flow as the collider data, except their object ID efficiencies, trigger efficiencies,  $b$ -tagging efficiencies are scaled (using the scale factors described in chapter 7) to reproduce the efficiencies of real data. They undergo the same event selection criteria and the steps involved in the  $WH$  analysis framework. All simulated signal and background events undergo identical event selection criteria as in data. Kinematic and geometric properties of electrons,  $\cancel{E}_T$  and jets are booked as histograms. QCD background is estimated using the loose and tight samples (will be discussed in section 8.5.6). The SM backgrounds are normalized to their cross sections except  $W +$  jets background which is normalized to the luminosity after subtracting all the other backgrounds from data (see section 8.6.1).

### 8.3 Data Quality

The data quality group [115] provides users with a list of runs and luminosity blocks (LBNs) that are flagged as *compromised* due to various reasons during data-taking. The runs and LBNs that are marked as corrupted by any of the calorimeter, SMT, CFT trackers, muon spectrometer and the luminosity system are removed before any selection criteria is applied. The `cal_event_quality` package [116] rejects events that are classified as bad for different running epochs. Some of the problems include ‘ring of fire, noon noise, missing crate and coherent noise’; the events corresponding to these epochs are removed. In addition, some of the luminosity blocks are not normalizable for a given trigger, which are eliminated from the

analysis. The percentage of events that are removed from the data set due to data quality issues is  $\sim 7\%$ .

## 8.4 Event Selection Criteria

### 8.4.1 Preselection Cuts

The RunIIA dataset ( $\sim 335$  million events), is the starting point for this analysis. Events are selected from the *EMinclusive* skim (see section 6.2 for definition) based on the *EMITRK* event flag. Additional selection criteria are applied to the EM object and jets — these referred as the preselection cuts:

- One calorimeter EM object with  $|ID| = 10, 11$  and transverse momentum  $p_T > 8$  GeV and a track with  $p_T > 5$  GeV matched to the EM object (*EMITRK* definition).
- EM Fraction:  $f_{EM} > 0.9$ .
- Isolation fraction:  $f_{iso} < 0.15$ .
- Seven-variable H-matrix  $\chi_{HM7}^2 < 50$ .
- Transverse momentum of the track matched to the EM cluster  $p_T^{trk} > 5$  GeV/c.
- $\chi^2$  probability of spatial track match  $> 0.0$ .
- Additionally the  $p_T$  of the EM object is required to be  $> 15$  GeV/c.
- At least two jets, each with  $p_T > 15$  GeV/c after jet energy scale corrections.

The total number of events passing the preselection cuts is  $\sim 590,000$  events.

### 8.4.2 Post-preselection Cuts

The event selection after preselection (post-preselection) is separated into two parts — the CC Analysis and the EC Analysis. The CC Analysis corresponds to the selection of events with an electron in the central region of the calorimeter (CC). In order to increase the acceptance, events having electrons in the forward region (end cap calorimeter region, EC) and the gap region situated between the central and the endcap calorimeter in the pseudorapidity range

$1.1 < |\eta_D| < 1.5$  (referred to as the ICD or gap region) are included in the analysis called the EC Analysis.

The post-preselection selection criteria is summarized below:

1. CC Analysis:

- Electron: The event must have exactly one reconstructed electron with a transverse momentum  $p_T > 15$  GeV/c within a pseudorapidity range  $|\eta| < 1.1$ .
- Missing transverse energy: Corrected  $\cancel{E}_T$  in the event is required to be  $> 20$  GeV.

2. EC Analysis:

- Electron: One reconstructed electron in the pseudorapidity region ( $1.1 < |\eta| < 3.0$ ) with  $p_T > 20$  GeV/c
- Missing transverse energy: Corrected  $\cancel{E}_T > 25$  GeV.

The selection criteria common to the CC and EC Analyses are given below:

- Jets: The jets used in this analysis are Run II cone type jets with a radius  $R = 0.5$ . All jets are required to pass the L1 confirmation (Eq. 5.18) in order to be considered for this analysis. In addition, the jets are required to satisfy all of the criteria explained in section 5.6. Events containing two or three jets with  $p_T > 25$  GeV/c for the leading jet and  $p_T > 20$  GeV/c for second and third jets are selected. The cuts are applied after their transverse momenta are corrected with the jet energy scale and ICD hot cells are removed. In addition, each jet must lie within a pseudorapidity  $|\eta| < 2.5$ . The following cuts ensure that the jet energy distribution in the various layers of the calorimeter is reasonable and that the jets are not constructed from spurious energy depositions:
  - Energy fraction in the EM layers of a jet is required to be  $0.05 < EMF < 0.95$ .
  - The energy fraction in the outermost layer (coarse hadronic) is required to be  $CHF < 0.4$ .
- Triangle cut: There is a small probability of low energy jets (which not electrons) passing the electron selection criteria. These jets are called *fake electrons*. In such cases, the dif-

ference between the electron and jet reconstruction algorithms leads to a small amount of  $\cancel{E}_T$  along the same direction as the electron. Jets can also have their energy mis-measured or mis-calibrated leading to a small amount of  $\cancel{E}_T$  back-to-back in azimuth with the jet. These sources of mismeasurement are difficult to model in the background measurement. Without sacrificing much signal in terms of signal acceptance, it is possible to eliminate these kinematic regions by applying a 2-d cut called the “triangle cut.” The following optimized triangle cut is applied to remove such events:  $\Delta\phi(\cancel{E}_T, e) > 1 - 0.25 \times \cancel{E}_T$ . The cut is shown as a solid red line in Fig. 8.3.

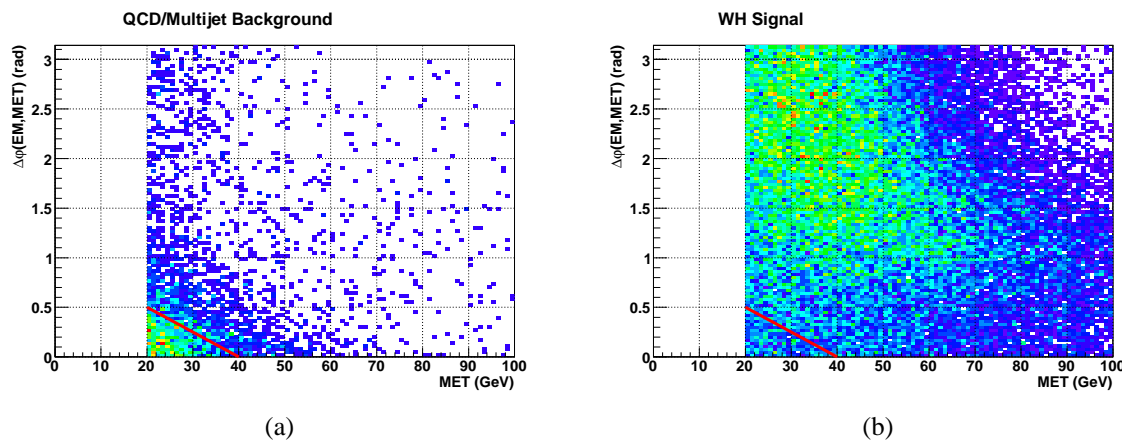


Figure 8.3. Distribution of the opening angle between electrons and the  $\cancel{E}_T$  as a function of  $\cancel{E}_T$  for (a) QCD/Multijet background sample and (b)  $WH$  signal sample. The triangle cut removes the area below the line intersecting the two axes. The effect of removing this area amounts to a negligible decrease in signal acceptance, while removing a substantial background.

- The EC and CC samples are each divided into two subsets called the *loose* and *tight* samples in order to facilitate the estimation of QCD/multijet backgrounds. The distinction between loose and tight samples is based on the electron likelihood requirement:
  - Loose Sample: EM likelihood  $> 0.2$
  - Tight Sample: EM likelihood  $> 0.85$

- In order to minimize backgrounds that contain two isolated leptons in the final state, such as those coming from  $Z$  and  $t\bar{t}$  production, the candidate events are required not to have isolated muons with  $p_T^\mu > 15$  GeV/c and no other electrons with  $p_T^e > 15$  GeV/c that satisfy the loose electron criteria and fail either  $p_T > 20$  GeV/c or  $|\eta| < 3.0$ .
- Events with an additional lepton (muon within  $|\eta| < 2.0$  or electron within  $|\eta| < 2.4$ ) isolated from jets and having a  $p_T > 20$  GeV/c are rejected to decrease the  $Z$  and  $t\bar{t}$  dilepton backgrounds.
- Events having a  $|z_{vtx}| < 60$  cm from the nominal interaction point and with at least three tracks originating from it are retained.

## 8.5 Background Modeling

The background processes can be classified into two categories: physics background and instrumental background. Physics background involves physical processes which have a final state similar to  $WH$  associated production. Instrumental backgrounds arise due to mismeasurement of final state objects, primarily electrons and jets. Since the source of mismeasurement is due to identifying low energy jets as electrons, and these jets often originate from the QCD processes like dijet/multijet production, the terms “instrumental” and “QCD/Multijet” backgrounds are used interchangeably.

### • Physics Background

#### 8.5.1 $t\bar{t}$ Production

Top quark pair production and decay is one of the SM backgrounds for the Higgs signal. Top pairs can be classified into two categories — dilepton channel in which two leptons,  $\cancel{E}_T$  and two  $b$ -jets are in the final state as shown in Fig. 8.4(a). The leptons can either be electrons or muons which includes indirect decays of  $\tau$  to electron or muon. If one of the leptons is missing (not accounted for in the reconstruction), then the final state can resemble the signal.

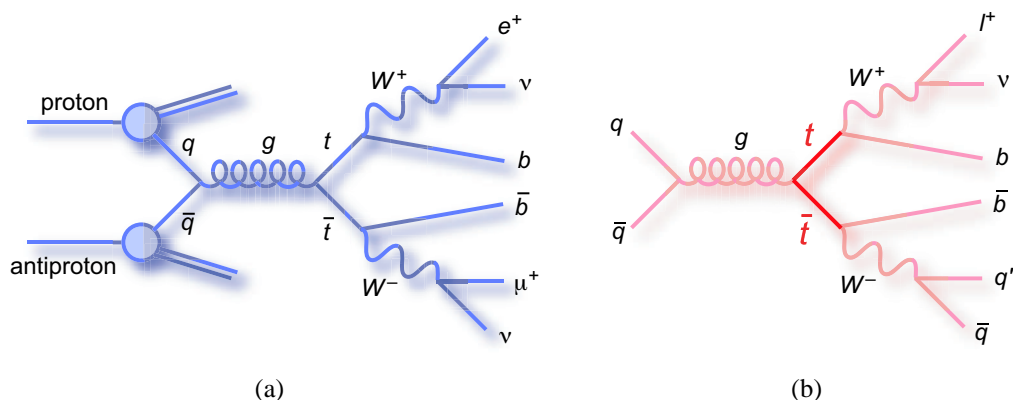


Figure 8.4. Feynman diagrams for top quark backgrounds: (a)  $t\bar{t} \rightarrow \ell\nu\nu b\bar{b}$  (b)  $t\bar{t} \rightarrow \ell\nu j b\bar{b}$ .

In the second category, a lepton, two light jets,  $\cancel{E}_T$  and two  $b$ -jets are produced which is shown in Fig. 8.4(b). If one of the jets from the hadronic decay of  $W$  is mismeasured leading to a  $\cancel{E}_T$  If the other jet is highly electromagnetic and overlaps with the lepton then the final state can resemble the signal. Another possibility is that one or more jets in the uninstrumented ICD region or those that escape detection due  $\phi$  module boundaries, leading to a fake  $\cancel{E}_T$  in the event.

### 8.5.2 Single Top Quark Production

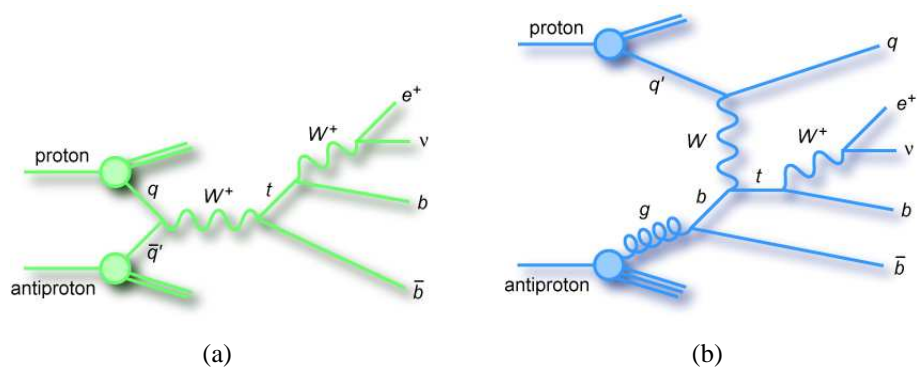


Figure 8.5. Feynman diagrams for the single top quark background: (a)  $s$ -channel  $tb \rightarrow \ell\nu b\bar{b}$  (b)  $t$ -channel  $tqb \rightarrow \ell\nu qb\bar{b}$ .



Single top production is a major source of physics background for Higgs boson production. The two main diagrams contributing to this background are shown in Fig. 8.5. The final state for  $s$ -channel single top production and decay is shown in Fig. 8.5(a). It includes a lepton, two  $b$ -jets and  $\cancel{E}_T$ , which is the same final state as the signal. The  $t$ -channel production has an additional light jet which, if mismeasured, or lost, will lead to an identical final state as the signal.

8.5.3 Diboson Production

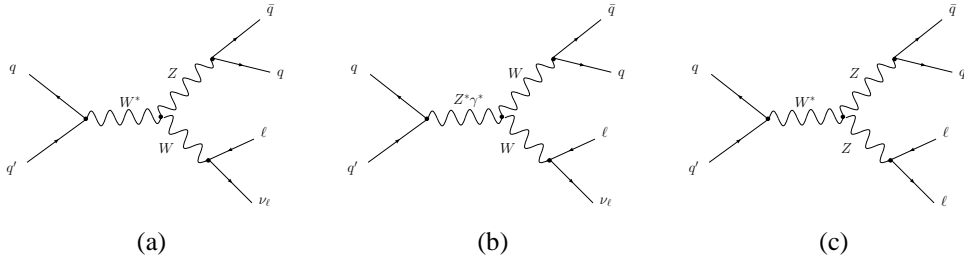


Figure 8.6. Feynman diagrams for diboson production: (a)  $s$ -channel  $W^* \rightarrow WZ$  (b)  $u$ -channel  $Z/\gamma \rightarrow WW$  and (c)  $W^* \rightarrow ZZ$  production.

Diboson production includes the  $WZ$ ,  $ZZ$  and  $WW$  processes. In each case there is a lepton and  $\cancel{E}_T$  plus a possible decay of one of the vector bosons into heavy jets, which can then become a background to the Higgs signal. Three possible leading order Feynman diagrams for the diboson production are shown in Fig: 8.6. In Fig. 8.6(a) one or more of the light jets from the diboson production are shown in Fig: 8.6. In Fig. 8.6(a) one or more of the light jets from  $Z$  decay can be  $b$ -tagged. It is also possible that the  $Z$  can decay directly into  $b\bar{b}$  pair which could lead to an identical final state. Similarly in Fig. 8.6(b) one of the  $W$  decays hadronically while the other decays leptonically. If one ore more jets are identified as  $b$  jets, this could fake the signal.  $ZZ$  dibosons can decay into two leptons and two jets. If one of the leptons escapes detection, there will be a net imbalance in momentum in the event which will fake the  $\cancel{E}_T$  and one or more jets could be falsely identified as  $b$ -jets. All the above signatures will lead to one

lepton,  $\cancel{E}_T$  and one or more  $b$ -tagged jets. Furthermore, one or more leptons may be lost in the  $\phi$  module boundaries leading to a fake  $\cancel{E}_T$ .

#### 8.5.4 $W$ +jets and $Z$ +jets Production

Production of weak vector bosons in association with jets is very common at the Tevatron. These can be either light or heavy flavor jets. In addition processes involving initial/final state gluons which hadronize to form jets is a common feature. In each case, when the vector bosons decay leptonically they can fake the signal process. Two of the many possible diagrams are shown in Fig. 8.7. In case of  $Z$  + jets, one of the leptons from  $Z$  decay may be lost (which leads to a fake  $\cancel{E}_T$  in the event, or mismeasured as a jet. One or more light-quark jets may be identified falsely as  $b$ -jets. This situation will lead to an identical final state as the signal.

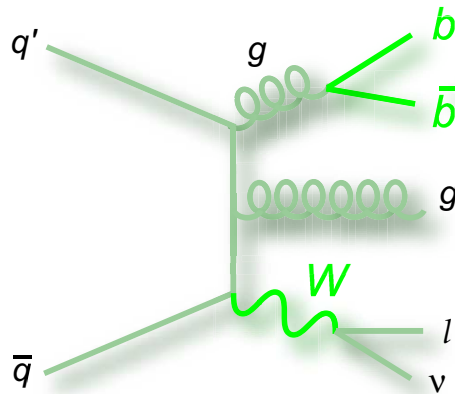


Figure 8.7. Feynman diagrams for  $W$ +jets production: (a) with a final state gluon jet and  $W$  decaying leptonically.

#### 8.5.5 $Wb\bar{b}$ Production

$Wb\bar{b}$  production is an *irreducible* background to the  $WH$  signal. The final state particles are identical to the  $WH$  signal, and hence there is no experimental way to distinguish the two,

as is evident from Fig. 8.8. This dominant background source can be distinguished from the signal by appealing to the event kinematics, especially the difference in shape of the kinematic distributions. The properties of the jets including the  $p_T$  of leading and next-to-leading jets, the angular separation between the jets, the invariant mass and  $p_T$  of the dijet system and other event shape variables like the transverse mass and  $p_T$  of the lepton- $\cancel{E}_T$  system can be used as variables. The difference in shape between  $WH$  signal and  $Wb\bar{b}$  background for these variables can be exploited by employing multivariate techniques (for example, a likelihood or a neural network discriminant) to separate them.

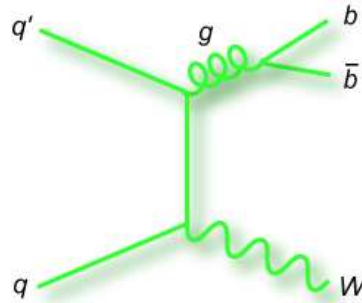


Figure 8.8. Feynman diagram indicating the irreducible  $Wb\bar{b}$  background. The final state is identical to the  $WH$  signal. However, the production cross sections for the  $WH$  and  $Wb\bar{b}$  processes are different.

- Instrumental Background

### 8.5.6 QCD/Multijet

Production of multiple jets in the final state is referred to as the QCD background in this analysis. Fig. 8.9 shows one possible scenario for multijet production. One or more jets in a multijet event can fake an electron. Two other jets may be falsely identified as  $b$ -tagged jets or a real  $b\bar{b}$  pair could originate from gluon splitting. If the energy of one or more jets is mismeasured or the jets are lost in the  $\phi$  cracks, they can lead to a  $\cancel{E}_T$  in the event. The large

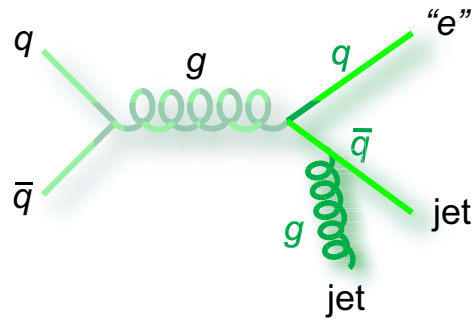


Figure 8.9. Feynman diagram for the multijet background. A jet can sometimes be falsely identified as an electron. Jets originating from light quarks ( $u, d, s$ ) or gluon jets may also be mis-identified as  $b$ -jets. Energy mismeasurement can lead to  $\cancel{E}_T$  in the event.

cross section of QCD multijets make them a significant background. All these scenarios could lead to the same final state as the  $WH$  signal.

The QCD/Multijet background is estimated using real data from two different samples: a loose sample in which events pass the electron selection criteria including a loose EM likelihood cut ( $> 0.2$ ), and a tight sample which is a subset of the loose sample satisfying a tighter EM likelihood cut ( $> 0.85$ ) and all other preselection cuts except the  $\cancel{E}_T$  cut.  $\cancel{E}_T$  is required to be  $< 10$  GeV to eliminate the presence of  $W \rightarrow \ell\nu$  decays. The fake rate and likelihood efficiencies are determined and the matrix equations are used to estimate the number of QCD multijet events for each differential distribution. The matrix method and estimation of the fake rate are explained below:

#### 8.5.6.1 Matrix Method

- Loose Sample

To estimate the QCD multijet background, a technique called the matrix method is used. This method is based on defining two samples of data: a loose sample with  $N_{loose}$  events in which the electron likelihood requirement (likelihood  $> 20\%$ ) is not strict and therefore the sample purity in terms of the number of real electrons is decreased. Essentially the sample

consists of real electrons which pass the tight analysis selection cuts (denoted by  $N_{EM}$ ), and fake electrons or jets from the multijet QCD background that pass the electron selection criteria denoted by  $N_{QCD}$ . This can be summarized as the first matrix equation defining the loose sample:

$$\mathbf{N}_{loose} = \mathbf{N}_{EM} + \mathbf{N}_{QCD} \quad (8.1)$$

- Tight Sample

The purity of the loose sample can be increased by requiring a tighter cut on the electron likelihood ( $> 85\%$ ), thus defining a subset of the loose sample denoted by  $N_{tight} \subset N_{loose}$ . This sample by construction has a negligible number fake electron candidates (*i.e.*, jets from the multijet QCD background that pass the electron selection criteria, thereby mimicking a real electron). In order to determine the number of fake electrons in the tight sample, one has to know the probability that a fake electron passes the tight electron requirements. This probability is denoted by  $\epsilon_{QCD}$ . Therefore the fraction of events in the tight sample that correspond to fake electrons are  $\epsilon_{QCD} \cdot N_{QCD}$ . Similarly, one has to estimate the efficiency of selecting real electrons which satisfy the likelihood requirements for a tight electron. This is the likelihood efficiency, denoted by  $\epsilon_{\ell}$ . The number of real electrons in the tight sample is then  $\epsilon_{\ell} \cdot N_{EM}$ . The second matrix equation is therefore the definition of the tight sample, which is the sum of the number of events with real electrons and number of events with fake electrons in the tight sample:

$$\mathbf{N}_{tight} = \epsilon_{\ell} \cdot \mathbf{N}_{EM} + \epsilon_{QCD} \cdot \mathbf{N}_{QCD} \quad (8.2)$$

The solution of the matrix equations is given in Eq. 8.3. The goal is to estimate the number of events wherein a fake electron from dijet/multijet processes passes the electron selection

criteria defined in the analysis. In order to determine  $N_{QCD}$ , we have to determine the fake rate  $\epsilon_{QCD}$  and the likelihood efficiency  $\epsilon_\ell$ . By the definition of loose and tight samples we know  $N_{loose}$  and  $N_{tight}$ , and the solution of the matrix equations for  $N_{QCD}$  can be used to estimate the QCD multijet background.

$$N_{QCD} = \frac{\epsilon_\ell \cdot N_{loose} - N_{tight}}{\epsilon_\ell - \epsilon_{QCD}} \quad \text{and} \quad N_{EM} = \frac{\epsilon_{QCD} \cdot N_{loose} - N_{tight}}{\epsilon_\ell - \epsilon_{QCD}} \quad (8.3)$$

#### 8.5.6.2 Estimation of Fake Rate ( $\epsilon_{QCD}$ )

The fake rate was estimated from the real data sample by selecting candidate events with all the preselection cuts defined in section 8.4 except the  $\cancel{E}_T$  cut. Since we are defining a fake electron sample, the low  $\cancel{E}_T$  cut, *i.e.*,  $\cancel{E}_T < 10$  GeV, is required in order to minimize contamination from true  $W$  bosons (a ‘ $W$ -veto’), which forms the signal sample for the current analysis. One of the jets is required to have an EM fraction  $f_{EM} < 0.7$  and be in the central calorimeter ( $|\eta| < 1.1$ ), and away from EM module boundaries, thus defining it to be a hadronic jet. Demanding the presence of one hadronic jet will reject candidate events where the  $Z$  boson decays into two electrons and one of them is mis-measured as a jet and artificial  $\cancel{E}_T$  resulting from it (a ‘ $Z$ -veto’). Another jet is required to satisfy all electron requirements except the electron likelihood selection, thereby defining a fake electron.

$$\epsilon_{QCD} = \frac{N_{fake}^{EM}(lh > 0.85)}{N_{fake}^{EM}(lh > 0.2)} \quad (8.4)$$

The fake rate is obtained by dividing the number of events containing at least one fake electron passing the tight electron selection criteria (*i.e.*, EM likelihood  $> 0.85$ ) denoted by  $N_{fake}^{EM}(lh > 0.85)$  by the total number of candidate events, each having a fake electron passing the loose selection criteria (*i.e.*, EM likelihood  $> 0.2$ ) denoted by  $N_{fake}^{EM}(lh > 0.2)$ . Thus the fake rate

depends on the definition of the initial loose selection. Although  $W$ - and  $Z$ -vetos are applied there is a small probability of real electrons from  $W$ 's or  $Z$ 's still remaining in the fake rate sample. This causes an artificial increase in the fake rate (black markers) due to contamination from real electrons. An estimate of the number of such real electrons from  $W$ +jets and  $Z$ +jets events (red markers) is shown in Fig. 8.10(a), which is a plot of the fake rate ( $\epsilon_{QCD}$ ) as a function of electron  $p_T$ . After subtracting this component from the fake rate sample, the

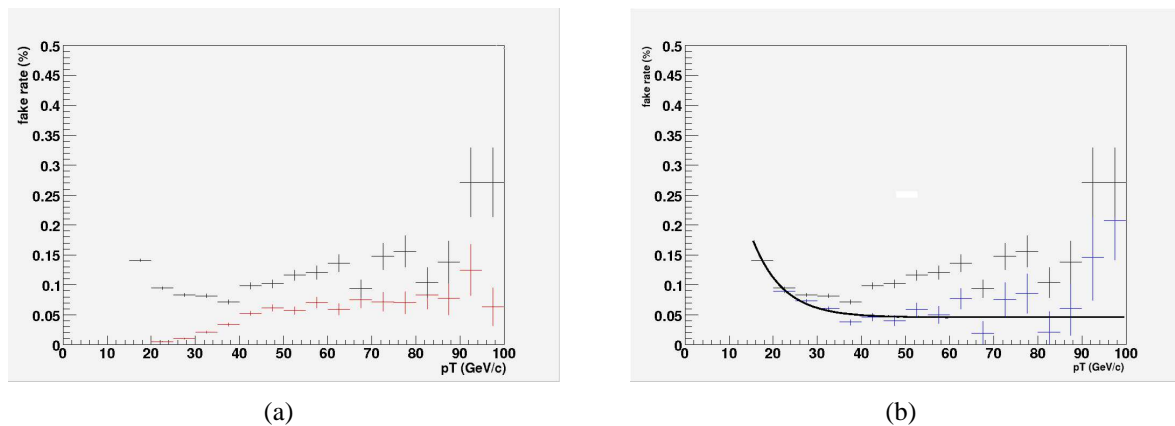


Figure 8.10. Fake rate in the central calorimeter region as a function of electron  $p_T$  is shown. (a) The black and red markers indicate data and real electron components estimated from  $W$ +jets and  $Z$ +jets simulations, respectively. (b) black and blue markers show the fake rate before and after subtracting real electron component. A fit to the fake rate is indicated by the solid black line.

artificial rise in fake rate is no longer observed, as indicated (blue markers) in Fig. 8.10(b). The fake rate is fit with a functional form  $\epsilon_{QCD} = \exp(-A \cdot p_T + B) + C$  which describes the data well. The fit parameters are summarized in Table 8.1.

At low electron  $p_T$  the QCD background is the largest component, and it falls off exponentially to a constant value for  $p_T > 30$  GeV/c. A minor variation in the fake rate is also observed for data collected during various epochs characterized by different trigger lists (v8-11, v12, v13 and v14). The fake rates measured for the different trigger lists are summarized in Table 8.2.

Table 8.1. QCD fake rate fit parameters for v8-v14 trigger lists.

Trigger List	A	B	C	$\chi^2/\text{dof}$
8-11	$0.103 \pm 0.008$	$0.646 \pm 0.156$	$0.054 \pm 0.002$	34.9/42
v12	$0.069 \pm 0.004$	$0.172 \pm 0.067$	$0.057 \pm 0.001$	64.3/47
v13	$0.086 \pm 0.004$	$0.488 \pm 0.080$	$0.060 \pm 0.001$	61.6/47
v14	$0.076 \pm 0.002$	$0.512 \pm 0.062$	$0.066 \pm 0.001$	31.7/47

Table 8.2. Fake rate for the CC and EC electron channels at  $p_T = 30$  GeV/c for v8-v14 trigger lists. Only statistical errors are shown.

Trigger List	Fake Rate 2 jets (%)		Fake Rate 3 jets (%)	
	CC	EC	CC	EC
v8-11	$5.4 \pm 0.2$	$6.3 \pm 0.2$	$6.0 \pm 0.2$	$7.7 \pm 0.2$
v12	$5.7 \pm 0.1$	$8.2 \pm 0.1$	$8.4 \pm 1.0$	$8.3 \pm 0.3$
v13	$6.0 \pm 0.1$	$8.5 \pm 0.1$	$8.2 \pm 1.0$	$10.3 \pm 1.0$
v14	$6.6 \pm 0.1$	$8.8 \pm 0.1$	$6.6 \pm 1.0$	$8.8 \pm 1.0$

### 8.5.6.3 Estimation of Likelihood Efficiency ( $\epsilon_\ell$ )

Likelihood efficiency is estimated for electrons passing the tight selection (*i.e.*, likelihood  $> 0.85$ ) as described in section 7.1.5. The dependence of likelihood efficiency on electron  $p_T$  is shown in Fig. 8.11. The QCD background is estimated for every differential distribution by applying the  $p_T$ -dependent fake rate and likelihood efficiency, using the solution for  $N_{QCD}$  (Eq. 8.3) for different trigger lists.

## 8.6 Summary of Data and Expected Background

The selection criteria (section 8.4) are applied to data and all the MC processes (section 6.5). For data, the events are required to pass the EM+Jet trigger suite (section 6.3). The EM+Jet trigger is not modeled for MC processes, but a 2-d binned trigger efficiency in  $p_T$  and  $\eta$  is applied (section 7.2).



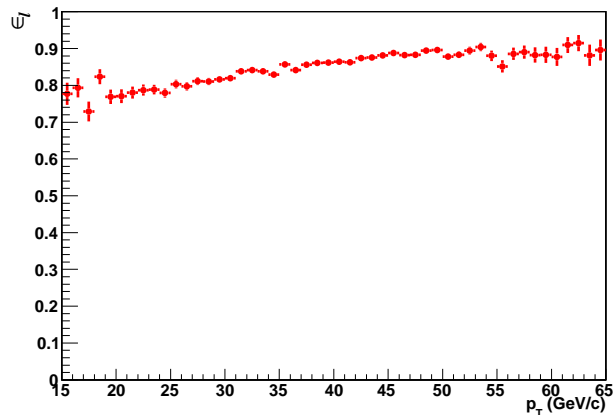


Figure 8.11. Likelihood efficiency for tight electrons (*i.e.*, likelihood  $> 0.85$ ) as a function of electron  $p_T$ . This quantity is used in estimate of  $N_{QCD}$  using the matrix equations.

Identification efficiencies are applied to MC events on a per object basis, *i.e.*, (electrons and jets, section 7.1.5 for electron and section 7.3.2 for jets). All efficiencies are parameterized or binned in terms of electron (jet)  $p_T$  of and detector pseudorapidity  $\eta_D$ . Jet energy scale corrections (section 7.3.1) are applied to correct the jets in data and MC. In addition, MC jets have their  $p_T$  smeared, shifted using the Jet SSR method (section 7.3.3). All efficiencies are folded into an ‘event weight’ which is applied to each MC event. Corrections for electrons and jets are propagated to the  $\cancel{E}_T$ .  $\cancel{E}_T$  is also corrected for the muons (section 7.4) after which the  $\cancel{E}_T$  is recomputed. Selected candidate events are studied by plotting the kinematic properties of electrons, jets,  $\cancel{E}_T$  and other topological variables. These properties are booked as histograms.

The QCD background is estimated using the loose/tight samples from data, together with the fake-rate (section 8.5.6.2) and likelihood efficiency (section 7), by solving the matrix equations bin by bin for each histogram. Simulated events are normalized to their cross section, except for the  $Wjj$  background process. Normalization is explained in the following section. ALPGEN processes with exclusive parton multiplicities are combined into a single inclusive sample using the method explained in section 4.2.2 (Combining Matched ALPGEN Samples).

### 8.6.1 Normalization

The simulated background processes are absolutely normalized to the SM predictions for their cross sections as summarized in Tables 6.4 - 6.7, with the exception of  $W$ +jets simulation, which is normalized to data. The normalization factor  $N_{data}/N_{MC}$  has a value  $\sim 0.95$ , when the NLO theoretical K-factor of 1.35 is applied for the simulated  $W$ +jets sample. The normalization factor is derived after subtracting the other expected background processes from the data. A comparison of data with the sum of the expected backgrounds is given in this section in the following order: CC Analysis ( $W$ +2jets), EC Analysis( $W$ +2jets). Kinematic properties of event for electrons,  $\cancel{E}_T$ ,  $W$ 's and jets show very good agreement.

### 8.6.2 Evidence for $W + 2$ jets Production

Kinematic properties of electrons, *i.e.*, energy ( $E_e$ ), transverse momentum ( $p_T^e$ ), the pseudorapidity  $\eta$  and the azimuthal angle  $\varphi^e$  are shown in Fig. 8.13. The scalar  $E_T$  and  $\cancel{E}_T \simeq p_T^\nu$  distributions are shown in Figs. 8.14(a) and 8.14(b), respectively. Plots shown correspond to the CC analysis. The kinematic properties of electrons and the  $\cancel{E}_T$  are used to reconstruct the  $W$  boson decay. The  $W$  transverse mass ( $M_{T,W}$ ) and transverse momentum ( $\mathbf{p}_{T,W}$ ) are defined as follows:

$$M_{T,W} = \sqrt{2 p_T^e p_T^\nu (1 - \cos(\varphi_e - \varphi_\nu))} \quad (8.5)$$

The agreement in shape and amplitude in the pre-tagged data and simulation is good, indicating a sound modeling of SM processes. The Jacobian peak of the reconstructed  $W$  is clearly visible (Figs. 8.14(c) and 8.14(d)). Since all candidate events require two jets in addition to the  $W$ , they provide the evidence for  $W + 2$ jet production. All plots shown in this section correspond to a signal process  $WH$  with  $m_H = 115 \text{ GeV}/c^2$ . The data/MC comparisons for other mass points for the Higgs signal display similar levels of agreement.

The jet properties are shown in Figs. 8.15 - 8.17. Corresponding plots for the EC analysis are given in Figs. 8.18 - 8.22. A subset of these events could possibly contain the  $WH$  signal process. In order to identify a possible Higgs signal resulting in two  $b$ -jets, it is necessary to perform the  $b$ -tagging procedure explained in the next section. A legend common to all the data/MC comparison plots is shown in Fig. 8.12



Figure 8.12. Legend for data and MC comparisons.

Figure 8.13 shows the kinematic properties of the electron candidates — the energy and  $p_T$  spectra, the pseudorapidity and azimuthal distributions. The expected background and observed data agree very well in shape. The effect of trigger turn-on on MC events are visible in the lower  $p_T$  region (*i.e.*,  $15 < p_T < 35$  GeV/c). The CC electrons are restricted to  $|\eta_D| < 1.1$ . As is expected, the electron  $\phi$  is uniformly distributed.

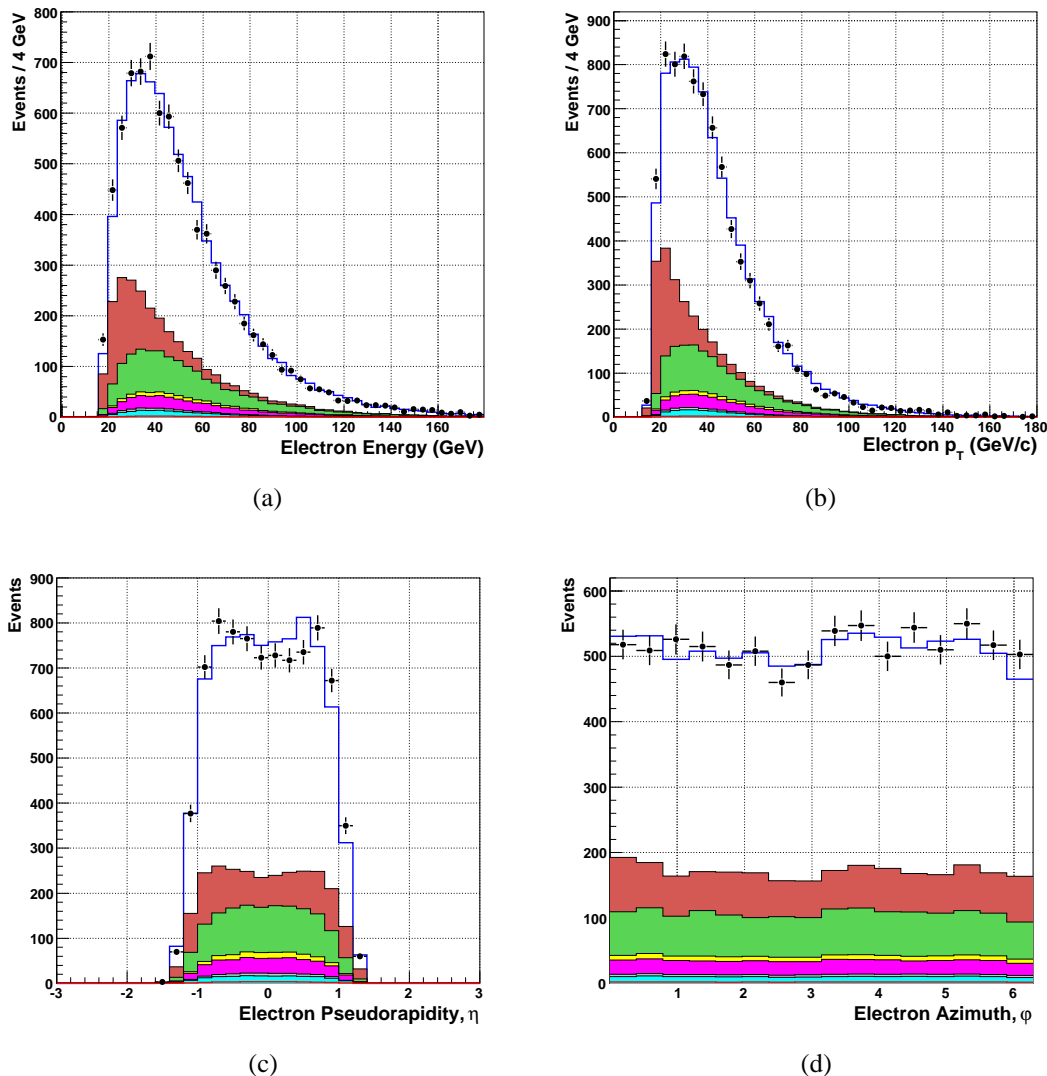


Figure 8.13. CC Analysis ( $W + 2$  Jets): Kinematic properties of the electron (a) Energy (GeV) (b) Transverse momentum  $p_T$  (GeV/c) (c) Pseudorapidity  $\eta$  (d) Azimuthal angle  $\varphi$  (rad).

Properties of  $W$  candidates are calculated from the electron and  $\cancel{E}_T$  kinematics using  $m_T = \sqrt{E_1^2 - \vec{p}_1^2}$ . Figures 8.14(a) and 8.14(b) show the scalar  $E_T$  and  $\cancel{E}_T$  distributions. A cut of  $\cancel{E}_T > 20$  GeV is applied to corrected  $\cancel{E}_T$  and is visible in Fig. 8.14(b). The  $\cancel{E}_T$  distribution shows a slight excess ( $< 1.5\sigma$ ) in the first bin, which is attributed to QCD background underestimated in that region.

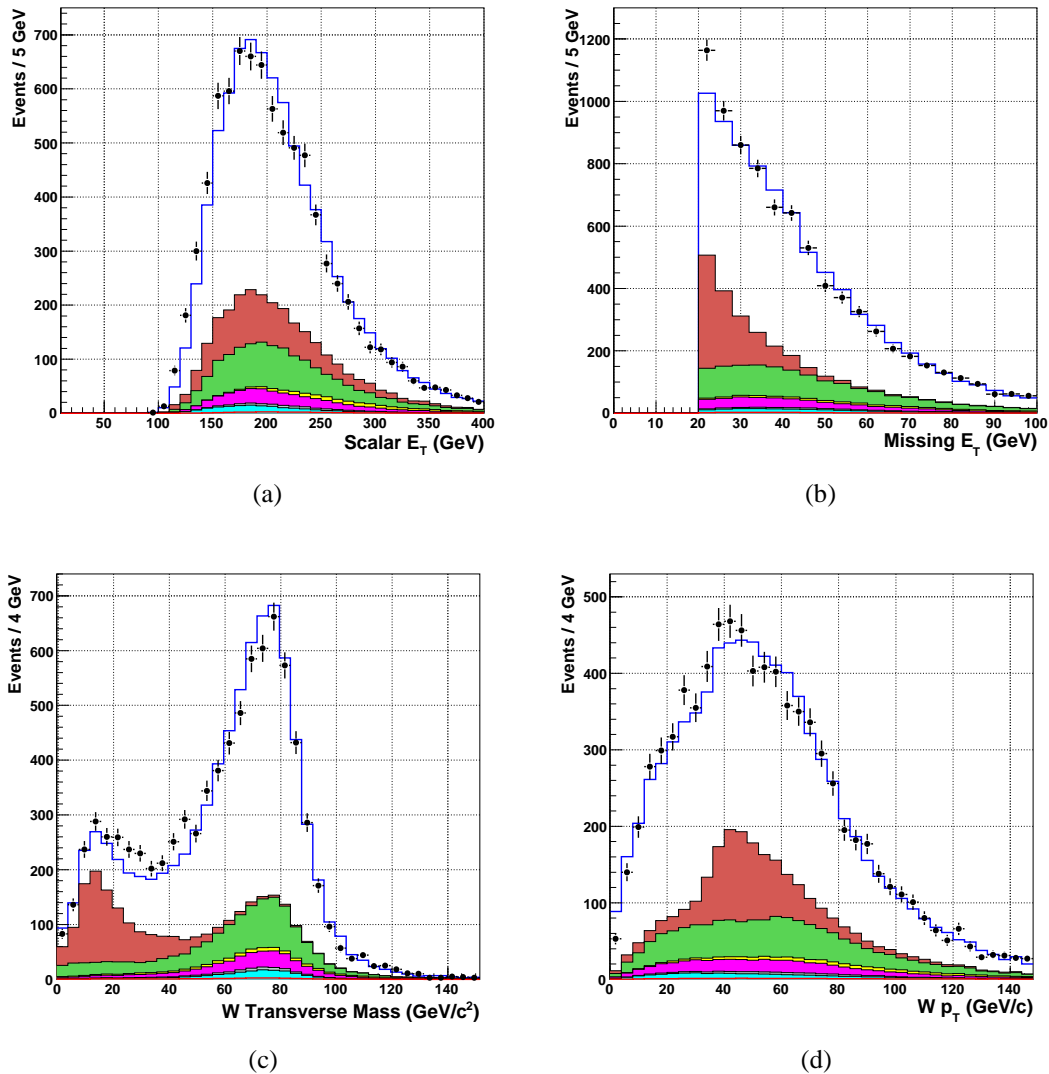


Figure 8.14. CC Analysis ( $W+2$  Jets): Properties of  $\nu_e$  and the  $W$  boson (a) Scalar  $E_T$  (GeV) (b) Missing  $E_T$  (GeV) (c)  $W$  transverse mass ( $\text{GeV}/c^2$ ) (d)  $W$  transverse momentum ( $\text{GeV}/c$ ).

The candidate events are required to have two jets in addition to the  $W$  boson. The  $W$  properties shown in Fig. 8.14(c) and Fig. 8.14(d) provide direct evidence for  $W$ +jets production. The Jacobian peak of the  $W$  transverse mass spectrum is clearly visible and well modeled by simulation. Comparison of data to the  $W$ +jets ALPGEN simulation provides a better description of EW processes with two or more jets in the final state compared to PYTHIA due

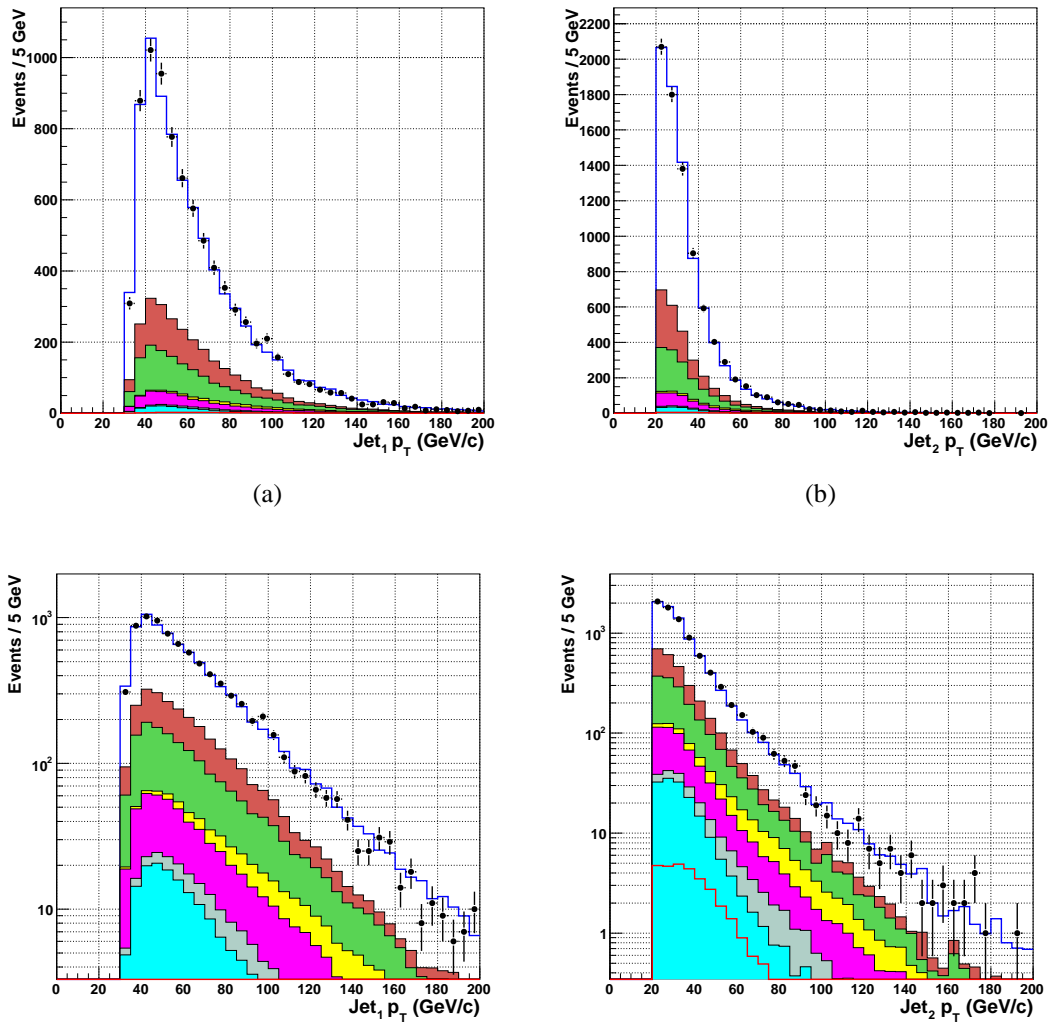


Figure 8.15. CC Analysis ( $W + 2$  Jets): Properties of jets. Top row (a) Leading Jet  $p_T$  (GeV/c) (b) Next-to-leading jet  $p_T$  (GeV/c). The plots in the bottom row are the same distributions but with a logarithmic vertical scale.

to the calculation of exact matrix elements of the elementary processes. The leading jet  $p_T$  cut is set to 25 GeV/c and the second jet is required to have a  $p_T$  larger than 20 GeV/c which is shown in Fig. 8.15. The expectation and data agree well over a wide kinematic range  $0 < p_T < 200$  GeV/c, for both the jets. These plots correspond to jet energy scale corrected  $p_T$ . The jet ID efficiencies are applied to MC jets. The jet pseudorapidity for leading jet is shown in

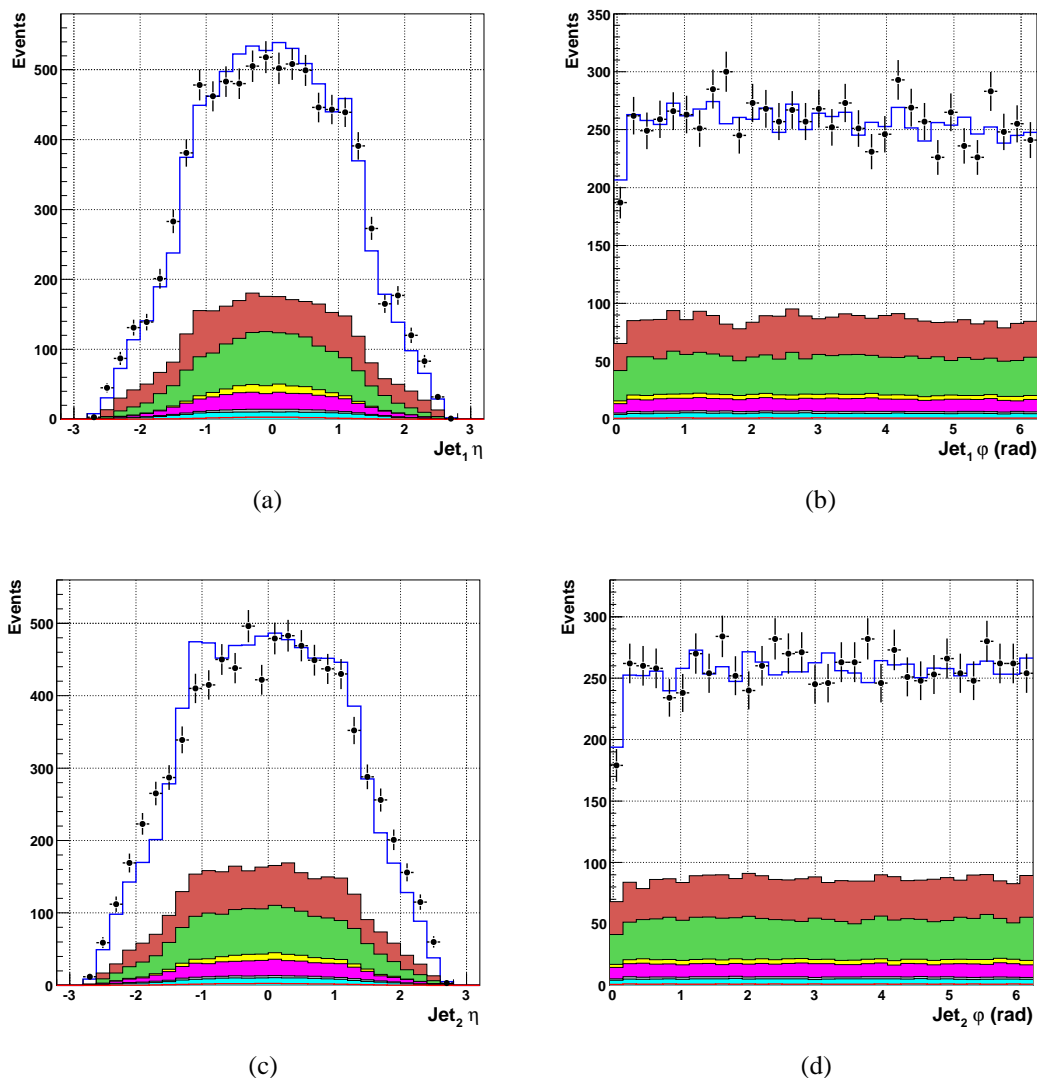


Figure 8.16. CC Analysis ( $W + 2$  Jets): Properties of jets. (a) Leading jet pseudorapidity (b) Leading jet azimuthal angle (rad) (c) Next-to-leading jet pseudorapidity (d) Next-to-leading jet azimuthal angle (rad).

Fig. 8.16(a) and the second jet in Fig. 8.16(c) and the corresponding azimuthal angle, *i.e.*,  $\phi$  distributions are shown in Fig. 8.16(b) and Fig. 8.16(d) respectively. The data and simulation show similar behavior and agree very well.

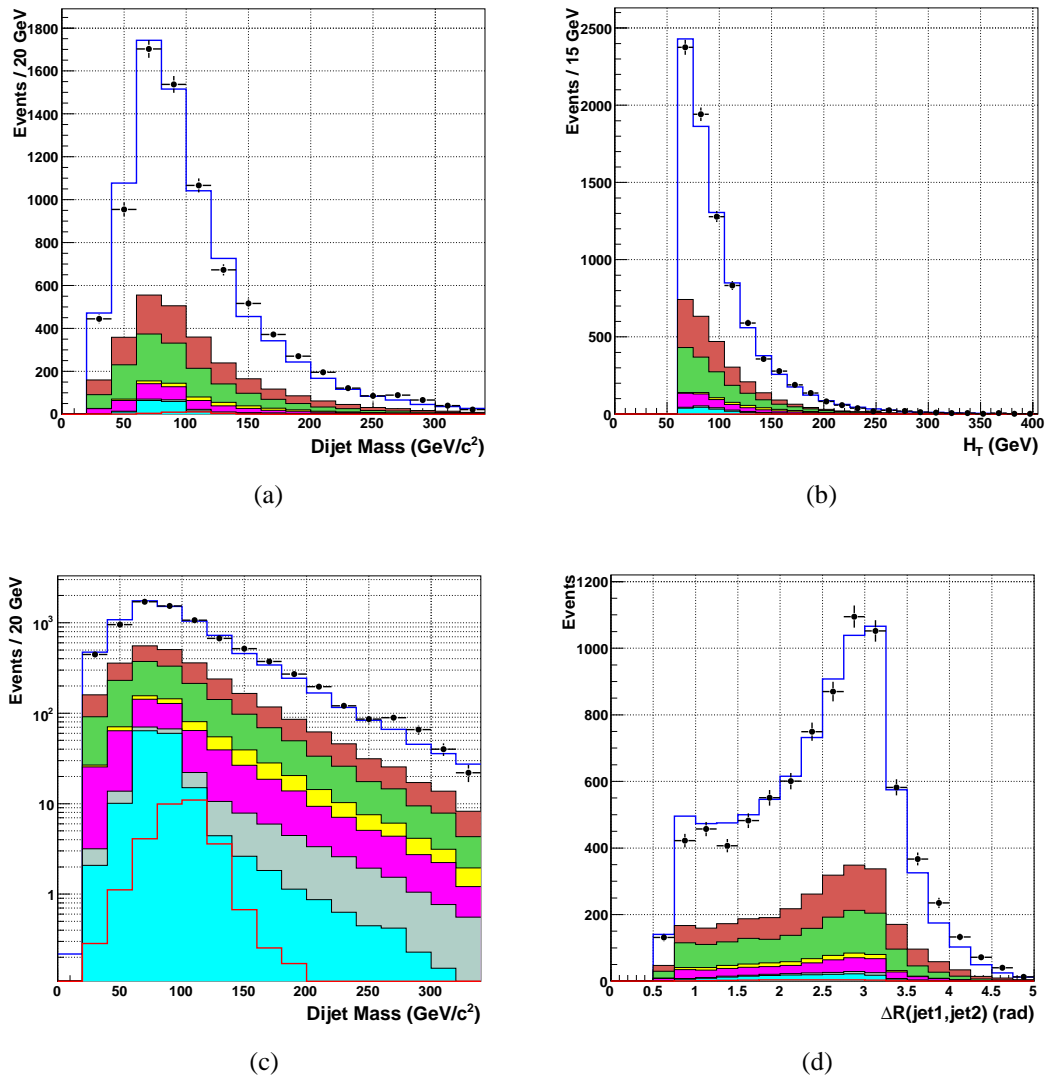


Figure 8.17. CC Analysis ( $W + 2$  Jets): Properties of jets. (a) Dijet invariant mass ( $\text{GeV}/c^2$ ) (b) Scalar sum of transverse momenta of jets ( $\text{GeV}/c$ ) (c) Dijet invariant mass in logarithmic scale ( $\text{GeV}/c^2$ ) (d) Separation between the leading and next-to-leading jets (rad) .

Sound background modeling should reproduce the shape and amplitude of dijet kinematic distributions. A few of them are shown in Fig. 8.17. The dijet invariant mass, scalar sum of the  $p_T$  of jets (*i.e.*,  $H_T$ ) and  $\Delta R = \sqrt{\Delta\eta^2 + \Delta\phi^2}$  of the two leading jets show good agreement in shape over the entire kinematic range. Figure 8.18 shows the kinematic properties of the electron candidates in the EC analysis; the energy and  $p_T$  spectra, the pseudorapidity



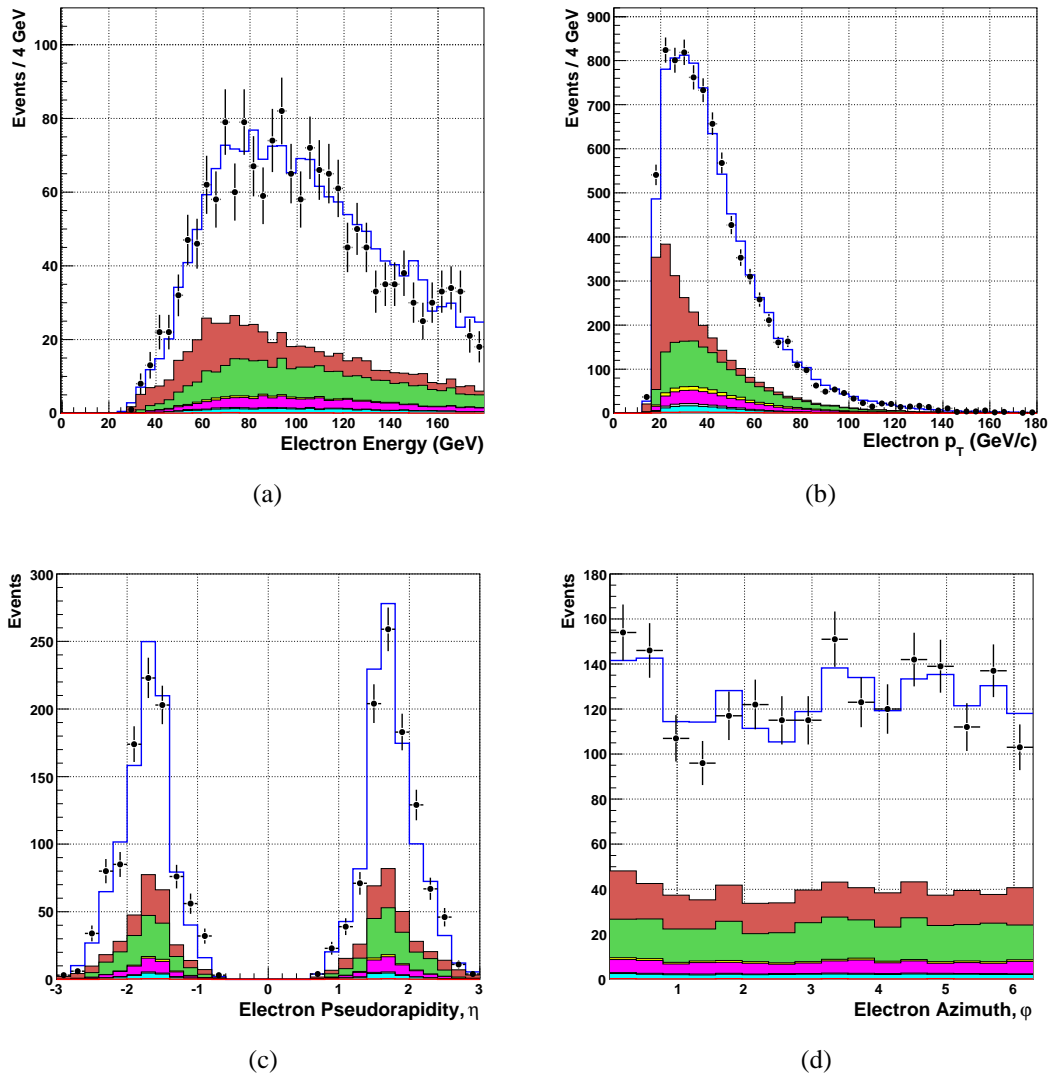


Figure 8.18. EC Analysis ( $W+2$  Jets): Kinematic properties of the electron (a) Energy (GeV) (b) Transverse momentum  $p_T$  (GeV/c) (c) Pseudorapidity  $\eta$  (d) Azimuthal angle  $\phi$  (rad) .

and azimuthal distributions. The EC electrons are restricted to  $1.1 < |\eta_D| < 3.0$ . Although the statistics are limited, the data and MC expectation agree well. Figure 8.19 shows the properties of the neutrino and the  $W$  bosons for the  $W+2$  jets EC analysis. The scalar  $E_T$  and  $\cancel{E}_T$  are shown in Figs. 8.19(a) and 8.19(b) respectively. The transverse mass and  $p_T$  of  $W$  bosons are shown in Figs. 8.19(c) and 8.19(d).

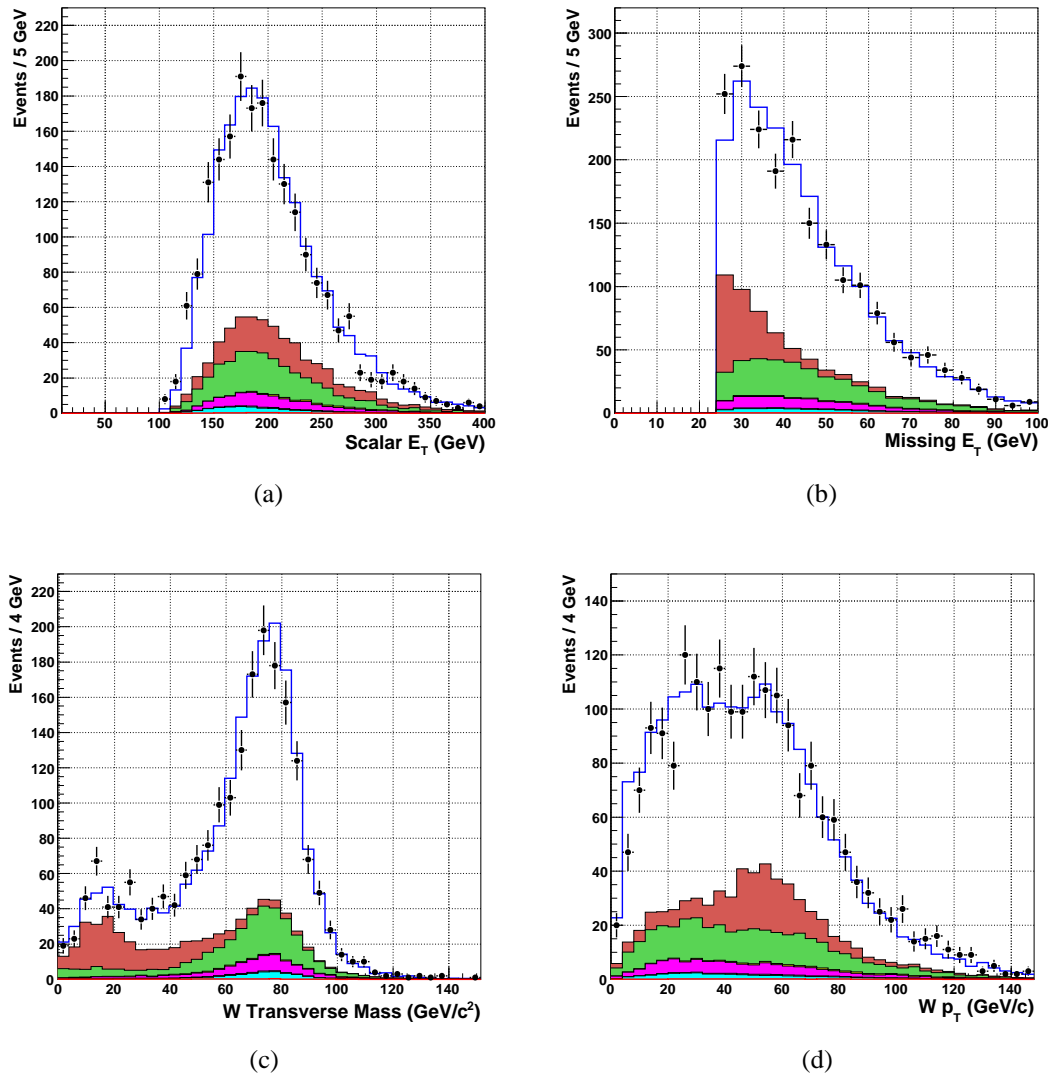


Figure 8.19. EC Analysis ( $W + 2$  Jets): Properties of  $\nu_e$  and the  $W$  boson (a) Scalar  $E_T$  (GeV) (b) Missing  $E_T$  (GeV) (c)  $W$  transverse mass ( $\text{GeV}/c^2$ ) (d)  $W$  transverse momentum ( $\text{GeV}/c$ ). Properties of  $W$  candidates are calculated from the electron and  $\cancel{E}_T$  kinematics using  $m_T = \sqrt{E_{\perp}^2 - \vec{p}_{\perp}^2}$  and are shown in (c) and (d).

The  $\cancel{E}_T$  cut for the EC analysis is set to 25  $\text{GeV}/c$  in order to reject QCD background. Lower values of  $\cancel{E}_T$  results in poor modeling of the QCD, in both the shape and estimated number of events. The  $\cancel{E}_T$  cut was optimized to this value to provide a reasonable description of  $\cancel{E}_T$  in the EC  $W + 2$  jets analysis. The properties of jets in the EC candidate events are

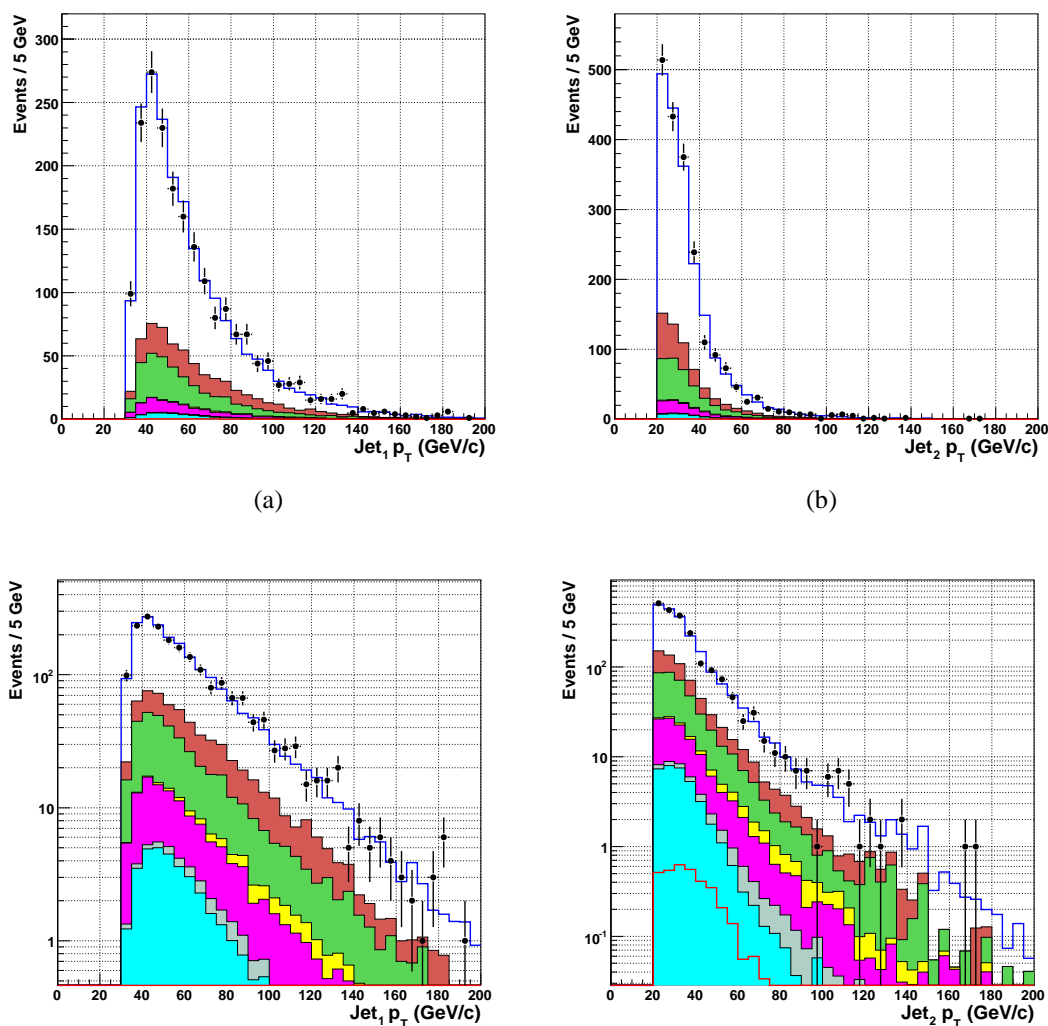


Figure 8.20. EC Analysis ( $W + 2$  Jets): Properties of jets. Top row (a) Leading Jet  $p_T$  (GeV/c) (b) Next-to-leading jet  $p_T$  (GeV/c). The plots in the bottom row are the same distributions but with a logarithmic vertical scale.

shown in Fig. 8.20. The next-to-leading jet  $p_T$  in Fig. 8.20(b) (and the corresponding semi-logarithmic plot in Fig. 8.20(d)) shows a less than  $1.5\sigma$  excess in data in the region  $100 < p_T < 125$  GeV/c, which is most likely due to a statistical fluctuation. The lack of statistics in higher  $p_T$  bins are evident, indicating a lack of high  $p_T$  jets in the forward  $\eta$  regions.

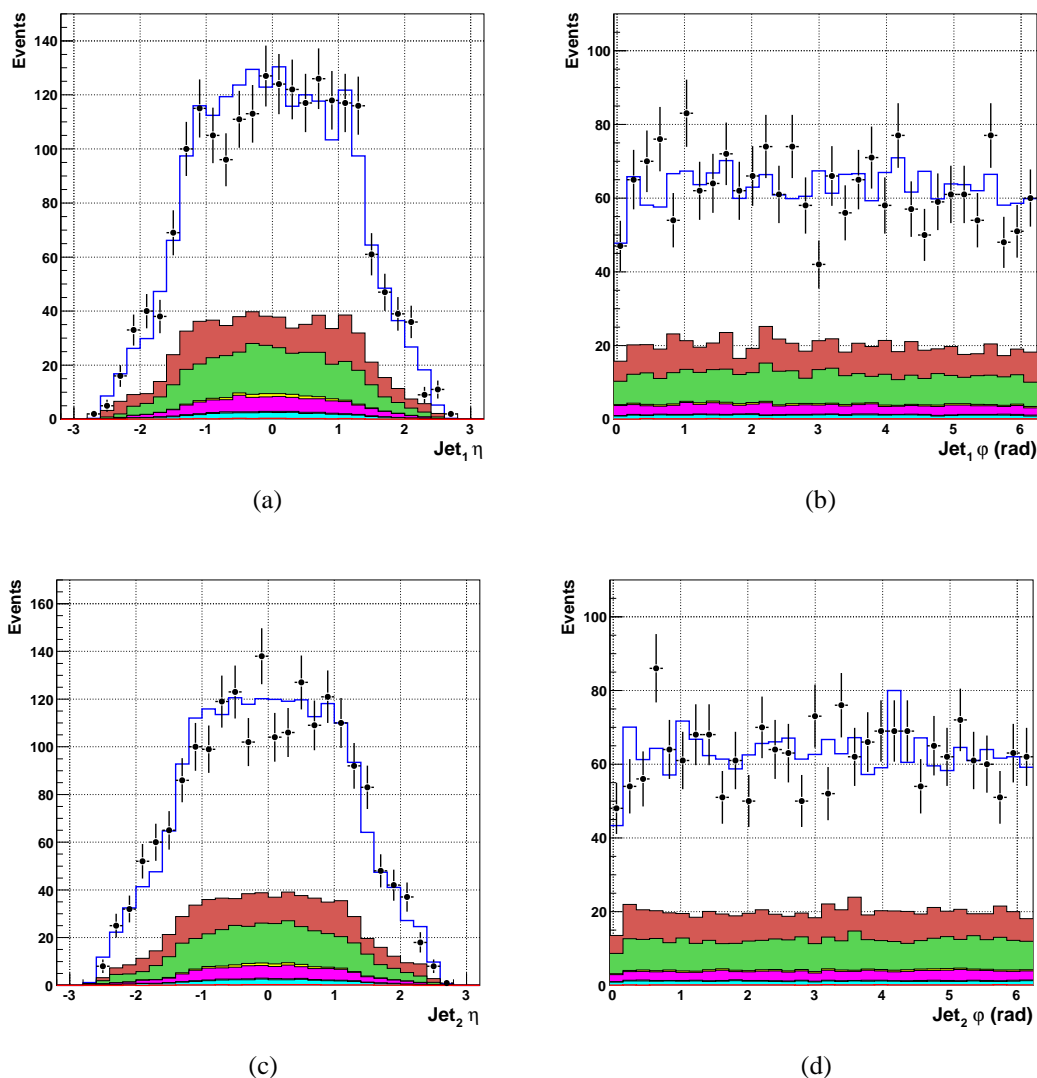


Figure 8.21. EC Analysis ( $W + 2$  Jets): Properties of jets. (a) Leading jet pseudorapidity (b) Leading jet azimuthal angle (rad) (c) Next-to-leading jet pseudorapidity (d) Next-to-leading jet azimuthal angle (rad) .

Figures 8.21(a) and 8.21(c) show the  $\eta$  of leading and next-to-leading jets respectively. The jet  $\phi$  distributions of leading and next-to-leading jets are shown in Fig 8.21(b) and Fig. 8.21(d) respectively. These distributions show good agreement with data.

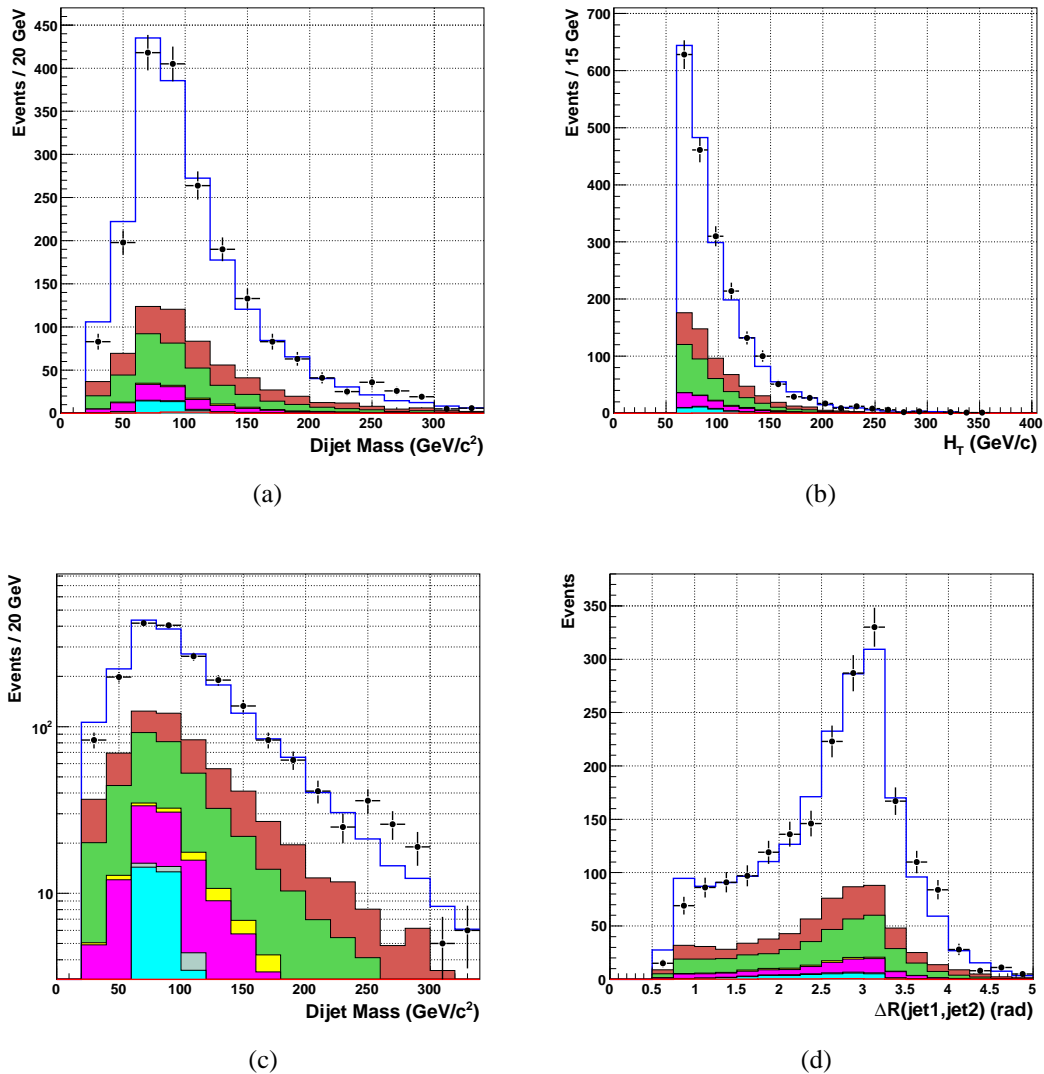


Figure 8.22. EC Analysis ( $W + 2$  Jets): Properties of jets. (a) Dijet invariant mass ( $\text{GeV}/c^2$ ) (b) Scalar sum of transverse momenta ( $H_T$ ) of jets ( $\text{GeV}/c$ ) (c) Dijet invariant mass in logarithmic scale ( $\text{GeV}/c^2$ ) (d) Separation between the leading and next-to-leading jets (rad) .

The dijet invariant mass,  $H_T$  and  $\Delta R$  of the two leading forward-jets are shown in Fig.8.22(a) (and in semi-logarithmic scale in Fig. 8.22(c)), Fig. 8.22(b) and Fig. 8.22(d) respectively. They show good agreement over the entire kinematic range.

## 8.7 $b$ -tagging

In order to apply NN  $b$ -tagging to the jets in the event, one has to choose a suitable operating point. Every operating point corresponds to a particular  $b$ -tagging efficiency and a fake rate. The available operating points on the NN output are summarized in section 5.9, Table 5.2. The primary goal is to obtain the best search sensitivity possible for a given set of optimized cuts, while maintaining a well-defined background model. In order to achieve this goal,  $b$ -tagging operating points are chosen to maximize the combined signal significance, *i.e.*,  $\alpha = S/\sqrt{B}$ , where  $S$  is the number of signal events and  $B$  is the total number of background events. The chosen operating points are listed in Table. 8.3.

Table 8.3. NN  $b$ -tagging efficiency and fake rate per jet for oldLoose and Tight operating points. The fake-rate/jet for a  $p_T = 50$  GeV/c jet is quoted for CC, EC and ICR jets.

	<b>oldLoose</b>	<b>Tight</b>
NN cut	> 0.50	> 0.775
$b$ -tagging Efficiency (%)	$59.3 \pm 1.45$	$47.6 \pm 1.52$
CC Fake Rate (%)	1.68	0.55
ICR Fake Rate (%)	1.50	0.41
EC Fake Rate (%)	1.35	0.30

In order to  $b$ -tag jets in an event, the operating point is set to *oldLoose* and  $b$ -tagging is performed. If both jets in the event are  $b$ -tagged, the event is considered to be double tagged (DT). If the event fails the double tagging criteria, the operating point is “tightened” to higher value of the NN cut (*i.e.*, *Tight*) and  $b$ -tagging is repeated. If at most one jet is  $b$ -tagged, the event is labeled as exclusive single tagged (EST). Thus DT and EST events form disjoint sets. The combined signal significance defined as the sum in quadrature of the EST and DT significance, *i.e.*,  $\alpha_{\text{EST}} \oplus \alpha_{\text{DT}}$  was found to be optimal for this particular choice of operating points among the many combinations that were studied for the CC analysis. [117]. An identical

$b$ -tagging procedure outlined above is followed for both the CC and EC analyses. Optimization of  $b$ -tagging operating points in the EC analysis was not studied. The operating points that were optimized for CC analysis was also used in the EC analysis. One of the improvements that could be carried out as a future work, would be to optimize the  $b$ -tagging for EC analyses.

### 8.7.1 Tagging MC Jets

The NN  $b$ -tagging algorithm cannot be applied directly to tag MC events due to large differences in tracking-related quantities in data and simulations (refer to section 7.5 for an explanation). Two equivalent approaches to  $b$ -tag jets in MC were introduced in section 7.5.1, the TSF and TRF methods.

$$\begin{aligned} W_{jet}^{\text{TSF}} &= \epsilon_{\text{taggability}}^{\text{MC}} \times \left( \frac{\epsilon_{\text{taggability}}^{\text{DATA}}}{\epsilon_{\text{taggability}}^{\text{MC}}} \right) \times \epsilon^{\text{MC}} \times \left( \frac{\epsilon_{b \rightarrow \mu}^{\text{DATA}}}{\epsilon_{b \rightarrow \mu}^{\text{MC}}} \right) \\ &= \epsilon_{\text{taggability}}^{\text{MC}} \times SF_{\text{taggability}} \times \epsilon^{\text{MC}} \times SF_{b \rightarrow \mu} \end{aligned} \quad (8.6)$$

In the TSF method, a weight  $W_{jet}^{\text{TSF}}$  is introduced to account for the difference in taggability and tagging efficiency between data and MC:

1. An MC jet is taggable if it satisfies the taggability criteria. Since the taggability of MC jets ( $\epsilon_{\text{taggability}}^{\text{MC}}$ ) is different from that of data, a taggability scale factor ( $SF_{\text{taggability}}$ ) is applied to correct for this difference.  $SF_{\text{taggability}}$  is parameterized as a function of jet  $\eta$  and  $p_T$  (section 7.5.3).
2. After correcting for the taggability of the MC jet, NN tagging is applied to it with an efficiency given by  $\epsilon^{\text{MC}}$ . If the NN probability of the tagged jet is greater than the NN cut the jet is considered tagged. The cuts are similar to that in data, *i.e.*, oldLoose and Tight for DT and EST, respectively.

3. The tagging efficiency for MC jets ( $\epsilon^{\text{MC}}$ ) is corrected using a scale factor ( $SF_{b \rightarrow \mu}$ ) given by Eq. 7.18. This scale factor is also used to construct the  $b$ -jet and  $c$ -jet TRF. A jet could be falsely identified as a  $b$ -jet when it is indeed a light quark jet. The jet is said to be mistagged. The  $SF_{b \rightarrow \mu}$  scale factor is determined only for inclusive  $b$  and  $c$  jets and not for light quark jets. Using this factor in tagging  $Wjj$  MC samples leads to an overestimation of its  $b$  content. The two jets in a  $Wjj$  sample could both be light quark jets or a combination of a light quark jet and a heavy flavor (either  $b$  or  $c$  quark) jet. The mistag rate for this sample was shown to be much higher when  $SF_{b \rightarrow \mu}$  was used [118] on a jet tagged with a ‘‘Tight’’ operating point used in EST. This however was not the case for the oldLoose operating point used in the DT analysis.
4. To quantify the overestimate, a sample of 500  $Wjj$  events were chosen and exclusively single tagged with the Tight operating point using both TRF and TSF methods. The  $b$ -content of this sample was estimated and the scale factor for the TSF method was adjusted to match the prediction of the sample’s  $b$ -content from the TRF method. This is based on the assumption that the Negative Tag Rate (NTR) of the TRF method correctly describes the tagging rate in data. The multiplicative factor for adjusting  $SF_{b \rightarrow \mu}$  was found to be  $0.42 \pm 0.05$  (stat.). A 25% systematic error assigned to this factor will be discussed in the next chapter.

The properties of  $b$ -tagged jets in the exclusive single tag (EST) and double tag (DT) analyses are presented in Figs. 8.23 — 8.25 for CC analysis.



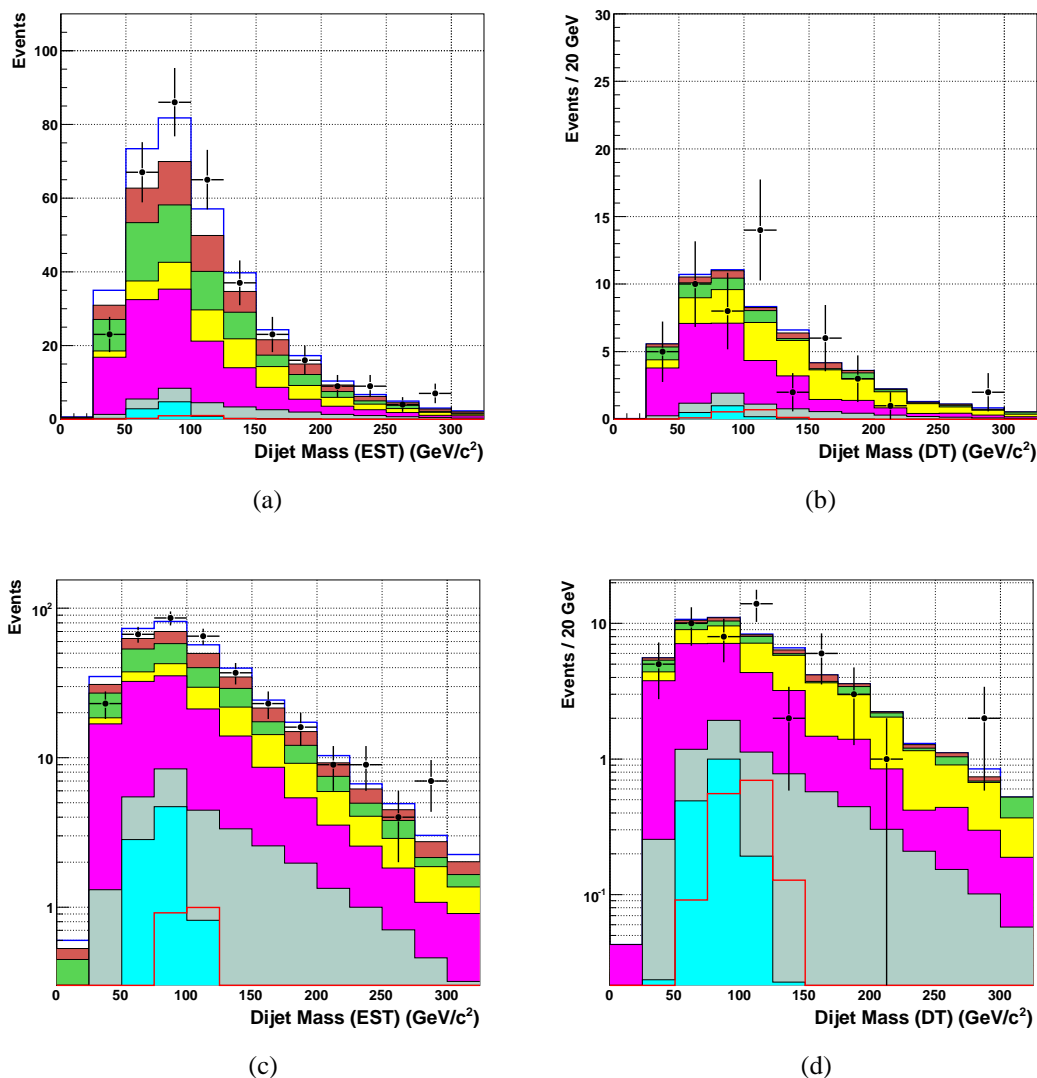


Figure 8.23. CC Analysis ( $W+2$  Jets, EST/DT): Properties of jets in exclusive single tagged (EST) and double tagged (DT) events. (a) Dijet mass (EST) ( $\text{GeV}/c^2$ ) (b) Dijet mass (DT) ( $\text{GeV}/c^2$ ). (c) and (d) The plots in the bottom row are the same distributions but with a logarithmic vertical scale.

Some of the conclusions that can be drawn upon careful examination of the plots are: there is a small excess ( $1.5\sigma$ ) in the dijet mass region between  $100 \text{ GeV}/c^2$  and  $120 \text{ GeV}/c^2$  in the observed data compared to the expectation from MC in the DT analysis. This excess is not observed in the EST analysis.

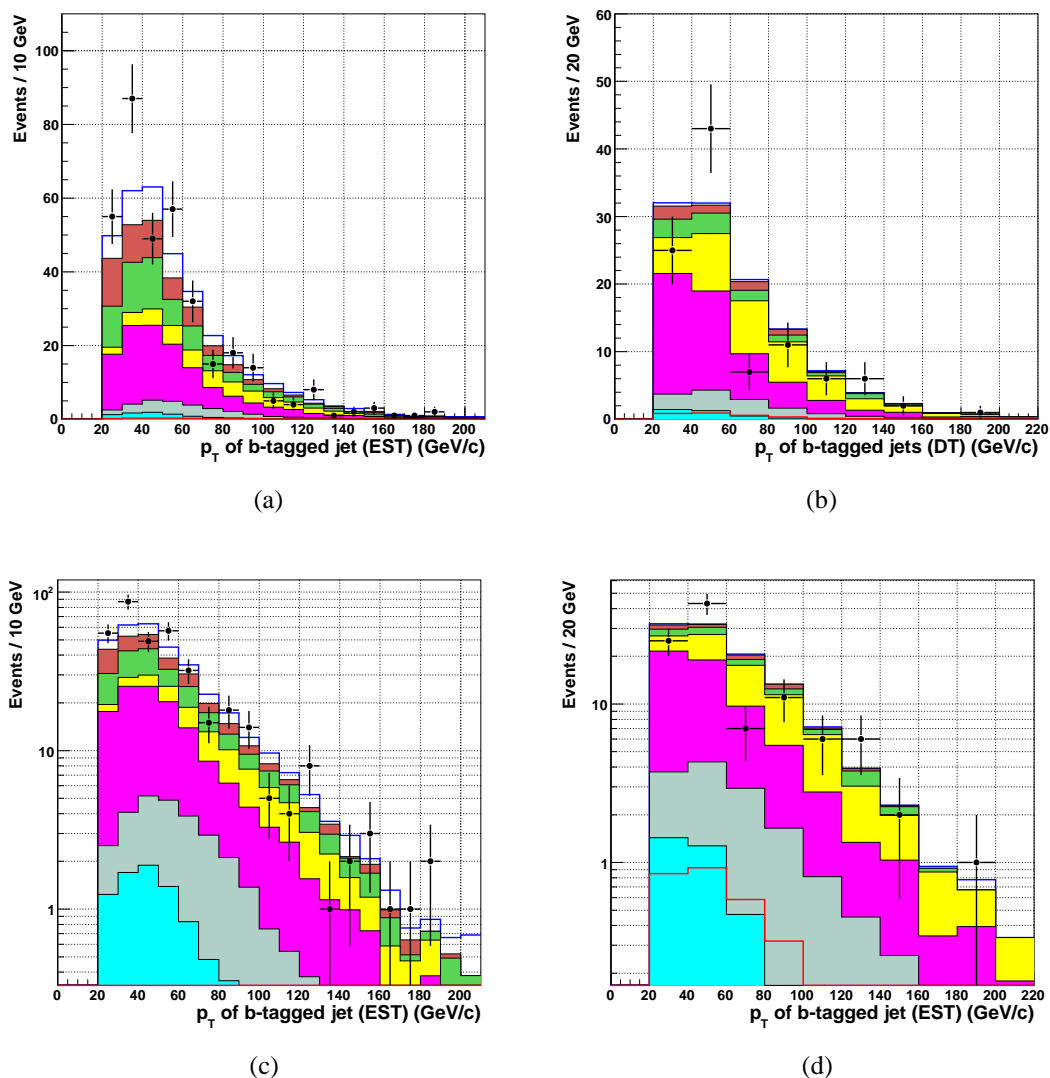


Figure 8.24. CC Analysis ( $W+2$  Jets, EST/DT): Properties of jets in exclusive single tagged (EST) and double tagged (DT) events. (a)  $p_T$  of  $b$ -tagged jets in the EST sample (GeV/c) (b)  $p_T$  of  $b$ -tagged jets in the DT sample (GeV/c) (c) and (d) The plots in the bottom row are the same distributions but with a logarithmic vertical scale.

This excess is attributed to the differences in  $b$ -tagging jets in MC and data, which was not further investigated further by the author. The jet properties for double tagged events for this analysis is not well understood. The shape of the expected background and the observed events are different.

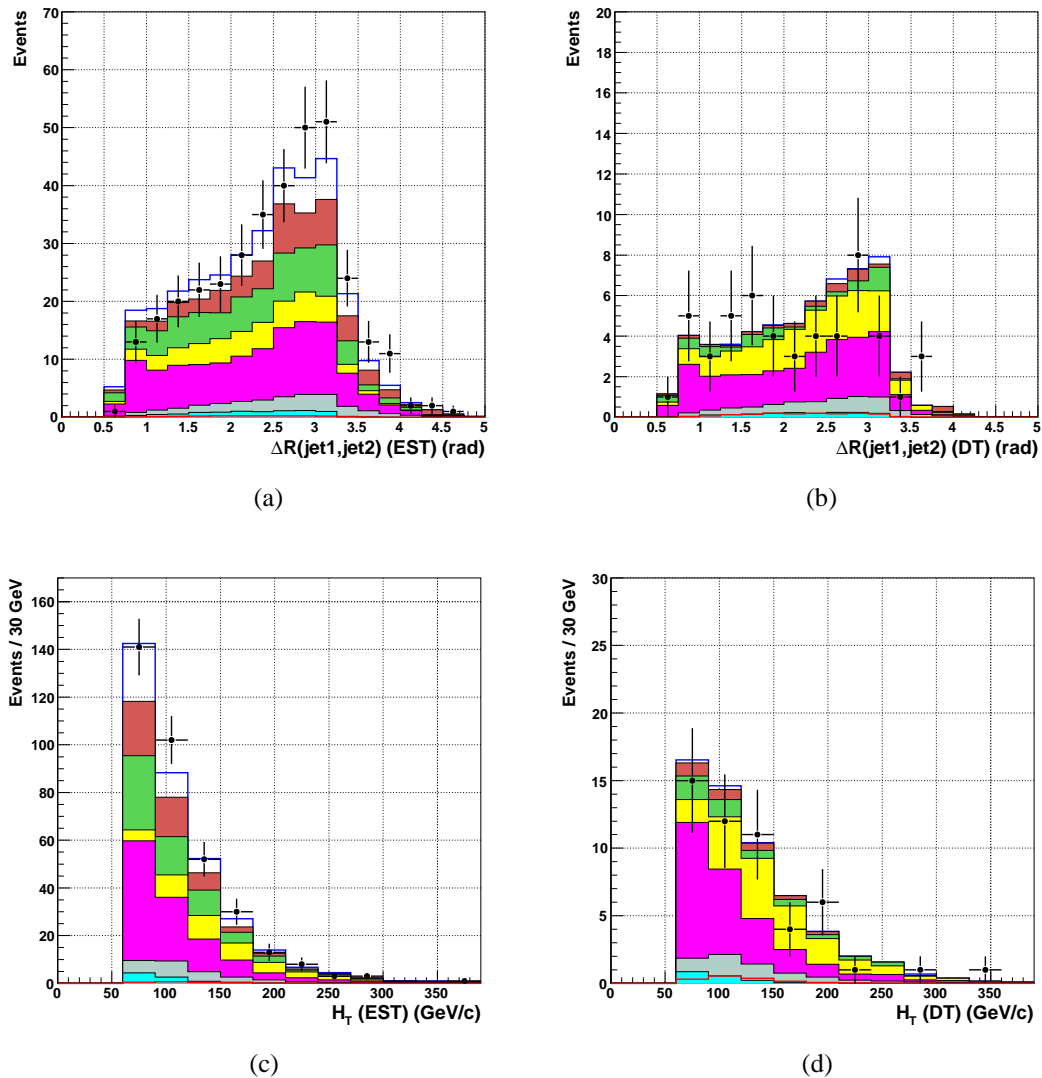


Figure 8.25. CC Analysis ( $W + 2$  Jets, EST/DT): Properties of jets in exclusive single tagged (EST) and double tagged (DT) events. (a) Separation ( $\Delta R$ ) between the two jets in the EST sample (rad) (b)  $\Delta R$  between the two jets in the DT events (rad) (c) Scalar sum of transverse momenta ( $H_T$ ) of jets in the EST sample (GeV/c) (d)  $H_T$  of jets in DT sample (GeV/c).

The dijet mass distributions of  $W + 2$ jet EC analyses are not included as input for setting cross section limits (which will be discussed in chapter 9). The dominant backgrounds to the Higgs signal after  $b$ -tagging are the single top production, the diboson production, the irreducible  $Wb\bar{b}$  production and  $t\bar{t}$  background.

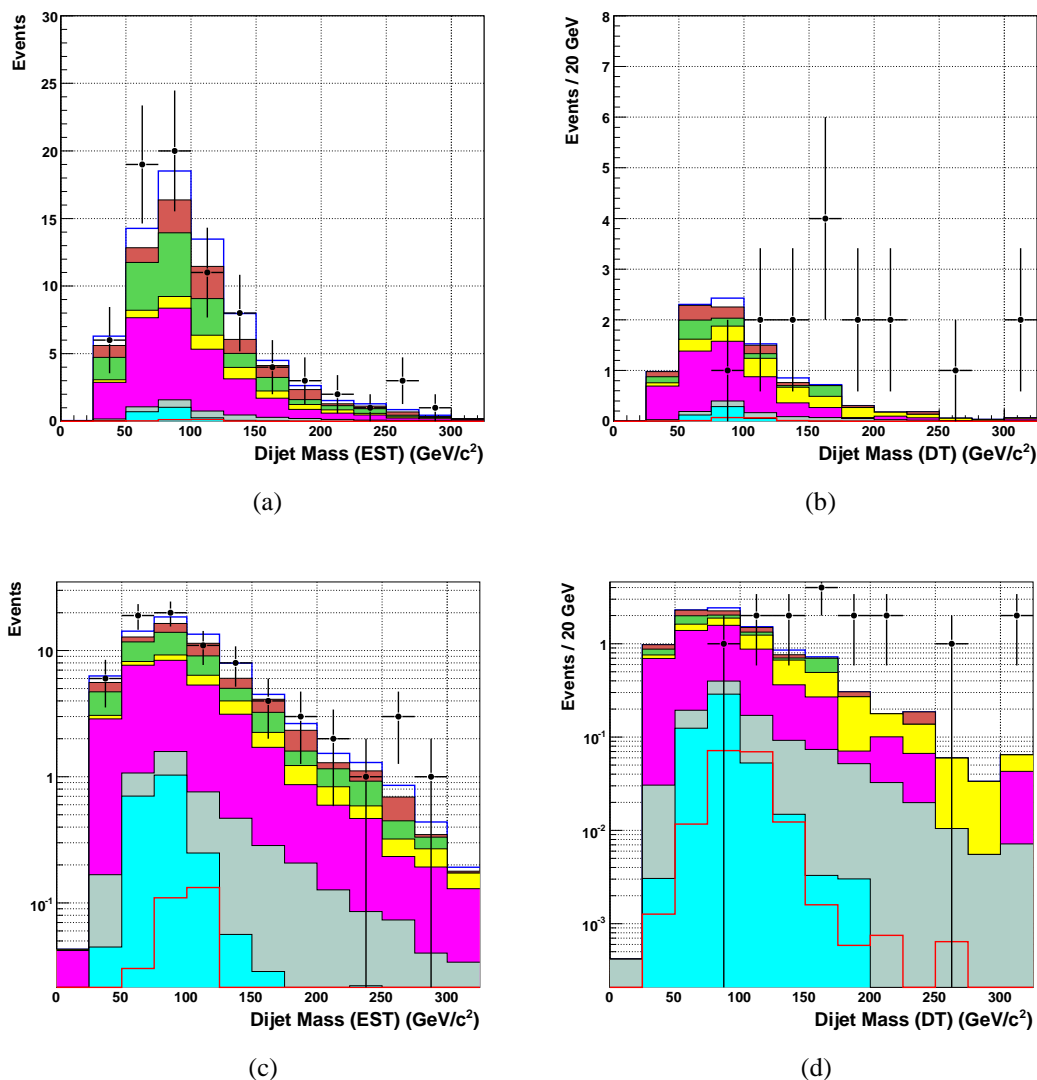


Figure 8.26. EC Analysis ( $W+2$  Jets, EST/DT): Properties of jets in exclusive single tagged (EST) and double tagged (DT) events. (a) Dijet mass (EST) ( $\text{GeV}/c^2$ ) (b) Dijet mass (DT) ( $\text{GeV}/c^2$ ). (c) and (d) The plots in the bottom row are the same distributions in logarithmic scale.

The excess of observed events in data is larger in the EC analysis. The shape of the jet  $p_T$  and  $H_T$  is not reproduced in the MC due to large differences in  $b$ -tagging in these events. The properties of jets and the dijet system are summarized in Figs. 8.26 — 8.28. Lack of statistics in these samples limit the ability to draw definitive conclusions about the EC double tagged

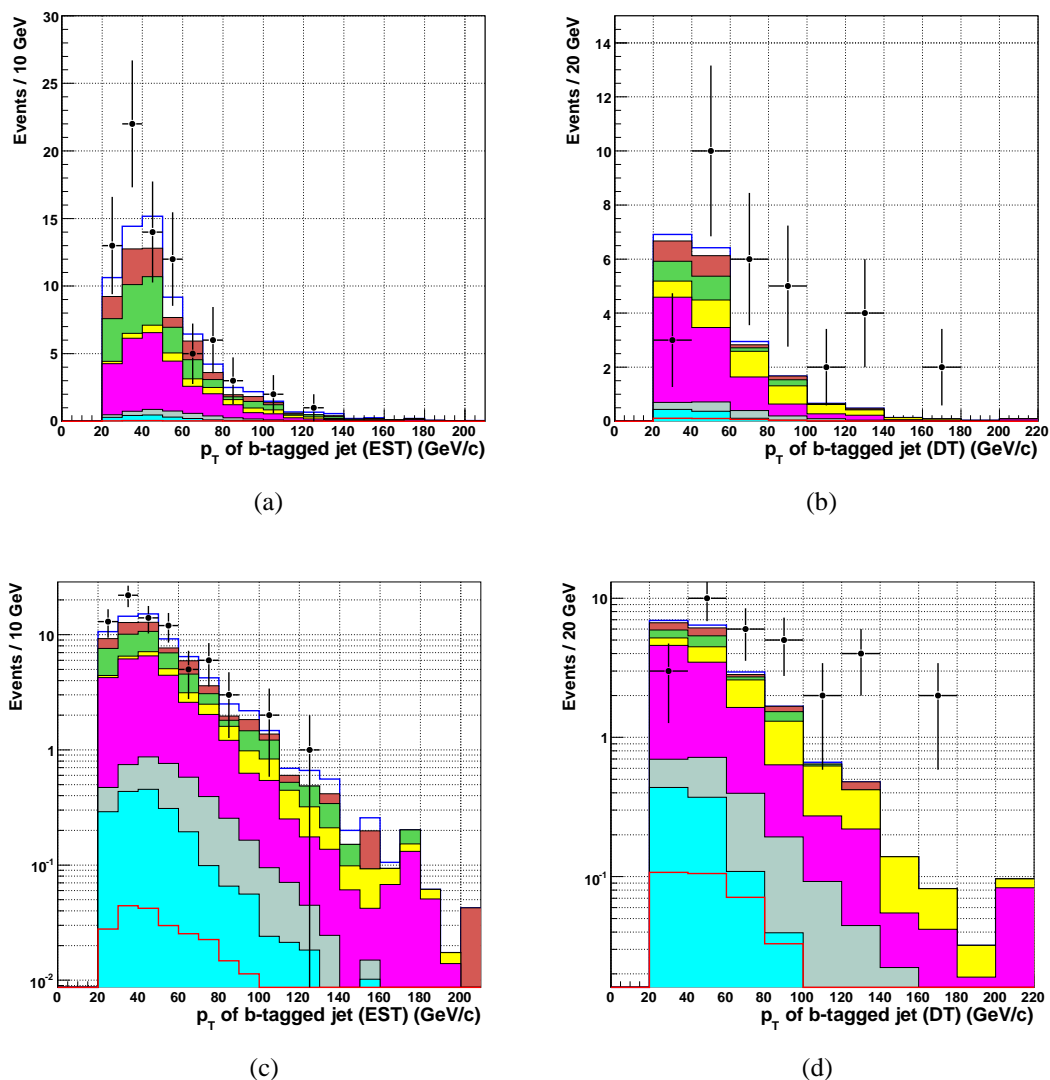


Figure 8.27. EC Analysis ( $W+ 2$  Jets, EST/DT): Properties of jets in exclusive single tagged (EST) and double tagged (DT) events. (a)  $p_T$  of  $b$ -tagged jet in the EST sample (GeV/c) (b)  $p_T$  of  $b$ -tagged jets in the DT sample (GeV/c) (c) and (d) The plots in the bottom row are the same distributions in logarithmic scale.

events. Although the jets are restricted to  $|\eta| < 2.5$ , there is a higher probability of mistagging  $b$ -jets in data compared to MC.

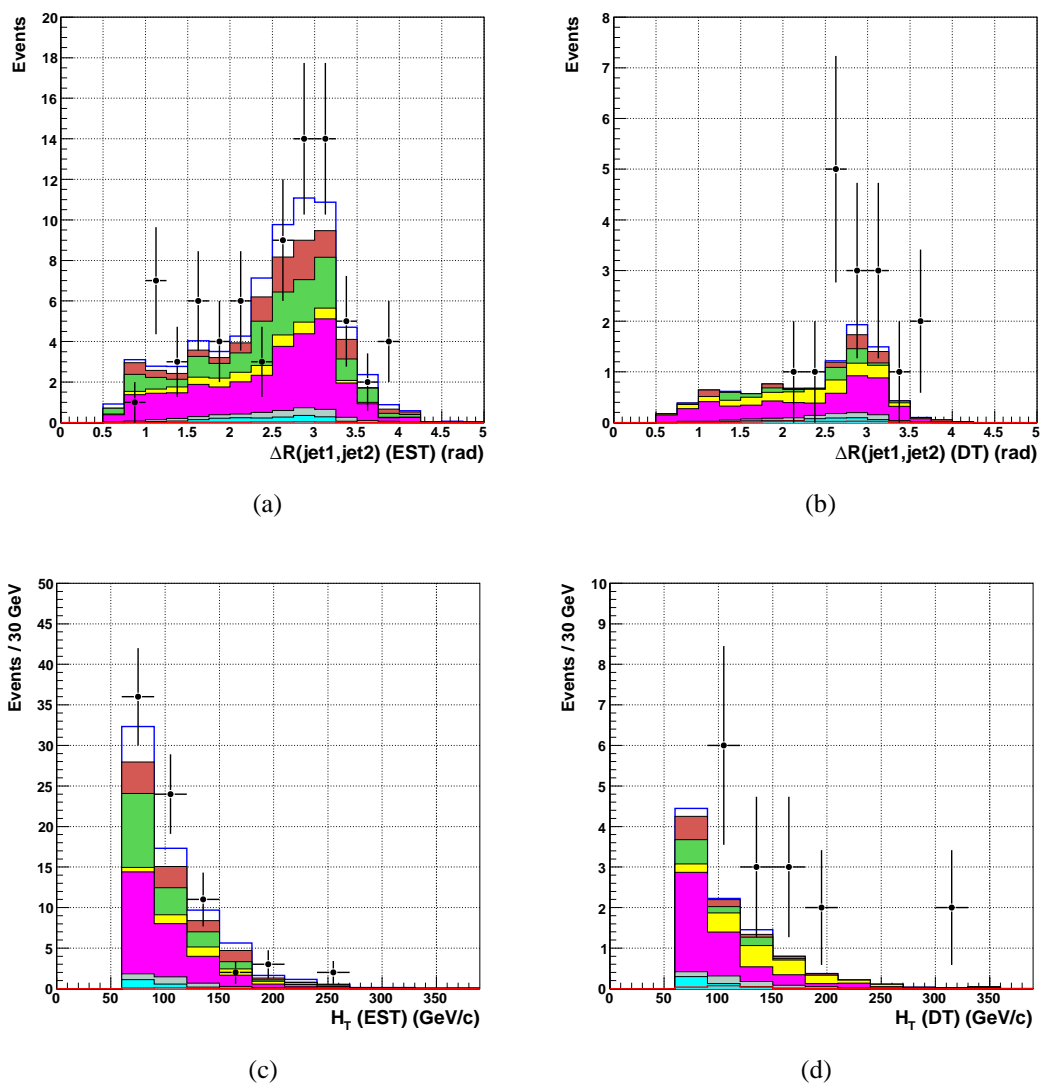


Figure 8.28. EC Analysis ( $W+ 2$  Jets, EST/DT): Properties of jets in exclusive single tagged (EST) and double tagged (DT) events. (a) Separation ( $\Delta R$ ) between the two jets in EST sample (rad) (b)  $\Delta R$  between two jets in the DT events (rad) (c) Scalar sum of transverse momenta ( $H_T$ ) of jets in the EST sample (GeV/c) (d)  $H_T$  of jets in the DT sample (GeV/c).

### 8.7.2 Event Yield

Event yield in the  $W + 2\text{jets}$  analysis is summarized in Tables. 8.4 and 8.5 for the CC and EC analyses, respectively. In the single tagged set, a total of 432 events are observed relative to an expectation of  $433.5 \pm 49.1$  events. As is evident from the table, the background due to top pairs, QCD and  $W + \text{jets}$  is a factor of four larger than the rare processes like the  $Wb\bar{b}$ ,  $WH$  and diboson ( $WW, ZZ$ ) production some of which are yet to be observed. Requiring two  $b$ -tags reduces these backgrounds and the signal significance increases, while the number of total expected and observed events becomes smaller. A total of 67 double tagged events are observed in data compared to a SM expectation of  $66.6 \pm 8.7$  events. The SM expectation is consistent with the number of observed events within the statistical and systematic uncertainties. No significant excess is observed.

Table 8.4. Summary of event yield for the  $W + 2\text{jets}$  (CC) Analysis. Observed events (last row) in data are compared to expected number of events from SM backgrounds (penultimate row) before  $b$ -tagging (column 2), after a single exclusive  $b$ -tag (column 3) and double  $b$ -tag (column 4). The  $W + \text{light jets}$  background is normalized to data (n.t.d) before  $b$ -tagging.

<b>Process</b>	<b><math>W + 2\text{jets}</math> CC-Analysis</b>	<b><math>W + 2\text{jets}</math> 1 <math>b</math>-jet</b>	<b><math>W + 2\text{jets}</math> 2 <math>b</math>-jets</b>
$WH$	$3.14 \pm 0.45$	$1.26 \pm 0.20$	$0.74 \pm 0.14$
$WZ$	$164.5 \pm 22.9$	$9.3 \pm 1.5$	$1.8 \pm 0.31$
$Wb\bar{b}$	$341.0 \pm 87.3$	$113.5 \pm 30.1$	$23.7 \pm 6.7$
$t\bar{t}$	$115.4 \pm 27.3$	$47.0 \pm 11.6$	$17.6 \pm 4.7$
Single top	$54.0 \pm 10.4$	$22.7 \pm 4.7$	$5.5 \pm 1.3$
QCD Multijet	$1084.0 \pm 162.6$	$53.4 \pm 10.0$	$2.8 \pm 0.9$
$W + \text{jets}$ (light,c)	$6516 \pm 740$	$116.2 \pm 33.8$	$5.7 \pm 1.9$
Total expectation	8274 (n.t.d.)	$362.2 \pm 48.0$	$57.1 \pm 8.6$
Observed Events	8275	354	51

Total errors (statistical and systematic) are quoted for the numbers in both tables. The estimate of systematic uncertainties is a topic in the next chapter. Theoretical uncertainties in

Table 8.5. Summary of event yield for the  $W + 2$  jets (EC) Analysis. Observed events in data are shown in the last row and are compared to expected number of events from SM backgrounds (penultimate row) before  $b$ -tagging, after an exclusive  $b$ -tag (EST) and double  $b$ -tag (DT). The  $W +$  light jets background is normalized to data.

<b>Process</b>	<b><math>W + 2</math>jets EC-Analysis</b>	<b><math>W + 2</math>jets 1 <math>b</math>-jet</b>	<b><math>W + 2</math>jets 2 <math>b</math>-jets</b>
$WH$	$0.36 \pm 0.05$	$0.16 \pm 0.02$	$0.09 \pm 0.02$
$WZ$	$35.8 \pm 5.0$	$2.2 \pm 0.3$	$0.5 \pm 0.08$
$Wb\bar{b}$	$80.8 \pm 20.7$	$26.9 \pm 7.1$	$4.4 \pm 1.2$
$t\bar{t}$	$11.7 \pm 2.8$	$5.0 \pm 1.2$	$2.0 \pm 0.5$
Single top	$6.4 \pm 1.2$	$2.8 \pm 0.6$	$0.6 \pm 0.1$
QCD Multijet	$231.8 \pm 34.8$	$10.0 \pm 1.9$	$0.9 \pm 0.3$
$W +$ jets (light,c)	$1648 \pm 187$	$24.4 \pm 7.1$	$1.1 \pm 0.4$
Total expectation	2014 (n.t.d.)	$71.3 \pm 10.3$	$9.5 \pm 1.4$
Observed Events	2015	78	16

the luminosity estimate are not included in the numbers presented but are considered for the limit setting procedure, also a topic of the next chapter.

The event yield in  $W + 2$  jets CC analysis is summarized in Table. 8.4. The largest background contribution for pre-tagged sample is from  $W +$  light jets, followed by QCD background. The irreducible  $Wb\bar{b}$  background, the  $t\bar{t}$  background, diboson production and single top production have a small contribution compared to the other two. After requiring an exclusive single  $b$ -tag, the  $Wjj$  background reduces dramatically, with the dominant contribution due to  $Wb\bar{b}$  and  $Wjj$ . By demanding two  $b$ -tagged jets, the  $Wjj$  and the QCD backgrounds are further reduced. In the double tagged sample, the largest background is  $Wb\bar{b}$  production followed by  $t\bar{t}$  production. The total expected background from all listed sources agree well with the observed number of events in data, within the statistical uncertainties for EST and DT  $W + 2$  jet CC analyses. In the  $W + 2$  jets EC analyses, similar behavior is seen in the expected and observed events as the CC analyses. The event yield for  $W + 2$  jets EC analyses are summarized in Table. 8.5.



### 8.7.3 $W + 3$ Jets Control Sample

In addition to the CC/EC EST/DT analyses, a control sample consisting of a  $W + 3$  jets selection with exactly the same selection criteria and  $b$ -tagging requirement as the  $W + 2$  jets was studied. The study of the control sample provides a cross check for the signal/background modeling in the  $W + 2$  jets. Additionally, it provides a means of including a signal process where the Higgs boson decays into two  $b$ -jets and radiates a gluon which forms the third jet. Plots of the dijet mass spectra before and after  $b$ -tagging are shown for the CC and EC analyses in Figs. 8.29(a) - 8.29(f). The event yield for CC and EC  $W+3$ jets analyses are tabulated in Tables. 8.6 and 8.7. The dijet mass spectra of EST and DT events for the control sample are shown in Fig 8.29. The agreement in shape and amplitude of the expected and observed events are very good to within  $1\sigma$  in the CC analyses. The EC analysis yields two events observed in data for double  $b$ -tagged jets (*i.e.*, Fig. 8.29(f)). The EC double tagged analysis is not used for limit setting.

Table 8.6. Summary of event yield for the  $W + 3$  jets (CC) Analysis. Observed events (last row) in data are compared to expected number of events from SM backgrounds (penultimate row) before  $b$ -tagging (column 2), after a single exclusive  $b$ -tag (column 3) and double  $b$ -tag (column 4). The  $W +$  light jets background is normalized to data (n.t.d) before  $b$ -tagging.

<b>Process</b>	<b><math>W + 3</math>jets CC-Analysis</b>	<b><math>W + 3</math>jets 1 <math>b</math>-jet</b>	<b><math>W + 3</math>jets 2 <math>b</math>-jets</b>
$WH$	$0.78 \pm 0.11$	$0.31 \pm 0.05$	$0.19 \pm 0.04$
$WZ$	$38.3 \pm 5.3$	$2.6 \pm 0.4$	$0.6 \pm 0.10$
$Wb\bar{b}$	$102.9 \pm 26.3$	$34.4 \pm 9.1$	$8.1 \pm 2.3$
$t\bar{t}$	$193.1 \pm 45.7$	$78.1 \pm 19.2$	$39.9 \pm 10.6$
Single top	$16.8 \pm 3.2$	$6.9 \pm 1.4$	$2.8 \pm 0.6$
QCD Multijet	$274.6 \pm 41.2$	$18.6 \pm 3.5$	$3.8 \pm 1.2$
$W +$ jets (light,c)	$968 \pm 109$	$28.5 \pm 8.3$	$2.7 \pm 0.9$
Total expectation	1593 (n.t.d.)	$169.1 \pm 23.2$	$57.8 \pm 11.0$
Observed Events	1594	136	46

Table 8.7. Summary of events for the  $W + 3$  jets (EC) Analysis. Observed events in data are shown in the last row and are compared to expected number of events from SM backgrounds (penultimate row) before  $b$ -tagging, after an exclusive  $b$ -tag (EST) and double  $b$ -tag (DT). The  $W +$  light jets background is normalized to data.

<b>Process</b>	<b><math>W + 3</math>jets EC-Analysis</b>	<b><math>W + 3</math>jets 1 <math>b</math>-jet</b>	<b><math>W + 3</math>jets 2 <math>b</math>-jets</b>
$WH$	$0.08 \pm 0.01$	$0.04 \pm 0.01$	$0.02 \pm 0.0$
$WZ$	$7.4 \pm 0.9$	$0.5 \pm 0.1$	$0.1 \pm 0.0$
$Wb\bar{b}$	$26.5 \pm 6.7$	$9.4 \pm 2.5$	$1.8 \pm 0.5$
$t\bar{t}$	$20.9 \pm 4.9$	$8.9 \pm 2.2$	$4.9 \pm 1.3$
Single top	$1.8 \pm 0.3$	$0.7 \pm 0.1$	$0.3 \pm 0.1$
QCD Multijet	$55.8 \pm 8.4$	$4.4 \pm 0.8$	$0.3 \pm 0.1$
$W +$ jets (light,c)	$328 \pm 39$	$7.8 \pm 2.3$	$0.7 \pm 0.2$
Total expectation	441 (n.t.d.)	$31.7 \pm 4.1$	$8.1 \pm 1.4$
Observed Events	441	28	2

The event yield in  $W + 3$  jets CC analysis is summarized in Table. 8.6. The largest background contribution for pre-tagged sample is from  $W +$  light jets, followed by QCD background. The irreducible  $Wb\bar{b}$  background, the  $t\bar{t}$  background, diboson production and single top production have a small contribution compared to the other two. After requiring an exclusive single  $b$ -tag, the  $Wjj$  background reduces dramatically, with the dominant contribution due to  $Wb\bar{b}$  and  $Wjj$ . By demanding two  $b$ -tagged jets, the  $Wjj$  and the QCD backgrounds are further reduced. In the double tagged sample, the largest background is  $Wb\bar{b}$  production followed by  $t\bar{t}$  production. The total expected background from all listed sources agree well with the observed number of events in data, within the statistical uncertainties for EST and DT  $W + 3$  jet CC analyses. The event yield for  $W + 3$  jets EC analyses are summarized in Table. 8.7. In the  $W + 3$  jets EC analyses, similar behavior is seen in the expected and observed events as the corresponding CC analyses.

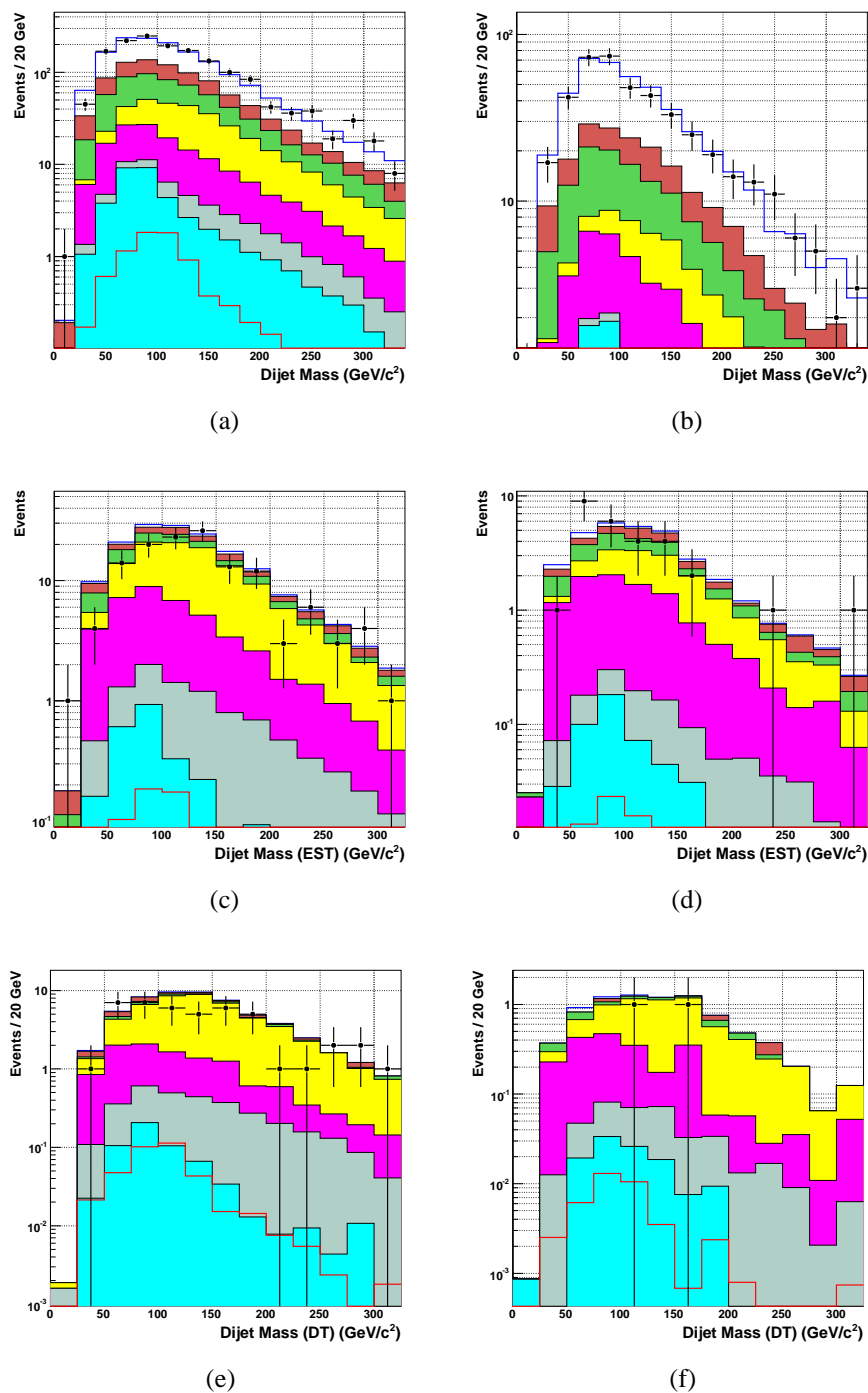


Figure 8.29. ( $W + 3$  Jets): Dijet mass spectra for the CC analysis (left column) and EC analysis (right column). Top row is before  $b$ -tagging, middle row is for an exclusive single tag, and in the bottom row two  $b$ -tags are required.

## CHAPTER 9

### SYSTEMATIC UNCERTAINTIES AND CROSS SECTION LIMITS

In the previous chapter, we modeled the signal and SM background processes, and then compared both to data using various kinematic properties of electrons,  $\cancel{E}_T$  and  $b$ -tagged jets. This chapter focuses on the determination of upper bounds on cross sections, at a particular confidence level, since we did not observe any excess of signal over the predicted background. In order to set limits we have to account for different sources of systematic uncertainties in our signal/background modeling, in addition to those originating from uncertainties in theoretical predictions of the cross sections for the signal and background processes involved. The systematic uncertainties in our background modeling are explained, followed by the limit setting procedure, and finally the cross section limits are presented.

#### 9.1 Background Uncertainties

Sources of uncertainties in the background estimate includes the scale factors applied to MC, the energy resolution of electrons and jets, and uncertainties in  $b$ -tagging and the scale factors associated with it. For each source of uncertainty, the central value of the uncertainty is varied by one standard deviation ( $\pm 1 \sigma$ ) and the analysis is carried out to estimate the number of expected signal and background events and in each source, the differences between the central value are taken as systematic uncertainty. These uncertainties are estimated separately for the single tag and double tag analyses.

### 9.1.1 Electron Reconstruction/Identification

The preselection and post-preselection efficiencies are applied to the MC electrons. Their central values are varied by  $\pm 1\sigma$  and the analysis is repeated. The systematic uncertainty is estimated to be 3%. This uncertainty estimate is based on the previous analysis [112] and has not been re-estimated in the current analysis.

### 9.1.2 Electron Energy Resolution/Smearing

The energy resolution of electrons is not modeled sufficiently well in the MC simulation. Additional energy smearing is applied to MC electrons to account for the difference between data and MC. The smearing parameters are extracted from the product of a calibration factor times a Gaussian distribution with a mean one and a small width representing the smearing function. The systematic error introduced by this smearing is estimated to be 3%. This uncertainty estimate is based on the previous analysis [112] and has not been re-estimated in the current analysis.

### 9.1.3 Trigger Efficiency

The uncertainty in trigger efficiency is estimated to be 3% for EM+Jet triggers. A systematic uncertainty of 1.2% for the EM+Jet trigger efficiency is assigned based on the efficiency change when a track match requirement on the probe electron is removed. A systematic uncertainty of 1.8% is assigned to the trigger efficiency based on the difference in the overall trigger efficiency between requiring a reconstructed jet with  $p_T > 20$  GeV and  $p_T > 25$  GeV after applying the jet energy scale corrections.

### 9.1.4 Jet Reconstruction/Identification

The difference in efficiency of the jet-ID cuts between data and simulation is quantified by the overall jet reconstruction efficiency scale factor. This scale factor has been studied in

data and MC simulations by several other analyses with final state similar to the one used in this analysis [119, 120]. The scale factor has been parametrized as a function of jet  $p_T$  and  $|\eta_d|$ . It is always smaller than one but differs from it by less than 2.5%. Jets in the simulation are rejected with a probability equal to one minus the scale factor. A systematic error of 3% is assigned to this efficiency ratio — this accounts for the difference between scale factors obtained when varying the cuts of the jet reconstruction efficiency. A 5% uncertainty is assigned for jet multiplicity modeling and jet fragmentation using an ALPGEN simulation of  $W$ +jet processes. The jet-ID and reconstruction efficiency uncertainty is 3% [105].

#### 9.1.5 Jet Energy Scale

The jet energy scale (JES) correction is varied by one standard deviation and the whole analysis is repeated. In the data, the JES uncertainty is composed of jet energy resolution uncertainty. In MC, the jet energy resolution uncertainty is not taken into account in the JES uncertainty. To account for this, the MC energy smearing is varied by the size of the jet energy resolution on MC. The uncertainty on the jet energy scale ranges from 5% to 12% for signal and all background processes.

#### 9.1.6 NN $b$ -tagging

Applying  $b$ -jet and  $c$ -jet tag rate functions to mis-tagged light quarks leads to an overestimation of the  $b$ -component of this sample when the *Tight* operating point is chosen (section 8.7.1). The scale factor is adjusted to match the prediction given by the tag rate function for a  $W$  + jets MC sample. Rescaling has little effect on the background in the EST analysis (increases by 7%) and no effect on the DT analysis. The systematic uncertainty introduced by the rescaling is 25%.

The  $p_T$  and  $\eta$  dependence of the tagging efficiency is used in deriving a systematic error on the data to MC scale factor. These are summarized below:

### 9.1.7 Estimation of QCD Background

The systematic uncertainty on the QCD background is estimated by varying the fake rate by its uncertainty ( $\pm 15\%$ ) in the subsample of events where a lepton is back-to-back with a jet in the transverse plane. The resulting variation in the QCD background, as determined by the matrix method, is considered to be the systematic uncertainty.

### 9.1.8 Luminosity

The uncertainty on the measured luminosity is 6.1% [121]. The luminosity error is accounted for as a fully correlated error between the single and double tag analyses and hence not added in quadrature with the other errors. However, the luminosity uncertainty is taken into account as an independent source for the purpose of limit setting in this analysis.

## 9.2 Theoretical Uncertainties

Theoretical uncertainties are related to the uncertainty in the cross sections used to generate the MC samples. Cross section errors for SM background processes used in Higgs searches are described in detail in [122] and are adopted for this analysis. They include:

- $t\bar{t}$ : The production cross section at NNLO is  $6.77 \pm 0.42$  pb with  $m_{top} = 175$  GeV/ $c^2$ . The relative error on the cross section yields a systematic uncertainty of 18%.

Table 9.1. Systematic errors on the data to MC scale factors for EST and DT analyses.

	EST (%)	DT (%)
<b>oldLoose</b>	4.0	3.0
<b>Tight</b>	6.0	4.0

- Single top production: The cross section at NLO in the  $s$ -channel is  $0.88 \pm 0.14$  pb and in the  $t$ -channel is  $1.98 \pm 0.30$  pb, which yield relative uncertainties of 16% and 15%, respectively.
- $WW$  or  $WZ$ : Diboson production cross sections have a relative uncertainty of 6% from PDF's and scale errors on the cross section of  $12.4 \pm 0.8$  pb for  $WW$  production.
- $Wjj$ : There are two sources of uncertainty for this process. The first is due to a normalization error arising from subtracting all other backgrounds except  $Wjj$  from data to estimate the number of  $Wjj$  events and the second is due to the flavor composition of the jets in  $Wjj$ . The jets can be either light quark jets or  $b/c$  quark jets, *i.e.*, the fractions of  $Wcj$ ,  $Wcc$ ,  $Wbb$ ,  $Wbj$  in the  $Wjj$  process must be estimated. The normalization error is  $\sim 4\%$ , and the flavor composition error is 4.8% for the EST analysis and 7.6% for the DT analysis. Adding them in quadrature leads to a total systematic error of 6% for EST and 9% for DT.
- $Wb\bar{b}$ : The uncertainty due to renormalization and factorization scales is estimated to be 17% by varying the scale settings, using the MCFM [123] program. In addition, a 4% parton distribution function (PDF) uncertainty is quoted, resulting in a total relative error of 18% on the cross section.
- K-factor: Cross sections for  $Wjj$  and  $Wb\bar{b}$  processes are calculated at LO and K-factors are used to scale them. A 20% uncertainty on the scale factors is assigned to both processes.

The sources of systematic uncertainties and their percentage values for the  $WH$  signal and all the backgrounds are listed in Table. 9.2 for the exclusive single tag analysis and in Table. 9.3 for double tag analysis. Systematic uncertainties estimated for CC analysis. Systematic uncertainties were not estimated for the EC analyses. For the limit setting, the CC systematic uncertainties were used. The largest sources of systematic uncertainty for exclusive single tag and double tag analyses are the  $b$ -tagging scale factor uncertainty and the jet energy scale



uncertainty. The largest source of theoretical uncertainty is due to cross section uncertainty and the K-factors for  $W_{jj}/W_{cj}$  and  $Wb\bar{b}$  production. All other sources are less than 5%. The total uncertainty ranges from 16% to 33%. The overall uncertainty is large — 25% - 33% for  $W_{jj}$  process followed by 26% - 28% for  $Wb\bar{b}$  production. The overall uncertainty on QCD is 15% for single tag analysis and 30% for double tag analysis.

Table 9.2. Summary of systematic uncertainties in exclusive single tag analysis.

Source	$WH$	$WZ$ $WW$	$Wb\bar{b}$ $Wc\bar{c}$	$W_{jj}$ $W_{cj}$	$t\bar{t}$	$tb$ $tqb$	QCD
Trigger eff.	3.0	3.0	3.0	3.0	3.0	3.0	-
Primary Vertex Reco.	4.0	4.0	4.0	4.0	4.0	4.0	-
EM ID/Reco eff.	3.0	3.0	3.0	3.0	3.0	3.0	-
EM Likelihood eff.	3.0	3.0	3.0	3.0	3.0	3.0	-
EM energy/smearing	4.0	4.0	4.0	4.0	4.0	4.0	-
Jet ID/Reco eff.	3.0	3.0	3.0	3.0	3.0	3.0	-
Jet multiplicity/frag.	5.0	5.0	5.0	5.0	5.0	5.0	-
Jet Energy Scale	9.0	8.0	9.0	9.0	12.0	5.0	-
Jet taggability	3.0	3.0	3.0	3.0	3.0	3.0	-
NN-tagger Scale Factor	6.1	6.5	6.1	15.0	6.1	6.1	-
Acceptance err.	14.8	14.4	14.8	19.1	16.8	12.8	-
Cross Section	6.0	6.0	9.0	9.0	16.0	16.0	-
Heavy-Flavor K-factor			20.0	20.0			-
<b>Total uncertainty (%)</b>	<b>16.0</b>	<b>15.6</b>	<b>26.5</b>	<b>29.1</b>	<b>24.6</b>	<b>20.5</b>	<b>18.8</b>

### 9.3 $WH$ Cross Section Limit

The goal of this analysis is to search for a possible signal of  $WH$  associated production. Measured data is compared with signal and background processes whose cross sections are consistent with those predicted by the Standard Model. Since no excess in signal was observed compared to the SM expectation, cross section upper limits at a 95% confidence level (CL)

Table 9.3. Summary of systematic uncertainties in double tag analysis.

Source	$WH$	$WZ$ $WW$	$Wb\bar{b}$ $Wc\bar{c}$	$Wjj$ $Wcj$	$t\bar{t}$	$tb$ $tqb$	QCD
Trigger eff.	3.0	3.0	3.0	3.0	3.0	3.0	-
Primary Vertex Reco.	4.0	4.0	4.0	4.0	4.0	4.0	-
EM ID/Reco eff.	3.0	3.0	3.0	3.0	3.0	3.0	-
EM Likelihood eff.	3.0	3.0	3.0	3.0	3.0	3.0	-
EM energy/smearing	4.0	4.0	4.0	4.0	4.0	4.0	-
Jet ID/Reco eff.	5.0	5.0	5.0	5.0	5.0	5.0	-
Jet multiplicity/frag.	5.0	5.0	5.0	5.0	5.0	5.0	-
Jet Energy Scale	9.0	6.0	9.0	8.0	12.0	5.0	-
Jet taggability	3.0	3.0	3.0	3.0	3.0	3.0	-
NN-tagger Scale Factor	11.2	11.2	11.2	21.0	11.2	11.2	-
Acceptance err.	18.0	16.7	18.0	25.0	19.7	16.4	-
Cross Section	6.0	6.0	9.0	9.0	16.0	16.0	-
Heavy-Flavor K-factor			20.0	20.0			-
<b>Total uncertainty (%)</b>	<b>19.0</b>	<b>17.8</b>	<b>28.4</b>	<b>33.2</b>	<b>26.7</b>	<b>22.9</b>	<b>30.6</b>

for production of the Higgs boson are derived. The limit calculation is based on a modified frequentist (see [124,125] for example) statistical approach. The limit setting procedure and the combination of different analyses to obtain a cross section limit are outlined in the subsequent sections. The limit calculation presented here follows the procedure outlined in [126].

### 9.3.1 Limit Calculation Method

The dijet mass spectrum for which one or more jets are  $b$ -tagged is the variable used to set upper limits on the production cross section for the Higgs boson. For each bin of the dijet mass distribution, we have a measure of the number of events observed in data,  $d$ , the expected number of background events,  $b$ , and expected number of signal events,  $s$  from our modeling of SM processes. Two hypotheses can be defined, and the observed data can be compared simultaneously with both:

- Background Only (Null) Hypothesis,  $H_0$ . This hypothesis corresponds to an absence of  $WH$  signal, and instead the data being consistent with the number of background events predicted by the SM.
- Signal+Background Hypothesis,  $H_1$ . This hypothesis corresponds to a  $WH$  signal being present. The observed data is consistent with a  $WH$  signal contribution in addition to the SM background.

To calculate the limits the following procedure is used:

1. Define a test statistic  $Q$  is which discriminates signal-like outcome from the background-like outcome. An optimal choice for the test statistic is shown to be the likelihood ratio [127, 128]:

$$Q = \frac{P(data|H_1)}{P(data|H_0)} \text{ where} \quad (9.1)$$

$$P(data|H_1) = \frac{e^{-(s+b)}(s+b)^d}{d!} \quad (9.2)$$

$$P(data|H_0) = \frac{e^{-b}b^d}{d!} \quad (9.3)$$

The likelihood ratio can be expressed in a form which is computationally easier by defining the log-likelihood ratio (LLR) test statistic:

$$\chi = -2 \ln Q \quad (9.4)$$

2. The test statistic expressed in terms of a specific observation (or hypothesis)  $n$ , can be written as:

$$\chi_n = 2 \left[ s - n \ln \left( 1 + \frac{s}{b} \right) \right] \quad (9.5)$$

Careful observation of Eq. 9.4 shows a singularity in the test statistic when  $b \rightarrow 0$ . Smoothing techniques using the Gaussian kernel approximation [129] are applied to mitigate the effect of limited statistics in the backgrounds leading to this singularity.

3. Define two Frequentist confidence levels:

$$CL_{s+b} = P_{H_1}(\chi \leq \chi_d) = \int_{-\infty}^{\chi_d} \left( \frac{dP_{H_1}}{d\chi} \right) d\chi \quad (9.6)$$

$$CL_b = P_{H_0}(\chi \leq \chi_d) = \int_{-\infty}^{\chi_d} \left( \frac{dP_{H_0}}{d\chi} \right) d\chi \quad (9.7)$$

The confidence level for excluding the possibility of signal production in addition to background (s+b hypothesis) is given by Eq. 9.6, which is the probability that the test statistic would be less than or equal to that observed in the data, assuming signal and background are present at their hypothesized levels. Similarly, we can assume a null signal and presence of only the background, and the probability that the test statistic would be less than or equal to that observed in data. This is given by Eq. 9.7.

4. Treating the two hypotheses as Poisson counting experiments with expected number of signal ( $s$ ), background ( $b$ ) and observed data ( $d$ ), generate pseudoexperiments randomly varied within the statistical and systematic uncertainties to simulate representative outcomes of repeated experiments measuring the values of  $s$ ,  $b$  and  $d$ . The Poisson probability distribution functions thus obtained will define the sample spaces from which these values are drawn. This step can be illustrated graphically as shown in Fig. 9.1
5. Marginalization: To include systematic uncertainties, rederive the mean value ( $\mu_s$ ) of the Poisson PDF during the  $i^{th}$  iteration of the pseudoexperiment, using a sum of individual Gaussian uncertainties for each source and for each uncertainty. In effect, the inclusion

of uncertainties has the effect of broadening the PDF's, thereby degrading the separation power of the likelihood ratio.

$$\mu_i^s = \mu^s \left[ 1 + \sum_{j=1}^N RGaus(\epsilon_j^s) \right] \quad (9.8)$$

6. Profiling is a method used to improve the search sensitivity by generating a “best fit” model of the data for a given set of  $d$ ,  $s$  and  $b$  values. In this approach the null hypothesis is adjusted such that the PDF's are maximized over the space of all possible values of systematic uncertainties. This procedure is called the profile-likelihood technique.
7. Construct a modified Frequentist confidence level [130, 131]:

$$CL_s = \frac{CL_{s+b}}{CL_b} \quad (9.9)$$

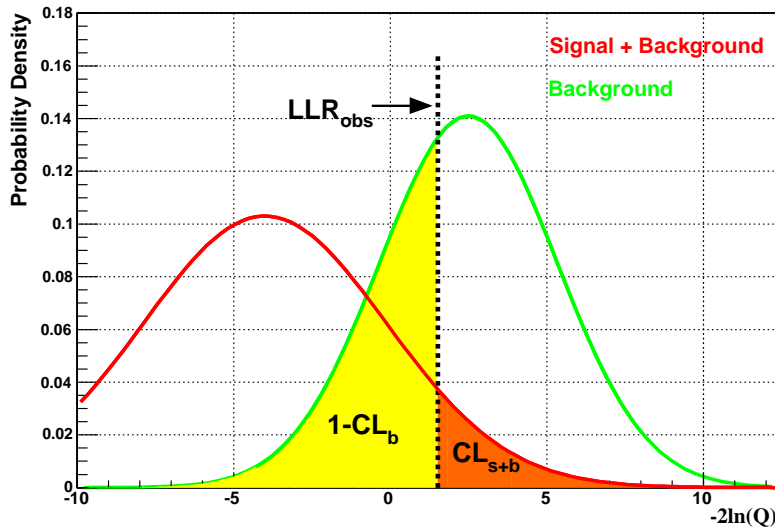


Figure 9.1. Illustration of the  $CL_S$  method. The green (red) curve represents the Poisson PDF  $dP_{H_0}/d\chi$  ( $dP_{H_1}/d\chi$ ) with mean value  $b$  ( $s + b$ ). The black dotted line indicates the observed LLR,  $\chi_d$ . The area under the green (red) curve to the right of  $\chi_d$  represents  $CL_b$  ( $CL_{s+b}$ ).

8. Assuming the  $WH$  signal rate to be  $R_s = \sigma_s \mathcal{L} \epsilon_s$ , where  $\sigma_s$  is the signal cross section,  $\mathcal{L}$  is the luminosity and  $\epsilon_s$  is the signal acceptance, the 95% CL limit can be calculated by calculating  $CL_s$  iteratively until it falls below 5% (*i.e.*,  $CL_s \leq 5\%$ ) and during each iteration, scaling the signal rate by a factor  $X_f$ . This process is applied for calculation of the expected limit (where the outcome matches the expected background) and the observed limit (where the outcome matches the observed data).
9. The 95% CL upper limit for the cross section is given by  $X_f \sigma_s$ .

#### 9.4 Cross Section Limits

Using the invariant dijet mass distributions for signal (with Higgs masses  $m_H \in \{105, 115, 125, 135, 145\}$  GeV/ $c^2$ ), along with the backgrounds and observed data, upper limits on the rate of associated  $WH$  production with  $H \rightarrow b\bar{b}$  are derived. Each distribution is binned to a 5 GeV/ $c^2$  mass resolution over the range  $0 < m_H < 200$  GeV/ $c^2$ . The expected background and signal distributions are smoothed via the Gaussian kernel approximation to lessen the impact of limited Monte Carlo statistics.

Limits are calculated at 95% confidence level using the semi-Frequentist  $CL_s$  approach with a Poisson log-likelihood ratio test statistic. The impact of systematic uncertainties is incorporated through marginalization of the Poisson probability distributions for signal and background via a Gaussian distribution. All correlations in systematic uncertainties are maintained between signal and background. The expected distributions for the background are evaluated by minimizing a profile likelihood function, referencing the shape and rate of the observed distributions in the sideband regions [132]. The sideband regions are defined by ignoring all bins with a signal to background ratio greater than  $10^{-3}$ . All derived upper limits are calculated using 50000 simulated outcomes and requiring an accuracy of 0.1% in the confidence levels, *i.e.*,  $94.9\% \leq CL_s \leq 95.1\%$ .

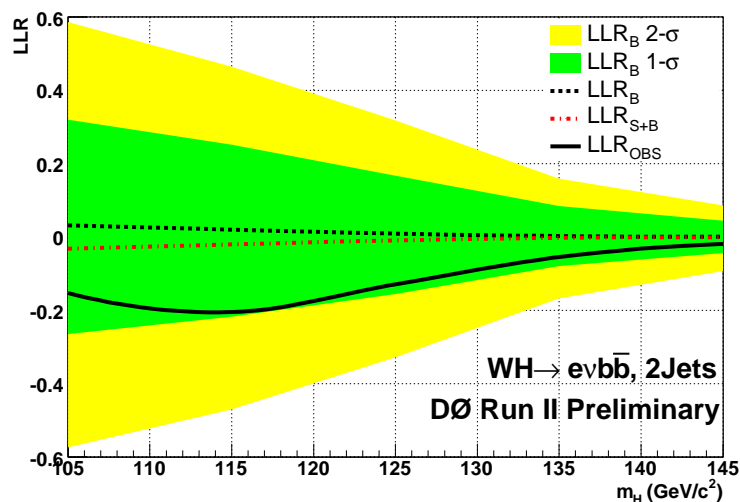
Both expected and observed upper limits are derived, wherein the evaluation of expected limits assumes a hypothetical outcome matching the expected background. The resulting upper limits are presented in two formats:

1. the cross section that can be excluded at 95% confidence level.
2. the ratio of the cross section to the expected SM Higgs production cross section.

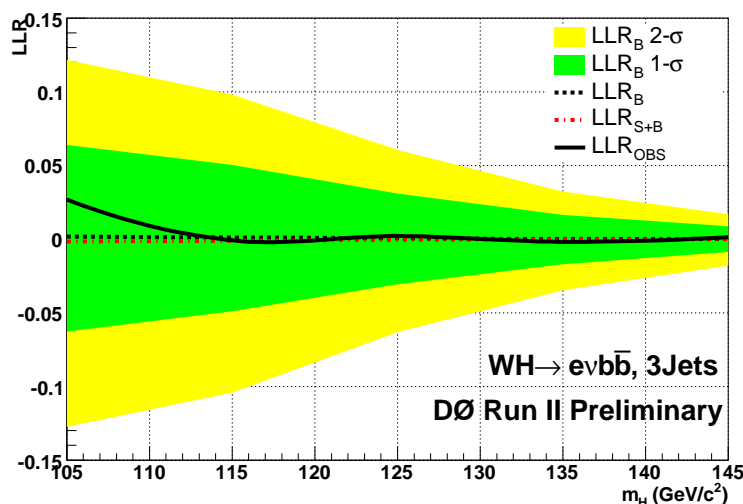
Figures 9.2(a) and 9.2(c) show the log-likelihood ratio (LLR) distributions for the  $WH \rightarrow e\nu b\bar{b}$  2-jet and 3-jet channels, respectively (single- and double-tags combined). Included in these figures are the LLR values for the signal+background hypothesis ( $LLR_{s+b}$ ), background-only hypothesis ( $LLR_b$ ), and the observed data ( $LLR_{obs}$ ). The shaded bands represent the 1 and 2 standard deviation ( $\sigma$ ) departures for  $LLR_b$ . These distributions can be interpreted as follows:

- The separation between  $LLR_b$  and  $LLR_{s+b}$  provides a measure of the overall power of the search, *i.e.*, the ability of the analysis to discriminate between the  $s + b$  and  $b$ -only hypotheses.
- The width of the  $LLR_b$  distribution (shown here as 1 and 2 standard deviation ( $\sigma$ ) bands) provides an estimate of how sensitive the analysis is to a signal-like fluctuation in data, taking account of the presence of systematic uncertainties. For example, when a  $1\text{-}\sigma$  background fluctuation is large compared to the signal expectation, the analysis sensitivity is thereby limited.
- The value of  $LLR_{obs}$  relative to  $LLR_{s+b}$  and  $LLR_b$  indicates whether the data distribution appears to be more signal-like or background-like. As noted above, the significance of any departures of  $LLR_{obs}$  from  $LLR_b$  can be evaluated by the width of the  $LLR_b$  distribution.

The LLR distributions for the  $W + 2$  jets analysis is shown in Fig. 9.2(a). The analysis can distinguish between  $LLR_{s+b}$  and  $LLR_b$  relatively well for Higgs masses below  $125 \text{ GeV}/c^2$  after which it loses its discrimination power. The  $LLR_{obs}$  value is less than zero for the entire Higgs mass range, which indicates that the data is more signal-like. This is due to the fact that



(a)



(b)

Figure 9.2. Log-likelihood ratio (LLR) distributions for null ( $LLR_b$ ) and signal+background ( $LLR_{s+b}$ ) hypotheses are compared to those observed in data ( $LLR_{obs}$ ). The green and yellow bands indicate the analysis sensitivity to a signal-like fluctuation in data at the 1- $\sigma$  and 2- $\sigma$  levels respectively with systematics included. (a) LLR plot for the  $W + 2$  jets (CC+EC) analysis and (b) LLR plot for the  $W + 3$  jets (CC+EC) analysis as a function of Higgs mass:  $105 < m_H < 145 \text{ GeV}/c^2$ .

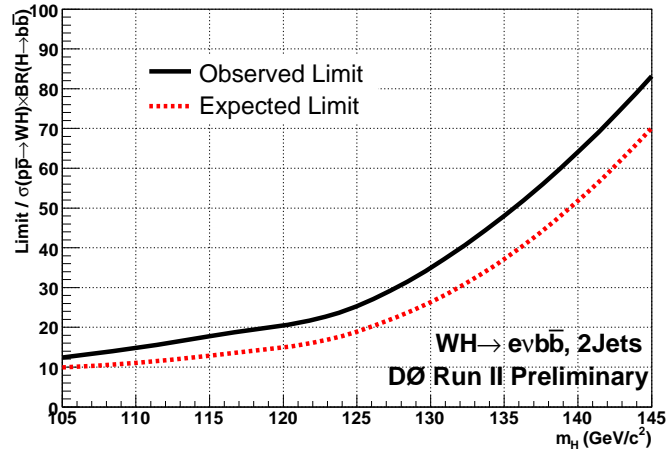
the number of events observed is in excess of that expected. The consequence of this fact is that the observed limit is larger (worse) than the expected limit for the entire range of Higgs masses. The data excess is within the 1 $\sigma$  (green band) of the background fluctuation. The



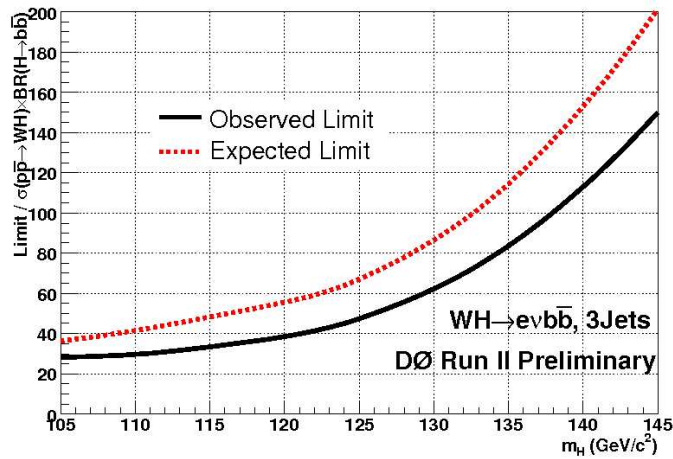
observed and expected limit-ratios are shown in Fig. 9.3(a), which corroborate the LLR plots. The observed limit-ratio is larger than the expected limit-ratio. For larger Higgs masses (*i.e.*,  $> 130 \text{ GeV}/c^2$ ), these ratios monotonically increase to large values.

Figure 9.2(b) shows a similar LLR plot for the  $W + 3$  jets analysis. The discrimination power of the analysis is poor, *i.e.*, the separation between  $\text{LLR}_{s+b}$  and  $\text{LLR}_b$  is extremely small. The  $\text{LLR}_{obs}$  is close to zero, with a small fluctuation at smaller Higgs masses, which indicates that the data is more background-like. The observed limit is therefore smaller (better) than the expected limit. The observed and expected limit-ratios of Fig. 9.3(b) illustrate this fact. The expected limit-ratio is larger (worse) than the observed limit-ratio for the entire range Higgs mass range.

The combination of all  $WH \rightarrow e\nu b\bar{b}$  analyses *i.e.*,  $W + 2$  jets (CC-EST and CC-DT) and  $W + 3$  jets (CC-EST and CC-DT), leads to the total expected and observed limits shown in Fig. 9.4. The observed limit for a Higgs mass of  $115 \text{ GeV}/c^2$  is  $2.4 \text{ pb}$  for  $W + 2$  jets CC analysis and  $1.96 \text{ pb}$  when combined with EC analysis. When this is combined with  $W + 3$  jets CC and EC analyses, the observed limit does not change. However, the expected limit for  $W + 2$  jets CC analysis is  $1.37 \text{ pb}$  and it improves when the EC and the  $W + 3$  jets analyses are combined. The best value for the expected limit is  $1.28 \text{ pb}$ . The cross section ratios obtained using the individual analyses are summarized in Table 9.4. The expected limit improves with the combination while the observed limit is insensitive to the combination.



(a)



(b)

Figure 9.3. Expected (median) and observed 95% CL upper limits on the cross section ratio for (a) the  $W + 2$  jets (CC+EC) analysis and (b) for the  $W + 3$  jets (CC+EC) analysis as a function of Higgs mass in the range  $105 < m_H < 145 \text{ GeV}/c^2$ .

Table 9.4. Expected ratio ( $\sigma_{exp}/\sigma_{SM}$ ) and observed ratio ( $\sigma_{obs}/\sigma_{SM}$ ) of upper limits for the production cross section of a  $115 \text{ GeV}/c^2$  Higgs boson compared to its SM prediction ( $\sigma_{SM} = 0.13 \text{ pb}$ ). The expected ratio is given in parantheses.

Analysis	CC	CC+EC
$W + 2j$	10.5(18.4)	10.1 (15.1)
$W + 2j$ and $W + 3j$	10.1 (20.7)	9.9 (18.4)

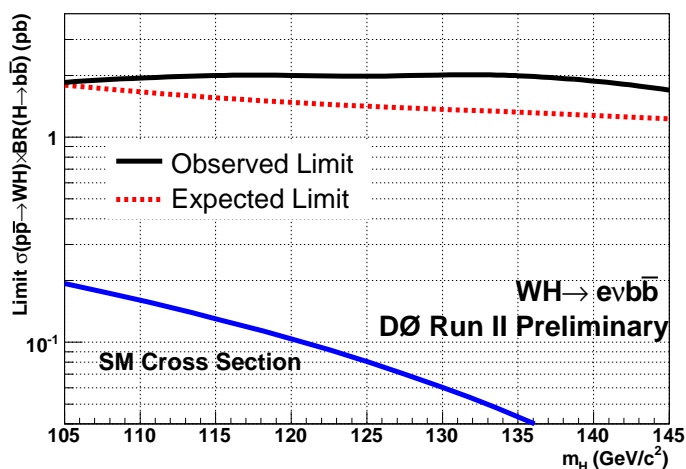


Figure 9.4. 95% confidence level cross section upper limits on  $WH$  associated production as a function of SM Higgs mass in the range  $105 < m_H < 145 \text{ GeV}/c^2$ , using the full combination of CC and EC analyses. Observed and expected (median) limits are shown and are compared to the SM expectation. Refer to Table 9.4 for the values of expected and observed limit ratios.

## CHAPTER 10

### CONCLUSIONS AND DISCUSSION

#### 10.1 Combined $WH \rightarrow \ell\nu b\bar{b}$ Result

To increase the sensitivity of the search, this analysis has been combined with a portion of the dataset from the Tevatron Run IIB (June 2006 to April 2007,  $0.63 \text{ fb}^{-1}$ ). The data from the two phases are analyzed separately before the combination. A similar analysis in the muon channel from the Higgs working group has also been added to enhance the search sensitivity. A neural net (NN) discriminant [133] is applied to the selected events from both analyses to discriminate signal from the SM background and a search is performed for the  $WH$  signal at high values of the discriminant. The results for the combined search  $p\bar{p} \rightarrow WH \rightarrow \ell\nu b\bar{b}$  are shown in Fig. 10.1.

The ratio of the expected and observed limits are shown as red-dotted and solid-black curves in Fig. 10.1(a). The cross section expectation from Standard Model is normalized to 1.0 and shown as a horizontal line with an abscissa of 1.0 for Higgs masses ranging from 105 to 145  $\text{GeV}/c^2$ . The expected and observed cross section limit ratio for a Higgs mass of 115  $\text{GeV}/c^2$  are 10 and 11 respectively. The expected (dotted red curve) and observed (solid red curve) cross section upper limits at 95% CL for the combination is shown in Fig. 10.1(b). This neural net analysis achieves a factor of ten improvement in sensitivity compared to the previous analysis by CDF (with  $320 \text{ pb}^{-1}$  of data shown as solid pink curve) and is comparable the sensitivity achieved by a similar analysis with a similar dataset of  $1.7 \text{ fb}^{-1}$  at the CDF experiment whose observed and expected limits are shown as solid and dotted blue curves.

The  $W + 2$  jets and  $W + 3$  jets events with exclusive single  $b$ -tags and double  $b$ -tags are analyzed with a NN-based selection using  $1.7 \text{ fb}^{-1}$  of  $D\bar{D}$  data and subsequently combined

to maximize the search sensitivity for  $WH$  associated production. No signal in excess of the SM is observed. 95% CL upper limits are derived on the production cross section  $\sigma(p\bar{p} \rightarrow WH) \times BR(H \rightarrow b\bar{b})$  as a function of Higgs mass in the range  $105 < m_H < 145 \text{ GeV}/c^2$ . The expected and observed limit are summarized in Table 10.1.

Table 10.1. 95% CL expected and observed limits on  $\sigma(p\bar{p} \rightarrow WH) \times BR(H \rightarrow b\bar{b})$  as a function of the Higgs mass [134].

$m_H$ (GeV/ $c^2$ )	expected limit (pb)	observed limit (pb)
105	1.29	1.42
115	1.16	1.42
125	1.12	1.41
135	0.94	1.16
145	0.84	1.06

## 10.2 Full SM Combination of $D\emptyset$ Searches

The SM Higgs searches performed by the  $D\emptyset$  experiment are organized into several final states (channels) in order to isolate a Higgs signal in specific decay mode. These analyses are optimized to provide maximum search sensitivity and be mutually exclusive after the application of all selection criteria. This allows for a combination of all the channels into a single search result. The list of channels used in the combination includes the current analysis among others, all of which are listed below:

1.  $p\bar{p} \rightarrow WH \rightarrow \ell \nu b\bar{b}$  ( $\ell = e, \mu, \tau \rightarrow e/\mu$ )
2.  $p\bar{p} \rightarrow ZH \rightarrow \ell \ell b\bar{b}$  ( $\ell = e, \mu, \nu$ )
3.  $p\bar{p} \rightarrow WH \rightarrow W W^+ W^-$
4.  $p\bar{p} \rightarrow H \rightarrow W^+ W^-$

The full combination includes twenty-one analyses. The LLR distributions are summed over all individual channels and over all bins in each channel. This summation ensures that the individual channel sensitivities are maintained. Systematics are treated as Gaussian uncertainties and correlations between the systematics is taken into account while establishing the limit. The result of the full combination is shown in Fig. 10.2.

One of the salient features of the full combination is the proximity of the expected/observed limits to the Standard Model expectation for a Higgs mass of  $160 \text{ GeV}/c^2$ , where  $p\bar{p} \rightarrow H \rightarrow W^+W^-$  dominates. The observed 90% CL limit ratio to SM cross sections for the full combination range from 8.3 at  $m_H = 115 \text{ GeV}/c^2$  to 3.5 at  $m_H = 160 \text{ GeV}/c^2$ . Similarly the expected cross section ratios range from 6.0 - 4.6 for the same mass range. A combination of CDF and DØ experiments is expected to yield maximum sensitivity in this region. The prospects for excluding (or otherwise discovering) a  $160 \text{ GeV}/c^2$  Higgs are bright by the end of the year 2009, when the Tevatron is expected to deliver  $8 \text{ fb}^{-1}$  per experiment.

### 10.3 Future Work

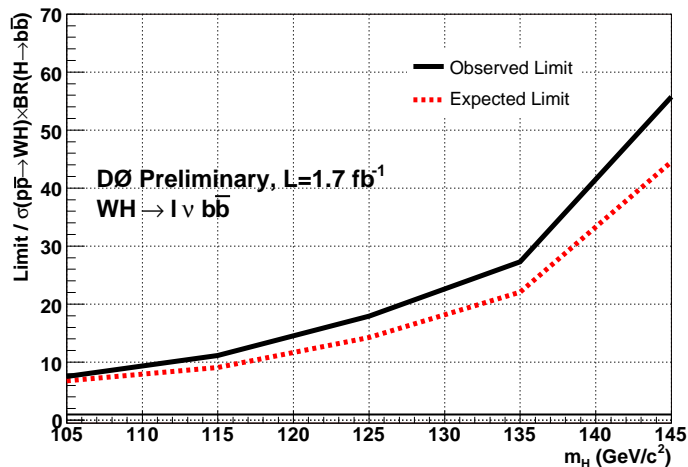
There are several ways of improving the analysis presented in this thesis, some of which are discussed here.

- **Dijet mass resolution:** The mass resolution of the dijet system which forms the main input variable for the search, can be improved. One of the ways it can be achieved is by improving the jet energy resolution of the constituent  $b$ -jets. This would dramatically improve the signal significance.
- **Electron ID:** The electron isolation can be combined with a an isolation on the track associated track to the EM cluster, which will significantly reduce the QCD fake rate. There is ample scope for improvement in the other selection criteria that distinguishes an electron from a jet.

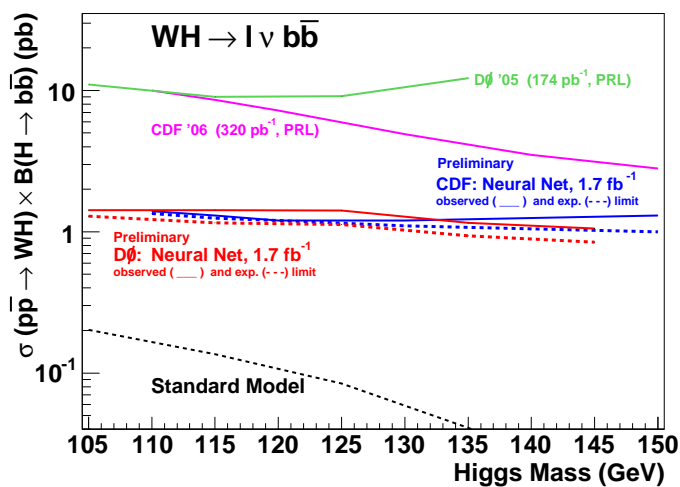
- $Wb\bar{b}$  and  $WH$  separation: It is possible to exploit the differences in the kinematic properties of  $WH$  and  $Wb\bar{b}$  in order to separate the two. Once these variables are identified, one could use multivariate techniques to obtain a separation between the two.
- $Wjj$  composition: The content of light quarks and heavy quarks in a  $Wjj$  sample could improve the  $b$ -tagging significantly. The amount of  $Wcj$ ,  $Wcc$ ,  $Wbj$  and  $Wbb$  in a  $Wjj$  sample will allow the  $b$ -tagging algorithm to exploit these ratios to efficiently tag  $b$ -quarks.
- Asymmetric  $b$ -tagging: Both jets in a  $W + 2$  jets analysis need not be tagged with the same criteria. There is a possibility of tagging the leading jet with a certain efficiency and a fake rate which is different from that used to tag the second jet. This could improve the EST and DT analyses significantly.
- Improvements in  $b$ -tagging will lead to a reduction of  $b$ -tagging systematic uncertainties. Similarly a reduction in systematic uncertainties due to improved lepton identification could lead to an improvement in search sensitivity. The theoretical uncertainties on the cross sections of certain rare processes are large. There is evidence for diboson production and single top production, but more accurate measurements on these quantities requires more statistics.

#### 10.4 Concluding Remarks

It is an exciting time for the Higgs searches at the Tevatron, leading into the era of the LHC. The increasing luminosity and consequently larger datasets for analyses aid these searches and uncover new challenges. The results of the Higgs searches at the Tevatron are a vital input to the new searches at the LHC experiments in the imminent future. A seven-fold increase in center-of-mass energy is unprecedented and could yield new insights into the nature of the Higgs boson and the EW symmetry breaking.



(a)



(b)

Figure 10.1. (a) Ratio of 95% upper CL limits on expected and observed cross sections to the SM expectation for the full combination (electron, muon, single tag and double tag) of Neural Net analyses, and (b) the 95% CL expected and observed cross section limits (in pb) as a function of Higgs mass. The Neural Net analysis is compared to an equivalent analysis with 1.7 fb<sup>-1</sup> data from the CDF collaboration, previous analyses with smaller datasets, and the SM expectation.



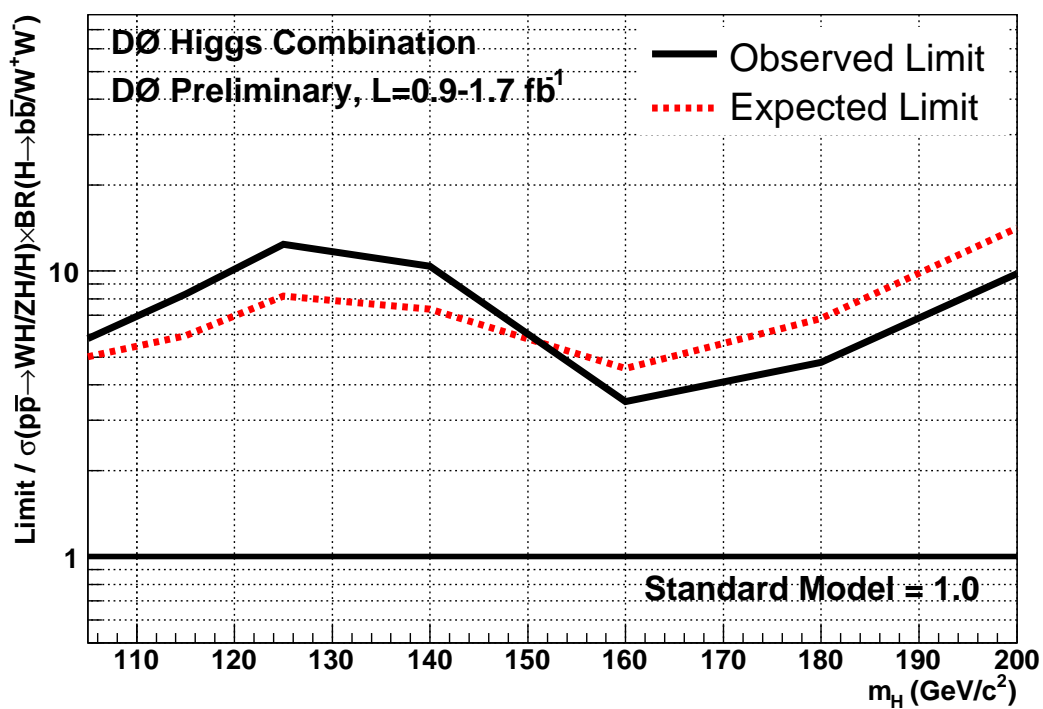


Figure 10.2. Expected and observed 95% CL cross section ratios for the combined  $WH$ ,  $ZH$ ,  $H$ ,  $H \rightarrow b\bar{b}$  and  $W^+W^-$  analyses, for a Higgs mass in the range  $105 \leq m_H \leq 200$  GeV/c<sup>2</sup>.

## REFERENCES

- [1] S. L. Glashow, *Nucl. Phys.* 22, 579, 1961.
- [2] S. Weinberg, *Phys. Rev. Lett.* 19, 1264, 1967.
- [3] A. Salam, ‘Proceedings to the Eighth Nobel Symposium’, N. Svartholm, Ed. John Wiley & Sons, 1968.
- [4] S. L. Glashow, J. Iliopoulos and L. Maiani, *Phys. Rev.* **D** 1285 1970.
- [5] C. Quigg, *Gauge Theories of Strong, Weak and Electromagnetic Interactions*, Addison-Wesley, ISBN 0-201-32832-1, 1997.
- [6] V. D. Barger and R. J. N. Philips, *Collider Physics*, Updated Ed. Addison-Wesley, ISBN 0-201-14945-1, 1996.
- [7] D. Griffiths, *Introduction to Elementary Particles*, John Wiley & Sons, ISBN 0-471-60386-4, 1987.
- [8] Refer to the following URL for a tour of the Standard Model - <http://particleadventure.org>
- [9] T. Hambye and K. Riesselmann, *Phys. Rev.* **D** 55, 7255, 1997.
- [10] LEP Electroweak Working Group web-page: <http://lepewwg.web.cern.ch/LEPEWWG/>
- [11] P. Higgs, Broken Symmetries, Massless Particles and Gauge Fields, *Phys. Lett.* 12, 132, 1964.
- [12] P. Higgs, Broken Symmetries and the Masses of the Gauge Bosons, *Phys. Lett.* 13, 508, 1964.
- [13] P. Higgs, Spontaneous Symmetry Breakdown without Massless Bosons, *Phys. Rev.* 145, 1156, 1966.

- [14] Results of the Tevatron Higgs Sensitivity Study, CDF and DØ Collaborations, FERMILAB-PUB-03/320-E, October 2003.
- [15] P. Fernandez *et al.*, “Combined Upper Limit on Standard Model Higgs Boson Production at CDF for Summer 2007”, [http://www-cdf.fnal.gov/physics/new/hdg/results/combcdf\\_070810/](http://www-cdf.fnal.gov/physics/new/hdg/results/combcdf_070810/)
- [16] J. Reising. Fermilab History and Archives Project. <http://history.fnal.gov/>, 2007.
- [17] F. Abe *et al.*, “Observation of Top Quark Production in  $p\bar{p}$  Collisions with the Collider Detector at Fermilab”, *Phys. Rev. Lett.* 74, 2626, 1995.
- [18] S. Abachi *et al.*, “Observation of the Top Quark”, *Phys. Rev. Lett.* 74, 2632, 1995.
- [19] Y. Mutaf. DØ Ph.D Thesis. SUNY at Stony Brook, 2005.
- [20] Fermilab Accelerator Division web pages and internal documents. <http://www-bd.fnal.gov>, 2007.
- [21] Fermilab Run II Handbook. <http://www-bd.fnal.gov/runII/index.html>, 2003.
- [22] C.W. Schmidt and C.D. Curtis. A 50 mA Negative Hydrogen Ion Source. *IEEE Transactions on Nuclear Science*, NS-26, 4120 (1979).
- [23] J. Thompson. Introduction to Colliding Beams at Fermilab. FERMILAB-TM-1909, 1994.
- [24] D. Patterson. The FNAL Linac. Fermilab Internal Note (unpublished). 1986.
- [25] The Fermilab Booster Rookie Book. [http://www-bdnew.fnal.gov/operations/rookie\\_books/Booster\\_V3\\_1.pdf](http://www-bdnew.fnal.gov/operations/rookie_books/Booster_V3_1.pdf) June 2006.
- [26] The Fermilab Main Injector Technical Design Handbook. [http://www-fmi.fnal.gov/fmiinternal/MI\\_Technical\\_Design/index.html](http://www-fmi.fnal.gov/fmiinternal/MI_Technical_Design/index.html) November 1995.
- [27] The Fermilab Anti-Proton Source Rookie Book. [http://www-bdnew.fnal.gov/operations/rookie\\_books/Pbar\\_V1\\_1.pdf](http://www-bdnew.fnal.gov/operations/rookie_books/Pbar_V1_1.pdf) July 2006.
- [28] The Tevatron Operations Terminology. <http://www.fnal.gov/pub/now/definitions/quench.html> July 2002.

- [29] The Fermilab Tevatron Rookie Book [http://www-bdnew.fnal.gov/operations/rookie\\_books/Tevatron\\_v1.pdf](http://www-bdnew.fnal.gov/operations/rookie_books/Tevatron_v1.pdf) September 2006.
- [30] The Upgraded D0 Detector. *Nucl. Instrum. Methods A* {565}, 463 (2006).
- [31] J. Brzezniak *et al.*, Conceptual Design of a 2 Tesla Superconducting Solenoid for the Fermilab DØ Detector Upgrade. FERMILAB-TM-1886, 1994.
- [32] P.Balm *et al.*, Magnetic Field Monitors for the DØ Solenoid. DØ Internal Note #3977 (2001).
- [33] DØ Collaboration. Silicon Tracker Technical Design Report. DØ Internal Note #2169 (1994).
- [34] DØ Collaboration. Central Fiber Tracker Technical Design Report. DØ Internal Note #4164 (1999).
- [35] M. Adams *et al.*, Central Preshower Detector Technical Design Report. <http://d0server1.fnal.gov/users/qianj/CPS/index.htm> January 1996.
- [36] K.D. Signore *et al.*, A Core Dump of Useful Information About the Central Preshower Detector. <http://d0server1.fnal.gov/users/qianj/CPS/index.htm> April 1999.
- [37] S. Abachi *et al.*, The DØ Collaboration: The DØ Detector. *Nucl. Instrum. Methods A* {338}, 185 (1994).
- [38] J. Krane, DØ Ph.D Thesis. University of Nebraska, 1998.
- [39] L. Sawyer *et al.*, Technical Design Report of the Upgrade of the ICD for DØ Run II. DØ Internal Note #2686 (1997).
- [40] A. Haas, DØ Ph.D Thesis. University of Washington, 2004.
- [41] B.S. Acharya *et al.*, Technical Design Report of the Central Muon System. DØ Internal Note #3365 (1998).
- [42] G. Alexeev *et al.*, Technical Design Report for the DØ Forward Muon Tracking Detector Based on Mini-drift Tubes. DØ Internal Note #3366 (1997).

- [43] T. Edwards *et al.*, Determination of the Effective Inelastic  $p\bar{p}$  Cross Section for the DØ Run II Luminosity Measurement. FERMILAB-TM-2278-E, 2004.
- [44] M. Abolins *et al.*, DØ Run II Level 1 Trigger Framework Technical Design Report. [http://www.pa.msu.edu/hep/d0/ftp/l1/framework/l1fw\\_tdr\\_05june98.txt](http://www.pa.msu.edu/hep/d0/ftp/l1/framework/l1fw_tdr_05june98.txt), 1998.
- [45] D. Edmunds *et al.*, Technical Design Report for the Level 2 Global Processor. DØ Internal Note #3402 (1998).
- [46] M. Adams *et al.*, Level 2 Calorimeter Preprocessor Technical Design Report. DØ Internal Note #3651 (1999).
- [47] A. Boehnlein *et al.*, Description of the DØ L3 Trigger software components. DØ Internal Note #3630 (1999).
- [48] T. Sjöstrand, L. Lönnblad, S. Mrenna and P. Skands ‘‘PYTHIA 6.3: Physics and manual’’, [arXiv:hep-ph/0308153](https://arxiv.org/abs/hep-ph/0308153), 2003.
- [49] M. L. Mangano, M. Moretti and R. Pittau, ‘‘Multijets Matrix Elements and Shower Evolution in Hadronic Collisions’’, *Nucl. Phys.* **B32**, 343. [arXiv:hep-ph/0108069](https://arxiv.org/abs/hep-ph/0108069), 2002.
- [50] M. L. Mangano, *et al.* ‘‘ALPGEN, a generator for hard multiparton processes in hadronic collisions’’, [arXiv:hep-ph/0206293](https://arxiv.org/abs/hep-ph/0206293), 2003.
- [51] A. Pukhov, *et al.* ‘‘CompHEP - a package for evaluation of Feynman diagrams and integration over multi-particle phase space’’, [arXiv:hep-ph/9908288v2](https://arxiv.org/abs/hep-ph/9908288v2), 2000.
- [52] J. Pumplin *et al.* New Generation of Parton Distributions with Uncertainties from Global QCD Analysis, [arXiv:hep-ph/0201195v3](https://arxiv.org/abs/hep-ph/0201195v3), 2002.
- [53] S. Gieseke, ‘‘Event Generators- New Developments’’, [arXiv:hep-ph/0210294v1](https://arxiv.org/abs/hep-ph/0210294v1), 2002.
- [54] V. N. Gribov, L. N. Lipatov. *Sov.J. Nucl. Phys.* **15**:438, 1972.
- [55] G. Altarelli and G. Parisi. *Nucl. Phys.* **B126**:298, 1977.
- [56] L. Dokshitzer. *Sov. Phys. JETP* **46**:641, 1977.
- [57] S. Höche *et al.*, ‘‘Matching Parton Showers and Matrix Elements’’, [arXiv:hep-ph/0602031v1](https://arxiv.org/abs/hep-ph/0602031v1), 2006.

- [58] M. L. Mangano, "Higher Order QCD Processes - ALPGEN", CERN Lecture,  
<http://www.wlap.org/atlas/computing/tutorials/montecarlo/2004/20040622-umwlap002-02-mangano/20040622-umwlap002-02-mangano.tgz>, 2004.
- [59] R. Michael Barnett, Howard E. Haber and G. L. Kane, "Implications of a systematic study of the CERN monojets for supersymmetry", *Phys. Rev. Lett.* 54(18):1983-1986, 1985.
- [60] Y. Fisyak and J. Womersley, "DØ GEANT Simulation of the Total Apparatus Response", DØ Internal Note #3191, 1997.
- [61] S. Eno *et al.*, DØSim <http://www-d0.fnal.gov/computing/MonteCarlo/simulation/d0sim.html>, 2001.
- [62] S. Agostinelli *et al.*, "GEANT4 - A Simulation Toolkit", *Nucl. Instrum. Methods* **A506**:250-303, 2003.
- [63] Fermilab Accelerator Division web page, <http://www-bdnew.fnal.gov/operations/lum/plum.gif>, 2007.
- [64] "Run II Software Algorithms", <http://www-d0.fnal.gov/computing/algorithms/#intro>
- [65] "Online measurement of Beam Luminosity and Exposed Luminosity for Run II",  
[http://www.pa.msu.edu/hep/d0/ftp/l1/framework/exposure\\_groups/measuring\\_luminosity\\_online.txt](http://www.pa.msu.edu/hep/d0/ftp/l1/framework/exposure_groups/measuring_luminosity_online.txt)
- [66] "The Updated DØ Luminosity Determination", DØ Internal Note #4328, 2004.
- [67] A. Khanov, "HTF: Histogramming Method for Finding Tracks. Algorithm Description", DØ Internal Note #3778, 2000.
- [68] G. Borissov, "Ordering a Chaos... Technical Details of AA Tracking", All DØ Meeting, 2003.
- [69] P. V. C. Hough, "Machine Analysis of Bubble Chamber Pictures", Int. Conf. on High Energy Accelerators and Instrumentation, CERN, 1959.

- [70] R. Fruhwirth, "Application of Kalman Filtering to Track and Vertex Fitting", *Nucl. Instrum. Methods* **A262**:444-450, 1987.
- [71] C. Tully and A. Schwartzman, "Primary Vertex Reconstruction by means of Adaptive Vertex Fitting", DØ Internal Note #4918, 2005.
- [72] A. Schwartzman and M. Narain, "Vertex Fitting means of Kalman Filter Technique", DØ Internal Note #3907, 2001.
- [73] S. Protopopescu, "EM Reconstruction Algorithms",  
<http://www-d0.fnal.gov/d0dist/dist/packages/emreco/devel/doc/EMReco.ps>,  
1999.
- [74] L. Duflot and M. Ridel, "The CellNN Algorithm: Cell Level Clustering in the DØ Calorimeter", DØ Internal Note #3923, 2001.
- [75] F. Beaudette, J.-F. Grivaz, "Road Method: An Algorithm for the Identification of Electrons in Jets", DØ Internal Note # 3976, 2002.
- [76] "Electron Likelihood Study", A. Kumar *et al.*, DØ Internal Note #4769, 2005.
- [77] M. Narain, "Electron Identification in the DØ Detector", Fermilab Meeting, DPF 92 FERMILAB-CONF-93-054-E, 1992.
- [78] M. Narain, U. Heintz, "A Likelihood Test for Electron ID", DØ Internal Note #2386, 1994.
- [79] N. Hadley, "Cone Algorithm for Jet Finding", DØ Internal Note #904, 1989.
- [80] G. C. Blazey *et al.*, "Run II Jet Physics", hep-ex/0005012 v2, 2000.
- [81] F. Aversa *et al.*, "Toward a Standardization of Jet Definition", Proceedings of Research Directions for the Decade. ISBN: 2147483647, 1990.
- [82] C. Gerber *et al.*, "Taggability in Pass2 p14 Data", DØ Internal Note #4995, 2005.
- [83] A. Schwartzman, M. Narain, "Track-Jet Studies using 3D Simple Jet Cone Algorithm", DØ Internal Note #3919, 2001.

- [84] L. Feligioni *et al.*, “Update on  $b$ -quark Jet Identification with Secondary Vertex Reconstruction using DØRECO p14”, DØ Internal Note #4414, 2004.
- [85] R. Demina *et al.*, “ $b$ -tagging with Counting Signed Impact Parameter method”, DØ Internal Note #4049, 2002.
- [86] D. Bloch *et al.*, “Performance of the JLIP  $b$ -tagger in p14”, DØ Internal Note #4348, 2004.
- [87] K. Hagiwara *et al.*, (PDG group) *Phys. Rev. D* 66, 2002.
- [88] G. Abbiendi *et al.*, (OPAL collaboration) *Eur. Phys. J. C* 85 73, 1999.
- [89] K. Hanagaki, J. Kasper, “Identification of  $b$ -jet by Soft Muon”, DØ Internal Note #4867, 2005.
- [90] G. Bernardi, Talk titled “Higgs Status and Plans for Summer”, May 2006.
- [91] T. Scanlon, “ $b$ -Tagging and the Search for Neutral Supersymmetric Higgs Bosons at DØ”, Ph.D. Thesis, Oct 2006.
- [92] J. R. Vlimant *et al.*, “Technical Description of the T42 Algorithm for the Calorimeter Noise Suppression”, DØ Internal Note #4146, 2003.
- [93] The ROOT System Homepage at <http://root.cern.ch>
- [94] Common Samples Group, “p17 Fixed Data and Monte Carlo for Summer”, <http://www-d0.fnal.gov/Run2Physics/cs/skimming/fixPass2p170903.html>
- [95] `lm_access` package documentation at [http://www-d0.fnal.gov/d0dist/dist/packages/lm\\_access/devel/doc/](http://www-d0.fnal.gov/d0dist/dist/packages/lm_access/devel/doc/)
- [96] N(NLO) T, Nunnemann, “Cross-Sections and K-Factors for Various Processes with Modern Parton Distribution Functions”, [http://www-clued0.fnal.gov/~nunne/cross-sections/nnlo\\_xsect.html](http://www-clued0.fnal.gov/~nunne/cross-sections/nnlo_xsect.html)
- [97] J. Hays *et al.*, “Single Electron Efficiencies in p17 Data and Monte Carlo Using d0correct from Release p18.05.00”, DØ Internal Note #5105, 2006.



- [98] DØ Trigger Simulator (TrigSim) Homepage, <http://www-d0.fnal.gov/computing/trigsim/trigsim.html>
- [99] V. Kaushik *et al.*, ‘Electron Trigger Efficiencies using Calorimeter Information in p17 Data’, DØ Internal Note #5138, 2006.
- [100] D. Gillberg *et al.*, ‘Measuring Jet Response using the Missing  $E_T$  Projection Fraction Method in  $\gamma$  + jet Events’, DØ Internal Note #4571, 2004.
- [101] ‘Jet Energy Scale and Resolutions Group public results page’, [http://www-d0.fnal.gov/phys\\_id/jes/public/plots\\_v7.1/](http://www-d0.fnal.gov/phys_id/jes/public/plots_v7.1/)
- [102] Jet Energy Scale Group, ‘Certified Jet Energy Scale Plots’, [http://www-d0.fnal.gov/phys\\_id/jes/d0\\_private/certified/v07-01-02/jetcorr.ps](http://www-d0.fnal.gov/phys_id/jes/d0_private/certified/v07-01-02/jetcorr.ps)
- [103] G. C. Blazey *et al.*, ‘Run II Jet Physics: Proc. of QCD and Weak Boson Physics in Run II’, hep-ex/000501, 2000.
- [104] N. Makovec and J-F. Grivaz, ‘Shifting, Smearing and Removing Simulated Jets’, DØ Internal Note #4914, 2005.
- [105] A. Harel *et al.*, ‘Combined JetID efficiency’, DØ Internal Note #5218, 2006.
- [106] S. Trincaz-Duvoid and P. Verdier, ‘Missing ET Reconstruction in p17’, DØ Internal Note #4474, 2004.
- [107] S. Calvet *et al.*, ‘Towards Missing ET Certification and Unclustered Energy Studies’, DØ Internal Note #4927, 2005.
- [108] T. Scanlon *et al.*, ‘Performance of the NN  $b$ -tagging Tool on p17 Data’, DØ Internal Note #5213, 2007.
- [109] T. Scanlon and M. Anastasoiaie ‘Performance of the NN  $b$ -tagging Tool on Pass2 Data’, DØ Internal Note #4890, 2005.
- [110] B. Clément, *et al.*, ‘SystemD or how to get Signal, Backgrounds and their Efficiencies with Real Data’, DØ Internal Note #4159, 2003.
- [111] DØ Collaboration, B. Abbott *et al.*, Phys. Rev. Lett. 94, 091902, 2005.

- [112] DØ Collaboration, B. Abbott *et al.*, DØ Internal Note 5054-CONF,  
<http://www-d0.fnal.gov/Run2Physics/WWW/results/prelim/HIGGS/H18/H18.pdf>
- [113] CDF Collaboration, “Search for  $H \rightarrow b\bar{b}$  Produced in Association with W Bosons in  $p\bar{p}$  Collisions at  $\sqrt{s} = 1.96$  TeV”, hep-ex/0512051, Accepted in Phys. Rev. Lett.
- [114] CDF Collaboration, A. Abulencia *et al.*, ICHEP, Moscow, 2006.
- [115] DØ Data Quality Group, “Finding out what is good/bad Data”, [http://www-d0.fnal.gov/computing/data\\_quality/d0\\_private/forusers.html](http://www-d0.fnal.gov/computing/data_quality/d0_private/forusers.html)
- [116] L. Duflot *et al.*, “cal\_evt\_quality package”, DØ Internal Note #4614, 2004.
- [117] DØ Collaboration, “A Search for  $WH$  Production at  $\sqrt{s} = 1.96$  TeV with 1  $fb^{-1}$  of Data”, DØ Internal # Note 5357-CONF, March 2007.
- [118] L. Sonnenschein and G. Bernardi, “Search for  $Wb\bar{b}$  and  $WH$  Production in  $p\bar{p}$  Collisions at  $\sqrt{s} = 1.96$  TeV”, DØ Internal Note #4633, 2005.
- [119] M. Klute, “Measurement of the  $t\bar{t}$  cross section at  $\sqrt{s} = 1.96$  TeV in  $\mu$ -plus-jets events”, DØ Internal Note #4185, 2003.
- [120] E. Busato, Jet ID Meeting, Presentation slides can be found at the following URL:  
[http://www-d0.fnal.gov/d0upgrade/d0\\_private/software/jetid/meetings2003/Jul08/busato.ppt](http://www-d0.fnal.gov/d0upgrade/d0_private/software/jetid/meetings2003/Jul08/busato.ppt)
- [121] Luminosity ID group, “Improved Determination of the DØ Luminosity”, DØ Internal Note #5140, 2006.
- [122] G. Bernardi, S. Choi and K. Hanagaki, “Cross Section Errors Used in the Higgs Searches”, DØ Internal Note #5043. 2006.
- [123] J. Campbell and K. Ellis, MCFM, “Monte Carlo for FeMtobarn Processes”, <http://mcfm.fnal.gov>
- [124] G. J. Feldman and R.D. Cousins, *Phys. Rev. D* **57**, 3873, 1998.
- [125] R. T. Cos, *Am. J. Phys* **14** 1946.
- [126] W. Fisher, “Calculating Limits for Combined Analyses”, DØ Internal Note #4975, 2006.

- [127] A. G. Frodsen, O. Skeggestad and H. Töfte, “Probability and Statistics in Particle Physics”, Universitetsforlaget, ISBN 82-00-01906-3, 1979.
- [128] M. G. Kendall and A. Stuart, “The Advanced Theory of Statistics”, vol. 2, 2<sup>nd</sup> ed., ch. 24. Charles Griffen & Company Limited, London, SBN 85264 011 0, 1967.
- [129] J. W. Tukey, “Exploratory Data Analysis”, Vol. 1, Chapter 7, Addison-Wesley, Reading, Mass., 1970 (limited preliminary edition)
- [130] T. Junk, *Nucl. Instrum. Methods A* 434:435, 1999.
- [131] A. Read, *J. Phys. G: Nucl. Part. Phys.* **28** 2693, 2002.
- [132] W. Fisher, “Systematics and Limit Calculations”, DØ Internal Note #5309, 2007.
- [133] G. Bernardi, Y. Enari, W Fisher, V Kaushik, J. Lellouch and M Sanders, “Search for  $WH$  Production using Neural Net Selection with  $1.7 \text{ fb}^{-1}$  of Run IIa Data”, DØ Internal Note #5470, Aug. 2007.
- [134] DØ Collaboration, “Search for  $WH$  Production using a Neural Network Approach”, DØInternal Note #5472-CONF, Aug. 2007.

## BIOGRAPHICAL STATEMENT

Venkatesh Kaushik earned his B.E in 1998 from Bangalore University, India, majoring in Mechanical Engineering. He arrived in U.S.A to pursue graduate studies and in 2002 he completed the requirements for M.S in Computer Science and Engineering at University of Texas at Arlington (UTA). After receiving M.S. in Physics in 2004, he carried out his doctoral research at Fermilab in Batavia, IL, and graduated with a Ph.D. in Physics from UTA in the fall of 2007. He looks forward to a successful research and teaching career as a physicist.